Italian National Agency for New Technologies,
Energy and Sustainable Economic Development

High Performance Computing on CRESCO infrastructure: research activities and results 2010-2011

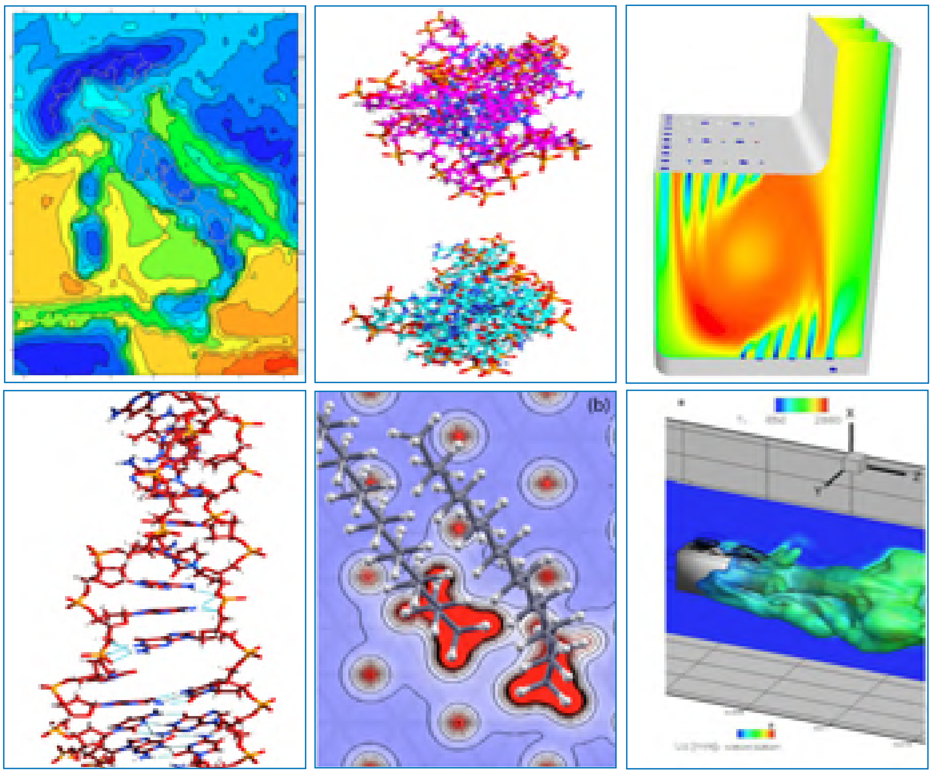

July 2012

This report was prepared by the New Projects and Web Applications Laboratory of ENEA's Technical Unit for Information Systems and ICT Developments (UTICT-PRA), from contributions provided by a selection of users of the CRESCO infrastructure.

Scientific Editor: *Delinda Piccinelli*, Enea, UTICT-PRA, Cr Frascati
Cover: *Amedeo Trolese*, Enea, UTICT-PRA, Cr Frascati

ISBN: 978-88-8286-268-8

INDEX

PREFACE

Following the standard established in previous years, this report presents a collection of papers on a range of scientific activities carried out with the extensive use of CRESCO clusters and of the entire ENEA-GRID computational infrastructure. In this new report, covering the period of activity from July 2010 to December 2011, scientific domains such as climate analysis, materials science, nuclear technologies, computational fluid dynamics are represented, which are the "traditional" key topics of ENEA are represented; but, also, interesting results are reported on biological systems, biomedical applications, and mathematical finance, testifying for an enlargement in scope of activities carried out on the facility by ENEA and its partners.

CRESCO, an acronym for Computational Centre for Research on Complex Systems, was established in 2008 in Portici research Centre through a grant provided in the framework of the European Regional Development Funds, and is now a facility based on Linux x86_64 with over 3,500 cores and 300 TB of raw data storage, connected through a 2x1 Gbits link to the Italian academic network infrastructure, managed by GARR. The facility is the main component of ENEA-GRID infrastructure, integrating all ENEA computational resources in a single logical environment following the computing GRID approach. Other smaller Linux CRESCO clusters are now in operation in the other ENEA sites, Frascati, Casaccia, Brindisi and Trisaia, for a total of about 800 cores and some computational activity is still performed on SP5 systems in Frascati.

As in previous years, CRESCO HPC systems have operated with maximum availability rate providing computational services both to ENEA research teams and to external users from academic and industrial communities. The utilization rate was steadily very high, effectively saturating the available computing power.

ENEA has been recently granted by the Italian Ministry of Research a project for new scientific infrastructures to be financed through the European Regional Development Funds. The project, among other things, will make possible the renewal of the computational equipment in our Portici Research Centre, and by the middle of 2013 a new CRESCO cluster with capabilities increased by one order of magnitude will be available. On one hand, this barely allows us to keep pace with the trends of a fast-moving world such as ICT; on the other, it will make available to our scientific communities an instrument to pursue answers to a new range of questions currently beyond feasibility.

The CRESCO Team

Technical Unit for Information Systems and ICT Development

ENEA-GRID infrastructure

D.Abate, F.Ambrosino, G.Aprea, T.Bastianelli, F.Beone, G.Bracco,
M.Caporicci, M.Chinnici, R.Ciavarella, A.Colavincenzo, A.Cucurullo,
P.D’Angelo, A.DellaCasa, M.DeRosa, A.Funel, G.Furini, D.Giammattei,
S.Giusepponi, R.Guadagni, G.Guarnieri, A.Mariano, G.Mencuccini,
C.Mercuri, S.Migliori, P.Ornelli, S.Pecoraro, A.Perozziello, A.Petricca,
S.Pierattini, S.Podda, F.Poggi, G.Ponti, A.Quintiliani, S.Raia,
A.Rocchi, A.Santoro, C.Sciò, F.Simoni.

ENEA – *Unità Tecnica Sviluppo Sistemi per l’Informatica e l'ICT* (UTICT)

Abstract

ENEA, the Italian Agency for New Technologies, Energy and Sustainable Economic Development, has 12 different research sites located in northern, central and southern Italy. In particular, 6 of them host computational facilities to allow the execution of serial and parallel jobs and advanced graphical applications. Those resources consist in a multitude of hardware and software platforms, composed by libraries, compilers, remote applications, cloud computing environment, and virtual labs. In this paper, we provide an insight of the ENEA-GRID infrastructure [1], whose main aim is to provide a unified and homogenous environment for the computational resources in ENEA, in such a way that researchers and their collaborators can perform their work despite of the location of the specific machine or of the specific hardware/software platform that is employed. ENEA-GRID manages heterogeneous resources and multi-platform systems in an optimized and transparent way.

1. Introduction

The availability of powerful computing systems, distributed over wide area and connected by high speed networks, has led to the development of the concept of computational GRID. The GRID is an attempt to provide a unified approach to heterogeneous computational resources located in distant sites and belonging, in the most general case, to institutions having very different types of activities.

The implementation of a computational GRID requires the definition of a set of tools for the uniform access to the available computing and storage resources. These tools must also assure the security of the grid operation and provide proper monitoring facilities.

The GRID approach has permitted to integrate in a unified system all the high performance computational resources available inside ENEA, the Italian Agency for New Technologies, Energy and Environment. ENEA activity takes place in 12 different sites located in northern, central and southern Italy. Local computational facilities are managed in 6 computer centers in each of the main sites, including resources for serial and parallel computing and advanced graphical post processing.

The ENEA-GRID infrastructure [1] permits to access to all these resources as a single virtual system, with an integrated computational power of more than 40 Tflops, provided by several multiplatform systems, i.e., AIX SP5 (~256 CPU), Linux x86_64 (~5000 cores provided by CRESCO cluster, described later in section 3), and special dedicated systems (e.g., GPU). The infrastructure has been in development since 1998. It has the following features:

- It offers a production quality, service oriented system;
- It covers most of the computational resources belonging to ENEA INFO Scientific Computation Service, connected in a Wide Area Network;
- It provides a unified user environment and an homogeneous access method for all ENEA researchers irrespective of their location;
- It implements tools to facilitate the integration of departments and individual resources and support to experimental facilities;
- It offers shared software among different platforms;
- It furnishes cloud computing based services, such as remote storage and virtualization.

The choice of ENEA-GRID components has been based on mature components, both proprietary and open sources, in order to provide good performances and service reliability. Those components are:

1. a unified graphical user interface (Java based web access provide by the FARO portal);
2. a resource manager, LSF (Load Sharing Facility) Multicluster;
3. a distributed file system, AFS (Andrew File System);
4. a parallel file system, GPFS (General Purpose File System), for high perrformance calculus;
5. an autentication system based on Kerberos 5;
6. a resource monitoring system based on the Zabbix open source software.

The rest of the paper is organized as follows. In section 2, we will describe each of the ENEA-GRID software main components. Section 3 provides a summarized description of the hardware resources in ENEA-GRID. Finally, section 4 illustrates the access modes to ENEA-GRID resources.

2. ENEA-GRID components

The ENEA-GRID infrastructure is based on several software components which interact with each other to offer an integrated GRID system to each reasearcher in ENEA. All those components are well-established technologies available for many platforms, thus being more suited for the needs of a composite infrastructure as ENEA-GRID. Here, we describe each of those software components.

2.1 OpenAFS

AFS [2] is a geographically distributed filesystem, originally developed at Carnegie Mellon University and developed as a product by Transarc Corporation (now IBM Pittsburgh Labs). It offers a client-server architecture for federated file sharing and replicated read-only content distribution, providing location independence, scalability, security, and transparent migration capabilities. AFS is available for a broad range of heterogeneous systems including UNIX, Linux, MacOS X, and Microsoft Windows. IBM branched the source of the AFS product and made a copy of the source available for community development and maintenance. They called this release OpenAFS. In 2006, ENEA has migrated its whole AFS infrastructure from the original IBM/Transarc implementation to OpenAFS.

An AFS infrastructure consists of DBservers (for storing metadata and authorization information), file servers (for storing actual files) and "kaservers" (to manage authentication, now deprecated). The DBservers host three different types of servers: *vlserver* (stores metadata), *ptsserver* (stores authorization information) and *backup server* (stores metadata for the snapshot volumes, described below). Additionally, any machine that wants to access AFS has to install a software called AFS client, which as written above is available for many different architectures.

A key feature of OpenAFS, which is exploited by ENEA-GRID, is its ability to differentiate the software it exposes among different platforms, through a peculiar parsing mechanism of filesystem paths. For instance, if a directory is named "@sys", the machine access a different directory whose name changes according to the software/hardware that is accessing AFS. In this way, any x86 machine with linux may access the *cc* version compiled for x86/linux, while a PowerPC with AIX by using the same path will access the cc version compiled for powerpc/AIX.

AFS authentication mechanism is based upon an internal implementation of Kerberos 5, which basically works assigning a token to each user, and the access to directories in AFS is granted according to the token available to the user. There are two different ways to use those tokens: *(i)* the token is assigned to all the processes belonging to the same user across the whole machine; *(ii)* the token is assigned only to the processes spawned by a specific shell (named *pagsh*), instead of being available to all the user processes across the machine. This last mechanism is the one most often used because of its versatility. The connected authorization mechanism is based on an ACL mechanism, much more powerful and flexible than the standard POSIX permissions.

AFS space is organized in logical units called *volumes*. Each AFS volume can be a read-write volume (fully accessible space), or a read-only one (a replica). Finally, a further feature of AFS is its ability to maintain a snapshot of the filesystem, stored in a special optimized backup volume. In ENEA, this snapshot is taken every night.

2.2 Kerberos 5

Kerberos [3] is a network add-on protocol that allows users to authenticate themselves through the services of a secure server. Services such as remote login, remote copy, secure inter-system file copying and other high-risk tasks are made considerably safer and more controllable.

Kerberos can be described as an identity-verifying proxy system. It can also be described as a trusted third-party authentication system. Kerberos provides only one function – the secure authentication of users on the network. It does not provide authorization functions (what users are allowed to do) or auditing functions (what those users did). After a client and server have used Kerberos to prove their identity, they can also encrypt all of their communications to assure privacy and data integrity as they go about their business.

There are two main different implementations of Kerberos 5, one from the Royal Institute of Technology, called Heimdal, and the other from the Massachussets Institute of Technology. In 2007 ENEA, has migrated its whole authentication infrastructure from the native Kerberos 4 implementation of AFS to the Kerberos 5 implementation of MIT.

2.3 LSF Multicluster

LSF MultiCluster [4] is a proprietary software developed by Platform, which extends an organization's range to share resources beyond a single Platform LSF cluster to span multiple geographically dispersed clusters, which is one of the typical GRID characteristics**.** It provides a single machine image when connecting individual High Performance Computing (HPC) cluster environments together. With Platform LSF MultiCluster, local ownership and control is maintained, ensuring priority access to any local cluster while providing global access across an enterprise's entire HPC infrastructure. The key features of LSF Multicluster that allows to use it for ENEA-GRID are its support for multiple Platforms/OS, its complex scheduling abilities, and its ability to make job exchange among different clusters (which allows a geographically distributed job submission infrastructure). LSF Multicluster can work in two different modalities, that are *(i)* Job forwarding, and *(ii)* Resource Leasing. In particular, Resource Leasing mode is basically a static allocation of resources to an external cluster, and as such is prone to waste. Additionally, the Resource Leasing technique is very hierarchical and unflexible in its configuration. Given the heterogeneous and unpredicatable traffic in ENEA, the chosen approach is Job Forwarding, since its loose and peer-federated approach is more tailored towards ENEA-GRID needs.

The LSF Multicluster software consists in a Master Batch server per local site, which must reside on one dedicated machines (more than one if fault tolerance is needed), and a license server, which usually also resides on a license-dedicated machine.

2.4 Zabbix monitoring system

ENEA-GRID resources are continuously monitored by means of the Zabbix [5] software. It is an open source system that exploits the hierarchical distributed organization of the ENEA-GRID WAN to monitor network components, resources and calculus services [6]. Zabbix communications in a distributed environment are client-server based, and such a feature allows to improve monitoring performances and data elaboration. The main characteristics of Zabbix in WAN network monitoring tasks are:

- Distributed real-time monitoring;
- Scalability;
- Web based monitoring and administrator console;
- Flexibility and extensibility (add-ons facilities provided by custom external scripts);
- Supporting of several operating system monitoring (e.g., Linux, AIX HP-UX, MacOS, Solaris e Win32)
- Data storage on various database systems (e.g., MySQL, PostgreSQL, SQLite, and Oracle)

2.5 Cloud computing

ENEA-GRID has been developed in order to offer services and calculus resources in a ubiquitous and remote way. In fact, it exports remote storage facilities (with OpenAFS file system), remote software and *Virtual Labs* (cf. section 2.6), which consist in thematic areas accessible via web where researchers and their staff can find set of software and documentation regarding specific research areas, e.g., fluid dynamics, material science, etc.

It is clear that ENEA-GRID characteristics are very close to the ones required by the new modern *cloud computing* trends. Besides these feature, it have been recently adopted a software toolkit to furnish virtualization services to ENEA-GRID users. In this direction, it has been adopted OpenNebula [7] as the virtualization manager. It is an open source project that has ad-hoc instruments to create and manage a cloud computing environment. It is able to operate in distributed an heterogeneous infrastructures, exporting services to users in a simple way.

OpenNebula acts as a middleware by furnishing a new architectural level to handle and coordinate several aspects related to the cloud system, such as virtual machines, physical resources, cloud storage and networking system, as shown in *figure 1*.

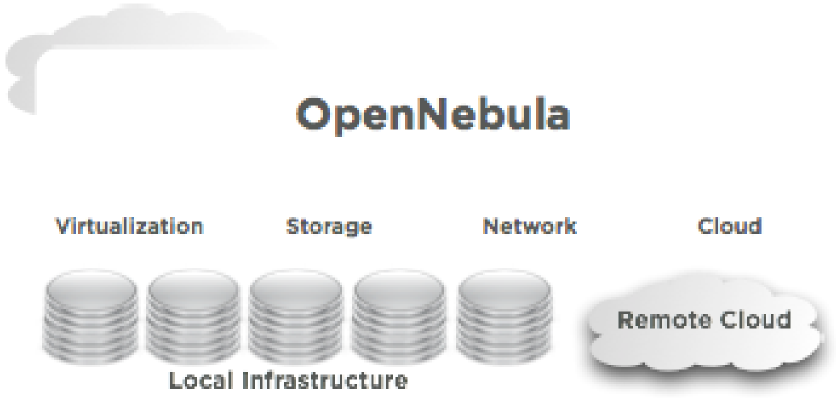

Figure 1 – *OpenNebula multi-tier conceptual architecture*

In ENEA-GRID, OpenNebula orchestrates user virtual machine handled by KVM as hypervisor [8]. Virtual machines are accessible via FARO ENEA-GRID web portal (cf. section 4.3) or via the Sunstone web portal, an administration tool in the cloud toolkit by which administrators can manage the whole cloud infrastructure and users are able to handle their virtual resources.

2.6 Virtual Labs

A *Virtual Lab* is an operating mode that allows the collaboration and the interaction among public and industrial actors to develop innovative applications, and knowledge exchange in specific areas. ENEA UTICT provides facilities to support scientific and applied research activities and services in several areas, which correspond to the related Labs:

- Material science
- Climate
- Nuclear fission
- Structure and material qualification
- 3D graphics
- Fluid dynamics

ENEA Virtual Labs furnish user support and encourage the adoption, the development, and the integration of techniques, methods, and computer science instruments, in order to support new planning activities. Virtual Lab facilities are available in ENEA-GRID via specific web portals (e.g., Neptunius[1] for computational fluid dynamics and fluid structure interactions), where software toolkit and documentation for each specific area are available in a customized user interface. Moreover, Virtual Labs are also accessible via the main ENEA-GRID web portal, i.e., FARO (cf. section 4.3).

---

[1] http://www.afs.enea.it/project/neptunius/

3. ENEA-GRID Hardware Infrastructure

ENEA-GRID hardware infrastructure has been developed in such a way that it is able to support ENEA researcher main requests, which cover a wide spectrum of applications in the domains of simulation, modelling, data analysis and 3D visualisation.

Many research centers contribute with their resources which have been populated over the years both by ENEA internal resources and by resources from funded projects (CAMPUS, TELEGRID, CRESCO). The main computational centers in ENEA host CRESCO clusters [9], which are located in the following sites:

- ***Portici***: CRESCO1 (672 cores 4U), CRESCO2 (2720 cores blades), IB CISCO 70xx, DDR Intel Clovertown,Tigerton, Nehalem, Westmere
- ***Frascati***: CRESCOF (480 cores twin square 2U, GPFS), IB Qlogic 12300 QDR, AMD 6172 Magnycours
- ***Casaccia***: CRESCOC (192 cores, twin 1U), IB Qlogic Silverstorm DDR, AMD 2427 Istanbul
- ***Brindisi***: CRESCOB (80 cores, 4 U, GPFS), GEthernet, Intel Tigerton
- ***Trisaia***: CRESCOT (16 cores,4U) Intel Tigerton

4. ENEA-GRID Interface

ENEA-GRID provides a unified view of distributed resources. In order to furnish a friendly but powerful user interface, it is possible to access to the GRID in several ways, each of which exports the same facilities and features in a different layout to satisfy various user skills. In general, cluster access is guaranteed by logging into one of its front-end nodes, independently of the specific technology adopted. Front-end nodes are used only to provide a contact point between calculus resources and users and are employed to run LSF applications, to compile application, and for short script editing operations.

In the following, the main technologies to access the ENEA-GRID resources will be described.

4.1 SSH

SSH (Secure SHell) is the most traditional way to access Unix-based servers and calculus centers. It is a network protocol for secure data communication based on public-key cryptography to authenticate the remote computer and allow it to authenticate the user. SSH is typically used to log into a remote machine and execute commands, but it also supports tunneling, forwarding TCP ports and X11 connections; it can transfer files using the associated SSH file transfer (SFTP) or secure copy (SCP) protocols. SSH uses the client-server model.

To establish a connection between a user device and a server with a running SSH daemon it is necessary to adopt a SSH client program, which is commonly and natively present on most modern operating systems; otherwise, several freeware, open source, and commercial third-part applications are available.

4.2 NX

NX technology [10] is a program that handles remote X Window System connections. It is developed by the italian software house NoMachine and exploits data compression techniques to improve the performance of the native X display protocol, in order to provide a high user experience also on slow networks. In addition, it wraps remote connections in SSH sessions for encryption.

ENEA-GRID provides NX based access to clusters by means of ad-hoc front-end machines running the open source version of NX server (i.e., FreeNX).

4.3 FARO web portal

FARO (Fast Access to Remote Objects) [11] is the result of software integration process which aims to furnish a centralized access to resources and services in ENEA-GRID. FARO is a web-based application developed in Java and provides a scure access to the whole ICT infrastructure in ENEA by means of NX technology.

FARO is simple to use and does not require particular software installed on the user machine: it only needs a web browser supporting Java applet execution to access to ENEA-GRID/CRESCO computational resources. It offers facilities for submitting job in the GRID, to perform remote graphical eleborations, for remote desktop session, as shown in the following *figure*.

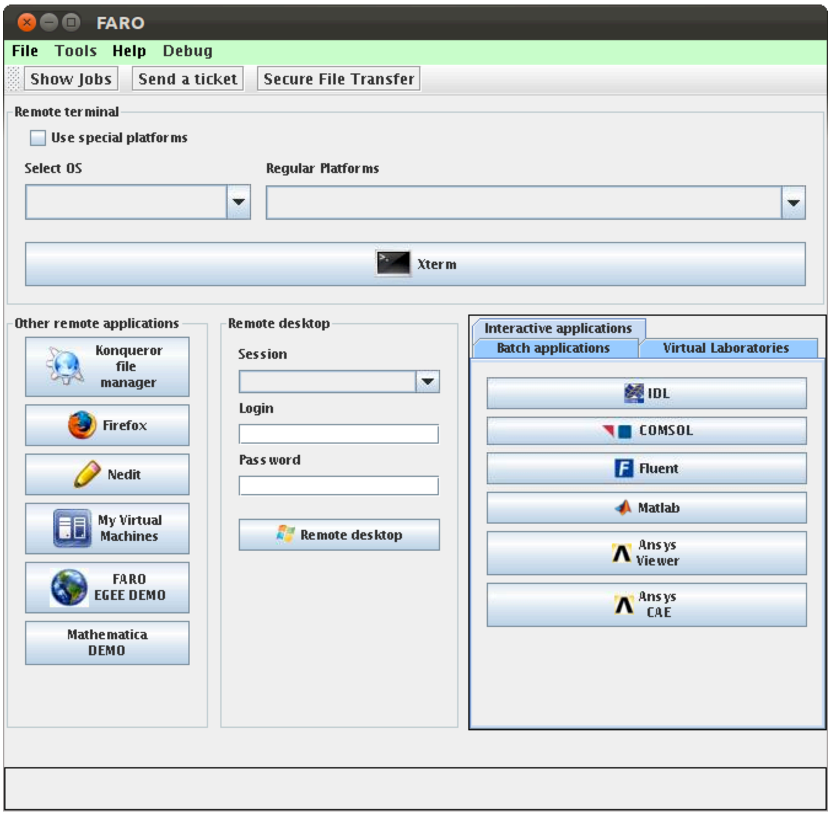

Figure 2 – *FARO web portal*

As it is possible to see in the figure, FARO has a set of sections which allow to interact with different modules in ENEA-GRID, such as remote terminal and desktop, virtual resources in the cloud infrastructures, remote applications, batch and interactive programs, and Virtual Labs.

References

[1] ENEA-GRID - http://www.eneagrid.enea.it/

[2] OpenAFS - http://openafs.org/

[3] Kerberos - http://web.mit.edu/Kerberos/

[4] LSF Multicluster - http://www.platform.com/workload-management/high-performance-computing/lp

[5] Zabbix - http://www.zabbix.com/

[6] Colavincenzo A., Petricca A., Giammattei D., Pecoraro S., Simoni F. *“Utilizzo di Zabbix per il Monitoring di risorse di calcolo e sistemi di storage su WAN in ambito GRID-Computing”* GARR Conference (2010)

[7] OpenNebula - http://opennebula.org/

[8] Ponti G., Secco A., Ambrosino F., Bracco G., Ciavarella R., Colavincenzo A., D'Angelo P., De Rosa M., Funel A., Guarnieri G., Giammattei D., Migliori S., Pecoraro S., Petricca A., Pierattini S., Podda S., Rocchi A., Sciò C. *“Esperimenti di Cloud Computing in ENEA-GRID”* GARR Conference (2011)

[9] Bracco G., Podda S., Migliori S., D’Angelo P., Quintiliani A., Giammattei D., De Rosa M., Pierattini S., Furini G., Guadagni R., Simoni F., Perozziello A., De Gaetano A., Pecoraro S., Santoro A., Sciò C., Rocchi A., Funel A., Raia S., Aprea G., Ferrara U., Novi D., Guarnirei G. *“CRESCO HPC System Integrated into ENEA-GRID Environment”* Final Workshop of the Grid Projects of the Italian National Operational Program 2000-2006 – Call 1575 (2009) pp. 151–155

[10] NX Technology - http://www.nomachine.com/

[11] Rocchi A., Pierattini S., Bracco G., Migliori S., Beone F., Sciò C., Petricca A. *“FARO: accesso WEB a risorse remote per l'industria e la ricerca”* GARR Conference (2010)

COMPUTATIONAL PERFORMANCES OF THE CRESCO HPC AMD OPTERON MAGNY-COURS CLUSTER

Agostino Funel

ENEA UTICT-HPC C. R. Portici

ABSTRACT

We present the results of computational performances measurements, in terms of floating point operations per second (flops), of one of the CRESCO (Computational Research Center for Complex Systems) [1] HPC (High Performance Computing) clusters belonging to ENEA-GRID infrastructure [2]. The cluster consists of 20 twin square (2 Rack Units) nodes, each with dual socket 12-Core AMD Opteron 6174 Magny-Cours, 2.2 GHz, 2 x 6 MB L3, 64 GB RAM for total 480 cores. The network interconnect is InfiniBand (IB) QLogic 12300 4X QDR 40 Gb/s. Computational performances have been measured by running HPL (High Performance Linpack) ([3], [4]), a benchmark widely used in the HPC community. We also report, a part the peak measure, how the flops rate varies with the memory load, and how cache hierarchy affects performances.

INTRODUCTION

It is not easy to define what is meant by computational performance of an HPC system. Intuitively, the more the number of mathematical operations can be performed per unit of time, the higher is the computational performance. The standard unit of measure is the flops, which is the number of floating point operations per second. There are many factors which may influence computer performances, for example I/O throughput, inter processor communication, memory hierarchy etc. Then, standard benchmarks have to be used to provide generally accepted results. There are many benchmarks around ([4], [5], [6]) and one of the most used is HPL. The HPL benchmark is used to rank supercomputers in the Top500 list ([7], [8]). The flops rate is evaluated by solving in parallel a dense linear system using LU factorization ([9], [10], [11]). HPL allows many parameters to be tuned and such a feature is useful for understanding how a supercomputer behaves when specific resources need to be stressed. Memory is a very important resource and its appropriate utilization is of the utmost importance for preventing waste of run time. In this work we use HPL to measure the best computational performance of the CRESCO HPC AMD Opteron Magny-Cours cluster and study how the system works at different levels of memory load. We also show how to exploit cache hierarchy according to the global memory load. In this way we give hints to users on how to tune their applications for using the cluster efficiently.

THE HPL BENCHMARK

In this section we briefly revisit the main features of the HPL benchmark. HPL solves a linear system of order *n*:

$$\mathrm{A} \cdot \mathrm{X} = \mathrm{B}, \quad A \in \Re^{n \times n}, \quad X, B \in \Re^{n} \qquad (1)$$

using LU factorization with row partial pivoting of the n by n+1 coefficient matrix:

$$P[A,B] = [[L,U],Y]. \quad (2)$$

P is the permutation matrix representing the row pivoting and L is the lower triangular matrix. P and L are applied to B as the factorization progresses. The solution is obtained by solving the upper triangular system:

$$U \cdot \mathrm{X} = Y. \quad (3)$$

The factorization requires $2n^3/3 - n^2/2$ operations and the solving phase $2n^2$ thus if t_s is the time to solution, the theoretical peak performance p_th (in Gflops/s) is given by:

$$p_{th} = \frac{\frac{2n^3}{3} + \frac{3n^2}{2}}{t_s} \cdot 10^{-9}. \quad (4)$$

There are many factors which influence the performances: latency and bandwidth of interconnection network, number of cores, cache and memory access etc. HPL allows to choose various parameters in order to match as best as possible the hardware characteristics of the system. The most relevant parameters are:

- n: the size of the problem which also determines the amount of memory. As each number is a double precision floating real which corresponds to 8 bytes, the memory request is about $8n^2$ bytes;
- n_B: the block size used for data distribution among processes and computation granularity;
- P × Q: a two dimensional grid of processes used to map the n by n+1 coefficient matrix. Before being mapped, the coefficient matrix are first partitioned into n_B by n_B blocks.

Under very general assumptions it can be shown that the HPL algorithm makes the leading term of time to solution t_s of order O(n^3). The time spent for communication is of order O(n^2). The HPL benchmark scales very well with the size n and the scaling does not depend strongly on the communication volume.

THE USED HPC SYSTEM

The HPL experiments were performed on the CRESCO AMD Opteron Magny-Cours cluster. This cluster is part of ENEA-GRID CRESCO infrastructure [1] and is located at the ENEA Frascati Research Centre. The cluster consists of 20 twin square (2 Rack Units) nodes, each with dual socket 12-Core AMD Opteron 6174 (Magny-Cours) processor, 2.2 GHz, 2x6 MB L3, 64 GB RAM for total 480 cores. The network interconnect is the high speed low latency InfiniBand (IB) QLogic 12300 4X QDR 40 Gb/s.

Figure 1 shows the AMD Opteron 6174 (Magny-Cours) processor. The 12-Core socket is symmetrically divided in two 6-Core parts each having a 6 MB L3 shared cache and 16 GB RAM. The RAM for each socket amounts to 32 GB. Each core has two independent caches: a 64 KB L1

and a 512 KB L2. The figure also show the presence of a HCA adapter which is QLogic type QLE7340, and Ethernet links.

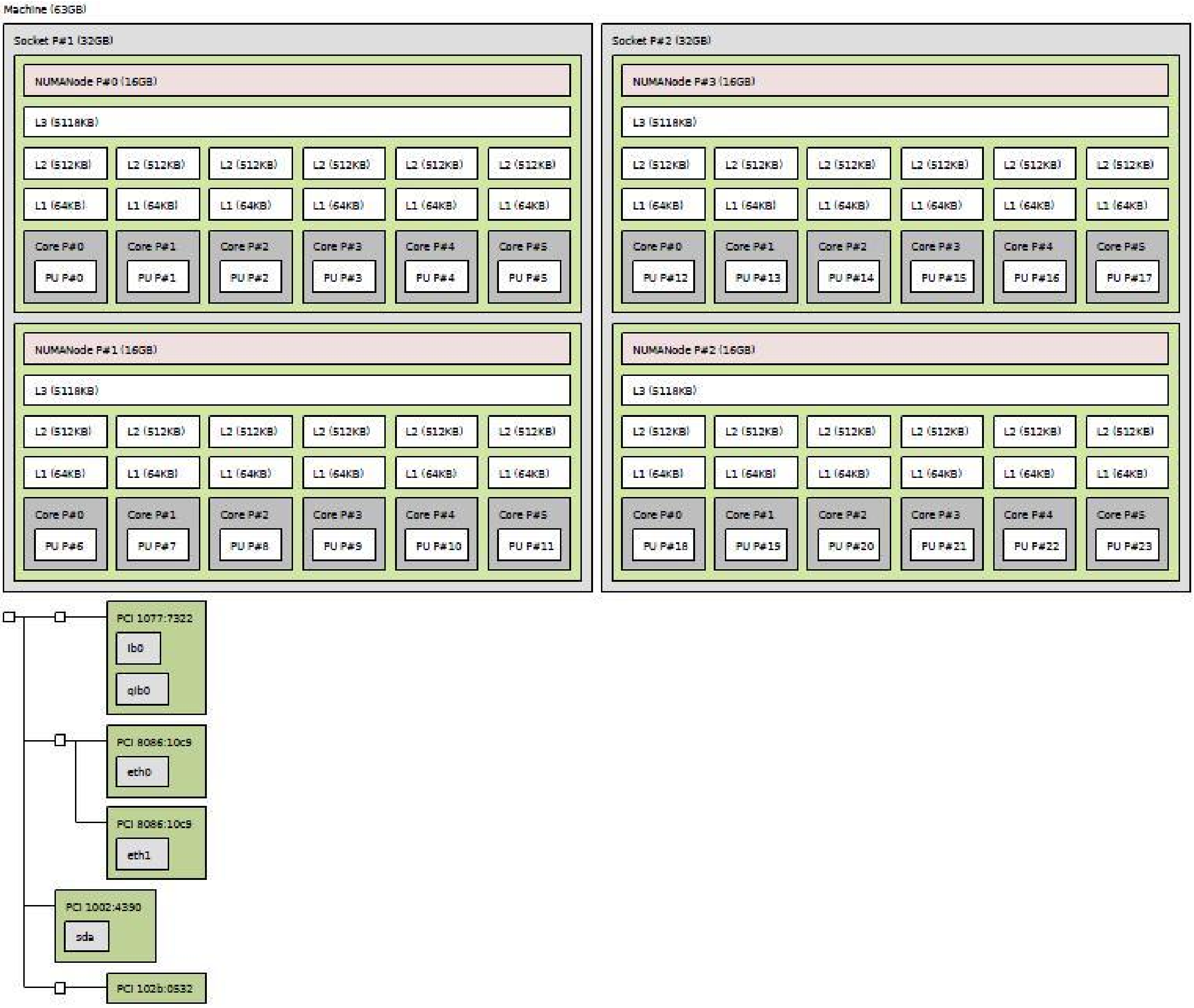

Figure1: *AMD Opteron 6174 dual 12-Core socket Magny-Cours processor.*

RESULTS

We present the experimental results obtained in the case of 1 nodes (24 cores) and 10 nodes (240 cores). In *table 1* are shown the theoretical and measured flops rates. The CRESCO Opteron Magny-Cours HPC cluster has an average efficiency of about 76%. The efficiency decreases of 2% when running HPL from 1 to 10 nodes. This is certainly also due to causes independent of CPU computation, like HPL initialization phase, spawning of processes, file system and memory access. However, the most important factor is the time spent in communication across the network which, thanks to the high speed InfiniBand interconnect, does not reduce sensibly the performances.

	Theoretical peak (Gflops/s)	Measured peak (Gflops/s)	Efficiency (%)
1 node (24 core)	211.2	162.9	77
10 nodes (240 cores)	1579.0	2112.0	75

Table 1: *HPL results for the CRESCO HPC Opetron Magny-Cours cluster.*

The dependence of flops rate on memory load is plotted in *figure 2* in the case of 10 nodes. The best result is obtained with 30% of global memory usage. When the memory required is 50% of the total available RAM (640 GB) the efficiency drops from 75% to 65%. As the reduction of efficiency, with respect the best performance, from 1 to 10 nodes is 2% and is mainly due to communication, other effects come into play. These may be cache hierarchy effects. In the worse cases some required data need to be fetched from the main physical memory instead of from the local fast caches.

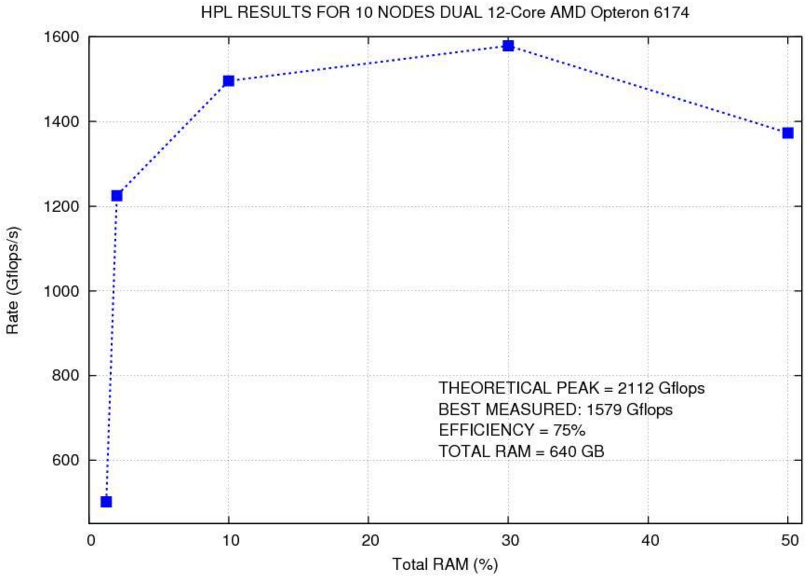

Figure 2: *Computational performance as a function of the memory load for 10 nodes (240 cores) of the CRESCO HPC Opteron Magny-Cours cluster.*

The HPL block size n_B is used for data distribution and computational granularity. Small values of n_B imply a better load balance but too small values may degrade performances because of cache missing and, consequently, no data reuse will occur. Also, performances may be degraded by the increased number of messages.

In *figure 3* is reported, for various memory loads, the flops rate as a function of the HPL block size for n_B = 64, 128, 256 in the case of 10 nodes. Block sizes n_B = 64 and 128 correspond, respectively, to 32 and 128 KB. AMD Opteron processor 6174 has cache levels L1 and L2 of size respectively 64 and 512 KB. It seems like to be true that with block sizes n_B = 64, 128 the computational granularity is not too coarse and L1 and L2 can be optimally filled. In fact, performances do not vary too much when using n_B = 64 or 128 within the memory load limit of 30% of the total available. Supposing the processor will try to fill in an ordered manner all its cache levels, with a block size n_B = 256, which corresponds to 512 KB, filling cache L1 first will leave out 64 KB on L2. The next block size allocation necessarily will be stored to L3. With n_B = 256 the granularity is such that the number of access to the less fast L3 cache will increase and performances will be reduced. When the memory load exceeds 30% of the total RAM a reduction of performance is observed even with n_B = 128. Cache hierarchy effects are not negligible. For example, experimental data show a reduction of performance of 9% and 11% with memory loads of, respectively, 10% and 50% of the total RAM.

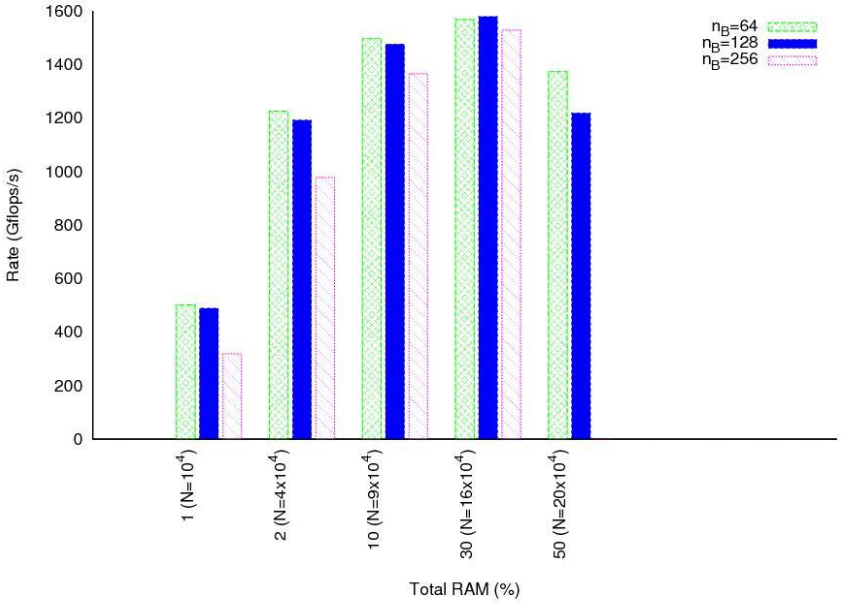

Figure 3: *Flops rate as a function of both memory load and HPL block size n_B for 10 nodes of the CRESCO HPC Opteron Magny-Cours cluster.*

SUMMARY

We have studied the computational performances of the CRESCO HPC Opteron Magny-Cours cluster. Experiments have been performed by running the HPL benchmark on 1 (24 cores) and 10 (240 cores) nodes. The system has an average efficiency of about 76% independently on the number of used cores. We have estimated the reduction of performances due to communication by comparing the best efficiency for 1 and 10 nodes, and found this effect amounts to about 2%. This is consistent with the HPL algorithm which is designed to scale very well independently on the communication volume. However, other factors may reduce sensibly computational performances. Because memory is a very important resource we have studied how the system behaves at different memory loads. The best result is obtained with a global memory load of 30% of total available RAM. With this memory request computational granularity effects are negligible because of good load balance and optimal usage of cache hierarchy.

REFERENCES

[1] Migliori, S., et al. "*CRESCO project: Computational RESearch center for COmplex systems*". ENEA: Italian National Agency for New Technologies, Energy and Sustainable Economic Development (2007). URL http://www.cresco.enea.it/.

[2] Bracco, G. "*Evoluzione dei cluster CRESCO di ENEA-GRID".* Workshop congiunto INFN CCR – GARR (2012). URL http://www.garr.it/a/eventi/workshop-garr/details/75-workshop-congiunto-infn-ccr-garr-2012.

[3] Petitet, A., Whaley, R.C., Dongarra, J.J., Cleary, A. "*Hpl: A portable implementation of the high-performance linpack benchmark for distributed-memory computers*". Innovative Computing Laboratory, Available online (2000). URL http://icl.cs.utk.edu/hpl/ and http://www.netlib.org/benchmark/hpl/.

[4] Dongarra, J., Luszczek, P., Petitet, A. "*The linpack benchmark: past, present and future. Concurrency and Computation*". Practice and Experience 15(9), 803–820 (2003).

[5] Luszczek, P., Dongarra, J., Kepner, J. "*Design and implementation of the hpc challenge benchmark suite*". CTWatch Quarterly 2(4A) (2006).

[6] Bailey, D., Barscz, E., Barton, J. et al. "*Nas parallel benchmarks*". NAS Technical Report RNR-94-007 (1994).

[7] Feitelson, G. "*On the interpretation of top500 data*". Intl. J. High Performance Comput. Applications 13(2), 146–153 (1999).

[8] Feitelson, D.G. "*The supercomputer industry in light of the top500 data*". Comput. in Science Engineering 7(1), 42–47 (2005).

[9] Dongarra, J., van de Geijn, R.A., Walker, D.W. "*Scalability issues affecting the design of a dense linear algebra library*". J. Parallel Distrib. Comput. 22(3), 523–537 (1994).

[10] Dongarra, J., Eijkhout, V., Luszczek, P. "*Recursive approach in sparse matrix LU factorization*". Scientific Programming 9(1), 51–60 (2001).

[11] Petitet, A.P., J.Dongarra, J. "*Algorithmic redistribution methods for block-cyclic decompositions*". IEEE Transactions on Parallel and Distributed Systems 10(12), 201–220 (1999).

CFD PARALLEL SIMULATION OF A CUTTING-EDGE SYNGAS BURNER USING ANSYS-FLUENT

A. Di Nardo, G. Calchetti, C. Mongiello
antonio.dinardo@enea.it
ENEA Casaccia - via Anguillarese 301-00123 Roma

Abstract

The burner designed is based on the trapped vortex technology. It offers several advantages as gas turbines burner and the systems experimented so far have limited mainly this technology at the pilot part of the whole burner. Aim of the work was to design a combustion chamber completely based on that principle, investigating the possibility to establish a MILD combustion regime, in case of syngas as fuel. The results of steady RANS simulations are presented in the following sections.

1. Introduction

CFD is an acronym that refers to "Computational Fluid Dynamics". CFD uses numerical methods to solve the fundamental nonlinear differential equations that describe fluid flow (the Navier-Stokes and allied equations) for predefined geometries and boundary conditions. The result is a wealth of predictions for flow velocity, temperature, density, and chemical concentrations for any region where flow occurs.

A key advantage of CFD is that it is a very compelling, non-intrusive, virtual modelling technique with powerful visualization capabilities, and engineers can evaluate the performance of a system configurations on the computer without the time, expense, and disruption required by experimentation.

CFD has seen dramatic growth over the last several decades. This technology has widely been applied to various engineering applications such as automobile and aircraft design, weather science, civil engineering, and oceanography.

The differences between syngas and natural gas combustion are mainly two:

- For the same power, fuel mass flow should be 4-8 times higher than natural gas, due to the lower calorific value.
- Premixed combustion of natural gas and air is one of the most commonly methods used for reducing NO_x emissions, by maintaining a sufficiently low flame temperature. This technique cannot be used with the syngas because of a significant presence of hydrogen and the consequent danger of flashback in fuel injection systems. For this reason it is necessary to use non-premixed diffusion flame, using diluents such as nitrogen, carbon dioxide and water, to lower flame temperatures and hence NO_x.

The trapped vortex technology offers several advantages as gas turbines burner:

1. It is possible to burn a variety of fuels with medium and low calorific value.
2. It is possible to operate at high excess air premixed regime, given the ability to support high-speed injections, which avoids flashback.
3. NO_x emissions reach extremely low levels without dilution or post-combustion treatments.
4. Produces the extension of the flammability limits and improves flame stability.

The systems developed so far use combustion in cavities as pilot flames for premixed high speed flows [1-6]. The goal is to design a device operating entirely with the principle of trapped vortices, improving mixing of hot combustion gases and fresh mixture, which is a prerequisite for a diluted combustion and at the most a MILD [7] combustion regime.

The prerequisite for a MILD combustion regime are: high temperature of the oxidant (above the auto-ignition temperature), a high turbulence level, a rapid and uniform mixing of fuel and oxidizer, a lean mixture, a low concentration of oxygen in the reaction zone and the recirculation of hot combustion products. It is clear that all these factors are closely interconnected. In fact, the internal exhaust gas recirculation requires the creation of a flows with characteristics that increase the levels of turbulence, thus producing a better and faster mixing. The gas recirculation clearly brings an increase in pre-combustion temperature and reduces the concentration of oxygen.

The introduction of MILD technologies in pressurized combustion is of great interest because it is potentially able to answer two main requirements:

1) a very low level of emissions and
2) an intrinsic thermo acoustic stability (humming).

Possible configurations of the system fall basically into two categories:

a) MILD systems with external control (outer recirculation, independent source of inert, sequential burning)
b) MILD systems with internal recirculation.

The type of application on the point a) is theoretically very promising from the point of view of both reducing pollutants and increasing the overall efficiency of the system, but it is associated with a higher complexity.

The difficulty in designing a prototype, arises from the fact that there are no standard design tools for this type of activity.

In spite of the highly innovative concept, its design and implementation involves the traditional issues of a gas turbine burner:

1. design a component with a suitable geometry taking into account the operating conditions;
2. ensure the absence of thermo acoustic oscillations;
3. ensure the stability of the burner;
4. ensure the absence of flashback phenomena.

2. Description

The TVC project is part of the ENEA-MSE (Ministry of Economic Development) framework. It concerns gas turbines using annular combustion chambers. The prototype to be realized, for simplicity of design and measurement, consists in a linearized sector of the annular chamber with a square section of size 190x190mm (*figure 1*).

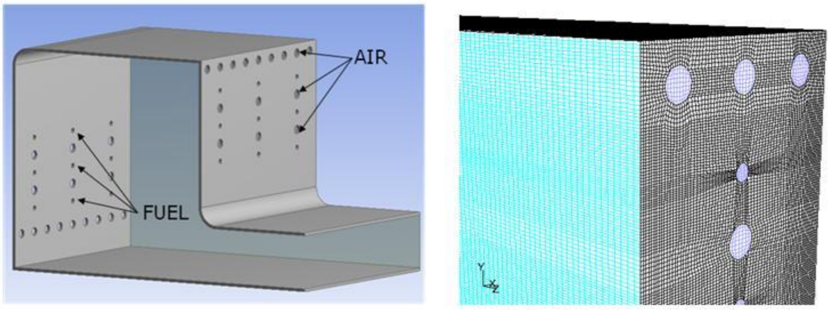

Figure 1: *Burner geometry and computational grid.*

The power density is about 15 MW/m^3 bar. The most obvious technique to create a vortex in a combustion chamber volume is to set one or more tangential flows. Two flows promote the formation of the vortex, while other streams of air and fuel, distributed among the tangential ones, feed the "vortex heart". The air flows placed in the middle provide primary oxidant to the combustion reaction, while the tangential ones provide the air excess, cool the walls and the combustion products, in analogy to what happens in the traditional combustion chambers, in which this process occurs in the axial direction. The primary and the global equivalence ratio were equal to 1.2 and 0.4, respectively.

Given the characteristics of the available test rig, the prototype will be tested under atmospheric pressure conditions. The combustion will be at a temperature of 700 K, corresponding to a compression ratio of about 20 bar, to simulate the real operating conditions. The syngas used will have the following composition: 19% H_2 - 31% CO - 50% N_2 LHV 6 MJ/kg.

3. CFD simulations

The simulations, performed with the ANSYS-FLUENT code on CRESCO platform, were carried out according to a steady RANS approach. Some preliminary tests were conducted on a computational grid made up of about 300000 hexahedral cells. We considered the time, in seconds, necessary to compute 500 iterations. If T1 is the time taken to calculate 500 iterations on a single processor and Tn is the time taken to calculate 500 iterations on n processors, the speed-up (S) was calculated using the relation S=T1/Tn, while efficiency (E) is E=S/n. The graphs are reported in *figure 2, 3*.

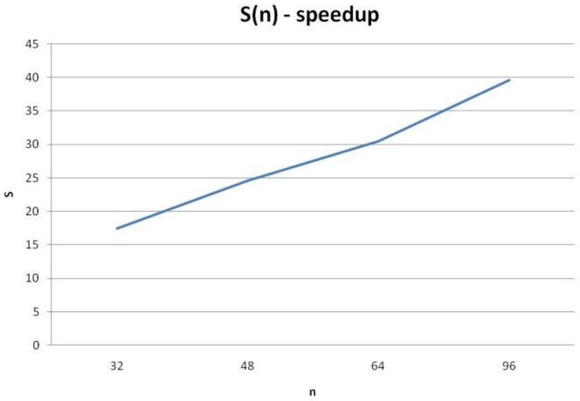

Figure 2: *Speed-up.*

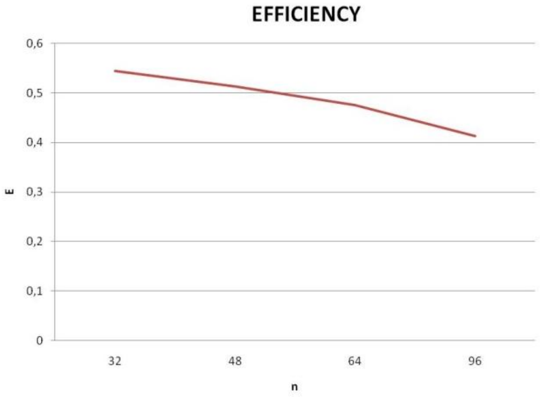

Figure 3: *Efficiency.*

The models adopted for chemical reactions and radiation are the EDC [8], in conjunction with a reduced mechanism [9] and the P1, respectively. NO_x were calculated in post-processing. In order to save computational resources, the simulations were conducted only on one sector of the whole prototype reported in the figure above, imposing a periodicity condition on side walls.

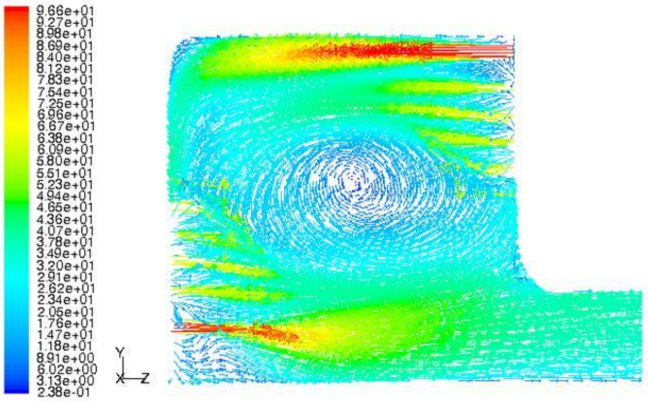

A big effort was made to properly modulate flow rates, velocities, momentum and minimum size of the combustion chamber. The resulting configuration establishes a perfect balance between the action of tangential flows, which tend to generate the vortex and the action of vertical flows that tend to destroy it *(figure 4)*. In this sense it is worth pointing out that it is especially the tangential flow, further from the outlet, the most effective.

Figure 4: *Flow field (m/s).*

The negative effects on vortex location and size resulting from a reduction of its strength, compared with the other inlets, were evident. In principle, a significant presence of hydrogen, very reactive, can produce elevated temperatures and fast reaction, especially near fuel inlets. For this reason inlet velocities are sufficiently high to generate a fast rotating vortex and then a rapid mixing. Further increase in fuel injection velocity has a negative influence on vortex shape and position, without slowing reaction and reducing temperature peaks.

Compared to axial combustors, the minimum space required for the vortex, results in an increase in volume and a reduction in power density. On the other hand, carbon monoxide content, with its slow chemical kinetic rate compared to natural gas, requires longer residence time.

As can be seen from the *figures* (*5, 6*), high temperature zones are concentrated in the vortex heart and the radical species are sufficiently distributed. This means that reactions take place within a larger volume than a conventional flame front. Experimental insights are necessary to asses if it is a MILD or a “flameless” regime. The emission indexes are EICO=3.59 g/kg$_{\mathrm{fuel}}$ and EINO$_x$≈ 0 g/kg$_{\mathrm{fuel}}$.

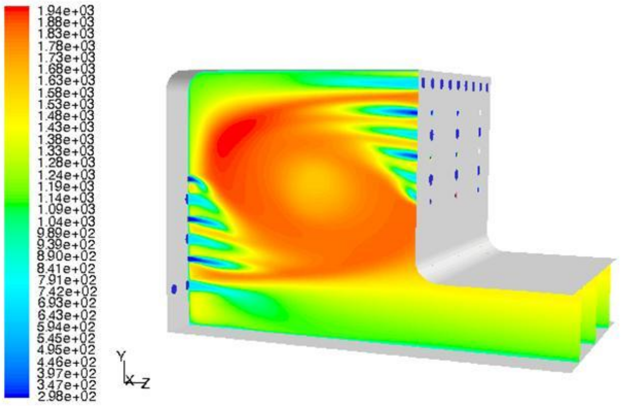

Figure 5: *Temperature field (K).*

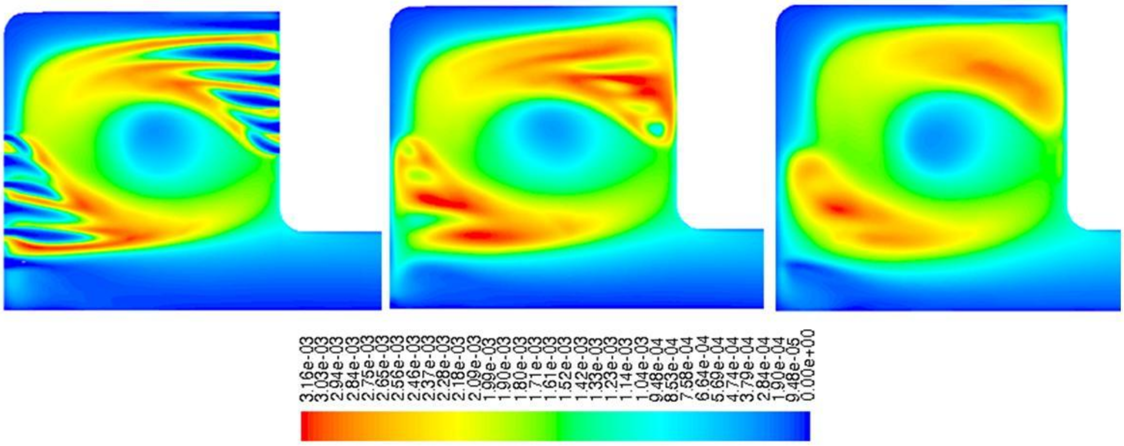

Figure 6: *OH mass fraction on different planes.*

4. Further comments

The effects of burner scaling was also analysed. In particular, the system was scaled maintaining constant inlet velocities. If one imagines to halve all sizes, the volume will be reduced by a factor 0.5x0.5x0.5=0.125, while the areas will be reduced by a factor of 0.5x0.5=0.25. Then mass flow-rates will be scaled by a factor of 0.25. Therefore, the power density (power/volume) will increase by a factor of 0.25/0.125=2. The simulations show that the behaviour of the burner remains unchanged, in terms of velocity, temperature, species, etc. fields. One can conclude that, if the overall size of the burner decrease, the power density increases according to the formula Power $^{0.5}$.

References:

[1] Tomasz Ochrymiuk, Janusz Badur *“Mild oxidation at the GT26 gas turbine: Numerical study via full chemistry”*. Task Quarterly 5 N°2, (2001) pp: 239-246.

[2] Flamme M. *“New combustion systems for gas turbines (NGT)”* Applied Thermal Engineering **24** (2004) 1551–1559.

[3] Levy Y., Sherbaum V., Arfi P. *“Basic Thermodynamics of FLOXCOM, the Low-NOX Gas Turbines Adiabatic Combustor”* Applied Thermal Engineering **24** (2004) 1593-1605.

[4] Levy Y., Sherbaum V. *“Parametric study of the FLOXCOM combustor” TAE Report* No. 920, Technion, (2003).

[5] Duwig C., Stankovic D., Fuchs L., Li G., Gutmark E. *“Experimental And Numerical Study Of Mild Combustion in a Model Gas Turbine Combustor”* Combust. Sci. and Tech. **180** (2008) 279–295.

[6] Lückerath R., Meier W., Aigner M. *“FLOX® Combustion at High Pressure With Different Fuel Compositions”* Journal of Engineering for Gas Turbines and Power **130** (2008).

[7] Cavaliere A., De Joannon M. *“Mild Combustion”* Progress in Energy and Combustion Science **30** (2004) 329–366.

[8] Magnussen B. F. *“On the Structure of Turbulence and a Generalized Eddy Dissipation Concept for Chemical Reaction in Turbulent Flow”* Nineteeth AIAA Meeting, St. Louis, (1981).

[9] Frassoldati A., Faravelli T., Ranzi E. *“The ignition, combustion and flame structure of carbon monoxide/hydrogen mixtures. Note 1: Detailed kinetic modeling of syngas combustion also in presence of nitrogen compounds”* International Journal of Hydrogen Energy **32** (2007) 3471 – 3485.

<MOLECULAR DYNAMICS SIMULATION OF Si/SiO$_2$ INTERFACES: PHONONS AND HEAT TRANSPORT STUDIES

Fabrizio Cleri, Evelyne Lampin, Quoc-Hoang Nguyen, Pierre-Arnaud Francioso and Pier Luca Palla

Institut d'Electronique, Microelectronique et Nanotechnologie (IEMN, Cnrs UMR 8520),
University of Lille I, LILLE (France)
fabrizio.cleri@univ-lille1.fr

1. Introduction

In our group we study the physical chemistry of nanostructured systems, macromolecular aggregates, and biomolecules, at finite temperature and pressure, and under constraints (mechanical, chemical, thermal, etc) by means of large-scale computer simulations. The physical-chemical phenomena of interest range from supramolecular ordering in small systems, to interfacial adhesion and aggregation, microscopic mechanics of biomolecules, mechanics and heat transport in nanostructures, modeling of nanodevices, and more. Due to the specific character of our home Institute, the IEMN (http://www.iemn.univ-lille1.fr), we are naturally interested in materials for advanced electronics and photonics applications, and we take part in several national and international projects, such as the FP7 Nanopack (http://www.nanopack.org), devoted to the study of nanotechnologies for interconnect and heat dissipation in next-geneation microelectronics, or the ANR Quasanova (http://www.im2np.fr/projets/quasanova.html), devoted to the study of advanced nanodevice architectures.

In this context, we produced a series of works about the nanostructured interfaces of Si and amorphous SiO$_2$, to study phonon confinement and heat transport in different nanostructures. Atomic-scale simulations, in which atoms in the solid (crystalline or disordered) are described explicitly, allow to describe collective thermal excitation of the atomic lattice (phonons), by using as the only input the interatomic potential describing the cohesion in the solid. It is worth noting that the atomistic simulations are here performed in the 3D space, with atoms free of moving in the whole domain, by contrast with atomic-lattice models in which atoms (yet explicitly described) occupy fixed lattice positions.

To understand the microscopic phonon-mediated processes at nanostructured junctions we resort to molecular dynamics (MD) simulation techniques [1]. Such method is particularly suitable for the proposed work, since it describes not only the phonon spectra (density of states) of the materials forming the junction, but also allows for explicit studies of the role of atomic bonding at the interface, and interfacial scattering of individual phonons with well defined frequency polarization [2-5]. More specifically, we want to address to address the following objectives:

(i) To relate the structure, bonding and phonon characteristics of the materials forming the junction, with the electronic and electron-phonon interaction properties.
(ii) To relate the structure, bonding and phonon characteristics of the materials forming the junction, with the interfacial thermal transport properties.
(iii) To identify the mechanisms governing scattering/transmission of phonons at the junction
(iv) To determine how do the length and the conformation of the nanostructured junction affect thermal conductance and transmission of individual phonons across the junction.

While the proposed studies are fundamental in nature, they are however designed to relate with real materials behavior. Therefore, the choice of model systems is dictated by the balance of model accuracy and need for model simplification, for example, with respect of chemical complexity, that enable efficient computations, data analysis and data interpretation. To achieve this, and to reach the objectives of the proposed research, we identified a small set of nanostructured model junctions, namely:

(a) Si nanoclusters embedded in a solid and fully dense SiO_2 matrix. Phonon properties can be related to the interface structure by computing phonon density of states projected on a layer-by-layer basis.

(b) Si/SiO_2 multilayer. In this system an amorphous SiO_2 layer is deposited on a crystalline silicon substrate. Heat transport can be studied by directing the heat flux perpendicular or parallel to the Si/SiO_2 planar interface.

The choice of the above systems was initially motivated by the search for nanostructured systems which could readily be integrated with existing microelectronics technology. However, in the course of the simulations, we came to realize that the problem of phonon localization and heat transfer across the amorphous/crystal interface is of a more fundamental nature. In fact, it turns out that such a question is yet to be fully addressed.

2. Structure of the amorphous silica / silicon interface

We started this part of the project motivated at first by the investigation of the luminescence experimentally observed in Si nanoclusters, which are seen as one of the components of future high-performance photovoltaic cell materials. In particular, mixed Si/SiOx are envisaged to enhance the photoluminescence of Si/silica matrices made with Si nanocrystals dispersed in the oxide, and doped with rare earth atoms such as Erbium. Si nanocrystals embedded in an insulating oxide are supposed to originate quantum confinement phenomena, as a function of the varying size and shape of the nanoparticle, which should modify the overall electronic structure of the oxide-covered Si nanoparticle. The appearance of surface (or rather, "interface") electronic states in such systems appears to be potentially implicated in some novel properties of such mixed systems.

In order to describe the Si/SiOx interface at the atomic scale, there are very few interatomic potentials available with well-established properties. In this first study we were interested also in the charge transfer at the interface between the silicon and its oxide. Therefore, Tersoff-like potentials, which are known to be very successful in Si-based materials, were not adapted to our case. To this purpose, we developed a mixed potential based on the well known three-body potential of Stillinger and Weber for pure Si, and on the Beest, Kramers & Van Santen (BKS) potential for stoichiometric silica phases, also used with success in amorphous silica. This latter is known to describe well the varying coordination and charge displacement in silica, when passing from α–quartz to β–cristobalite and other crystalline phases. We devised an algorithm to define the mixing of the interactions at the interface, where some Si atoms from bulk silicon can interact with Si and O atoms from the amorphous silica. Variable charges were defined, to explicitly take into account the charge transfer at the interface. In our model, Si atoms can change continuously their effective charge, from the value 0 in the bulk of the Si nanoparticle, to their formal value of $-1.2e$ in amorphous silica, with values at the interface zone adjusted so as to match the ab-initio calculated coordination and charge displacements in stoichiometric crystalline interfaces.

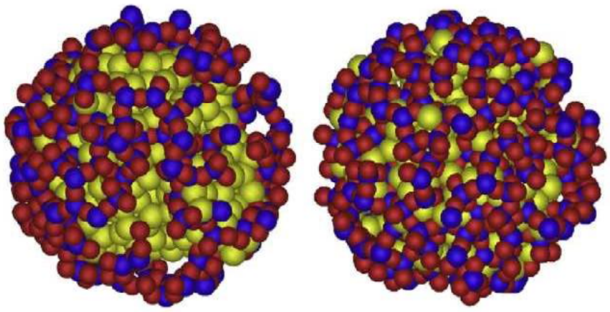

Figure 1: *SiO_2 coverage (red=Si, blue=O) of a bulk Si cluster (yellow) of 500 atoms embedded in a fully dense amorphous silica matrix. Left, spherical cluster; right: icosahedral facetted cluster. The spherical shape is more stable up to about 5000 atoms size. Note that the oxide coverage is highly irregular for the spherical cluster. (Only the nearmost layer of oxide is shown for clarity).*

Classical molecular dynamics simulations realized with this mixed potential model at relatively low temperatures, showed that the Si-oxide interface (*figure 1*) is rather rough for spherical clusters (the most stable form of Si clusters for sizes up to about 5000 atoms, corresponding to a diameter of about 10-11 nm), compared to more homogeneous coverage for the faceted (and higher-energy) cluster of the same size. The Si-O-Si* bonding bridges (characterized by one Si atom belonging to the nanoparticle, and one Si atom belonging to the amorphous silica) appear to be very important in determining the detailed atomic and electronic structure of the interface (note that we called such bridges with the '*' symbol, to underscore the fact that the O atom in such case can be displaced in a non-symmetric position between the two Si atoms, compared to bridges at the interface in which both Si atoms belong to either the cluster or to the oxyde). The vibrational spectrum (*figure 2*), or phonon density of states, obtained from the Fourier transform of the partial velocity autocorrelation function, displays a peak at 12.2 Thz, strongly localized in the interface atoms region (see the blue curve in figure 2b). This peak could be at the origin of quantum confinement effects, and could originate the luminescence experimentally observed. However, in order to validate this hypothesis, electron-phonon coupling calculations on such a structure should be realized. In the next future we will couple such MD-calculated atomic structures with tight-binding simulations, in order to determine the coupling intensity of the eventual electron-phonon interaction.

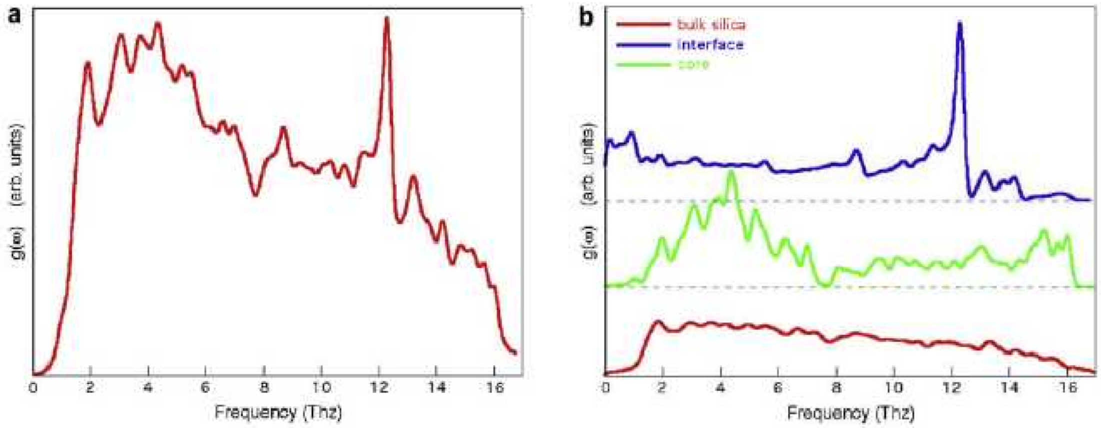

Figure 2: *Vibrational density of states for the spherical cluster embedded in a silica matrix. (a) total; (b) decomposed into bulk Si cluster (green), silica matrix (red) and interface region (blue) defined as a thickness of ±5 Angstrom about the limiting surface. The 12.2 Thz peak is attributed to the Si-O-Si* bridges at the Si-oxide interface, and could represent a signature of quantum confinement.*

For this study we used a special purpose code, TINKMD, resulting from the coupling of our old, in-house code HELLF, well established for the molecular dynamics of solid phases, and the freeware code TINKER, originally developed at the Notre-Dame University (USA) for the MD simulations of large proteins and biomolecules. The efficient use of TINKMD in such a problem is limited mostly by the Coulomb interactions among the partial charges, which requires the use of an Ewal sum algorithm to obtain a converged sum of the 1/r electrostatic terms. The Ewald sum is partly performed in the real space with a cut-off, and partly in the conjugate Fourier space by means of an infinite sum. This limitation makes the parallelization rather difficult, but not impossible in general. Therefore we have not considered parallelizing our code at this stage. The typical jobs were run on a single core, each run lasting many hundreds of CPU time, however with a very limited demand of RAM memory. This made possible to run several jobs in parallel, with different initial parameters. The results have been published in a paper appeared in *Solid State Science* [6].

3. Heat transport across the silicon/silica interface

The most straightforward method in determining thermal conductivity is related to the classical Fourier's Law, $J_\mu = -\kappa_{\mu\nu}\ (\partial T/\partial x_\nu)$, J_μ being a component of the thermal current (flux) vector, $\kappa_{\mu\nu}$ an element of the thermal conductivity tensor (with units of energy per unit time, length (i.e., thickness) and degrees K), and $\partial T/\partial x_\nu$ is the gradient of the temperature T in a steady–state heat flow condition. The interfacial thermal resistance R is empirically defined as the inverse of the conductance coefficient relating the temperature discontinuity across an interface, to the thermal flux, $J=G\Delta T$. Therefore $R=1/G$, with units of $(\text{length})^2$(deg K)/W. This thermal resistance generally differs from the "contact" resistance, as it exists even at atomically perfect interfaces.

In our first attempts to determine the thermal conductance of the interface, we performed standard non-equilibrium molecular dynamics (NEMD) calculations, monitoring the temperature jump at the interface between two adjoining solids. Elongated atomistic samples of the Si/silica interface with length ranging from 45 to 200 nm along *z*, and cross-section of 4.8 or 19.4 nm^2 in the *xy* plane were constructed (*figure 3*). The samples contained therefore 16,000 to 200,000 atoms, half of the total length being crystalline Si (*c*Si), while the remaining half being either amorphous Si (*a*Si) or amorphous silica (*a*SiO_2). For this study, we selected the interatomic potential of Tersoff for Si-based systems, as modified by Munetoh et al. to include the oxide.

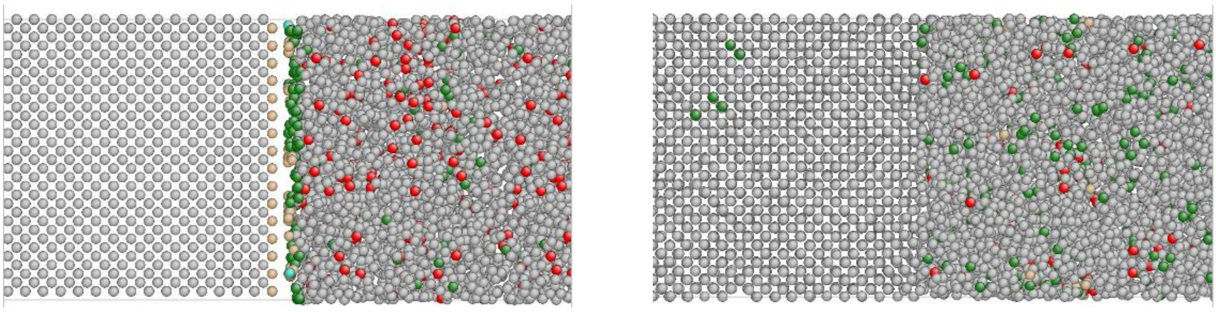

Figure 3: *Example of the structure of a c-Si/a-Si interface, before (left) and after (right) the annealing and equilibration cycle. The colors indicate atom coordination: grey=4-fold, green=3-fold, red=5-fold. (Only the central portion of a much elongated system in the z-direction is shown, for clarity).*

After each sample was firstly equilibrated at 500 K as described above, a heat source (T=550K, width 22 Å) was introduced at mid–length of the *c*Si block, while a heat sink (450K, 22Å) was set at mid–length of the amorphous block. After another 100 ps of stabilization of the thermal gradient along the *z*-direction of the supercell, the temperature profile was recorded in slices of 2Å-width, and averaged during 1ns, to ensure a good convergence. *Figure 4* below gives the temperature profile for the two interfaces, for a system of 4.3x4.3x98 nm^3 (~114,000 and ~91,000 atoms for *c*Si/*a*SiO_2 and *c*Si/*a*Si respectively).

The temperature profile is nearly flat in the *c*Si part, and the exhibits a steep slope in *a*Si or *a*SiO$_2$, due to the much higher conductivity of *c*Si than both *a*Si and *a*SiO$_2$. The latter material shows a substantial nonlinearity of the temperature close to the interface. However, neither of the two temperature profiles shows any visible drop at the interface, differently from what usually observed for other interfaces (the temperature drop representing a direct measure of the Kapitza resistance, via the estimation of the thermal energy flux). This behavior could be due to the large difference in thermal conductivities on each side of the interface, leading to the large decrease of the temperature in the less conductive part (*a*Si or *a*SiO$_2$), which could hide the effect of the interface itself.

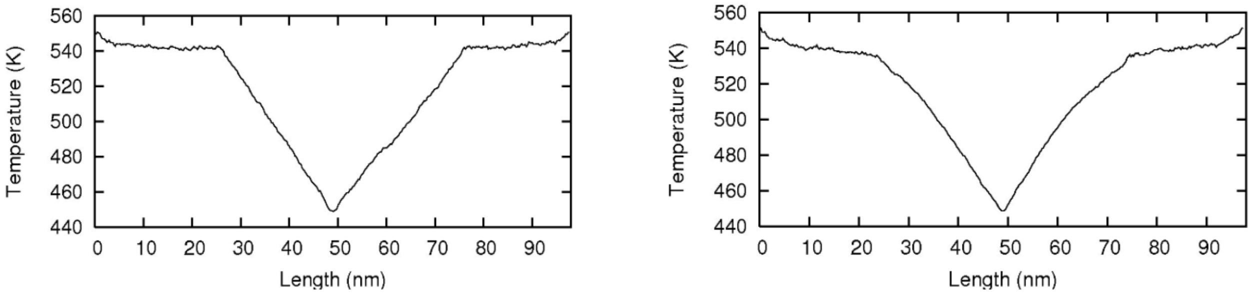

Figure 4: *Temperature profiles at stationary state for a crystalline Si / amorphous Si interface (left) and a crystalline Si / amorphous silica interface (right), composed of 50 nm of crystal and 50 nm of amorphous in both cases. The heat source is located at 0 and 100 nm (repeated because of periodic boundary conditions, while the heat sink is located at about 50 nm. The two amorphous regions extend between 25 and 75 nm of length, the rest being crystalline Si.*

Another possibility being that the temperature drop does not exist at all in, this case. Indeed, the extraction of an interface temperature in such extreme conditions shows one of the limitations of the NEMD method, namely the need to define temperature differences over lengths much smaller than the typical phonon mean free path, besides the difficulty of imagining a physical gradient of $>10^9$ K/m over such a nm–thin region, and the computational need to estimate the absolute thermal energy flux, J, during the same simulation.

Therefore we repeated the calculations with a novel AEMD method which we introduced recently, based on the extraction of the *bulk* temperature for a larger system, i.e., 10,000 to 100,000 atoms. The principle is to equilibrate each of the two sides of the interface at two different temperatures, before following the equilibration to a common temperature, resulting from heat transfer through the interface. Such a computational procedure is akin to the laser-flash method for the measure of thermal diffusivity, applicable with some variant also down to nanostructured materials, in which a highly localized temperature transient is impulsively created and monitored in time. Notably, in such a transient case the relevant quantity is the *thermal diffusivity* α, that is the ratio of the conductance to the volumetric specific heat. From the 1-D Fourier equation, the general solution for the time evolution of the temperature difference can be shown to be represented by a sum of exponentials, each with a relaxation time inversely proportional to α.

For the AEMD simulations, the *c*Si part was equilibrated at 600K and the *a*Si or *a*SiO$_2$ at 400K, during 100 ps. In practice, each half of the atomistic system was homogeneously heated while the other was frozen in place, the final equilibrium velocities were recorded, and a new simulation was initiated with each half of the system starting from its own (Maxwell-Boltzmann) equilibrium velocity distribution. The total system is subsequently left free to attain equilibrium under constant-{NVE} constraints, i.e. in the microcanonical ensemble, therefore the total energy is conserved and the system reaches an average temperature determined by the ratio of the total mass times the heat capacity of the two materials. The ensemble–averaged, instantaneous temperature of each subsystem (*c*Si, *a*Si, *a*SiO_2) was recorded, and the temperature difference, (*X*=*a*Si or *a*SiO_2) could be estimated during each AEMD run.

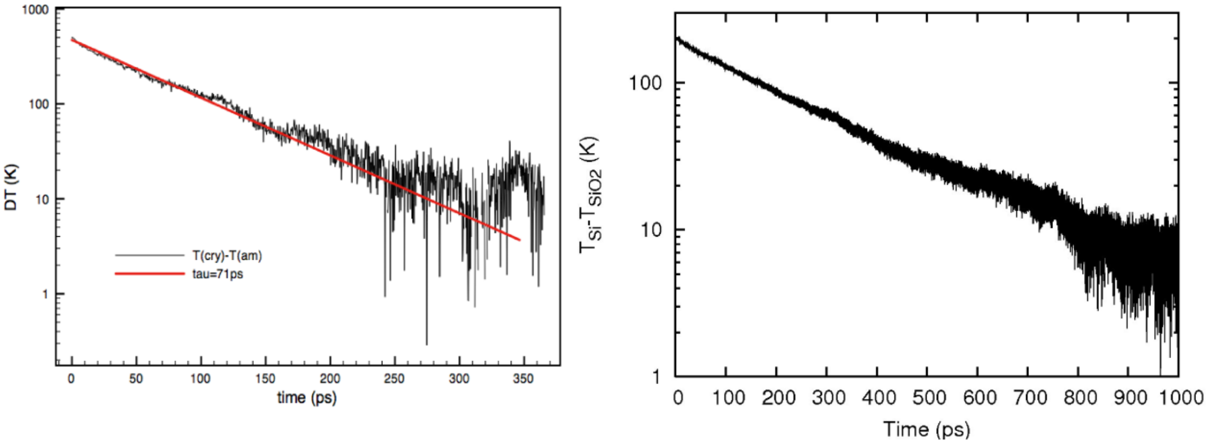

Figure 5: *Semi-log plot of the temperature difference as a function of simulation time at constant-{NVE}, between crystal and amorphous blocks in contact, calculated with the AEMD method. Initial temperature difference is 200 K (crystal at T=600 K, amorphous at T=400 K), Left : cSi/aSi. Right: cSi/a*SiO_2.

As shown in *figure 5*, the approach to equilibrium appears indeed to proceed by following a unique decaying exponential, τ. This value of τ can be extracted by fitting the ΔT vs. t profile on a semilog scale covering many decades, and is related to the interface conductance G by the relation:

$$G = \frac{1}{\tau}\left(\frac{3k_B}{2A}\frac{N_c N_a}{N_c + N_a}\right) \qquad [1]$$

where k_B is the Boltzmann constant, A is the interface cross-section, N_c and N_a are the number of atoms, respectively, in the crystalline and amorphous parts. Table 1 below summarizes the results obtained for the two interfaces for systems of varying length, G being given in MW/K/m^2.

	System size $x \times y \times z$ **(nm^3)**	**n. of atoms**	G
*c*Si/*a*Si	4.3×4.3×46	21,504/21,000	164 +/– 6
	4.3×4.3×98	48,080/45,000	130 +/– 5
	4.3×4.3×203	95,232/93,000	75 +/– 5
*c*Si/*a*SiO_2	2.2×2.2×53	5,824/10,083	157 +/– 8
	4.4×4.4×46	22,016/32,400	214 +/– 10
	4.4×4.4×98	48,080/68,400	112 +/– 6
	4.4×4.4×203	235,120	87 +/– 5

Table 1: *Thermal conductance G (MW* $K^{-1}m^{-2}$*) of cSi/aSi and cSi/a*SiO_2 *interfaces.*

It appears rather clearly that the interface conductance is very similar between the two interface at all sizes, meaning that the effect of disordering (phase transformation between crystal and amorphous) should be the main responsible for the difference, the chemistry playing a minor role. However, it will also be noted that the absolute value of *G* decreases with increasing length of the system, down to quite low values. We performed a scaling test by progressively reducing the size of the amorphous region compared to the crystalline Si, and obtained asymptotic values of *G* of about 25 ± 5 MW K^{-1} m^{-2} for the interface with aSi, and 52 ± 5 MW K^{-1} m^{-2} for $aSiO_2$.

It is to be noted that the direct experimental determination of the heat conductance at Si–silica interfaces is affected by a rather large scatter of values, going from about 50 [7], to 75–200 [8], up to about 400–450 MW K^{-1} m^{-2} [9] as a function of the different experimental arrangement. It is likely that part of the difficulty in this special case also originates from the very large mismatch in thermal conductivities of crystalline Si (*c*Si) and amorphous silica ($a\mathrm{SiO}_2$), $k(c\mathrm{Si})$ =140 W K^{-1} m^{-1} and $k(a\mathrm{SiO}_2)$ ~1.5 W K^{-1} m^{-1} at T=300K, as well as amorphous Si, $k(a\mathrm{Si})$ ~2 W K^{-1} m^{-1}. Therefore a limiting lower bound in the range 50-70 MW K^{-1} m^{-2} as indicated by the AEMD calculations should not be considered far from the reality.

For this study we turned to a version of the DL_POLY code, developed at Daresbury Laboratories (UK), for which we made the appropriate modifications in order to extract the information about thermal evolution of the system. The code is highly parallelized and runs efficiently, with a fairly good scaling up to thousands of computing cores. We ran typical jobs on 32/64 IBM-SP5 cores at ENEA Frascati, and at the SP6 of IDRIS in Saclay. The results have been published in a paper appeared in *Applied Physics Letters* [10].

References

[1] Xue, L., Keblinski, P., Phillpot, S. R., Choi, S. U., and Eastman, J. A., *Two regimes of thermal resistance at a liquid-solid interface*, J. Chem. Phys. **118** (2003) 337

[2] Li, J., Porter, L., and Yip, S., *Atomistic modeling of finite-temperature properties of crystalline β–SiC : II. Thermal conductivity and effects of point defects*. J. of Nucl. Mater. **255** (1998) 139

[3] Volz, S. G., and Chen, G., *Molecular dynamics simulation of thermal conductivity of silicon crystals*, Phys. Rev. B **61** (2000) 2651

[4] Keblinski, P., Phillpot, S. R., Choi, S. U., and Eastman, J. A., *Mechanisms of heat flow in suspensions of nano-sized particles (nanofluids).* Int. J. of Heat & Mass Transfer **45** (2002) 855

[5] Prasher, R. S., Hu, X. J., Chalopin, Y., Mingo, N., Lofgreen, K., Volz, S., Cleri, F., Keblinski, P., *Turning carbon nanotubes from exceptional heat conductors into insulators*. Phys. Rev. Lett. **102**, (2009) 105901

[6] Soulairol, R, and Cleri, F., *Interface structure of silicon nanocrystals embedded in a silica matrix*, Sol. St. Sci. **12** (2010) 139

[7] Lee, S.-M., and Cahill, D., *Heat transport in thin dielectric films*. J. Appl. Phys. **81** (1997) 2590

[8] Kato, R., and Hatta, I., Int. J. Thermophys. **29** (2008) 2062

[9] Hurley, D. H., Khafizov, M., and Shinde, S. L., *Measurement of the Kapitza resistance across a bicrystal interface*. J. Appl. Phys. **109** (2010) 083504

[10] Lampin, E., Nguyen, Q.-H., Francioso, P. A., and Cleri., F., *Thermal boundary resistance at silicon-silica interfaces by molecular dynamics simulations*, Appl. Phys. Lett. **100** (2012) 131906.

COMPUTATIONAL CHARACTERIZATION OF TARTRATE-BASED TACE INHIBITORS

C. Guardiani[a] **and P. Procacci**[a,b]

[a] *Department of Chemistry, University of Florence, Italy*
[b] *Corresponding author:* **piero.procacci@unifi.it**

ABSTRACT

Small-molecule inhibitors of Tumor Necrosis factor alpha Converting Enzyme (TACE) are a promising therapeutic tool for Rheumatoid Arthritis, Multiple Sclerosis and other autoimmune diseases. Here we report on Hamiltonian Replica Exchange Molecular dynamics simulations of three tartrate-based TACE inhibitors. The simulations show that irrespective of the inhibition constant, the three drugs in bulk solvent adopt a common compact conformation whereby the hydrophobic right-hand side and left-hand side substituents are packed against each other and the hydroxyls necessary for Zinc chelation in the TACE active site are exposed toward the solvent. Since the drugs in complex with TACE are expected to be in the extended conformation, our results support the hypothesis of a structural rearrangement upon ligand binding. The proposed mechanism may have important implications for the rational drug design.

INTRODUCTION

Autoimmune diseases comprize more than 50 distinct diseases and syndromes and affect about 5% of the population in Europe and North America [1]. Examples of autoimmune disorders include Rheumatoid Arthritis (RA), Multiple Sclerosis (MS), juvenile diabetes and Crohn disease. In Europe alone, rheumatic diseases impose an economic burden of 200 billion euro per year. Despite the broad array of clinical forms, a remarkable emerging feature of autoimmune diseases is the central role played by Tumor Necrosis factor alpha (TNFα) [2]. TNFα is a pro-inflammatory cytokine normally involved in the protection of the body from infective agents. TNFα is expressed as an homotrimeric 26 kDa membrane protein (mTNFα) that is cleaved by TNFα Converting Enzyme (TACE), a sheddase that releases a 17 kDa soluble form (sTNFα). TNFα signaling occurs through the interaction with two receptors: TNFR1 can interact with both mTNFα and sTNFα and induces a strong pro-inflammatory response; TNFR2 can only be activated by the trans-membrane form mTNFα and induces anti-inflammatory and immuno-modulating responses [3]. In Rheumatoid Arthritis the soluble TNFα released by activated macrophages interacts with the TNFR1 receptor constitutively expressed on fibroblasts and chondrocytes of the joints activating a signaling pathway that culminates in the expression and secretion of Matrix Metalloproteinases MMP-1 and MMP-13 that hydrolize the collagen of the joint cartilage severely impairing its function [4]. The upstream inhibition of this pathway was successfully achieved using genetically engineered antibodies against TNFα such as Etanercept, Infliximab and Adalimumab [5]. The involvement of TNFα in Multiple Sclerosis was more elusive. Indeed, for over a decade it has been known that TNFα was overproduced in the serum and cerebro-spinal fluid of MS patients and could be detected in the brain lesions identified through Magnetic Resonance Imaging [6]. Unexpectedly, however, the use of anti-TNFα antibodies like Lenercept, led to an exacerbation of the disease with an increase in the number, length and intensity of the relapses [7]. This paradoxycal behaviour is caused by the inhibition of the immuno-modulating mTNFα/TNFR2 signaling that always accompanies the block of the sTNFα/TNFR1 pathway when using aspecific antibodies. The current trend is therefore to inhibit the sTNFα/TNFR1 signaling while sparing the mTNFα/TNFR2 axis [3]. This can be achieved either blocking the TNFR1 receptor or targeting the soluble form of TNFα. The latter strategy also includes the inhibition of the TACE enzyme that releases the soluble form of TNFα from its membrane precursor. The design of small molecule TACE inhibitors would be extremely beneficial also for RA patients since recombinant antibodies can not be orally administered and they are extremely expensive.

The design of selective TACE inhibitors has frustrated medicinal chemists for over three decades due to cross-reactivity with Matrix Metalloproteinases that share with TACE the common architecture of the metzincin superfamily [8]. The use of broad-spectrum inhibitors resulted in severe dose-limiting side-effects that prevented the clinical application of these compounds. The catalytic domain of TACE is characterized by a five-stranded β-sheet with four parallel and a single antiparallel strand, strand IV, that together with helix C delimits a long binding groove [9]. Helix C provides the consensus sequence HEXXHXXGXXH that includes three critical histidines (His405, His409, His415) that coordinate a Zinc ion located at the center of the binding groove. In the absence of any ligand the Zinc ion is also coordinated by a water molecule that is polarized by the interaction with Glu406 also located in the consensus sequence. Effective inhibitors must displace the catalytic water molecules to bind the zinc ion and they must comprise a number of groups capable of fitting into the binding pockets located along the binding groove. Conventionally the peptide substrate side-chains towards the carboxyl end are labeled P1', P2' and P3', while the groups towards the N-terminus are designed P1, P2 and P3. These groups fit into specific pockets named S1', S2', S3' and S1, S2, S3 respectively. As a consequence, TACE and MMP inhibitors are comprised of two main units [8]: a peptidomimetic backbone designed to recognize the primed pockets, and a zinc chelating group. The strongest zinc binding group (ZBG) currently employed is hydroxamate that acts as a bidentate chelator. The strength of this interaction however, can override the contribution of other groups of the drug limiting selectivity [10]. This is why a number of zinc binding groups with affinity lower than that of hydroxamate are currently being tested.

A novel promising family of TACE inhibitors is represented by bis-amides of L-tartaric acid first developed by Rosner et al [11]. These compounds feature a tartrate core linking a left hand side (LHS) and right hand side (RHS) substituent through amide bonds. The tartrate core acts as a tridentate Zinc chelator while the RHS (R)-1-(4-(1H-pyrazol-1-yl)phenyl)ethanamine group fits into the S1' and S3' pockets. This group fully exploits the specific features of TACE that is characterized by a tunnel connecting the S1' and S3' pockets. Moreover, thanks to the central position if the Zinc binding group, these drugs can target both primed and non-primed pockets, the latter being often neglected by traditional hydroxamate inhibitors. The current challenge is to optimize the LHS group. Despite the massive efforts by Dai et al [12] the results were not satisfactory. This underscores the necessity of a rational drug design approach and motivates our choice to computationally investigate this class of compounds.

In our opinion a less investigated reason for the failure of first-generation ihibitors is the neglect of the relation between the structure of the molecule in bulk solvent and its conformation when bound to the target enzyme. This is why we performed Hamiltonian Replica Exchange Molecular Dynamics (REMD) simulations [13] of a set of tartrate-derived inhibitors in bulk solvent. Anticipating our results, our simulations showed that all the drugs, irrespective of their inhibition constant adopted an almost identical compact conformation with the hydrophobic LHS and RHS substituents closely packed against each other. This conformation is very different from the extended structure of the drug in complex with the enzyme that was revealed from X-ray crystallography [12]. This suggests that the drug must undergo a structural reorganization upon binding to the enzyme. Consequently, it can be predicted that only ligands without groups clashing with the enzyme during the isomerization process, will result in stable inhibited complexes. This provides a guiding principle for rational drug design that could be generalized to the design of other enzyme inhibitors.

METHODS

In this work we simulated three tartrate-based inhibitors designed by Dai *et al.* that will be referred to as Drug-1, Drug-38 and Drug-44 in agreement with the original nomenclature used in Ref [12]. As shown in *Figure 1* all the compounds share a common central tartrate core linked through a secondary amide with a (R)-1-(4-1H-pyrazol-1-yl)phenyl)ethanamine group (the right hand side group, RHS).

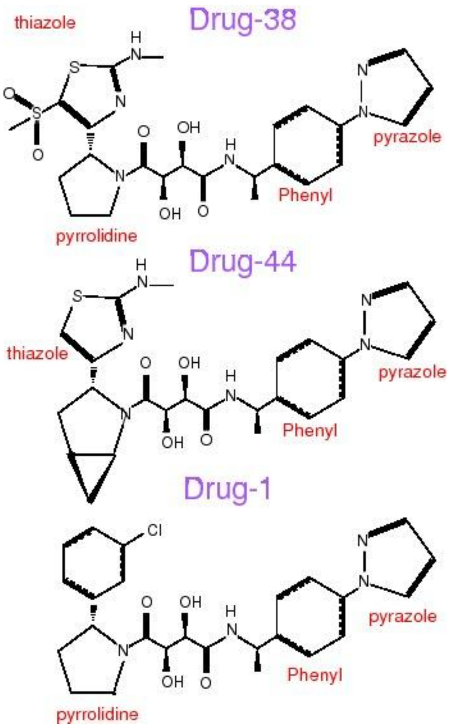

Figure 1*:* *Chemical structures of the three tartrate-based TACE inhibitors analyzed in this work.*

The difference among the drugs must be sought in their specific left hand side (LHS) substituents. Drug-1 shows a very good binding affinity for TACE (K_i = 0.8 nM) and its LHS group is a 2-(3-chlorophenyl)pyrrolidyl unit. In Drug-38 a 2-aminothiazole ring is linked to a methyl-sulphonil group at 5-position, and mono-methylated on its 2-amine group resulting in an excellent TACE affinity (K_i = 0.4 nM). Drug-44 can be ideally derived from Drug-38 by removing the methylsulfonyl group and fusing the pyrrolidine group with a cyclopropyl ring. This modification significantly spoils the TACE affinity increasing the inhibition constant to 531 nM. The initial conformation of Drug-38 was taken from the Protein Data Bank (PDB ID: 3O64). From this structure we extracted the common scaffold of the tartrate inhibitors that we modified with the *Molefacture* plugin of the VMD program [14] to build Drug-1 and Drug-44. These structures underwent a geometric optimization with the Gaussian program [15] at the SCF level using the 6-31G* basis set. Atomic charges were computed using the ESP scheme and then symmetrized to RESP charges using the Antechamber program [16].

All Molecular Dynamics simulations were performed with the ORAC suite of programs [17,18] using the General Amber Force Field (GAFF) [19]. After minimization *in vacuo* (2500 steps of steepest descent followed by 2500 step of conjugate gradient minimization), the drugs were solvated with 512 water molecules in a simple cubic box with periodic boundary conditions and they were equilibrated for 100 ps in the isothermal-isobaric ensemble at T=300 *K* and p=1 *atm.* The last configuration obtained during the equilibration stage was used as the starting point for Hamiltonian Replica Exchange Molecular Dynamics (REMD) [13] simulations with 8 replicas each simulated for 8 ns.

In Hamiltonian REM, *N* replicas of the system are simulated in parallel with different sets of scaling coefficients that act as weights for different additive components of the potential energy. At regular time intervals *N/2* exchanges are attempted among replicas with neighboring sets of coefficients and the exchanges are accepted or rejected according to a Metropolis-like criterion. If the scaling coefficients are appropriately chosen, when the potential energies of the two replicas involved in the exchange are substituted in the expression for the acceptance probability, the less relevant energy terms will cancel out and the acceptance probability will depend on a small subset of degrees of freedom reducing the number of necessary replicas and thus the computational cost of the simulation. The REM algorithm is therefore intrinsically parallel and thus perfectly suited to be ran on massively parallel supercomputers. The efficiency of the algorithm is further increased by keeping the communication among processors to a minimum. In fact most implementations, instead of exchanging among replicas the coordinates of a macromolecular system, equivalently exchange only the temperatures or a small vector of scaling coefficients.

In our simulations only the torsional potential was scaled throughout the replica progression with maximum and minimum scaling factors (1.0, 0.2) corresponding to effective temperatures of 300 *K* and 1000 *K* respectively. In order to avoid the energy instability deriving from atom clashes, in the case of Drug-38 the minimal scaling coefficient was set to 0.3, reducing the maximal effective temperature to 1000 *K*. For each drug, the simulated extended (generalized) system included multiple independent 8-replicas batteries of trajectories as described in Ref. [20]. Exchanges between adjacent replicas within a battery were attempted every 100 *fs* with an average acceptance probability of 25%. Conformations were saved every 500 *fs* producing a total of 16000 configurations per replica (8 ns of simulation per drug).

The large number of configurations of the equilibrium ensemble of the target replica were analyzed through Quality Threshold clustering [21]. This algorithm requires a distance matrix for all pairs of structures of the population. The structural metrics that we chose was the maximum difference between corresponding pairs of carbon atoms. For each structure in the ensemble the algorithm builds a candidate cluster in such a way that the distance between any two structures of the cluster do not exceed the cutoff distance (that we chose to be d_c= 2.0 Å. The program then retains only the largest cluster and removes its structures from the population. The procedure is iterated until all structures of the populations are used.

RESULTS

Valuable information can be attained by submitting the equilibrium population of the different drugs to Quality-Threshold clustering and overlaying the representatives of the most populated cluster of each drug. The structures are overlaid so as to minimize the RMSD of heavy atoms of the common part, *i.e.* the tartrate core and the RHS pyrazol-phenyl-ethanamine group. First of all it is informative to compare the structure of Drug-38 when bound to TACE (PDB ID: 3O64) and after equilibration in the bulk solvent. As shown in *figure 2*, the structure equilibrated in the bulk solvent is much more compact than the crystal conformation.

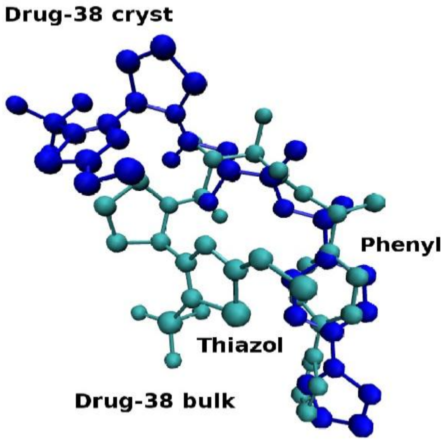

Figure 2. *Comparison of the conformations adopted by Drug-38 in bulk solvent (cyan; structure closest to the centroid of the most populated cluster) and in complex with TACE (blue; PDB ID: 3O64). The structures have been overlaid so as to minimize the RMSD of heavy atoms of the common scaffold of this family of inhibitors i.e. the tartrate core and the RHS pyrazol-phenyl-ethanamine group.*

This occurs because both the LHS and RHS substituents are hydrophobic and in an aqueous environment they tend to pack against each other. In particular, a very close contact can be observed between the phenyl group of the RHS substituent and the thiazol ring of the LHS one. It is worthwhile noticing that the compact conformation adopted by the drug in water, optimally exposes the two hydroxyl groups of the tartrate core that will chelate the Zinc ion in the catalytic pocket of TACE. It can then be hypothesized that the drug-enzyme collision trajectories in which the two chelating oxygens are properly oriented towards the Zinc ion, can end up in an intermediate so stable to allow enough time for the isomerization of the drug. This can simply occur through a rotation around the bond linking the two hydroxyl binding carbons of the tartrate core, possibly followed by a reorientation of the thiazol ring with respect to the pyrrolidine group.

Another structural comparison is illustrated in *Figure 3* showing the representatives of the most populated cluster of Drug-1, Drug-38 and Drug-44 after REM equilibration in water. The three structures all show the compact motif with the hydrophobic RHS and LHS groups packed against each other. Drug-1 and Drug-38, the most powerful TACE inhibitors (K_i: 0.8 and 0.4 nM respectively) show almost identical structures. In particular, the chloro-phenyl ring of the LHS substituent of Drug-1 is parallel and almost parfectly superposed to the thiazol ring of Drug-38.

The pyrrolydyl rings of the two drugs are also parallel even if more distant from one another. Quite surprisingly. however, Figure 3 reveals that the bulk structure of the two optimal TACE binders is also very similar to the structure of Drug-44, the worst inhibitor of the series analyzed by Dai *et al*, featuring K_i of 531 nM. The RHS group of Drug-44 is not perfectly superposed to its counterparts in Drug-1 and Drug-38. In fact, the pyrazol ring of Drug-44 is rotated by almost 90 degrees with respect to the corresponding ring in Drug-1 and Drug-38 and the phenyl ring is also rotated even if less dramatically. By contrast, in the LHS substituent, the cyclopropyl-fused pyrrolidine ring occupies an intermediate position between the pyrrolidine rings of Drug-1 and Drug-38 and is almost perfectly superposed to the pyrrolidine ring of Drug-1. The thiazol ring of Drug-44 lies in the same plane as the thiazol ring of Drug-38 but is rotated with respect to it by 180 degrees so that the methyl-amino group is oriented on the opposite side.

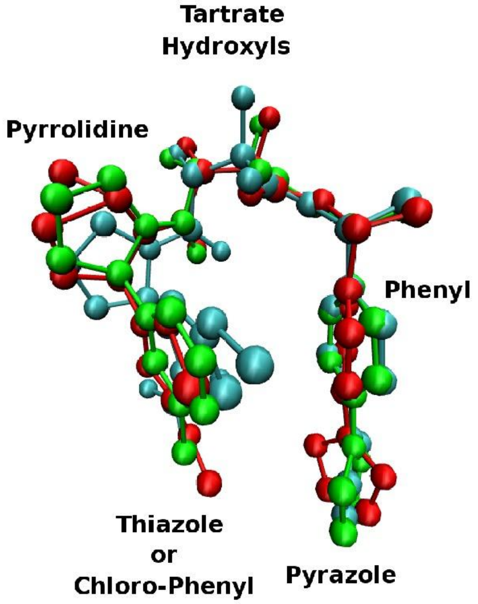

Figure 3. *Overlay of the representatives of the most populated clusters of Drug-1 (green), Drug-38 (cyan), and Drug-44 (red). The structures have been overlaid so as to minimize the RMSD of heavy atoms of the common scaffold of this family of inhibitors i.e. the tartrate core and the RHS pyrazol-phenyl-ethanamine group.*

The thiazol ring of Drug-44 also lies in the same plane as the chloro-phenyl ring of Drug-1 but the overlap is not complete.

Taken together, these results suggest that the bulk structure of both strong and weak TACE ligands is very similar so that there is no detectable correlation between the structure of the drug in the bulk solvent and its inhibition constant for TACE. This leads to the working hypothesis that what determines the strength of the inhibitor is the ability to shift from the compact conformation that is stable in the water environment to an extended conformation similar to the one exhibited by Drug-38 in the crystal complex with TACE.

What is to be expected is that the presence of specific groups in the drugs will lead to clashes with the enzyme during the conformational change so that the intermediate will be broken. Conversely the presence of other particular groups may enable the establishment of favorable contacts with the enzyme stabilizing their intermediate and favoring the structural transition to the extended conformation. The nature of the groups favoring and preventing the conformational change will be investigated through REM simulations with harmonic restraints.

CONCLUSIONS

We have simulated three recently disclosed tartrate-derived TACE inhibitors [12] with potential applications to the treatment of Rheumatoid Arthritis, Multiple Sclerosis and other autoimmune diseases. In order to perform an efficient exploration of the conformational ensemble of this molecules despite the rugged energy landscape, we performed Hamiltonian Replica Exchange Molecular Dynamics simulations [13]. Even if our work is still at a very early stage, the results suggest that the bulk structure of both strong and weak TACE ligands is very similar so that there is no detectable correlation between the structure of the drug in the bulk solvent and its inhibition constant for TACE. This leads to the working hypothesis that what determines the strength of the inhibitor is the ability to shift from the compact conformation that is stable in the water environment to an extended conformation similar to the one exhibited by Drug-38 in the crystal complex with TACE. What is to be expected is that the presence of specific groups in the drugs will lead to clashes with the enzyme during the conformational change so that the intermediate will be broken. Conversely the presence of other particular groups may enable the establishment of favorable contacts with the enzyme stabilizing the intermediate and favoring the structural transition to the extended conformation. The validation of this hypothesis would pave the way to the rational design of inhibitors of TACE and possibly some related Matrix Metalloproteinases. It is therefore our intention to proceed in this investigation through restrained Hamiltonian REMD simulations of the drug/TACE complex.

ACKNOWLEDGEMENTS

This work was performed as a part of the project *In silico assessment of peptides with potential pharmaceutical properties for Multiple sclerosis* supported by the Regione Toscana (Regional Health Research Program 2009). We thank Samuele Pierattini of the ENEA team for his constant and competent technical support on the CRESCO facility.

References

[1] PERSIDIS A.
"Autoimmune disease drug discovery"
Nature Biotech. **17** (1999) pp 1038-1039

[2] NEWTON R.C., SOLOMON, K.A., COVINGTON M.B., DECICCO C.P., HALEY P.J., FRIEDMAN S.M., VADDI K.
"Biology of TACE inhibition"
Ann. Rheum. Dis. **60** (2001) pp iii25-iii32

[3] VAN HAUWERMEIREN F., VANDENBROUCKE R.E., LIBERT C.
"Treatment of TNF mediated diseases by selective inhibition of soluble TNF or TNFR1"
Cytokine & Growth Factor Reviews **22** (2011) pp 311-319

[4] VINCENTI M.P., BRINCKERHOFF C.E.
"Transcriptional regulation of collagenase (MMP-1, MMP-13) genes in arthritis: integration of complex signaling pathways for the recruitment of gene-specific transcription factors"
Arthritis Res. **4** (2002) pp 157-164

[5] HASEGAWA A., TAKASAKI W., GREENE M.I., MURALI R.
"Modifying TNF alpha for Therapeutic Use A Perspective on the TNF Receptor"
Mini Rev. Med. Chem. **1**, (2001) pp 5-16

[6] SHARIEF M.K., HENTGES R.
"Association between tumor necrosis factor-alpha and disease progression in patients with multiple sclerosis"
N. Engl. J. Med. **325** (1991) pp 467-472

[7] THE LENERCEPT MULTIPLE SCLEROSIS STUDY GROUP AND THE UNIVERSITY OF BRITISH COLUMBIA MS/MRI ANALYSIS GROUP.
"TNF neutralization in MS: results of a randomized, placebo-controlled multicenter study"
Neurology 53 (1999) pp 457-465

[8] DASGUPTA S., MURUMKAR P.R., GIRIDHAR R., YADAV M.R.
"Current perspective of TACE inhibitors: a review"
Bioorg. Med. Chem. **17** (2009) pp 444-459

[9] MASKOS K., FERNANDEZ-CATALAN C., HUBER R., BOURENKOV G.P., BARTUNIK H. ET AL.
"Crystal structure of the catalytic domain of human tumor necrosis factor-alpha-converting enzyme"
Proc. Natl. Acad. Sci. USA **95** (1998) pp 3408-3412

[10] TU G.G., XU W.F., Huang H.M., LI S.H.
"Progress in the development of matrix metalloproteinase inhibitors"
Curr. Med. Chem. **15** (2008) pp 1388-1395.

[11] ROSNER K.E., GUO Z., ORTH P., SHIPPS G.W. Jr, BELANGER D.B.
"The discovery of novel tartrate-based TNF-alpha converting enzyme (TACE) inhibitors"

Bioorg. Med. Chem. Lett. **20** (2010) pp 1189-1193

[12] DAI C., LI D., POPOVICI-MULLER J., ZHAO L., GIRIJAVALLABHAN V.M. ET AL.
"2-(2-Aminothiazol-4-yl)pyrrolidine-based tartrate diamides as potent, selective and orally bioavailable TACE inhibitors"
Bioorg. Med. Chem. Lett. **21** (2011) pp 3172-3176

[13] FUKUNISHI H., WATANABE O., TAKADA S.
"On the Hamiltonian replica exchange method for efficient sampling of biomolecular systems: application to protein structure prediction"
J. Chem. Phys. **116** (2002) pp 9058-9067

[14] HUMPHREY W., DALKE A., SCHULTEN K.
"VMD - Visual Molecular Dynamics"
J. Molec. Graphics **14** (1996) pp 33-38

[15] FRISCH M.J., TRUCKS G.W., SCHLEGEL H.B. SCUSERIA G.E., ROBB M.A. ET AL.
Gaussian 09, Revision A.01, 2009

[16] WANG J., WANG W., KOLLMAN P.A. CASE D.A.
"Automatic atom type and bond type perception in molecular mechanical calculations".
Journal of Molecular Graphics and Modelling **25** (2006) pp 247260

[17] PROCACCI P., DARDEN T.A., PACI E., MARCHI M.
"ORAC: a molecular dynamics program to simulate complex molecular systems with realistic electrostatic interacions"
J. Comp. Chem. **18** (1997) pp 1848-1862

[18] MARSILI S., SIGNORINI G.F., CHELLI R., MARCHI M. PROCACCI P.
"ORAC: a molecular dynamics simulation program to explore free energy surfaces in biomolecular systems at the atomistic level"
J. Comp. Chem. **31** (2010) pp 1106-1116

[19] WANG J., WOLF R.M., CALDWELL J.W., KOLLMAN, P.A., CASE D.A.
"Development and testing of a general AMBER force field".
J. Comp. Chem. **25** (2004) pp 1157-1174

[20] C. GUARDIANi, G. F. SIGNORINI, R. LIVI, A.M. PAPINI, and P. PROCACCI
"*Conformational Landscape of N-Glycosylated Peptides Detecting Autoantibodies in Multiple Sclerosis,Revealed by Hamiltonian Replica Exchange*"
J. Phys. Chem. B (2012) ASAP article, DOI: 10.1021/jp301442n

[21] HEYER L.J., KRUGLYAK S. YOOSEPH S.
"Exploring Expression Data: Identification and Analysis of Coexpressed Genes"
Genome Res. **9** (1999) pp 1106-1115

DETERMINATION OF MULTI-YEAR ATMOSPHERIC TRANSFER MATRICES FOR GAINS-ITALY MODEL

Gino Briganti(a), Giuseppe Calori(c), Andrea Cappelletti(a), Luisella Ciancarella(b), Massimo D'Isidoro(b), Sandro Finardi(c), Lina Vitali(b)

(a) ENEA Territorial Office of Pisa
(b) ENEA Bologna
(c) ARIANET s.r.l. Milano, via Gilino, 9 - http://www.aria-net.it

INTRODUCTION

European Union thematic strategies on air pollution control and prevention are outlined also with the support of the GAINS-Europe model (Greenhouse gas - Air Pollution Interactions and Synergies), the integrated assessment model of impact and costs developed by IIASA (International Institute for Applied Systems Analysis, Laxenburg Austria) [1]. Specifically, the purpose is to identify alternative strategies to reduce acidification, eutrophication, ozone background levels (to minimize the impact on vegetation and health) and population exposure to fine particulate matter (PM).

The European Commission is promoting a "Thematic strategy on air pollution" [2] integrating the current legislation and focused to achieve air quality levels preserving both human health and environment quality. In particular, the Commission establishes the targets to be achieved by year 2020, through the development of suitable "integrated" measures, such as the update of existing legislation and the involvement of sectors and policies that may threat air quality.

As a consequence, all EU countries are required to comply with Directive 2008/50/EC, implementing such Thematic Strategy. Italy has now its own national air quality modeling system (AMS) and the national version of the GAINS model (GAINS-Italy [3]), which have been developed to better depict its morphological complexity of its terrain and the related meteorological-diffusive patterns, and to better analyze the regional emission control scenarios. In fact, the Italian Ministry for the Environment, Land and Sea (MATTM) has decided to adopt its own national model, to support decision-making related to air quality policies at local, national and international levels, and to detail at the national scale the quantitative studies on which the European Thematic Strategy is based. MATTM promoted and financed the MINNI project, submitted by ENEA, aiming to develop a "National integrated model supporting international negotiations on air quality policy" [4].

The integrated assessment model of impact and costs, GAINS, uses the approach of the atmospheric transfer matrices (ATMs) to estimate how changes in emission scenarios can affect pollutant concentrations and ground deposition. This is an approximate method, justified by administrators needs to get near real-time feedback on multiple scenarios analyses, despite the heavy computational resources (in terms of both CPU and elapsed time) which the involved yearly runs of the complete AMS would require.

This technical report illustrates the activities related to multi-year ATMs preparation, performed under the agreement with MATTM concerning "MINNI modeling system update and preparation of scenarios of emission and ground deposition/concentration of some air pollutants".

ATM DEFINITION

GAINS considers the following emitted precursors: SO_2, NO_x, VOC[1], NH_3 and PM_{10}[2]. In *table 1* are reported the influence of such precursors on the target pollutants (GAINS indicators) that give significant impacts on health and vegetation.

Nitrogen oxides influence all the GAINS indicators: they actually control the ozone cycle [5], their oxidized compounds (nitrates) are one of the chemical components of PM and they also determine soil acidification (nitric acid) and eutrophication (nutrient nitrogen). Primary emitted PM affects PM_{10} concentrations only. Since VOCs are precursors of oxidative processes, they determine ozone concentrations and influence PM_{10} levels due to oxidation of SO_2 and NO_x to sulfates and nitrates respectively; moreover, part of non-reactive VOCs condensates as PM_{10}. Finally, ammonia affects the concentrations of PM_{10}, as ammonium salt, and determines the ground deposition of nutrient nitrogen.

	Health		Ecosystems		
	PM	O_3	O_3	Acidification	Eutrophication
SO_2	X			X	
NO_x	X	X	X	X	X
VOC	X	X	X		
NH_3	X			X	X
PM_{10}	X				

Table 1 – *Relationship between the emissions of precursors (rows) and GAINS indicators (columns).*

ATMs are source-receptor relationships expressing the variation of concentrations/depositions in each grid point of the domain as a response to variations of precursor emissions for given sets of sources. In GAINS-Italy the twenty regions are the set of sources considered. The ATMs represent the linear approximation of the response of the atmospheric system in a neighborhood of the reference conditions, as shown by the following definition (Eq. 1).

i, k = regional aggregates

$$t_{i\alpha}^{P} = \left.\frac{\partial C_\alpha}{\partial E_i^P}\right|_{S0} \qquad t_{i\alpha}^{P} \cong \frac{\Delta C_\alpha}{\Delta E_i^P} = \frac{C_\alpha^0 - C_\alpha}{E_i^0\, x}$$

$$\Delta C_\alpha = \sum_{\substack{i\in I\\ P\in J}} t_{i\alpha}^{P} \Delta E_i^P + \sum_{\substack{i,k\in I\\ P,Q\in J}} \frac{\partial^2 C_\alpha}{\partial E_i^P \partial E_k^Q} \Delta E_i^P \Delta E_k^Q + O(\Delta E^3)$$

$$\Delta C_\alpha \cong \sum_{\substack{i\in I\\ P\in J}} t_{i\alpha}^{P} \Delta E_i^P \quad \Leftarrow \quad \textit{Linear approximation}$$

α = lattice receptors

P, Q = precursors (J ensemble of precursors)

E_i = total yearly emission from the i-th region

C_α = yearly averaged concentration over receptor α

$t_{i\alpha}$ = ATM coefficients

$S0$ = reference scenario

x= emission reduction factor

Eq. 1 – Calculation scheme of the ATM terms

---

[1] Volatile organic compounds.

[2] Particulate matter with aerodynamic diameter up to 10 μm.

An analogous definition is valid also for the depositions. The smaller are the emission variations in a neighborhood of the reference conditions, the more accurate will be the prediction from Eq. 1.

It is worth to point out that the $t_{i\alpha}$ coefficients depend both on the emission reference scenario and the meteorology, so in principle new ATM calculations are needed when the reference emissions or meteorological conditions are significantly changed.

It is however important to get a "stable" definition of matrices coefficients, averaged as much as possible over a broad spectrum of weather conditions: in fact, whereas the emissions may somehow be put under control, it is obviously not possible to govern or modify the weather conditions. Strictly speaking, pollutants emissions also affect the weather, but these are long-term changes, typically considered in global climate studies, that lie outside this context. Evaluations of meteorological inter-annual variability are hence useful, and they were actually carried out. Meteorology-averaged ATMs were estimated by firstly averaging the concentration fields calculated over multiple meteorological years and then applying the prescriptions of Eq. 1 for the calculation of $t_{i\alpha}$.

SIMULATIONS SETUP

The chemical-diffusive simulations were conducted by using the FARM code (Flexible Regional Atmospheric Model) [6], a three-dimensional Eulerian model with K-type turbulence closure that accounts for the transport, chemical reactions and ground deposition of atmospheric pollutants. The version used is the 2.13.5 with SAPRC90 chemical mechanism [7] and AERO3 model for aerosols [8], parallelized by means of OpenMP paradigm.

The GAINS 2015 inventory without climate package [9], hereinafter identified by "GAINSnoCP 2015", was selected as the reference emission database.

The emission fields were calculated by means of the version 5.1 of EMGR (Emission Manager), a package of procedures (bash, make-files and Fortran executables) that, starting from total annual emissions at provincial level, allows their speciation, grid allocation and temporal modulation.

Unlike FARM, EMGR is only running in a multi-serial way, because parallelization is not suitable to the kind of the calculation required.

The initial and boundary conditions for the chemical species have been provided from the Unified EMEP model data [10], running at lower spatial resolution over the whole European area.

Input meteorological fields for FARM have been prepared by using the RAMS code (Regional Atmospheric Modeling System - Colorado State University, [11]), a prognostic non-hydrostatic model. Initial and boundary conditions were obtained from the ECMWF analysis fields (European Centre For Medium-Range Weather Forecast, [12]). Simulations were performed in nudging mode, using ground-based synoptic observations and upper-air soundings provided by WMO (World Meteorological Organization) network, available through ECMWF databases.

The meteorological database produced in MINNI Project covers years 1999, 2003, 2005 and 2007. The fields are defined over an horizontal regular grid of 67x75 points at 20 km spatial resolution over the whole Italian area and 16 irregularly spaced vertical levels, from 20 to 10000 m above ground level. For year 1999, RAMS outputs archives, previously processed on 12 levels, were re-processed to fit the chosen grid.

For each meteorological year, the ATM coefficients were calculated by running the atmospheric modeling system 101 times (20 regions x 5 precursors, plus the reference scenario), performed by using the reference emission scenario. For each run, the regional reference emissions of each precursor were alternately and selectively abated by 25%, an amount wich is compatible with the expected abatement ranges. Additional runs with an abatement of 50% of NOx emissions of Lombardy, Lazio and Campania regions were also performed, to introduce second order terms in the series expansion of Eq. 1, allowing a better fit of ozone concentrations near the large urban areas of Milan, Rome and Naples, were stronger non-linearities are present.

STORAGE AND COMPUTING TIMES

For the purpose of ATMs calculations it is enough to save only the 2D output fields of a small number of indicators/pollutants produced by the air quality model, hence allowing a strong reduction of the memory requirements with respect to full model outputs. The storage amount needed for ATMs is 220 GB/year, leading to a total of 0.88 TB. A small additional memory, about 100 GB, is required for field emissions.

With the best performance settings, i.e. using OpenMP FARM version and 8 processors (corresponding to the maximum computing speed), each run lasts about 4 days in terms of "elapsed time", corresponding to 32 days in terms of total CPU. Then, the computation time for a complete ATM, relative to one meteorological year, is about 3200 days of CPU. The sum for all 4 matrices therefore corresponds to 35 years of CPU.

FARM runs were performed using 4 or 8 processors, depending on available computing slots and queues lasting up to 24 hours. In order to use 24-hour queues, each 1-year run were splitted in 37 concatenated 10-days runs.
An average of 25-30 batches at a time were submitted to avoid the occupation of all the free resources, therefore allowing to complete the calculation of each matrix in about three weeks.

On the contrary, the emission preparation have required a different approach with respect to FARM. Both the limited availability of multi-serial queues and the massive use of I/O fluxes between CPU and storage disks needed by the EMGR, did not allowed the splitting of the yearly batches. Moreover, the mentioned I/O fluxes imposed the selection of hosts with both large enough local disks and fast data transfer speed.
As a general rule, no more than 3-6 1-year batches at a time were submitted, each of them lasting about 10 hours. The overall computing time was about 10 days. Therefore, although emission fields calculation is more straightforward then the concentrations/deposition one, waiting times were comparables. At the moment, however, the operational version 5.3 of EMGR is available, allowing a reduction of more than 95% of the temporal modulation of the emissions and thus leading to a more optimized multi-serial management of emission fields calculations.

Despite of this huge CPU demand, the gathered information is very valuable: once summarized an introduced in GAINS, it allows an administrator who wants to explore the effects of emission abatement policies to reconstruct and compare multiple scenarios in near real-time, by means of Eq. 1. Once the suitable scenario has been selected, it is anyway recommended a thorough check of the resulting concentrations/deposition through the application the complete atmospheric modeling suite.

RESULTS

Before using the ATMs in GAINS it was deemed appropriate to conduct a detailed analysis, comparing the predictions of the levels of concentration/deposition guessed by means of the ATMs with those calculated by using “control” full runs performed by the AMS.
The comparison has been conducted for two scenarios: a) “GAINSnoCP 2020”, that is a 5-year forward projection of “GAINSnoCP 2015” (*table 2*); b) the hypothetic scenario “minus25”, corresponding to a systematic abatement of 25% of all the precursors for each region, except for NO_x, reduced by 30%.

Precursor Region	SO_2 [%]	NO_x [%]	NH_3 [%]	VOC [%]	PM10 [%]
Abruzzo	5.45	-21.24	-6.14	-7.07	-3.83
Basilicata	-2.22	-18.45	-5.93	-2.29	-2.40
Calabria	-3.61	-18.99	-6.02	-4.16	-4.22
Campania	5.27	-20.12	-7.85	-7.94	-4.25
Emilia Romagna	-0.70	-19.82	-5.46	-7.44	-4.43
Friuli Venezia Giulia	-1.11	-19.05	-9.46	-5.39	-4.03
Lazio	-4.31	-23.86	-8.01	-7.44	-4.91
Liguria	-1.40	-15.64	-11.98	-6.51	-1.87
Lombardy	-9.56	-17.01	-5.17	-5.18	-3.79
Marche	-0.31	-23.84	-10.00	-5.26	-4.49
Molise	-0.92	-16.46	-4.75	-2.91	0.50
Piedmont	-4.89	-17.54	-5.75	1.09	-2.44
Puglia	-2.04	-13.44	-13.83	-6.00	-3.71
Sardinia	-4.68	-13.24	-4.26	-3.62	-3.34
Sicily	-1.31	-13.33	-8.17	-7.86	-4.35
Trentino Alto Adige	-19.20	-26.49	-4.18	-3.41	-4.47
Tuscany	0.46	-15.29	-10.32	-5.23	-1.74
Umbria	-7.48	-17.47	-10.03	-6.98	-2.80
Valle d’Aosta	-14.35	-18.10	-3.90	-2.35	0.79
Veneto	-0.88	-15.14	-7.47	-3.64	-1.28

Table 2 – *Percentage changes in emission scenario "GAINSnoCP 2020" compared to "GAINSnoCP 2015."*

Figure 1a shows the comparison between the complete simulation and the reconstruction with the ATMs method for the a) case, concerning the ozone indicator SOMO35 [13]. In *figure 1b* are instead shown the analogous comparisons concerning the b) case.

While GAINSnoCP 2020 scenario is reproduced in a more reliable way, the approximation resulting from the ATMs appears to be consistent also for the larger variations implied by minus25 scenarios, confirming the robustness of the approximate method and the possibility of its use in GAINS-Italy for the comparative screening of multiple scenarios.

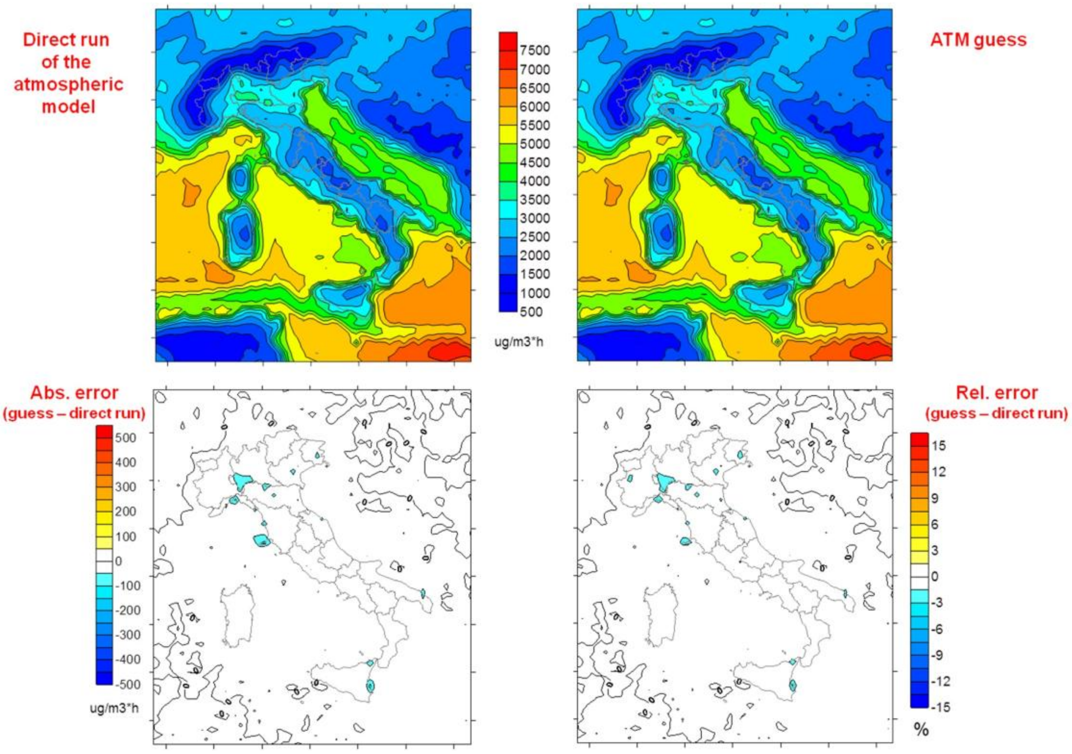

Figure 1a – *Ozone, "GAINSnoCP 2020" scenario: comparison between SOMO35 indicator computed through a complete run of the AMS (top left) and ATM estimate (top right). Bottom: absolute (left) and relative (right) errors between ATM and AMS calculations.*

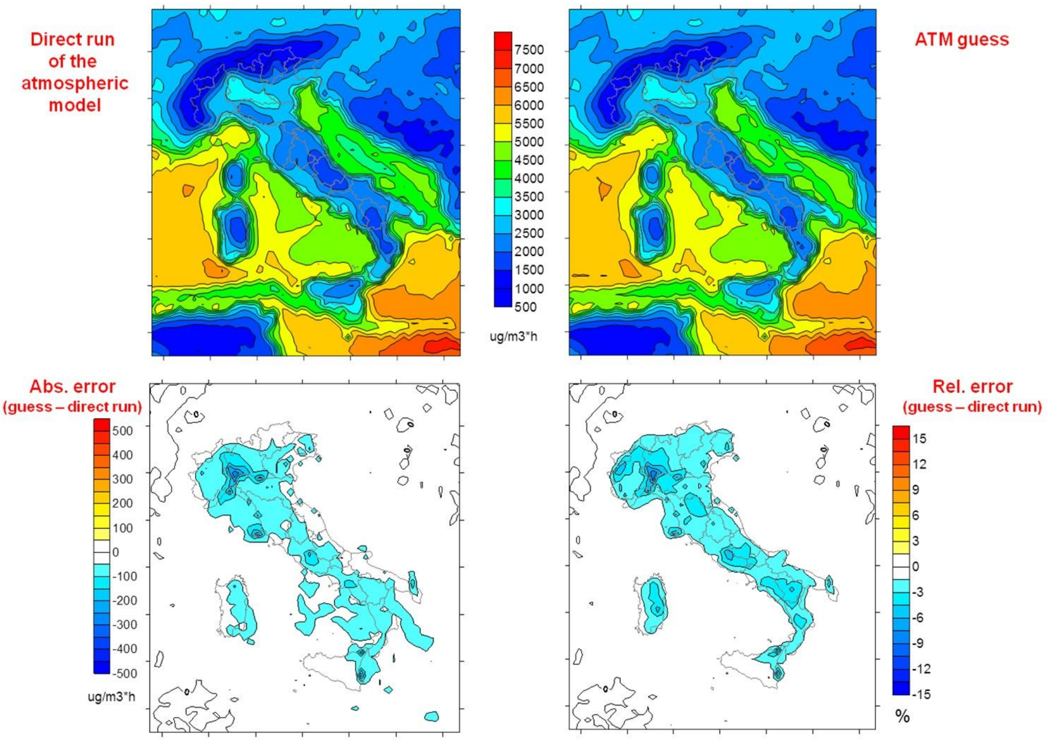

Figure 1b – *As Fig 1°. But for "minus25" scenario.*

RIFERIMENTI BIBLIOGRAFICI

[1] http://gains.iiasa.ac.at/index.php/home-page.

[2] COM(2005)446 *"Communication from the Commission to the Council and the European Parliament: Thematic strategy on air pollution"* September 21, 2005.

[3] D'ELIA I., BENCARDINO M., CIANCARELLA L., CONTALDI M., VIALETTO G. *"Technical and Non-Technical Measures for air pollution emission reduction: The integrated assessment of the regional Air Quality Management Plans through the Italian national model"* Atmospheric Environment **43** (2009) pp. 6182-6189.

[4] http://www.minni.org.

[5] SEINFELD J.H., PANDIS S.N. *"Atmospheric Chemistry and Physics, from Air Pollution to Climate Change"* John Wiley, New York (1998), ISBN 0-471-17816-0.

[6] SILIBELLO C., CALORI G., BRUSASCA G., GIUDICI A., ANGELINO E., FOSSATI G., PERONI E., BUGANZA E. *"Modelling of PM_{10} concentrations over Milano urban area using two aerosol modules"* Environmental Modelling and Software **23** (2008) pp 333-343.

[7] CARTER W.P.L. *"A detailed mechanism for the gas-phase atmospheric reactions of organic compounds"* Atmospheric Environment **24** A 3 (1990) pp 481-518.

[8] BINKOWSKI F.S. *"The aerosol portion of Models-3 CMAQ. In Science algorithms of the EPA Models-3 Community Multiscale Air Quality (CMAQ) modeling system. Part II: Chapters 9-18."* D.W. Byun, and J.K.S. Ching (Eds.). EPA-600/R-99/030, National Exposure Research Laboratory, U.S. Environmental Protection Agency, Research Triangle Park, NC, 10-1-10-16.

[9] http://gains.iiasa.ac.at/index.php/policyapplications/eu-climate-a-energy-package.

[10] COTTON, W.R., PIELKE R. A., WALKO R. L. , LISTON G. E., TREMBACK C. J., JIANG H., MCANELLY R. L., HARRINGTON J. Y., NICHOLLS M. E., CARRIO G. G. AND MCFADDEN J. P. *"RAMS 2001: Current status anf future directions"* Meteorol. Atmos. Phys. **82** (2003) pp 5-29.

[11] http://www.emep.int.

[12] http://www.ecmwf.int.

[13] AMANN M., BERTOK I., COFALA J., GYARFAS F., HEYES C., KLIMONT Z., et al. *"Baseline scenarios for the clean air for Europe (CAFE) programme. Final Report"* Contract No B4-3040/2002/340248/MAR/C1, Laxenburg, IIASA Austria.

HYDROPHOBIC COATINGS ON HYDROGENATED (111) SILICON SURFACE

Fabrizio Gala and Giuseppe Zollo

Dipartimento di Scienze di Base e Applicate per l'Ingegneria (Sezione di Fisica),
Università "La Sapienza", Via A. Scarpa 14-16, 00161 Rome, Italy

I. Introduction

The novel interest in fluid dynamics at the nano scale has pointed out the need for a better understanding of transport properties of liquids in contact with a solid surface. The subject is of great interest in the fabrication of nano-sized devices for the analysis of biological species, such as proteins or DNA [1-2]. Nowadays gel electrophoresis is still the standard method for separating proteins; however the randomness of the gel's structure makes it difficult to tune properly these devices in order to control protein selectivity. As an alternative, nanofluidic molecular sieving systems, implemented in the framework of the semiconductor nano-technology, have been proposed and applied successfully for biomolecules of various size[3-4]. Such devices are made of long channels designed on a Silicon substrate by standard photolithography technique; if an external electric field is applied and the device is soaked in an electrolyte solution containing the biological material to be separated, the sieving mechanism is obtained by alternating thick and thin regions in the canal through which the different molecules are driven and from which they escape with different time scales. These nano-canals may suffer of electro-osmotic effects due to charged walls: the ionic particles of the electrolyte solution are forced by the electrostatic interactions to rearrange themselves in the liquid in order to screen the charge at the interface thus forming an electrical double layer (EDL) of adsorbed and semi mobile particles. The coupling between the ions of the EDL and the diffusing biomolecules affects both the resolution and the fine tuning of the nano-canals. A standard method to avoid this problem is to deposit on the surface a hydrophobic, self-assembled monolayer (SAM) with an ending methyl group, as chlorodimethyloctylsilane [5] ($CH_3(CH_2)_7Si(CH_3)_2Cl$), octadecyltriethoxysilane[6] ($CH_3(CH_2)_{17}Si(OC_2H_5)_3$), or octadecyltriclorosilane[7] ($CH_3(CH_2)_{17}SiCl_3$)(OTS); in particular the latter one has revealed a good choice for surface modifications and functionalization applications[8] mainly because of the high quality of the SAM produced, i.e. a great stability and a certain facility of forming uniform and complete self-assembled monolayers. Following few preliminary results published elsewhere[12], in this article we report on accurate ab-initio atomistic models of adhesion patterns of n-alkane and n-alkyne-silane as building blocks of hydrophobic SAM on hydrogenated (111) Si surface.

II. Theoretical Method

The properties of SAMs onto the (111) Si surface have been studied by first principles calculations based on density functional theory (DFT). A generalized gradient approximation (GGA), using Perdew-Burke-Ernzerhof formula[13] (PBE) for the electron exchange and correlation energy have been employed, and norm-conserving pseudo potentials have been constructed with Troullier-Martins scheme[14] in the framework of a plane wave basis set expansion. All the first-principles calculations have been performed using the QUANTUM-ESPRESSO package[15], with a plane wave energy cut-off of 150 Ry for the wave functions. The silicon surface has been modelled as a three layer slab of 96 atoms with 32 Si atoms per layer,the vacuum region have been chosen to be equal to 18 Si atomic layers (≈4.3 nm) and all the dangling bonds of the Si slab have been passivated with H atoms. Periodic boundary conditions (PBC) have been employed together with a dipole correction rectifying the artificial electric field across the slab induced by PBC[16]. The (111) surface has been chosen to lay in the xy plane, while the minimum energy configuration has been obtained using the Broyden-Fletcher-Goldfarb-Shanno (BFGS) method[17] together with the Hellmann-Feynman forces acting on the ions. All the calculations have been performed using a (2x2x1) Mokhorst-Pack *k*-point grid[18] for the Brillouin zone sampling that has been proven to guarantee the total energy convergence as confirmed by several accurate tests performed on the Si surface concerning the total energy convergence with the energy cut-off and the *k*-point mesh. The ionic minimization has been done until the convergence threshold of 0.001 a.u. of the total force was reached. The precursors used for the surface functionalization have been chosen looking at the experimental literature: indeed both the octadecane and the OTS are among the most commonly used polymers for hydrophobic coatings of Si. In the OTS case, however, we consider the hydroxylated molecule because in water solution the Cl atoms are replaced by the -(OH) groups via the reaction $CH_3(CH_2)_{17}SiCl_3+H_2O \leftrightarrow CH_3(CH_2)_{17}Si(OH)_3+3HCl$. The molecule adsorption occurs following one of the two reactions:

$$\left.\begin{array}{c} CH_3(CH_2)_{17}Si(OH)_3 \\ (CH_3)_2(CH_2)_{16} \end{array}\right\} + \mathrm{H{:}Si} \leftrightarrow \mathrm{A/H{:}Si} + B_{(g)} \qquad (1)$$

where H:Si indicates the silicon surface passivated with hydrogen atoms, A/H:Si is the molecule (OTS or 18-alkyl) adsorbed onto such a surface and $B_{(g)}$ is in general a gaseous hydrogenated molecule containing a H atom coming form the adsorption site of the surface. The adsorption energies of reactions in Eq. (1) are defined as:

$$E_{ads} = E(\mathrm{A/H{:}Si}) + E(B) - \left\{\begin{array}{c} E(CH_3(CH_2)_{17}Si(OH)_3) \\ E(CH_3)_2(CH_2)_{16}) \end{array}\right\} - E(\mathrm{H{:}Si}) \qquad (2)$$

The adhesion bond between the molecule and the surface has been analyzed with the aid of maximally localized Wannier functions[19] (MLWFs) $w_n(\mathbf{r}-\mathbf{R})$ centered on it, and associated with band n in cell $\mathbf{R}$, evaluated through the Wannier90 pacakge[20]. Using the ground state electron charge density $\rho_{el}(\mathbf{r})$ of the different configurations studied, we have calculated the total electrostatic potential by solving the Poisson equation in the reciprocal space[16][21] with the Fourier transform of the total charge density $\rho(\mathbf{r})=\rho_{el}(\mathbf{r})+\rho_{ion}(\mathbf{r})$ as a source function. The ionic part of such density is modelled as a superposition of delta functions in the real space: $\rho_{ion}(\mathbf{r})=\sum_j Z_j^{val}\delta^{(3)}(\mathbf{r}-\mathbf{R}_j)$, where Z_j^{val} and $\mathbf{R}_j$ are the valence charge and the position of the j-th ion in the supercell, respectively. From the obtained potential field maps, the force field of short range strong dipolar interactions, such as hydrogen bonding, will be evidenced and studied while qualitative indications will be deduced concerning the weaker long range Van der Waals dipolar interactions; it is known, indeed, that state of the art time independent DFT calculations, in both the LDA and GGA approximations, are affected by inaccuracies concerning the long-range Van der Waals interactions due to the formulation of the exchange-correlation electron many-body energy term[22], even though a general qualitative scenario can be still inferred at this level of theory. However, wherever required by the system examined, such as in the case of the two 18-alkyl polymers adsorbed at adjacent sites, we have used a semi-empirical correction to evaluate more precisely the long range dispersion forces and their contribution to the total energy[23].

III. Result and discussion

1. The 18-alkyl case

The adhesion of an octadecane molecule onto (111) Si:H surface occurs through the formation of a Si-C bond. First of all we have found the equilibrium Si-C bond length keeping fixed the tetrahedral coordinations of the C atoms. The equilibrium length of the adhesion bond is found to be d_{SiC} = 0.188 nm that is quite close to the values reported in the literature for tetrahedrally coordinated SiC politypes[24]. Then we have performed a sequence of preliminary static calculations by varyng the direction of the polymer chain with respect to the normal axis **n** aligned along the [111] direction and two reference in-plane axes on the (111) Si surface, $\mathbf{e}_1$ and $\mathbf{e}_2$ (see *figure 1(a)*). Therefore we have used two configuration angles φ_1, φ_2 between the Si-C bond direction and the unit vectors $\mathbf{e}_1$ and $\mathbf{e}_2$ respectively in the ($\mathbf{n}$,$\mathbf{e}_1$) and in the ($\mathbf{n}$,$\mathbf{e}_2$) planes and one rotation angle θ of the Si-C bond direction around the the [111] direction, namely the angle formed between the projection of the polymer axis onto the (111) Si surface and the reference in-plane direction $\mathbf{e}_1$ (see *figure 1(b)*).

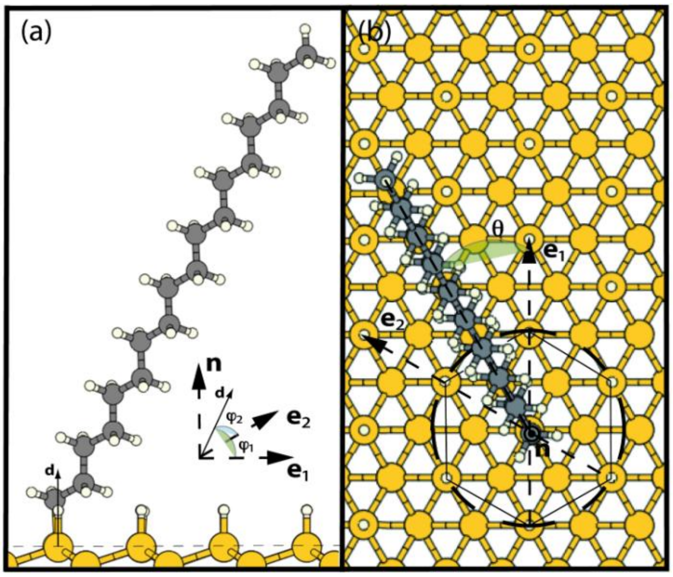

Figure 1 - *Adsorption configuration of the alkyl chain onto the (111) Si:H surface. The adhesion geometry is described in terms of the* φ_1 *and* φ_2 *angles, formed by the Si-C bond direction with respect to the surface unit vectors* $\mathbf{e}_1$ *and* $\mathbf{e}_2$*, and the* θ *angle between the polymer chain projection onto the surface and the* $\mathbf{e}_1$ *unit vector (see the text). The configuration angles are changed statically during the constrained first optimization stage.*

The results collected are shown in *figure 2(a)* where it clearly emerges that the minimum energy configuration obtained is the one with the Si-C bond aligned along the [111] direction, i.e. the one preserving the tetrahedral coordination of Si; therefore the tilt angle θ_{tilt}= 35° formed between the direction of the polymer chain and the [111] direction is constrained by the tetraherdal coordination of the Si and the C atoms involved in the adhesion configuration.

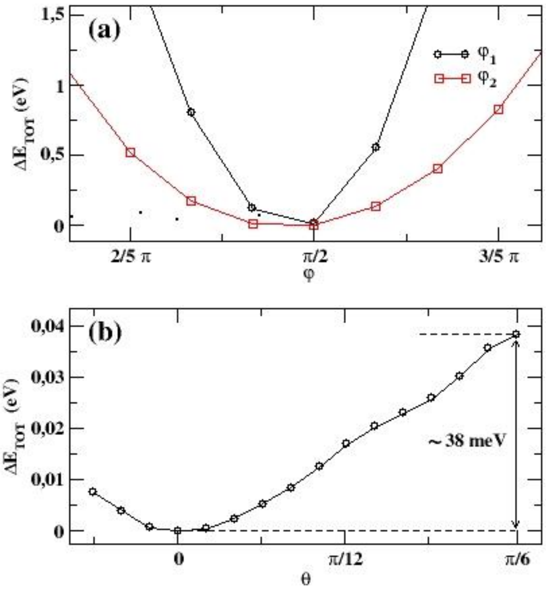

Figure 2 - *Total energies for different* $CH_3(CH_2)_{17}/H:Si$ *configurations obtained during the constrained first optimization stage (see the caption of Fig. 1) by varying either* φ_1/φ_2 *(with* $\theta=\theta_{min}= 0$*) (a) or* θ *(with* $\varphi_1=\varphi_2=\pi/2$*) (b). All the energies are referred to the most stable configuration. Both the static calculations have been performed with the fixed Si-C adhesion bond of 0.188 nm as discussed in the text.*

The static calculations performed by varying θ with $\varphi_1=\varphi_2=\pi/2$ are reported in *figure 2(b)* evidencing that the minimum energy configuration is the one with $\theta=0°$ or, equivalently, $\theta=n\pi/3$ (n = 0,1,..,5), that guarantees the weakest interaction between the next lowermost hydrogens of the polymer and the hydrogenated Si surface; this result is in qualitative agreement with previous experimental measurements[9] and evidences, as expected, that the most stable configuration is simply driven by the sp^3 coordination constraints of C and Si atoms and by the steric hindrance between the hydrogen atoms of the alkyl chain and the ones onto the hydrogenated surface. The energy barrier for rotations around the equilibrium Si-C bond direction (i.e. around the [111] axis) is only 38 meV that, using simple transition state theory considerations[25] leads to the estimate of the rotation frequency of 10^{-1} s^{-1} at room temperature (RT). Hence high coverage values are most probably prevented because the available Si surface adsorption sites, that are neighbors of a 18-alkyl functionalized surface site, are hindered by the thermal rotation of the polymer; this circumstance, together with the observation that strain effects at high coverage values may result in instabilities of the alkyl monolayer[26], may limit the coverage of the (111) Si surface with alkyl chains, even for long reaction times, in agreement with the experimental finding of partial coverage of hydrogenated (111) Si surface (about 50% mono layer (ML)) with fragmented island shaped MLs[27]. It should also be kept in mind that the alkyl chain may be in various different isomeric configurations that are about 86 meV higher in energy for each eclipsed geometry involving neighboring CH_2 monomers and also this circumstance may affect the coverage limit[28] at higher temperature than RT. Starting from the previous minimum energy configuration, the system has been fully relaxed as detailed in the previous section; the ground state configuration of the 18-alkyl adhesion on (111) Si:H, reported in *figure 3(a)*, differs slightly from the one discussed previously because, despite θ is unchanged, the φ_1 and φ_2 values are equally modified by a small quantity $\Delta\varphi$= 5° while the tilt angle value is θ_{tilt}=33, indicating that the adhesion geometry is still led by the tetrahedral coordination of Si and C.

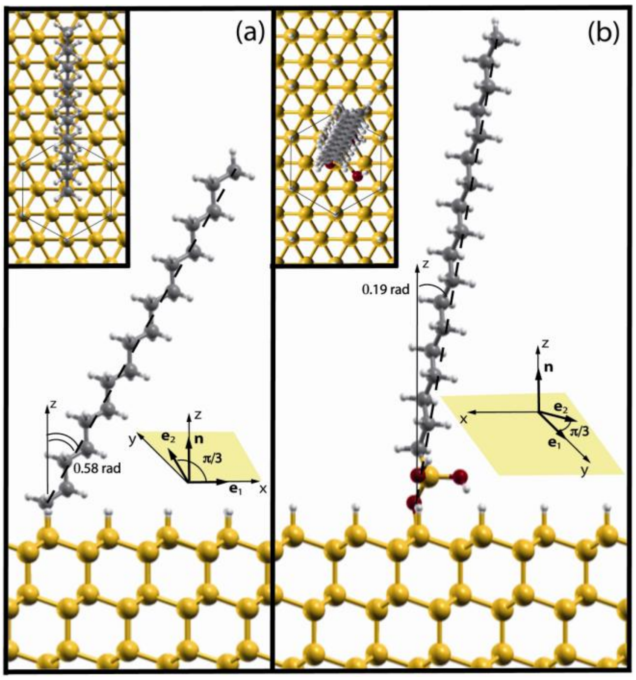

Figure 3 - *Fully relaxed configuration of the 18-alkyl chain (a) and the hydoxilated OTS molecule (b) adsorbed onto the hydorgenated (111) Si surface. In the insets the (111) plane view is reported for both the configurations.*

In order to check this circumstance we have compared the Si-C adhesion bond length and the Si-C-C adhesion angle of the fully relaxed 18-alkyl adhesion geometry with the same quantities in a fully relaxed hydroxylated OTS molecule that may also be used as precursor for the formation of a monolayer of pure alkyl chains as pointed out experimentally[31-32]; we found that these values are larger by about +0.05 nm and +0.6° with respect to the OTS values that are respectively d_{SiC}= 0.186 nm and α_{SiCC}=115.2°; moreover the Löwdin population analysis shows a small variation Δq= -0.15 e^- of the charge on the C atom involved in the bridge bond compared to the $CH_3(CH_2)_{17}Si(OH)_3$ case.

The nature of the chemical bonding between the molecule and the Si surface has been investigated looking at the electron charge density profile in the plane containing the adhesion bond and at the Wannier function centered on it; the results reported in *figure 4* show that this bond has a clear σ character between two sp^3 hybrid valence orbitals belonging to Si and C; the MLWF centre is shifted towards the C atom by about 17% with respect to the bond mid point as expected due to the larger electronegativity of the C atom.

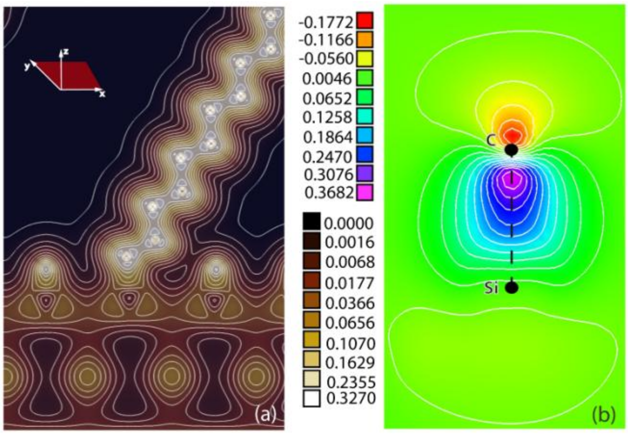

Figure 4 - *Charge density map (in e^- units) in the (010) plane containing the Si-C adhesion bond (a). Contour plot in the (010) plane of the maximally localized Wannier function centered on the Si-C adhesion bond of the alkyl molecule and the (111) Si surface (b). The MLWFs (in units of $a_0^{-3/2}$) observed along the Si-C bond direction reveal the σ bonding features between two sp^3 hybrids belonging to Si and C.*

We have explored two possible reaction pathways for the deposition of a 18-alkyl onto a (111) Si:H surface involving either an hydroxylated OTS or a 18-alkane as precursors:

$$\left.\begin{array}{c} CH_3(CH_2)_{17}Si(OH)_3 \\ (CH_3)_2(CH_2)_{16} \end{array}\right\} + H{:}Si \leftrightarrow \left\{\begin{array}{c} CH_3(CH_2)_{17}/H{:}Si + HSi(OH)_{3(g)} \\ CH_3(CH_2)_{17}/H{:}Si \;+\; H_{2(g)} \end{array}\right. \tag{5}$$

The calculated reaction energy values, reported in *table I*, show that the reaction is endothermic using OTS as precursors (E_{ads} =0.16 eV in parentheses in Table I), needing additional thermal energy mainly to separate the $–Si(OH)_3$ radical from the OTS molecule before proceeding to the adhesion onto the surface; on the contrary the reaction is highly exothermic for the n-alkane case (E_{ads} = -2.38 eV), in agreement with previous experimental results[31-32].

TABLE I. Adsorption Energy for the various configurations considered in the present work.

Configuration	**E_{ads}(eV)**
$CH_3(CH_2)_{17}/H{:}Si$	-2.38 (+0.16)
$2xCH_3(CH_2)_{17}/H{:}Si$	-4.63 (+0.45)
$CH_3(CH_2)_{17}Si(OH)_2O/H{:}Si$	-0.64
$2xCH_3(CH_2)_{17}Si(OH)_2O/H{:}Si$	-1.47

2. The OTS case

The simplest chemical path that may be used to deposit OTS monolayers on a hydrogenated (111) Si surface must involve the octadecyltrihydroxysilane as a precursor obtained in water solution from OTS. In this way, the surface functionalization proceeds via the following reaction:

$$CH_3(CH_2)_{17}Si(OH)_3+H{:}Si\leftrightarrow CH_3(CH_2)_{17}Si(OH)_2O/H{:}Si+H_{2(g)} \tag{6}$$

where the polymer is expected to be bonded to the silicon surface through an oxygen atom forming two Si-O bonds, one with the Si atom belonging to the OTS molecule and the other with a Si atom onto the (111) surface.

As for the alkyl case, for computational reasons we have initially studied the energetics and the configurations of the deposited molecule by total energy calculations without structural relaxation; the different configurations have been explored by varying the direction of the Si-O bond at the topmost Si layer with the silane group constrained at its original tetrahedral geometry. Thus, similarly to the 18-alkyl case, the static calculations have been performed by changing the rotation angle θ around the [111] axis (see *figure 5*) and the two angles φ_1 and φ_2 between the Si-O bond at the topmost Si layer and the $\mathbf{e}_1$, $\mathbf{e}_2$ unit vectors thus setting the chain orientation respectively in the planes ($\mathbf{e}_1$,**n**) and ($\mathbf{e}_2$,**n**).

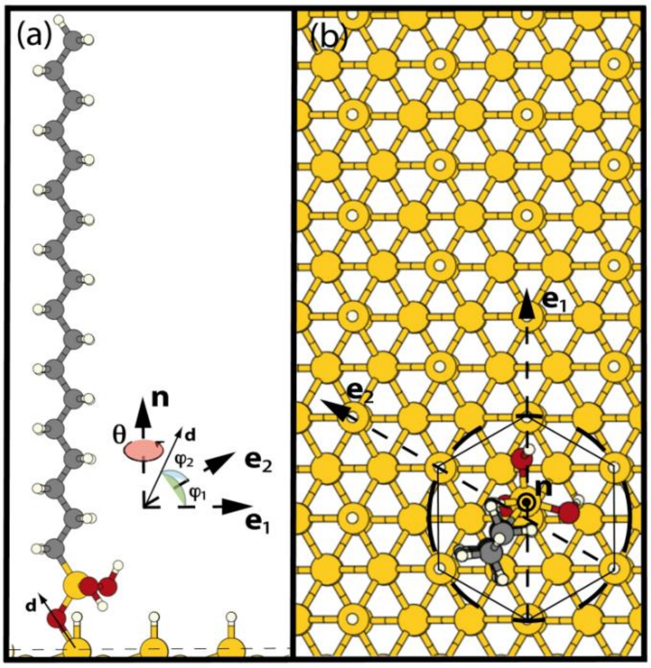

Figure 5 - *Adsorption configuration of the alkyl chain onto the (111) Si:H surface. The adhesion geometry is described in terms of the* φ_1 *and* φ_2 *angles, respectively formed by the Si-O bond direction (**d**) and the surface unit vectors* $\mathbf{e}_1$ *and* $\mathbf{e}_2$*, and the θ angle between the polymer chain projection onto the surface and the* $\mathbf{e}_1$ *unit vector (see the text). The configuration angles are changed statically during the constrained first optimization stage.*

Moreover we have also explored other configurations that differ by the orientation of the hydroxyl groups in the silane structure because these groups interact with the hydrogens at the Si surface. The energy values of the various configurations obtained by varying φ_1, φ_2 and θ are shown in *figure 6(a)* and *figure 6(b)* respectively. The minimum energy configuration obtained by varying φ is reported in *figure 6(a)* and shows a slight distortion of the bond angle orientation with respect the surface normal vector (of 6°).

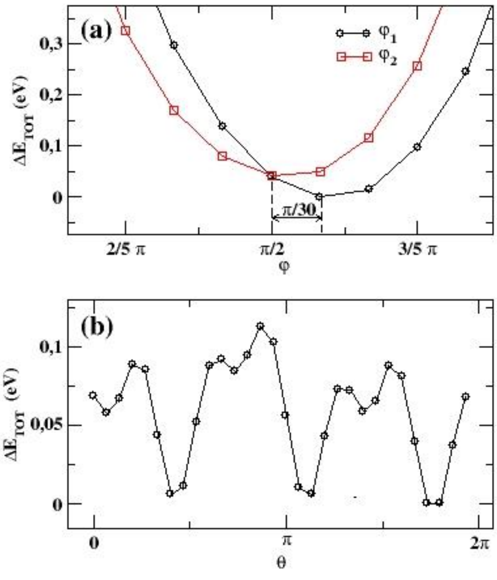

Figure 6 - *Total energies for different adsorption configurations of a hydroxylated OTS molecule onto the (111) Si:H surface obtained during the constrained first optimization stage (see the caption of Fig. 5 for the details) by varying* φ_1 *(*φ_2*) with* $\theta=\theta_{min}=0$ *(a)) or θ (with* $\varphi_2=\pi/2$ *and* $\varphi_1=\varphi_2+\pi/30$*) (b). All the energies are referred to the most stable configuration. Both the static calculations have been performed with Si-O adhesion bond length constrained at its equilibrium value* $d_{SiO}=0.165$ *nm in a fully relaxed* $CH_3(CH_2)_{17}Si(OH)_3$ *molecule.*

The energy variation with θ exhibits the expected quasi-periodic behaviour with clear energy minima and maxima reflecting the interaction between the two hydroxyl groups in the silane structure and the hydrogen atoms on the Si topmost layer; indeed, the most stable configuration is the one with the largest distance between the hydrogen atoms of the hydroxyl groups and the ones at the topmost Si layer; the lone pairs of the oxygen atoms, instead, are unlikely to interact with the hydrogens onto the Si surface that are too far away. The energy barrier measured between the highest energy configuration and the most stable one is ΔE=0.1 eV and is large enough to prevent any rotation around the [111] axis at RT. Then a full structural optimization has been performed following the prescriptions discussed in the section II; the resulting minimum energy configuration is shown in *figure 3(b)*; it is worth noting that the equilibrium final positions of the two hydroxyl groups have been somehow constrained by the repulsive interaction with the hydrogen atoms bonded onto the surface. The tilt angle between the main direction of the polymer chain and the [111] surface normal is θ_{tilt} = 10.9°, in good agreement with the experimental measurements[10][11]. The equilibrium configuration of the OTS adhesion obtained after the full relaxation is quite similar to the fully relaxed configuration of the isolated hydroxylated OTS molecule with no significant geometrical difference even in the sylane group; moreover the bond distance between the Si atom of the surface and the O atom of the molecule has been found to be d_{SiO}= 0.165nm, i.e. almost the same Si-O distance in the isolated molecule. The hydroxylated OTS polymer is the natural precursor for deposition onto the hydrogenated (111) Si surface and the calculation of the adsorption energy, reported in *table I*, gives E_{ads}=-0.64 eV revealing that the adsorption reaction is exothermic; it must be emphasized, however, that the adsorption energy in this case is about four times lower than the adsorption energy of one 18-alkyl with the 18-alkane as precursor and, as a consequence, it is expected that, at least in principle, this last reaction should be largely favoured. The electron charge density map of the ground state configuration, reported in *figure 7(a)*, reveals that a significant charge transfer occurs with respect to the isolated hydroxylated molecule involving, in particular, the O atom connecting the Si surface and the silane group. Indeed the Löwdin population analysis shows that the electron charge on the oxygen atom is reduced by Δq=0.3 e^- with respect to its charge in the OH group of the isolated OTS case (q=6.45 e^- for O and q=0.55 e^- for H); this surprising charge depletion of the O atom is accompanied by a slight increase of the negative charge belonging to the first C atom of the polymer chain. The other O atoms belonging to the OH groups not involved in the bond with the surface, on the contrary, do not show any charge transfer with respect to the isolated OTS molecule; in this case the valence electron charge belonging to an oxygen atom, that contains the contributes from the two lone pairs, is also increased by half an electron transferred from the bonded H atoms, thus resulting in a negative charge density excess that might be involved in long range interactions between two or more OTS molecules adsorbed at adjacent sites of a silicon surface.

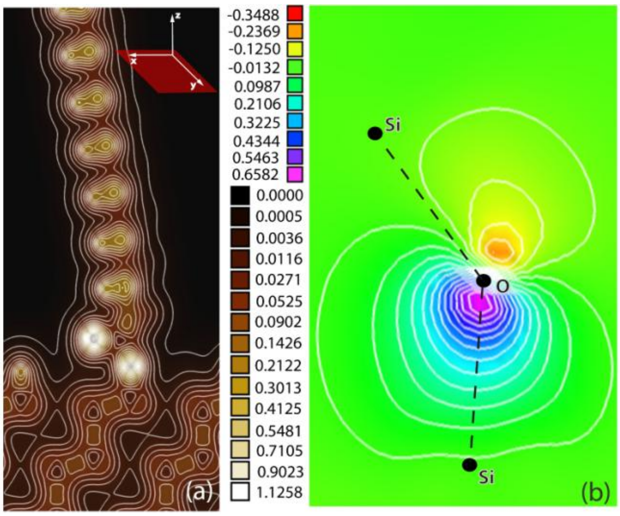

Figure 7 - *Charge density map (in e^- units) in the (010) plane containing the Si-O adhesion bond (a). Contour plot in the (010) plane of the MLWFs centered on the Si-O adhesion bond between the hydroxylated OTS molecule and the (111) Si surface (b). The MLWFs (in units of $a_0^{-3/2}$) observed along the Si-O bond direction evidences a slight distortion of the σ bond between Si and O.*

Interaction of hydrophobic polymers on (111) Si:H surface

1. The 18-alkyl case

Multiple adsorption events may occur at different sites independently through the reaction $n\mathrm{CH_3(CH_2)_{16}CH_3}+\mathrm{H{:}Si}\leftrightarrow n\mathrm{CH_3(CH_2)_{17}/H{:}Si}+n\mathrm{H_{2(g)}}$, $n \geq 2$. The interaction is entirely due to long-range electrostatic forces between chain tails and steric hindrance phenomena, with the related distortions of the two neighboring molecules. Thus, first of all we have calculated the total electrostatic potential V(**r**) generated by the dipolar charge density of the 18-alkyl chain; the density map of V(**r**) in the mid-plane between the H atoms of the Si(111) surface and the H atoms of the lowest $\mathrm{CH_2}$ trimer of the alkyl chain, reported in *figure. 8(a)*, evidences, as expected, a positive electrostatic potential that implies necessarily a repulsive interaction (thus an energy increase) between adjacent polymeric chains adsorbed onto the (111) Si surface.

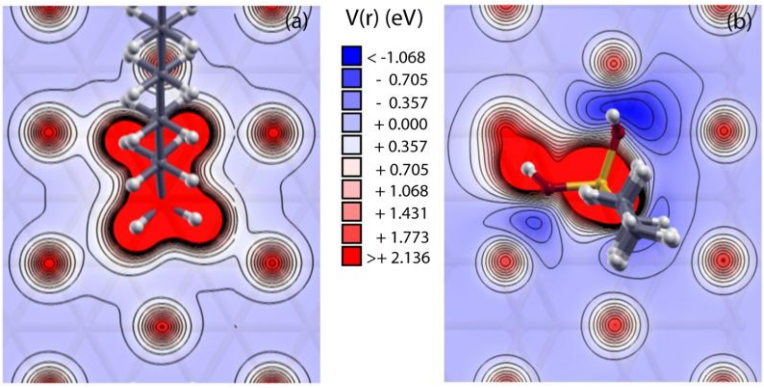

Figure 8 - *Density maps of the electrostatic potential for the ground state adsorption configurations in the 18-alkyl (a) and the OTS (b) cases. The density maps have been drawn onto meaningful planes parallel to the (111) Si surface, respectively: (a) the mid-plane between the topmost H atoms of The Si:H surface and the lowermost H atom of the alkyl chain (i.e. the one of the lowermost –$\mathrm{CH_2}$ trimer); (b) the mid-plane between the topmost H atoms of the H:Si surface and the lowermost H atom belonging to the OH groups. The distances from the surface are 0.07 nm in (a) and 0.073 nm in (b).*

Subsequently we have studied the system involving two alkyl chains adsorbed on adjacent sites of the Si (111) surface; the starting configuration, with the two alkyl chains initially parallel to each other, has been fully relaxed following the prescription discussed in Sec. II and the final ground state configuration is reported in *figure 9*. The ground state configuration obtained, keeps almost unchanged the tetrahedral coordination of the surface Si atom for both the polymers, but one of the two molecules undergoes a bending in the lower part of the chain that allows the upper part of the polymers to stay almost parallel (see *figure 9(a)*). Hence, at the end of the unconstrained relaxation run of this system, the two chains undergo a substantial repulsion with the upper part of the chains being about 0.583 nm apart. Thus the energy increase due to the bending distortion occurring in one of the two molecules is overcompensated by the energy decrease due to the mutual repulsion. The calculation of the adsorption energy in the present case gives E_{ads}=-4.63 eV revealing that, despite being highly exothermic, the adsorption of two 18-alkyl molecules at adjacent sites is unstable against the adsorption of two isolated molecules that would involve an adsorption energy of E_{ads}=-4.76 eV. The energy increase due to the distortion induced by the interaction between the adjacent chains can be calculated simply as:

$$E_b = \Delta E = E(2A/H{:}Si) + E(H{:}Si) - 2E(A/H{:}Si) \tag{7}$$

where E(2A/H:Si) is the total energy of the supercell containing two adjacent alkyl chains adsorbed onto the hydrogenated Si slab, E(H:Si) is the total energy of the hydrogenated Si slab and E(A/H:Si) is the total energy of the supercell containing one alkyl chain adsorbed onto the hydrogenated Si slab; the positive binding energy value obtained, E_b=56 meV, evidences that simple alkyl chains are definitely unfit as building blocks for dense and homogeneous hydrophobic films onto hydrogenated (111) Si surface because the alkyl adsorption at distant sites is energetically favoured with respect to the adsorption at adjacent sites. The case under study can be potentially affected by the inaccuracies concerning the long-range interactions between polymer chain tails arising from the used formulation of the exchange-correlation energy[23], as a consequence, in the present case we have corrected the total Energy in order t ogive a better estimate of the long-range interactions by adding a sempiempirical correction to the total energy of the various systems involved in the calculation of the binding energy form Eq. (7)[23]. In the case under study the contribution to the total energy of the system from the empirical dispersion term is E_d=-1.52 Ry that is approximately 0.12% of the total energy. The inclusion of this attractive term forces the two molecules to stay closer but does not change the sign of the binding energy that remains positive (E_b=12 meV) meaning that isolated alkyl chains are energetically favoured with respect to the case of the two molecules adsorbed on nearest sites, in agreement with the previous DFT calculations where the dispersion term was omitted.

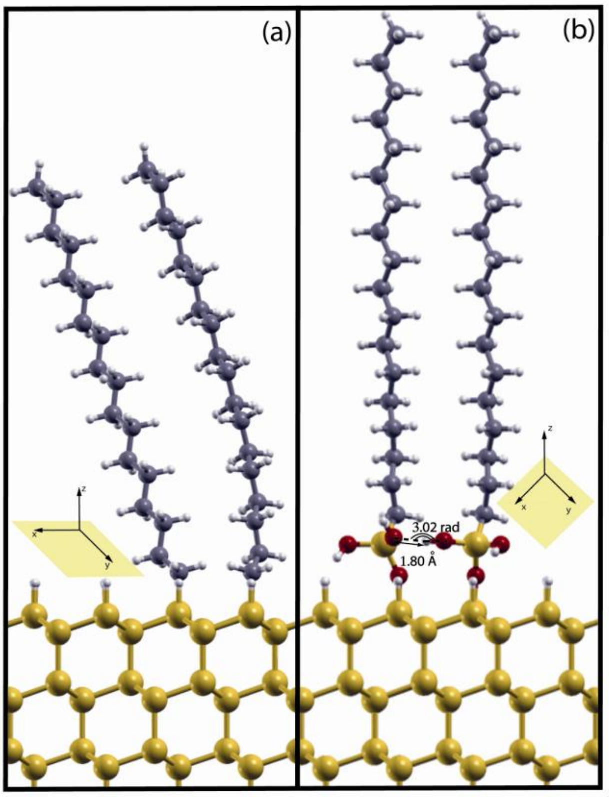

Figure 9 - *Fully relaxed configurations of two polymers adsorbed at adjacent sites onto the hydrogenated (111) Si surface for the 18-alkyl (a) and the hydroxylated OTS (b) cases.*

2. The OTS case

The interaction between two hydroxylated OTS polymers adsorbed at adjacent sites onto the (111) Si surface depends on the dipolar potential field in the vicinity of the polymer chain that is strongly affected by the presence of the hydroxyl polar groups. The total electrostatic potential field V(**r**) generated by an isolated OTS molecule deposited onto the (111) Si surface has been calculated by solving the Poisson equation with the ground state charge density obtained in the case of the fully relaxed adsorption configuration. In *figure 10(a)* it is shown the density map of the potential field in the mid-plane (parallel to the Si surface) between the topmost H atoms of the Si surface and the lowermost H atom of the OTS hydroxyl groups. The density map clearly evidences the negative potential area related to the O lone-pairs that co-exist with the positive potential regions originating from the alkyl chain. Thus the OH groups favor the interaction, via a H-bond, of the OTS with the positive charges of the unscreened hydrogens of a second hydroxylated OTS molecule, eventually adsorbed at an adjacent site of the (111) surface. Since Pauling[31], the hydrogen bond has been recognised to play a crucial role to understand the short range order in polar liquids and between polar molecules; it has been shown, moreover, that the hydrogen bond is also partially covalent[32] and thus it is expected that PBE based DFT calculations can describe it accurately within the accuracy limits here required. Hence we have performed a full relaxation of the hydrogenated Si slab with two hydroxylated OTS molecules adsorbed at adjacent sites; the starting configuration has been chosen with two exactly parallel OTS molecules on nearest sites of the (111) surface.

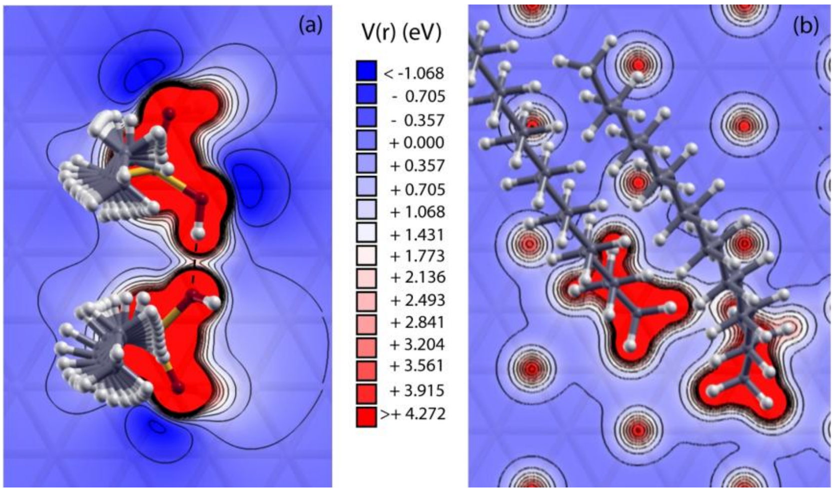

Figure 10 - *Density maps of the electrostatic potential for the ground state configurations of two polymers adsorbed at adjacent sites onto the hydrogenated (111) Si surface. The density maps for the OTS (a) and the 18-alkyl (b) cases have been drawn onto meaningful planes parallel to the (111) Si surface, namely the one that in the OTS case contains the (almost) linear H-bond between the OH radicals of the two molecules (a) and the middle plane between the topmost H atoms of the Si surface and the lowermost H atoms belonging to the alkyl chain (b) (almost he same as Fig. 8(b)).*

The adsorption energy calculated with respect to the ground state configuration of hydroxylated OTS molecules is $E_{ads}=E(2A/H{:}Si)-2(E(A)-E(H_2))=-1.47$ eV (see *table I*) that, compared to the adsorption energy of an isolated OTS molecule, indicates that the adsorption at adjacent sites is favoured against the adsorption of the isolated molecules. During the relaxation process, one of the two OTS molecules started rotating around its own axis until the H atom, belonging to one of the two OH groups, approached the O atom belonging to one of the hydroxyl groups of the other OTS, thus confirming that the geometry optimisation is determined by the dipolar interaction originating from the hydroxyl groups of the interacting molecules, i.e. by the formation of one hydrogen bond. In the ground state configuration that is reported in *figure 9(b)* the measurement of the hydrogen bond length and angle are respectively $d_{OH}=0.18$ nm and $\alpha_{OHO}=173°$ suggesting the formation of an almost linear H-bond. Unlike the 18-alkyl case, the calculation of the binding energy in the present case gives $E_b=-0.19$ eV evidencing that the system of two interacting molecules adsorbed at adjacent sites is stable against the isolated adsorbed OTS molecules. Because the relaxation pattern results in the torsion of both the chains, we have evaluated the torsion energy by calculating the total energy of an isolated and distorted OTS deposited onto the Si surface that, referred to the energy of the ground state OTS adsorption configuration, gives $\Delta E_{torsion}=0.085$ eV; using this value, we can now evaluate the energy gain involved in the hydrogen bond as: $E_{Hbond}=E(2A/H{:}Si)+E(H{:}Si)-2[E(A/H{:}Si)+\Delta E_{torsion}]=E_b-2E_{torsion}$, resulting in $E_{Hbond}=-0.36$ eV. The values of the H-bond distance and angle here obtained are close to the typical fingerprints of the H-bond measured by x-ray diffraction in ice[34-35], respectively $d_{OH}=0.175$ nm and $\alpha_{OHO}=180°$ while the H-bond energy value here obtained is slightly larger than the consensus in ice ($E_{Hbond}=0.29$ eV}) revealing that in this case the H-bond has a noteworthy stabilizing value that is certainly the origin of the observed self assembling patterns in the experiments.

Moreover it is worth noting that the computational scheme chosen, and particularly the PBE functional formula, is certainly suitable to handle accurately the physics and the chemistry of (111) Si surface hydrophobic functionalization with OTS SAMs. For the sake of clarity in *figure 10(a)* the potential in the system is drawn containing two interacting polymers for both the OTS and the 18-alkyl cases. In the OTS case. the V(**r**) density map, drawn in the plane containing the O-H-O atoms, evidences the existence of a significant potential energy region [V(**r**)≈1.7 eV] connecting the two adjacent polymers that is the result of the H-bond between the O lone pair (that is located below the plane where the density map is considered) and the positive H (see *figure 10(a)).* It is worth noting the torsional deformation of both the hydroxylated OTS polymers occurring for steric reason because the H-bond keeps the two polymers quite close each other; the torsional deformation, indeed, relaxes part of the elastic interaction between the polymers and thus contributes to set the binding energy at negative values. This circumstance is in striking contrast with the case of the two alkyl chains, where a stiffly separation has happened with no other apparent interactions during the relaxation process, as evidenced also by the V(**r**) density map reported in Fig. 10(b) with negligible potential energy values in a region in between the two polymers.

Acknowledgements

Computational resources have been provided by CASPUR under under HPC Grant 2010 and the ENEA-GRID CRESCO project. Isosurfaces in the figures have been plotted with XCrysDen code[34] ; the authors wish to thank Dr.G.Giovannetti for many helpful discussion concerning the subject treated in the present study.

References

[1] SCHOCH R., HAN J., RENAUD P. “*Transport phenomena in nanofluidics*” Rev. Mod. Phys. **80** (2008) pp. 839-883.

[2] PENNATHUR S., SANTIAGO J. “*Electrokinetic Transport in Nanochannels. 1. Theory*” Anal. Chem. **77** (2005) pp. 6772-6781.

[3] HAN J., TURNER S., CRAIGHEAD H. “*Entropic Trapping and Escape of Long DNA Molecules at Submicron Size Constriction*” Phys. Rev. Lett. **83** (1999) pp. 1688-1691.

[4] FU J., MAO P., HAN J. *“Nanofilter array chip for fast gel-free biomolecule separation”* Appl. Phys. Lett. **87** (2005) pp. 263902/1-263902/3.

[5] JOSEPH P., TABELING P.*“Direct measurement of the apparent slip length”*Phys. Rev. E **71** (2005) pp. 035303/1-035303/4.

[6] ZHU Y., GRANICK S. “*Rate-Dependent Slip of Newtonian Liquid at Smooth Surfaces*” Phys. Rev. Lett. **87** (2001) pp. 096105/1- 096105/4.

[7] COTTIN-BIZONNE C., CROSS B., STEINBERGER A., CHARLAIX E. “*Boundary Slip on Smooth Hydrophobic Surfaces: Intrinsic Effects and Possible Artifacts*” Phys. Rev. Lett. **94**(2005) pp. 056102/1-056102/4.

[8] ULMAN A. “*Formation and Structure of Self-Assembled Monolayers*” Chem. Rev. **96** (1996) pp. 1533-1554.

[9] LINFORD M., FENTER P., EISENBERGER P., CHIDSEY C. “*Alkyl Monolayers on Silicon prepared from 1-Alkenes and Hydrogen-Terminated Silicon*” J.Am.Chem.Soc. **117** (1995) pp. 3145-3155.

[10] ALLARA D., PARIKH A., RONDELEZ F. “*Evidence for a Unique Chain Organization in Long Chain Silane Monolayers Deposited on Two Widely Different Solid Substrates*” Langmuir **11** (1995) pp. 2357-2360.

[11] JEON N., FINNIE K., BRANSHAW K., NUZZO R. “*Structure and Stability of Patterned Self-Assembled Films of Octadecyltrichlorosilane Formed by Contact Printing*” Langmuir **13** (1997) pp. 3382-3391.

[12] CHINAPPI M., GALA F., ZOLLO G., CASCIOLA C. M. “*Tilting angle and water slippage over hydrophobic coatings*” Phil. Trans. R. Soc. A **369** (2011) pp. 2537-2545.

[13] PREDEW J., BURKE K., ERNZERHOF M. ”*Generalized Gradient Approximation Made Simple*” Phys. Rev. Lett. **77** (1996) pp. 3865-3868.

[14] TROULLIER N., MARTINS J. “*Efficient pseudopotentials for plane-wave calculations*” Phys. Rev. B **43** (1991) pp. 1993-2006.

[15] GIANNOZZI P., BARONI S., BONINI N., CALANDRA M., CAR R., CAVAZZONI C., CERESOLI D., et al. *“QUANTUM ESPRESSO: a modular and open-source software project for quantum simulations of materials”* J. Phys.: Condens. Matter **21** (2009) pp. 395502/1-395502/19.

[16] BENGTSSON L., “*Dipole correction for surface supercell calculations*” Phys. Rev. B **59** (1999) pp. 12301-12304.

[17] FLETCHER R. “*A new approach to variable metric algorithms*” The Computer Journal **13** (1970) 317-322.

[18] MOKHORST H., PACK J. “*Special points for Brillouin-zone integrations*” Phys. Rev. B **13** (1976) pp. 5188-5192.

[19] MARZARI N., VANDERBILT D.”*Maximally localized generalized Wannier functions for composite energy bands*” Phys. Rev. B **56** (1987) pp.12847-12865.

[20] MOSTOFI A., YATES J., LEE Y.-S., SOUZA I., VANDERBILT D., MARZARI N. “*Wannier90: A tool for obtaining maximally-localised Wannier functions*” Comput. Phys. Commun. **178** (2008) pp. 685-699.

[21] NATAN A., KRONIK L., SHAPIRA Y. “*Computing surface dipoles and potentials of self-assembled monolayers from first principles*” Appl. Surf. Sci. **252** (2006) pp. 7608-7613.

[22] KOHN W., MEIR Y., MAKAROV D. “*van der Waals Energies in Density Functional Theory”* Phys. Rev. Lett. **80** (1998) pp. 4153-4156.

[23] GRIMME S. “*Semiempirical GGA-type density functional constructed with a long-range dispersion correction*” J. Comput. Chem. **27** (2006) pp. 1787-1799.

[24] TAYLOR A., JONES R. M. "*Silicon Carbide - A High Temperature Semiconductor*" (1960) Pergamon Press.

[25] LADLER K., KING M. C. J. "*Development of transition-state theory*"J. Phys. Chem. **87** (1983) pp. 2657-2664.

[26] NEMANICK E., SOLARES S., GODDARD W. A., LEWIS N. "*Quantum Mechanics Calculations of the Thermodynamically Controlled Coverage and Structure of Alkyl Monolayers on Si(111) Surfaces*" J. Phys. Chem. B **110** (2006) pp. 14842-14848.

[27] SIEVAL A., VAN DEN HOUT B., ZUILHOF H., SUDHÖLTER E. "*Molecular Modeling of Alkyl Monolayers on the Si(111) Surface*" Langmuir **16** (2000) pp. 2987-2990.

[28] SMITH J. G. "*Organic Chemistry"* (2007) McGraw-Hill.

[29] LINFORD M., CHIDSEY C. "*Alkyl monolayers covalently bonded to silicon surfaces*" J.Am.Chem.Soc. **115** (1993) pp.12631-12632.

[30] CICERO R., LINFORD M., CHIDSEY E. "*Photoreactivity of Unsaturated Compounds with Hydrogen-Terminated Silicon(111)*" Langmuir **16** (2000) pp. 5688-5695.

[31] PAULING L. "*The Structure and Entropy of Ice and of Other Crystals with Some Randomness of Atomic Arrangement*" J. Am. Chem. Soc. **57** (1935) pp. 2680-2684.

[32] ISAACS E., SHUKLA A., PLATZMAN P., HAMANN D., BARBIELLINI B., TULK C. "*Covalency of the Hydrogen Bond in Ice: A Direct X-Ray Measurement*" Phys. Rev. Lett. **82** (199) pp. 600-603.

[33] BRILL V. R., TIPPE A. "*Gitterparameter von Eis I bei tiefen Temperaturen*" Acta Crystallogr. **23** (1967) pp. 343-345.

[34] KOKALJ A. "*Computer graphics and graphical user interfaces as tools in simulations of matter at the atomic scale*" Comput. Mater. Sci **28** (2003) pp. 155-168.

Calculation of di-interstitials diffusion barriers in GaAs by Density Functional Theory

Giuseppe Zollo and Fabrizio Gala

Dipartimento di Scienze di Base e Applicate per l'Ingegneria (Sezione di Fisica)
Università "La Sapienza"
Via A. Scarpa 14-16, 00161 Rome, Italy

I. Introduction

Intrinsic interstitials in elemental and compound semiconductors have recently been considered for modelling the core structure of extrinsic extended defects in implanted and annealed semiconductors[1-2]. In low-temperature grown gallium arsenide, the measured arsenic excess has been related to the formation of As interstititials [3] or, alternatively, to As antisites [4]. Moreover, intrinsic interstitials have been demonstrated to play a crucial role in the diffusion processes of p-type dopants in GaAs [5-6]. However, differently from vacancies and antisites studies [7-10], experimental evidences of self-interstitials in III-V compound semiconductors are rare and indirect being often inferred from diffusion experiments of dopant species [5-6][11-12] or from the observation of extended defects [13-17]. Theoretical predictions of the intrinsic interstitials main properties in GaAs have been attempted since the beginning of the '90s in the framework of the density functional theory (DFT) with limited computational resources [18-19]; then, this matter has been recently revised taking advantage from the enormous improvement of the computational techniques and resources in the last twenty years [20-28]. Moreover, the theoretical study of small complexes involving intrinsic interstitial in GaAs has evidenced that di-interstitials are stable against the components independently on theirstoichiometric ratio [24][28]. Hence, in ion implanted semiconductors, for instance, it may happen that not all the Frenkel pairs recombine and self-interstitials, thanks to heir high mobility, can migrate and form di-interstitial complexes. Recently, a semi- empirical tight binding molecular dynamics scheme has been employed to study the ground state configurations of self-interstitial aggregates I_n with $n \geq 2$ showing that I_5 behave as a stable "building block" of the core structure of extended defects in GaAs[1]; moreover, on the basis of the binding energy values calculated, it was demonstrated that both single interstitials I_1 and di-interstitials I_2 may participate to the aggregation processes favouring the coalescence of large aggregates. However the aggregation in large clusters may effectively take place only if I_1 and I_2 are able to migrate fast. While it is commonly recognised that isolated self-interstitials are quite mobile[5-6][11], no data are available concerning di-interstitials to the authors knowledge. In this article we report and discuss the calculations of diffusion energy barriers encountered by As based di-interstitials in GaAs.

II. Computational Method

All the calculations have been performed in the framework of time independent Density Functional Theory (DFT) with the spin unpolarized local-density approximation (LDA) for the exchange-correlation functional[29] that has revealed to be appropriate also for solated interstitials[20][24] [28]; the exchange-correlation energy and potential have been calculated with the Perdew-Zunger parametrization[30] of the Ceperley-Alder data[31]. The ionic potentials have been replaced by norm conserving Hamann type pseudopotentials (PPs) [32] in the Kleinman-Bylander form[33] for both Ga and As atoms. All the calculations have been performed using periodic boundary conditions and plane waves expansions of the electron wave-functions and density. It is well known that convergence may be quite tricky for interstitials due to the possible artifacts that arise from the spurious elastic interaction and wavefunction overlap among the supercell replicas[34][20]. As a consequence, sufficiently large cubic supercells have been employed, containing 218 (217) atoms, 216 GaAs lattice atoms and two (one) interstitials, that, as already shown in previous articles, guarantee the convergence by sampling the first Brillouin zone at the Γ point and by using an energy cutoff of 15 Ry for the wave-functions[20][24][28]. This computational scheme is appropriate even in the case of heavily charged configurations[28][35]. The ground-state electron density for each atomic configuration has been obtained by the Williams-Soler algorithm[36] whereas the ground state atomic configurations of the studied complexes have been fully relaxed using the BFGS scheme [37].

The energy barriers for diffusion along various directions have been calculated at 0 K, i.e. without the entropic term; in particular, some of the principal lattice directions, such as [100], [110], [111], etc. have been taken into account as detailed in the next section. Moreover, due to the geometry and the symmetry properties of the various I_1 and I_2 configurations studied, the directions belonging to the <110> set that are equivalent in a perfect lattice, are actually different for diffusion and therefore have been checked accordingly. It is known that the LDA approximation of the exchange-correlation functional results in an underestimation of the band gap; however, the properties here investigated depend only on the total energy that is much more robust in the LDA fashion. Concerning the migration barriers, indeed, the LDA approximation may either underestimate or overestimate the GGA calculations, being sometimes closer to the experimental results[38-39]. Recent migration barrier calculations of vacancies and interstitials in GaAs, performed using LDA, have shown similar results to the ones obtained with PBE, at least concerning interstitials[25][40]. In any case the As migration barriers have been re-calculated as reference values as the main aim of the present article is to compare the diffusion barriers of I_2 complexes to the isolated interstitial ones. The energy landscapes for diffusion have been sampled by moving the atoms of the complex along the chosen direction step by step: after each step, the structure has been fully relaxed, except for the moved atom that is constrained to relax in the plane orthogonal to the direction of motion. The step length has been chosen depending on the distance from the ”saddle point”, being 0.14 Å close to it and 0.28 Å elsewhere. The adopted technique is based on the PCG (Projected Conjugate Gradient) method proposed recently[41] and resembles closely the popular nudged elastic band method[42] used for the minimum energy path search; in the present case, instead, the adopted PCG method appears more appropriate because also larger barriers, i.e. the ones found for diffusion along various directions, were calculated. The same technique has been recently used to study the bi-stability properties of charged As di-interstitial in GaAs[28]. All the calculations have been performed with a private distribution of the code FINGER[43].

The binding energy calculations are based on the Zhang and Northrup formulation of the defects formation energy[44] and on the related experimental and theoretical data concerning the bulk phases involved[45-47]. We just remind here that the formation energy of a given neutral defect in GaAs is:

$$E_F = E_D - n_{Ga}\mu_{Ga} - n_{As}\mu_{As} \qquad (1)$$

where E_D is the total energy of the defect supercell containing n_{Gs} (n_{As}) Ga (As) atoms and μ_{Ga} (μ_{As}) are the Ga (As) chemical potentials. Recalling that $\mu_{GaAs} = \mu_{Ga} + \mu_{As}$, the equation (1) can be rewritten as:

$$E_F = E_D - \mu_{GaAs}(n_{Ga} + n_{As})/2 - (n_{Ga} - n_{As})(\mu^b_{Ga} - \mu^b_{As}+\Delta\mu)/2 \qquad (2)$$

where μ^b_{Ga} and μ^b_{As} are the chemical potentials of the relevant bulk phases and

$$\Delta\mu = (\mu_{Ga} - \mu_{As}) - (\mu^b_{Ga} - \mu^b_{As}) \qquad (3)$$

The binding energy of a di-interstitial is the energy gain of the complex with respect to the isolated interstitials; thus, given the formation energy of the di-interstitial E_F its binding energy is:

$$E_b = (n_i^{Ga}\, E_F{}^{Ga}{}_i + n_i^{As}\, E_F{}^{As}{}_i - E_F) \qquad (4)$$

where n_i^{Ga}, n_i^{As} are respectively the numbers of Ga and As interstitials involved in the complex, and $E_F{}^{Ga}{}_i$, $E_F{}^{As}{}_i$ are the formation energies of the Ga and As isolated interstitials[44].

III. Results and discussion

We have preliminarily calculated the diffusion barriers of As self-interstitials whose ground state configuration is the "As [110] dumbbell", namely a dumbbell configuration at an As lattice with the As-As site bond aligned along one direction of the <110> set[11][18-20].

Thus, taken one As dumbbell along $[10\bar{1}]$ direction [see *figure 1(a)*], we have calculated its diffusion barriers along some of the principal lattice directions following the prescriptions detailed in the previous section. The results are shown in *figure 1(b)* where the total energy and the position of the As atom are referred respectively to the same quantities measured in the case of a stable, fully relaxed As dumbbell. The lowest energy path occurs by moving the As atom along the [101] direction that is perpendicular to the dumbbell axis and is characterised by an energy barrier of ΔE≈ 300 meV between the dumbbell and the hexagonal configurations, the last one being 230 meV higher in energy. Moving further the As atom along [101], a tetrahedral configuration with four Ga neighbours is finally obtained. If the As atom moves along the dumbbell axis, a larger energy barrier of ΔE≈ 420 meV is experienced between two adjacent ground state dumbbell configurations, the saddle point consisting of a tetrahedral As self-interstitial.

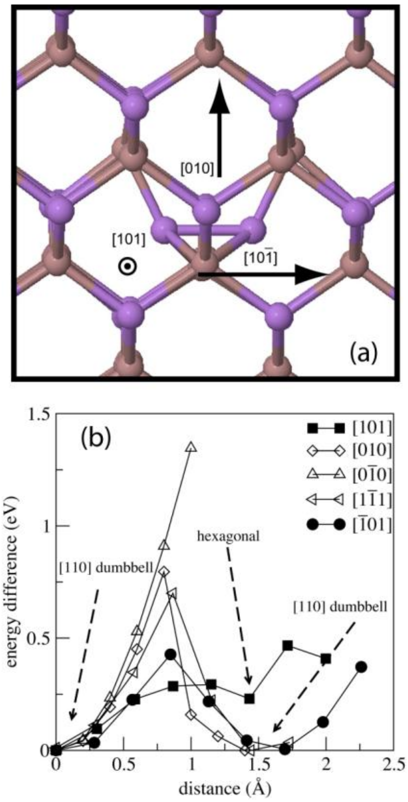

Figure *1* - *As dumbbell self-interstitial diffusion. Geometry and reference lattice directions (a); landscape of the energy difference obtained by moving the As interstitial along some of the principal lattice directions (b); the total energy is referred to the one of the As dumbbell self-interstitial ground state configuration.*

The barriers sampled as the As interstitial is moved along the [010] and the $[1\bar{1}1]$ directions are larger, being respectively ΔE≈ 700 meV and ΔE≈ 800 meV: as these barriers are exceeded, a <110> dumbbell configuration oriented differently is still present at the same lattice site. The $[10\bar{1}]$ ground state As dumbbell configuration may also move along another non-equivalent direction of the < 110 > set, namely the out of plane [110] one (or the $[\bar{1}\bar{1}0]$ one) that forms an angle θ = 60° with respect to the dumbbell axis.

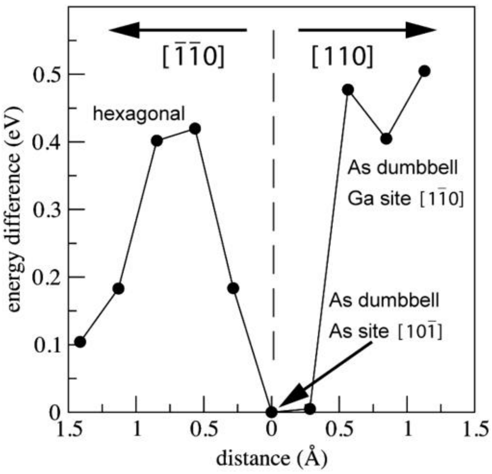

Figure 2 - *Total energy landscapes sampled along the [110] lattice direction for diffusion steps of the As interstitial; the total energy is referred to the one of the As dumbbell self-interstitial ground state configuration.*

If the As atom moves along $[\bar{1}\bar{1}0]$, a hexagonal configuration is encountered before forming another As dumbbell at a different As lattice site while if it is moved along [110], the As atom approaches a Ga site forming there a dumbbell along $[1\bar{1}0]$ that is 400 meV higher in energy (see *figure 2*). This last case deserves further consideration: from this complex, indeed, either As or Ga diffusion may occur from the original Ga lattice site: in the first case, As migration along [110] results in the formation of a ground state As [101] dumbbell at the adjacent As lattice site from which the As interstitial can diffuse further, as already detailed previously; in the second case, instead, a different energy landscape is sampled for Ga diffusion along the two orthogonal [101] and $[10\bar{1}]$ directions, as shown in *figure 3(a)*; the large energy barrier measured seems to suggest that the substitution reaction As_i + Ga → As_{Ga} + Ga_i is unlikely; however a low reaction energy path can be found if the structure obtained at the fifth diffusion step along [101] is fully relaxed: from the relaxed configuration, indeed, diffusion can proceed further along the $[10\bar{1}]$ orthogonal direction resulting in a low energy ”zig-zag” diffusion path for Ga (see *figure 3(b)* and the relevant diffusion barrier reported in *table 1*) showing that As antisites may form easily as a consequence of As diffusion in GaAs via thesubstitution reaction
As_i + Ga → As_{Ga}+ Ga_i.

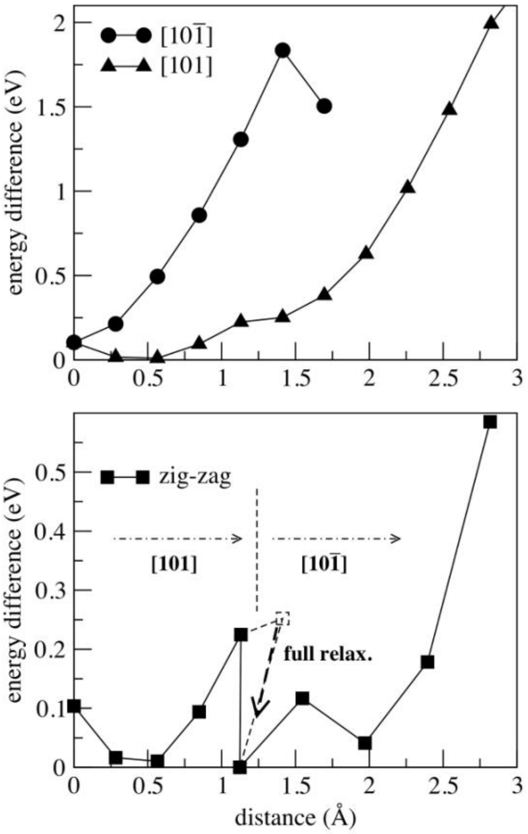

Figure 3 - *Energy differences sampled in a substitution reaction at the Ga site As_i + Ga → As_{Ga} + Ga_i along two directions of the <110> set (a); the same energy differences obtained in a zig-zag diffusion with one intermediate step fully relaxed (b) (see the text).*

Table I - *Lowest energy barriers for diffusion along the relevant lattice directions of the I_1 and I_2 configurations studied. In the last column are reported the meta-stable configurations obtained as soon as the barriers are exceeded.*

Starting Configuration	Lattice direction	ΔE (meV)	Final configuration
As_1 dumbell	[101]	300	hexagonal (unstable)
Ga_1 substitution reaction	[101] →$[\bar{1}01]$	225	As antisite + Ga_1 tetrahedral
As_1Ga_1	$[\bar{1}01]$	290	Fig. 5(b)
As_2	[101] / $[\bar{1}01]$	550	Fig. 6(f) / Fig. 6(h)

Concerning the di-interstitials, we have first examined the diffusion properties of the stoichiomentric As_1Ga_1 complex. Its ground state configuration has been studied recently by both total energy ab-initio calculations and tight binding [24][26][28] and is characterized by an isosceles triangular structure in the (101) plane (with a C_{2v} point group symmetry) made of two interstitials and one As atom sharing one As lattice site and with the As-As bond aligned along, f.i., the $[10\bar{1}]$ direction. In *figure 4* are reported the energy landscapes sampled as either one of the two As or the Ga atoms of the complex are moved along the principal lattice directions. Low migration barriers of ΔE≈ 290 and ΔE≈ 360 meV are measured if As moves along $[\bar{1}01]$ and [101] respectively.

In the first case, as the As atoms moves, the As-As bond is stretched and the Ga interstitial is dragged in the same direction so that the As_1Ga_1 complex migrates almost rigidly (with a barrier even smaller than the one measured for As dumbbells) jumping from an As row to an adjacent Ga row where the di-interstitial geometry is reversed (see *figure 5(b)*).

If the As atom is moved in the opposite direction (i.e. $[10\bar{1}]$), the diffusion pattern observed is almost the same but, as the As-As bond is compressed, a larger energy barrier of about 500 meV is measured before getting again the As_1Ga_1 ground state configuration. In the second case, the As atom moving along [101] still experiences, at least initially, a small energy barrier (but larger than the previous case) because, after the first few steps, a new meta-stable configuration, unknown before, is obtained that consists of one As and one Ga self-interstitials placed at adjacent tetrahedralsites and interacting each other [see *figure 5(c)*] and is about 340 meV larger in energy than the ground state.

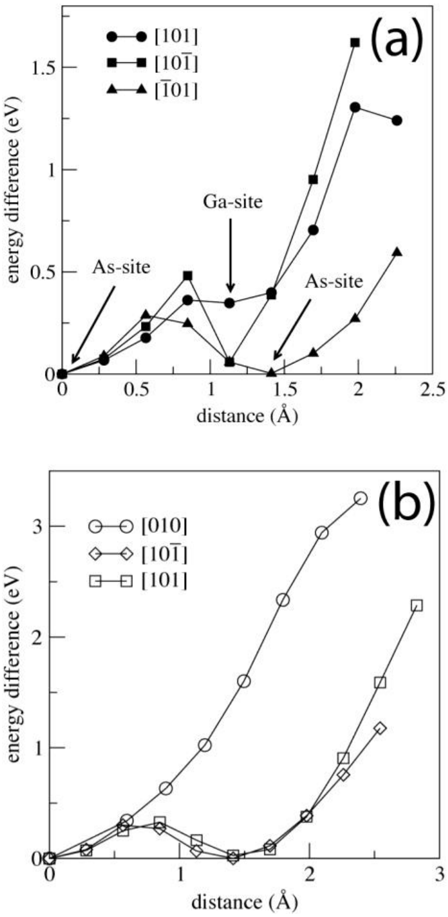

Figure 4 - *Energy differences sampled along different lattice directions for diffusion steps of the As interstitial (a) or the Ga interstitial (b) involved in the stoichiometric di-interstitial complex As_1Ga_1. The total energy is referred to the one of the As_1Ga_1 ground state configuration.*

The As_1Ga_1 di-interstitial may also diffuse via Ga and the migration energies sampled in this case are shown in *figure 4*; while migration is inhibited along [010], it is favoured along the $[10\bar{1}]$ and the [101] directions where small diffusion barriers of ΔE≈ 300 meV and ΔE≈ 320 meV have been measured respectively. Anyway, despite the similarity of the barriers encountered, the phenomena occurring in these two cases are quite different; in the first case, the moving Ga atom drags the As atoms in the same direction and diffusion proceeds likewise the previous analogous case where As atoms were moved; in the second case, on the contrary, a meta-stable configuration is obtained with the Ga interstitial located at a tetrahedral site close to the As dumbbell that remains at the original As site (see *figure 5(d)*);

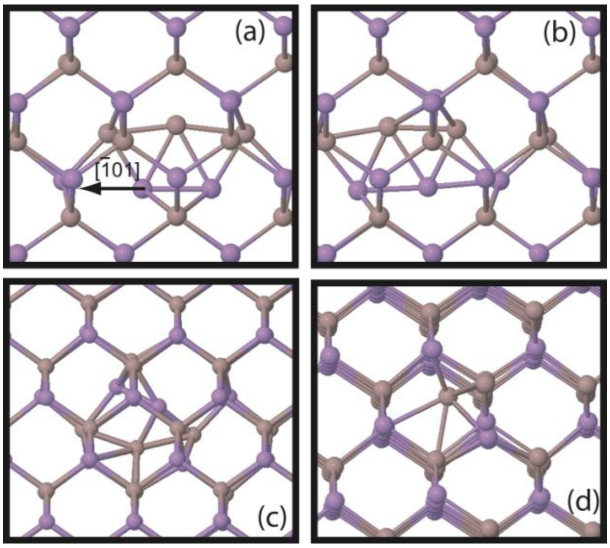

Figure 5 - *Diffusion pattern of the As_1Ga_1 complex obtained by moving the top As atom along the* $[\bar{1}01]$ *direction ((a) and (b)); in (c) and (d) are depicted the meta-stable configurations obtained, respectively, after diffusion steps of either the As (c) or the Ga (d) atoms along the [101] lattice direction.*

this configuration is just ΔE≈ 30 meV larger in energy than the As_1Ga_1 ground state (as a consequence its binding energy is E_b = 2.21 eV, only 30 meV smaller than the ground state one [28, 24]) and can be obtained also in the context of a ”capture” process when a diffusing Ga atom approaches an As dumbbell or viceversa. As a consequence, the meta-stable configuration found is an intermediate state in the capture/release processes occurring when As_1Ga_1 either forms or dissolves. Hence, the rate limiting barrier for the As1 Ga1 formation is the one between the present intermediate configuration and the one involving two well separated As and Ga interstitials, being thus nearly equal to the diffusion barriers of the isolated interstitials. Ultimately it comes out that the diffusion of isolated As or Ga interstitials and the formation of As_1Ga_1 complexes are concurrent phenomena occurring, with quite similar energy barriers, wherever As and Ga interstitials are both present.

Recent ab-initio total energy calculations have predicted As_2 as the most stable di- interstitial in GaAs [24][28]; its ground state configuration is made of three As atoms (two interstitials and one lattice atom) that share one As lattice site forming a bi-stable triangular structure with C_{1h} symmetry, two As atoms being aligned in a dumbbell fashion along one of the <110> directions. As shown in *figure 6(a)-(b)*, As_2 can diffuse by moving either the top ”As” atom (labelled as $As_{(1)}$) or one of the two As atoms of the dumbbell (labelled as $As_{(2)}$) and the energy landscapes obtained are reported in *figure 7*.

Concerning $As_{(1)}$, the barrier measured for the direction $[10\bar{1}]$ is ΔE≈ 820 meV [see *figure 7(a)*], i.e. 120 meV larger than the energy barrier between the two equivalent ground state configurations along the [101] bi-stability pattern[28]. At the saddle point, a distorted As_2 configuration is formed at an adjacent Ga lattice [see *figure 6(c)*] that, as the barrier is exceeded by moving two steps further, results in the formation of a ”reversed” As_2 ground state configuration at the nearest As lattice with the As dumbbell aligned along [101] [see *figure 6(d)*].

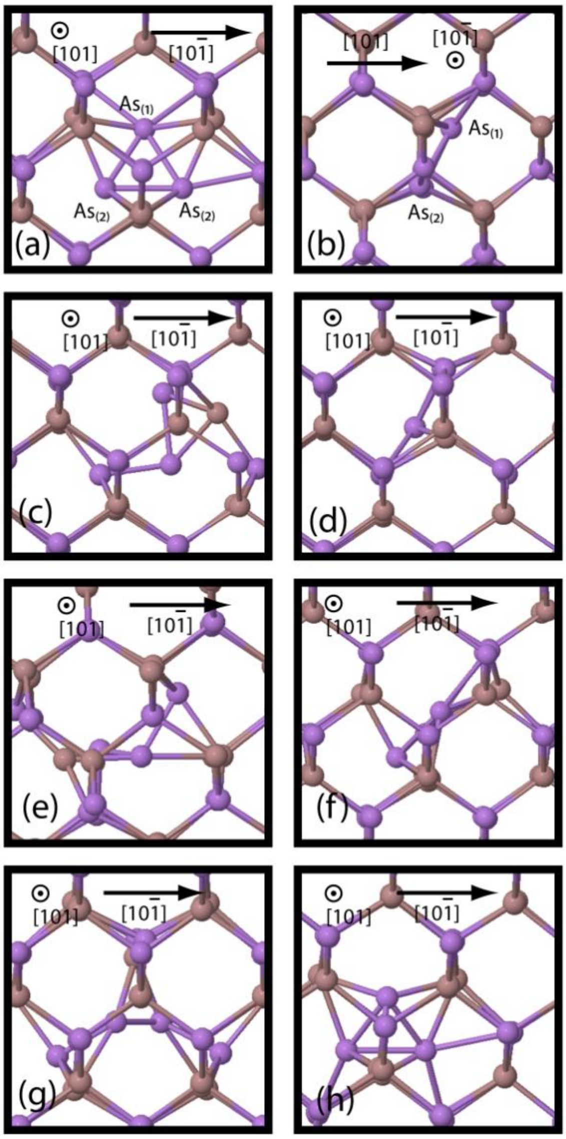

Figure 6 - *Configurations obtained for diffusion of the As_2 di-interstitial complex. As_2 di-interstitial ground state configuration ((a) and (b)); transition (c) and final (d) configurations obtained by moving the ”top” As atom along the $[10\bar{1}]$ direction; transition (e) and final (f) configurations obtained as one of the $As_{(2)}$ atoms moves along the [101] direction; transition (g) and final (h) configurations obtained as one of the $As_{(2)}$ atoms moves along the $[\bar{1}01]$ direction.*

On the contrary, as $As_{(1)}$ is moved along the [101] direction, no diffusion occurs but, rather, a dissociation/capture phenomenon involving two As dumbbells with a capture radius of about 1.6-1.8 Å: beyond this distance, indeed, two, almost independent, As dumbells at adjacent As sites appear as also testified by a total energy increase with respect to the ground state di-interstitial nearly equal to the As_2 binding energy ($E_b = 2.35$ eV [20][24][28]) [see *figure 7(a)*]. The same energy curve, moreover, shows that the "activation" energy of the capture phenomenon, i.e. the energy barrier that an As dumbbell must overcome to get into the capture radius of another one, is of the same order as the As dumbbell diffusion barrier; therefore it can be stated that the aggregation process is rate limitedby the As dumbbell diffusion barrier of 300 meV.

As mentioned before, As_2 may diffuse also via $As_{(2)}$. The total energy values sampled in this case are shown in *figure 7(b)* evidencing that, except for the $[\bar{1}0\bar{1}]$ direction, the migration barriers measured are much wider than the ones found so far extending over a larger distance between 2.5 Å and 3.0 Å. Moreover, the barrier heights measured $\Delta E \approx 550$ meV are smaller than the ones encountered by $As_{(1)}$ but still 250 meV larger than the As dumbbell diffusion barrier. The widest barrier of approximately 3.0 Å is obtained by moving the $As_{(2)}$ atom along the [101] direction where the energy plateau corresponds to a set of very similar transition configurations depicted in *figure 6(e)* and made of two As interstitials at close tetrahedral sites along two orthogonal < 110 > channels; once the plateau is overtaken, another As_2 ground state configuration forms at an adjacentAs lattice site and, consequently, As_2 migrates through the GaAs lattice [see *figure 6(f)*]. A similar phenomenon occurs when the $As_{(2)}$ atom moves along $[\bar{1}01]$ but in this case the plateau is shorter (about 1 Å) and the saddle point configuration consists of two As interstitials and one Ga lattice atom occupying close tetrahedral sites in the vicinity of a Ga lattice site [see *figure 6(g)*]. The migration energies obtained by moving $As_{(2)}$ are very close because both the saddle configurations are made of two As interstitials at close tetrahedral sites.

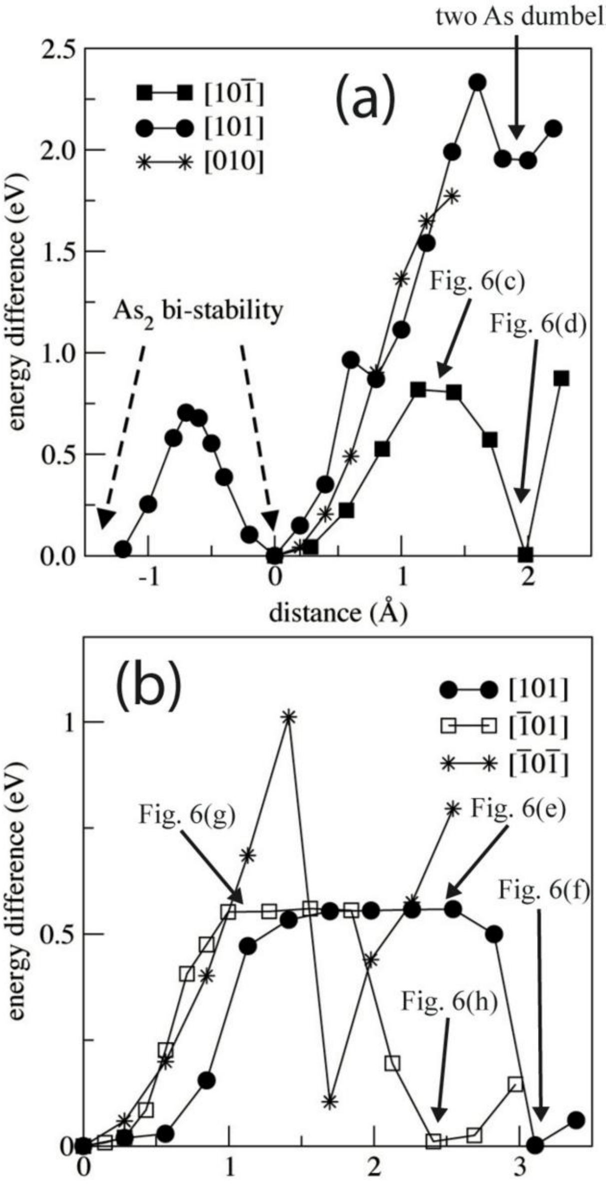

Figure 7 - *Total energy differences sampled by moving along some of the principal lattice direction either the $As_{(1)}$ atom (a) or one of the $As_{(2)}$ atoms (b) belonging to the As_2 di-interstitial complex. The total energy is referred to the one of the As_2 ground state configuration (see Fig. 6(a),(b)).*

In the end, the As_2 migration patterns examined have evidenced dissociation phenomena that involve large energy barriers, capture processes with low activation barriers (similar to the As interstitial diffusion barriers) and diffusion processes; in this last case, the minimum energy barrier measured is 550 meV that is more than 50% larger than the As dumbbell diffusion barrier. These results indicate that the diffusion of isolated As dumbbells and the formation of As_2 di-interstitial complexes are concurrent phenomena with the same rate and that neutral As_2 complexes, once formed, diffuse more slowly; hence the scenario here drawn entails rapid diffusion of As self-interstitials that may interact and easily form stable, slowly migrating di-interstitials.

Acknowledgements

Computational resources have been provided by CASPUR (Consorzio Interuniversitario per le Applicazioni di Supercalcolo per Università e Ricerca) under HPC Grants 2010/2011 and the Italian National Agency for New technology, Energy and the Environment (ENEA) under the ENEA-GRID CRESCO pro ject. We warmly acknowledge these institutions for contributing to the present article.

References

[1] GALA F., ZOLLO G. "*Nucleation and first-stage growth processes of extrinsic defects in GaAs friggere by self-interstitials*" Phys. Rev. B **80** (2009) pp. 174113/1-174113/13.

[2] KIM J., KIRCHHOFF F., AULBUR W. G., WILKINS J. W., KHAN F. S., KRESSE G. *"Thermally Activated Reorientation of Di-interstitial Defects in Silicon*" Phys. Rev. Lett. **83** (1999) pp. 1990-1993.

[3] KUNSÁGI-MÁTÉ S., SCHÜR C., VÉGH E., MAREK T., STRUNK H. P., "*Molecular-dynamics-based model for the formation of arsenic interstitials during low–temperature growth of GaAs*" Phys. Rev. B **72** (2005) pp. 075315/1-075315/5.

[4] STAAB T. E. M., NIEMINEN R. M., GEBAUER J., LUYSBERG M., KRAUSE-REHBERG R., HAUGK M., FRAUENHEIM TH. "*Do Arsenic Interstitials Really Exist in As-Rich GaAs?*" Phys. Rev. Lett. **87** (2001) pp. 45504/1-45504/4.

[5] BRACHT H., BROTZMANN S. "*Zinc diffusion in gallium arsenide and the properties of gallium interstitials*" Phys. Rev. B **71** (2005) pp. 115216/1-115216/10.

[6] BÖSKER G., STOLWIJK N. A., THGORDSON J. V., ANDERSSON T. G., SÖDERVALL U., "*Diffusion of Nitrogen from a Buried Doping Layer in Gallium Arsenide Revealing the Prominent Role of As Interstitials*" 1998 Phys. Rev. Lett. **81** (1998) pp. 3443-3446.

[7] SAARINEN K., HAUTOJÄRVI P., LANKI P., CORBEL C. "*Ionization levels of As vacancies in as-grown GaAs studied by positron-lifetime spectroscopy*" Phys. Rev. B **44** (1991) pp. 10585-10600.

[8] BOURGOIN J. C., VON BARDELEBEN H .J., STIÈVENARD D., "*Native defects in gallium arsenide*" J. Appl. Phys. **64** (1988) pp. R65-R91.

[9] FUKUYAMA A., IKARI T., AKASHI Y., SUEMITSU M. "*Interdefect correlation during thermal recovery of EL2 in semi-insulating GaAs: Proposal of a three-center-complex model*" Phys. Rev. B **67** (2003) pp. 113202/1-113202/4.

[10] HURLE D. T. J. "*A thermodynamic analysis of native point defect and dopant solubilities in zinc-blende III–V semiconductors*" J. Appl. Phys. **107** (2010) pp. 121301/1-121301/47.

[11] SCHOLZ R. F., GÖSELE U. "*Phosphorus and antimony in GaAs as tracers for self-diffusion on the arsenic sublattice*" J. Appl. Phys. **87** (2000) pp. 704-710.

[12] NOAK M., KEHR K. W., WENZL H. "*Fast interstitial diffusion in As-pressure annealed GaAs*" J. Cryst. Growth **178** (1997) pp. 438-444.

[13] VITALI G., ZOLLO G,. PIZZUTO C., ROSSI M., MANNO D., KALITZOVA M., "*Cross−sectional high resolution electron microscopy of Zn+ implanted and low−power pulsed−laser annealed GaAs*" Appl. Phys. Lett**.** **69** (1996) pp. 4072-4074.

[14] ZOLLO G., PIZZUTO C., VITALI G., KALITZOVA M., MANNO D. "*High resolution transmission electron microscopy of elevated temperature Zn+ implanted and low-power pulsed laser annealed GaAs*" 2000 J. Appl. Phys. **88** (2000) pp. 1806-1810.

[15] VITALI G., PIZZUTO C., ZOLLO G., KARPUZOV D., KALITZOVA M., VAN DER HEIDE P., SCAMARCIO G., SPAGNOLO V., CHIAVARONE L., MANNO D. "*Structural reordering and electrical activation of ion-implanted GaAs and InP due to laser annealing in a controller atmosphere*" Phys. Rev. B **59** (1999) pp. 2986-2994.

[16] ZOLLO G., PALUMBO L., ROSSI M., VITALI G. "*Temperature behavior of implanted and pulsed laser irradiated GaAs*" Appl. Phys. A: Materials Science and Processing **56** (1993) pp. 409-411.

[17] VITALI G., ROSSI M., PIZZUTO C., ZOLLO G., KALITZOVA M. "*Low power pulsed laser annealing of* Zn^+*-implanted InP: first endeavours*" Mater. Sci. and Eng. B **38** (1996) pp. 72-75.

[18] CHADI D. J. "*Self-interstitial bonding configurations in GaAs and Si*"1992 Phys. Rev. B **46** (1992) pp. 9400-9407.

[19] NORTHRUP J. E., ZHANG S. B. "*Dopant and defect energetics: Si in GaAs*" Phys. Rev. B **47** (1993) pp. 6791-6794.

[20] ZOLLO G., NIEMINEN R. M. "*Small self-interstitial clusters in GaAs*" J. Phys.: Condens. Matter **15** (2003) pp. 843-853.

[21] ZOLLO G., TARUS J., NIEMINEN R. M. "*Reliability of analytical potentials for point-defect simulation in GaAs*" J. Phys.: Condens. Matter **16** (2004) pp. 3923-3932.

[22] SCHICK J. T., MORGAN C. G., PAPOULIAS P. “*First-principles study of As interstitials in GaAs:Convergence, relaxation, and formation energy*” Phys. Rev. B **66** (2002) pp. 195302/1- 195302/10.

[23] LANDMAN J. I., MORGAN C. G., SCHICK J. T., PAPOULIAS P., KUMAR A., “*Arsenic interstitials and interstitial complexes in low-temperature grown GaAs*” Phys. Rev. B **55** (1997) pp. 15581-15586.

[24] ZOLLO G., LEE Y. J., A., NIEMINEN R. M. “*Properties of intrinsic di-interstitials in GaAs*” J. Phys.: Condens. Matter **16** (2004) pp. 8991- 9000.

[25] SCHULTZ P. A., VON LILIENFELD O. A. “*Simple intrinsic defects in gallium arsenide*” Modelling Simul. Mater. Sci. Eng. **17** (2009) pp. 084007/1-084007/35.

[26] VOLPE M, ZOLLO G., COLOMBO L. “*Structural, electronic, and energetic properties of small self- interstitial clusters in GaAs by tight-binding molecular dynamics*” Phys. Rev. B **71** (2005) pp. 075207/1-075207/6.

[27] ZOLLO G., GALA F. “*Stability of I_3 complexes in III-V compound semiconductors by tight-binding molecular dynamics*” Phys. Rev. B 75 (2007) pp. 115205/1-115205/7.

[28] ZOLLO G., GALA F. “*Properties of charged intrinsic di-interstitials in GaAs*” Phys. Rev. B **77** (2008) pp. 094125/1-094125/7.

[29] KOHN W., SHAM L. J. “*Self-Consistent Equations Including Exchange and Correlation Effects*” Phys. Rev. **140 (**1965**)** pp. A1133-A1138.

[30] PERDEW J. P., ZUNGER A. “*Self-interaction correction to density-functional approximations for many-electron systems*” Phys. Rev. B 23 (1981) pp. 5048-5079.

[31] CEPERLEY D. M., ALDER B. J. “*Ground State of the Electron Gas by a Stochastic Method*” Phys. Rev. Lett. **45** (1980) pp. 566-569.

[32] HAMANN D. R. “*Generalized norm-conserving pseudopotentials*” Phys. Rev. B **40** (1989) pp. 2980-2987.

[33] KLEINMAN L., BYLANDER D. M. “*Efficacious Form for Model Pseudopotentials*” Phys. Rev. Lett. **48** (1982) pp. 1425-1428.

[34] PUSKA M. J., PYKK S., PESOLA M., NIEMINEN R. M. “*Convergence of supercell calculations for point defects in semiconductors: Vacancy in silicon*” Phys. Rev. B **58** (1998) pp. 1318-1325.

[35] EL-MELLOUHI F., MOUSSEAU N. “*Self-vacancies in gallium arsenide: An ab initio calculation*” Phys. Rev. B **71** (2005) pp. 125207/1-125207/12.

[36] WILLIAMS A. R., SOLER J. Bull. Am. Phys. Soc. **32** (1987) pp. 562.

[37] DENNIS J. E., SCHNABEL R. B. “*Numerical Methods for Unconstrained Optimization and Non-linear Equations*” Prentice Hall, Englewood Cliffs, NJ-USA (1983).

[38] WINDL W., BUNEA M. M., STUMPF R., DUNHAM S. T., MASQUELIER M. P., “*First-Principles Study of Boron Diffusion in Silicon*”Phys. Rev. Lett. **83** (1999) pp. 4345-4348.

[39] LEUNG W.-K., NEEDS R. J., RAJAGOPAL G., ITOH S., IHARA S. “*Calculations of Silicon Self-Interstitial Defects*” Phys. Rev. Lett. **83** (1999) pp. 2351-2354.

[40] EL-MELLOUHI F., MOUSSEAU N. “*Ab initio characterization of arsenic vacancy diffusion pathways in GaAs with SIEST-A-RT*” Appl. Phys A **86** (2005) pp. 309-312.

[41] KAUKONEN M., PERÄJOKI J., NIEMINEN R. M., JUNGNICKEL G., FRAUENHEIM TH., “*Locally activated Monte Carlo method for long-time-scale simulations*” Phys. Rev. B **61** (2000) pp. 980-987.

[42] JÓNSSON H., MILLS G., JACOBSEN K. W. “*Nudged elastic band method for finding minimum energy paths of transitions*” In Berne B. J., Ciccotti G., Cockert D. F. “*Classical and Quantum Dynamics in Condensed Phase Simulations*” World Scientific (1998) pp. 385-404.

[43] The code FINGER (FINnish General Electron Relaxator) is based on the techniques detailed in the paper by Laasonen K., Paquarello A., Car R., Lee C., Vanderbilt D. [Phys. Rev. B **47** (1993) pp.10142-10153] and was developed at Helsinki University of Technology, Espoo, Finland.

[44] ZHANG S. B., NORTHRUP J. E. “*Chemical potential dependence of defect formation energies in GaAs: Application to Ga self-diffusion*” Phys. Rev. Lett. **67** (1991) pp. 2339-2342.

[45] HALZEN F., MARTIN A. D. “*CRC Handbook of Chemistry and Physics*” 67th ed. R. C. West, CRC, Boca Raton, FL-USA (1986).

[46] BERNASCONI M., CHIAROTTI G. L., TOSATTI E. “*Ab initio calculations of structural and electronic properties of gallium solid-state phases*” Phys. Rev B **52** (1995) pp. 9988-9998.

[47] NEEDS R. J., MARTIN R. M., NIELSEN O. H. “T*otal-energy calculations of the structural propertie of the group-V element arsenic*” Phys. Rev. B **33** (1986) pp. 3778-3784.

Many-Body effects in silicon-based 2D systems

P. Gori(1,2), M. Marsili(1,3), V. Garbuio(1,3), A. Mosca Conte(1,3), C. Violante(1,3)
and Olivia Pulci(1,2,3)

(1)*European Theoretical Spectroscopy Facility*
(2)*CNR-ISM, Via del Fosso del Cavaliere 100, 00133 Roma*
(3)*Dipartimento di Fisica, Università di Roma 'Tor Vergata'*
Via della Ricerca Scientifica 1 - 00133 Roma

Introduction

We report here on the calculations performed thanks to the ENEA-CRESCO facility.
Our work was based on Density Functional Theory (DFT) [1] and Many-Body Perturbation theory (MBPT) [2] within the Green's function formalism.
We have studied silicon-based two dimensional systems, mainly the Silicon(111)2×1 negative buckling surface, and truly 2-D systems that are graphene-like honeycomb structures, based on silicon instead of carbon atoms.
While the calculations running on the ENEA-CRESCO facility have been mainly carried out by the authors of this report, the complete studies to which we will refer are due to the work of many collaborators, which appear as coauthors in the publications.

Methods

Density Functional Theory (in Local Density or Generalized Gradient Approximations) [1] has been used to determine the geometrical structures of the systems under study. For the excited state properties of the systems we moved to MBPT. In particular, as a second step, the GW approximation [3] has been used to calculate the electronic band structures, including self-energy corrections. As a third step, the optical properties (macroscopic dielectric function), with the inclusion of excitonic effects, have been calculated in the framework of the Bethe-Salpeter Equation [4].
Codes used:
ESPRESSO (www.quantum-espresso.org), EXC (http://etsf.polytechnique.fr/exc/), YAMBO (http://www.yambo-code.org/), GW, DP (http://www.dp-code.org/) .

RESULTS

Si(111)2×1: positive and negative buckling

The Si(111)2×1 is one of the most studied surfaces [5]. Its reconstruction is described by the Pandey model with a buckling of the topmost atoms. With relation to the sign of the buckling, there are two slightly different geometric structures (isomers), conventionally named positive buckling and negative buckling. STM measurements suggest that the positive buckling isomer is the stable configuration at room temperature but a recent work [6], involving STS measurements, has shown the coexistence of both the isomers, at very low temperature, for highly n-doped Si(111)2×1 specimens. There is hence the necessity to deepen the study of the negative buckling isomer, almost completely neglected in literature, especially for what concerns its optical properties. In this work we have studied the structural, electronic and optical properties of both the isomers of Si(111)2×1 within the Density Functional Theory and

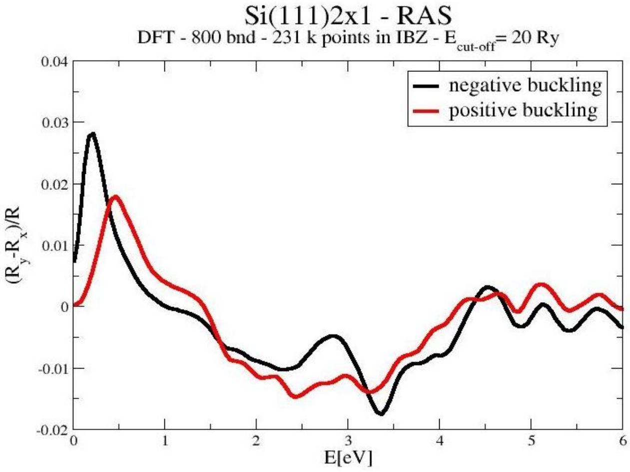

Many-Body Perturbation Theory. Our results (see *figure1*) may show to experimentalists the way to prove the coexistence of the two isomers [7].

Figure 1: *Calculated DFT Reflectance Anisotropy spectra for the positive and negative buckling Si(111)2×1.*

Giant excitonic effects in hydrogenated silicene (silicane)

The realization of graphene [8], the two-dimensional (2D) sp^2 -bonded form of carbon (C), and of its derivatives has led to a revolution in the fields of condensed matter physics, basic science, and device technology. The progress in the study of the outstanding properties of graphene and its derivatives has generated much interest for its hypothetical silicon (Si) counterparts, silicene. We show by first-principles calculations that, due to depressed screening and enhanced two-dimensional confinement, excitonic resonances with giant oscillator strength appear in hydrogenated Si layers, which qualitatively and quantitatively differ from those of graphane.
Their large exciton binding energies and oscillator strengths (see *figure 2*) make them promising for observation of novel physical effects and application in optoelectronic devices on the nanoscale.

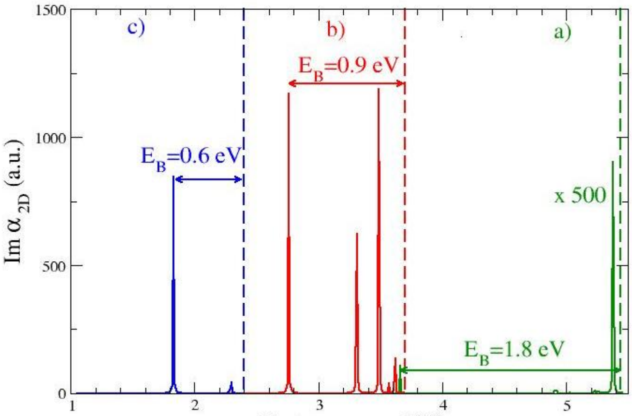

Figure 2: *Bound excitons in silicane (b, red plot). For comparison, also those in graphane (a, green) and germanane (c, blue) are shown. E_B is the exciton binding energy.*

Due to the number of k-points that have to be employed for the convergence of the optical properties (234-k in the Irreducible part of the Brillouine Zone, IBZ), the use of high performance parallel platforms, as CRESCO is, was mandatory. The results have been published in [9]

Side-dependent escape for electrons in silicongraphane (2D-SiC:H)

The structural and electronic properties of SiC-based two-dimensional (2D) crystals are studied by means of density functional theory and many-body perturbation theory. Such properties cannot simply be interpolated between graphene and silicene.

The replacement of half of the C atoms by Si atoms opens a large direct electronic gap and destroys the Dirac cones. Hydrogenation further opens the gap (see *figure 3*) and significantly reduces the electron affinity to 0.1 or 1.8 eV in dependence on the carbon or silicon termination of the 2D crystal surface, thus showing a unique direction dependent ionization potential (see *figure 4*). This suggests the use of 2D-SiC:H as electron or hole filter.

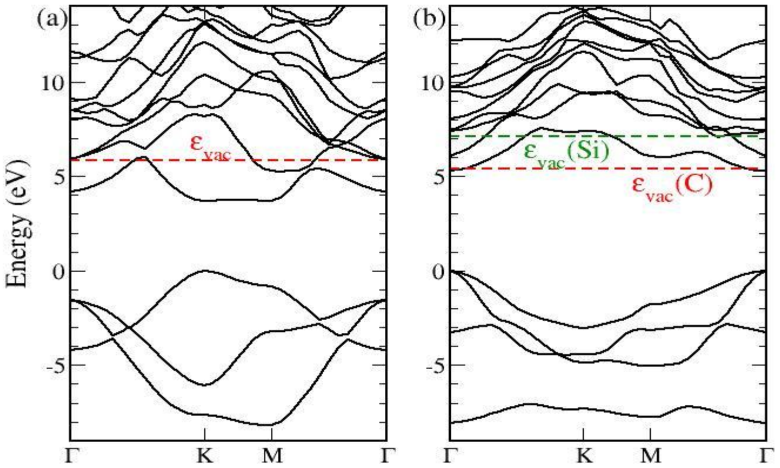

Figure 3: *Calculated band structure in silicongraphene (a) and silicongraphane (b). The dashed lines represent the vacuum levels.*

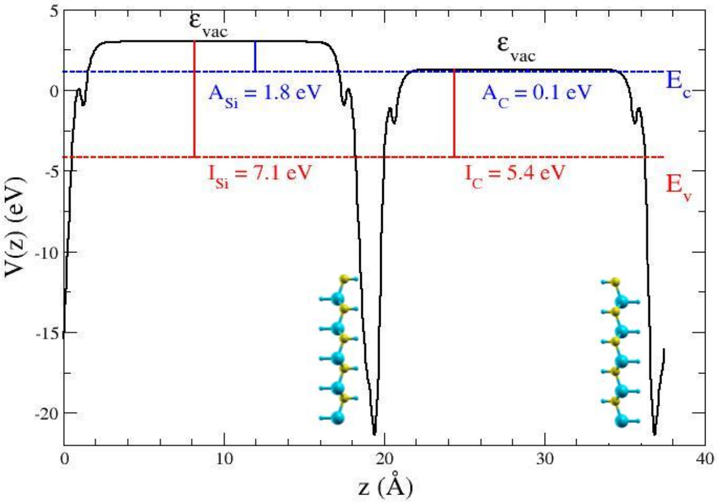

Figure 4: *Average electrostatic potential versus the direction perpendicular to the silicongraphane sheet (shown in the configuration used with opposite dipole moments)* .

Due to the number of k-points that have to be employed for the convergence of the electronic and optical properties (50×50×1 k-points in the BZ), also in this case, the use of a high performance parallel platform as CRESCO has been crucial. Our results have partially been published in [10]. Another manuscript in is preparation.

CONCLUSIONS

In this report we have presented some of the results obtained in the study of the excited state properties of two dimensional systems. Our calculations, based on Density Functional Theory and Many-Body Perturbation theory, have been performed thanks to the ENEA-CRESCO facility.

We have studied silicon-based systems, namely the Silicon(111)2×1 negative buckling surface, and graphene-like honeycomb structures with silicon replacing carbon atoms, in part or completely.

The 2-dimensional nature of the systems under study, together with the high number of k-points that have to be employed for the convergence of the electronic and optical properties of these surfaces, make the use of high performance parallel platforms, as CRESCO is, mandatory.

Bibliography

[1] P. Hohenberg and W. Kohn "*Inhomogeneous Electron Gas*" Phys. Rev. **136**, B864 (1964); W. Kohn and L. J. Sham *"Self-Consistent Equations Including Exchange and Correlation Effects"* Phys. Rev. **140**, A1113 (1965); R. M. Dreizler and E. K. U. Gross "*Density Functional Theory*" (Springer-Verlag, Heidelberg, 1990); R. O. Jones and O. Gunnarsson *"The density functional formalism, its applications and prospects"* Rev. Mod. Phys. **61**, 689 (1989).

[2] L. Fetter and J. D. Walecka "*Quantum Theory of Many Body Systems"* (McGraw-Hill, New York, 1981); R. D. Mattuck "*A Guide to Feynman Diagrams in the Many Body Problem"* (McGraw-Hill, New York, 1976).

[3] L. Hedin *"New Method for Calculating the One-Particle Green's Function with Application to the Electron-Gas Problem"* Phys. Rev. **139**, A796 (1965). L. Hedin and B. J. Lundquist, in: Solid State Physics, Vol. **23**, edited by H. Ehrenreich, F. Seitz, and D. Turnbull (Academic Press, New York, 1969), p. 1; F. Aryasetiawan and O. Gunnarsson *"The GW method"* Rep. Prog. Phys. **61**, 237 (1998); W. G. Aulbur, L. Johsson and J. W. Wilkins *"Quasiparticle Calculations in Solid"* Solid State Phys. **54**, 1–218 (2000).

[4] for a review see for example G. Onida, L. Reining and A. Rubio "*Electronic excitations: density-functional versus many-body Green's-function approaches"* Rev. Mod. Phys. **74**, 601 (2002).

[5] see for example M. Rohlfing and S. G. Louie *"Excitons and Optical Spectrum of the Si(111)-(2x1) Surface"* Phys. Rev. Lett. **83**, 856 (1999) and ref. therein.

[6] G. Bussetti, B. Bonanni, S. Cirilli, A. Violante, M. Russo, C. Goletti, P. Chiaradia, O. Pulci, M. Palummo, R. Del Sole, P. Gargiani, M. G. Betti, C. Mariani, R. M. Feenstra, G. Meyer, and K. H. Rieder *"Coexistence of Negatively and Positively Buckled Isomers on n+-Doped Si(111)-2x1"* Phys. Rev. Lett. **106**, 067601-1 (2011).

[7] C. Violante, A. Mosca Conte, F. Bechstedt, O. Pulci, in preparation

[8] M. I. Katsnelson *"Graphene: carbon in two dimensions",* Materials Today **10,** 20 (2007)

[9] O. Pulci, P. Gori, M. Marsili, V. Garbuio, R. Del Sole, F. Bechstedt *"Strong excitons in novel two-dimensional crystals: silicane and germanane",* EPL. **98**, 37004 (2012).

[10] P. Gori, O. Pulci, M. Marsili, F. Bechstedt *"Side-dependent electron escape from Grapheme-and graphane-like SiC layers"*, Appl. Phys. Lett. **100**, 043110 (2012).

MONTE CARLO APPLICATIONS FOR THE TRANSPORT OF RADIOACTIVE GAMMA SOURCES

Giuseppe A. Marzo
ENEA, C. R. Casaccia, Roma

1. Introduction

In the late ’50s, the advent of commercial nuclear reactors made possible the large scale production of radioisotopes and gamma ray emitters like Cesium-137 and Cobalt-60, which became a common radiation source for medical and industrial applications. Currently, Co-60 is almost solely used as the gamma radiation source for industrial use because of its easy production method, its non-solubility in water [1], and short half-life (5.27 years) as opposed to Cs-137 (30.17 years), that minimizes issues related to the management of disused sources. Co-60 is extensively used for medical applications as source for radiation therapy [2] and it has been proved effective as radiation source for various research activities [e.g., 3]. Industrial applications of gamma radiation include sterilization of health care products, cleaning of water and sewage sludge disinfection, irradiation of food and agriculture products for various end objectives, such as disinfestation, shelf life extension, sprout inhibition, pest control, and sterilization [4]. Moreover, gamma radiation is used for materials modification such as polymerization, polymer crosslinking, and gemstone colorization [5]. Other important applications imply the use of small sources (either in terms of activity and physical dimensions) for density measurements and radiography of thick welded plates.

Disused gammas sources can retain a significant amount of radioactivity (from hundreds of MBq to several GBq) that still poses safety concerns on their handling and transport. In this context a detailed knowledge of their radiation field would provide the necessary information for taking actions in preventing unnecessary doses to the workers and the population by optimizing transport procedures and handling operations. Gamma sources are also the most suitable type of radioactive material for use in a dirty bomb [6] and therefore diversion must be prevented. The detailed knowledge of the energy spectrum of these radioactive sources under distinct geometric and physical conditions might yield to a higher sensitivity in detecting such materials.

Monte Carlo codes are suitable to precisely characterize the radiation field of typical gamma sources in different packaging conditions. Here, examples of applications are reported to prove usefulness of the approach in checking the compliance with the regulations for their transport, the health risk of possible radiation exposure, and the potential for detecting such materials.

2. Modeling approach and Monte Carlo

The geometry and the materials constituting a typical transport packaging of a spent Co-60 source have been modeled as previously described by [7]. The packaging is constituted by a drum which includes a small lead irradiator where the source is enclosed. The irradiator is suspended in a filling made of polyethylene chips and the whole packaging is surrounded by air. The drum is a truncated cone with a capacity of 60 liters made of 5 mm-thick iron. To simulate the polyethylene chips, the internal volume of the drum was filled with polyethylene assuming a density of 0.5 g/cm^3 to take into account the air that fills the gaps between the chips.

The irradiator was modeled by a lead sphere with a radius of 7 cm and a concentric spherical cavity of 2.5 cm in diameter where the Co-60 source is placed. The adopted source is an isotropic point source emitting gamma rays at 1.1732 and 1.3325 MeV with the expected probability.

A Monte Carlo photon transport code has been applied for tracking down the gamma photons emitted by the source, including the less energetic secondary photons resulting by the interaction of the source photons with the surrounding materials. This allowed for the evaluation of the three-dimensional radiation field inside and outside the packaging, and the corresponding equivalent dose useful for checking the compliance with the regulations and the health risk of possible radiation exposure. The code adopted was A General Monte Carlo n-Particle Transport Code, Version 5 (MCNP) [8]. MCNP is a general-purpose Monte Carlo n-particle code that can be used for neutron, photon, electron or coupled neutron/photon/electron transport. For photons, it takes into account of incoherent and coherent scattering, fluorescent emission after photoelectric absorption, absorption in pair production with local emission of annihilation radiation, and bremsstrahlung [9]. The volume occupied by the packaging, and its surroundings, is divided in small rectangular cells whose larger dimension is few centimeters. The contribution of each transported photon is tallied in each cell in terms of track lengths, thus the average flux in each cell is estimated from the track length density [8]. The average flux is then converted to equivalent dose using the 1977 ANSI/ANS [10] and ICRP-21 [11] photon flux-to-dose rate conversion factors [8].

3. Results

The Monte Carlo simulation was stopped after having tracked the history of $1x10^9$ photons generated by the source. This number of tracked source photons allows for an average relative uncertainty of 1% associated with the results. The total equivalent dose associated with the calculated radiation field is illustrated in Figure 1 for the case of an irradiator displaced by 5 cm with respect to the rotation axis of the drum. This is an easily occurring condition for sources not properly packaged. The color bars refer to the specific case of a 300 MBq Co-60 source transported in the packaging, a typical value of residual activity for a disused commercial Co-60 source. With reference to *figure 1*, the arrows indicates the presence of a hot-spot on the drum surface. The total equivalent dose in this point of the packaging exceeds 0.2 mSv/h which is the maximum allowed contact dose by local regulations on the external surface of a packaging in case of transport of a 60 liters drum [7].

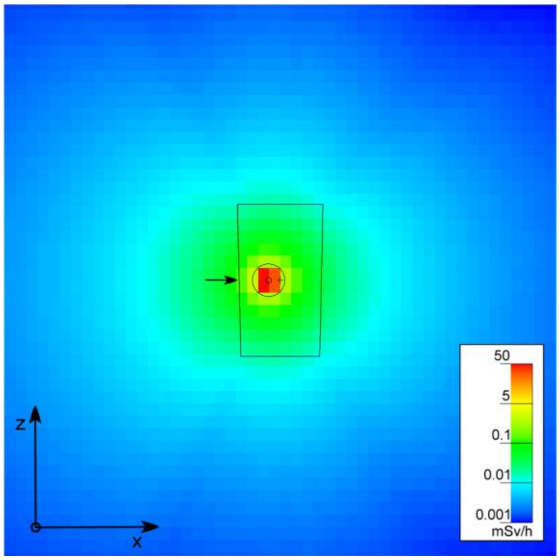

Figure 1 - *From [7]. Orthogonal projection of the radiation field (expressed in total equivalent dose) generated by a transport packaging with a 300 MBq Co-60 source. Drum is represented by the truncated cone drawn with a black line. The irradiator is represented by the black circle.*

A more realistic case of a transport packaging is a 3x3x3 assembly of 60 liters drums. In this case the irradiator enclosing the Co-60 source is properly centered in each drum which contains a 300 MBq Co-60 source. The resulting radiation field in terms of equivalent dose for this simple geometry is illustrated in *figure 2*. The total equivalent dose on the external side of the drum assembly is about 0.3 mSv/h, exceeding the maximum allowed contact dose by local regulations [7].

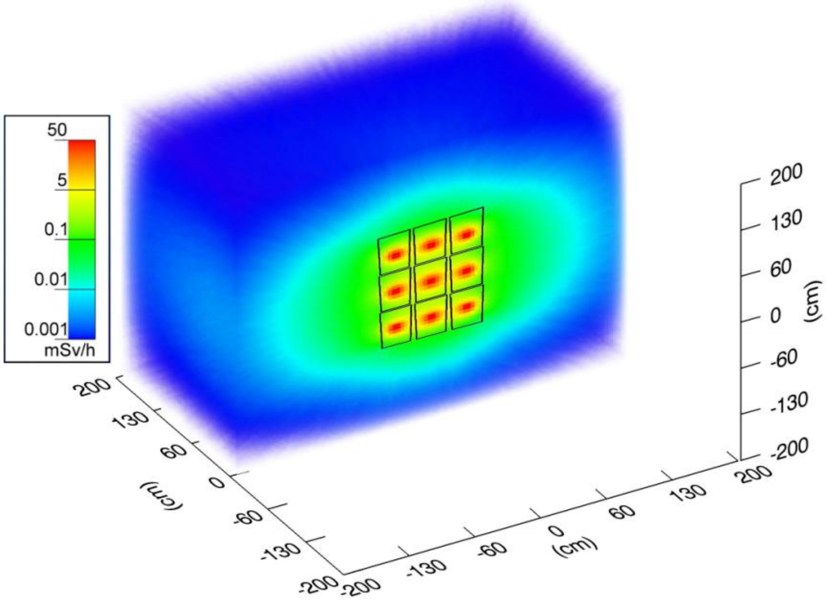

Figure 2 - *Three-dimensional colored sub-volume representing the total equivalent dose generated by an assembly of 3x3x3 drums. Drums are outlined in black.*

So far in this work, the Monte Carlo approach has been used to investigate the geometry of the radiation field generated by a transport packaging but it can be conveniently exploited to describe its spectral energy distribution. To illustrate a simple case, in *figure 3* is reported the energy spectrum of a Co-60 source in terms of photon flux in different geometric and physical conditions.

Figure 3 - *Energy spectrum of the radiation emitted by a Co-60 source (expressed in photon flux). The black line represents the flux in the immediate vicinity of the source. The blue line is the flux behind a thick lead shield and the cyan line is the flux at 1 meter afar from the lead shield. Dots represent the standard deviation associated with the curves.*

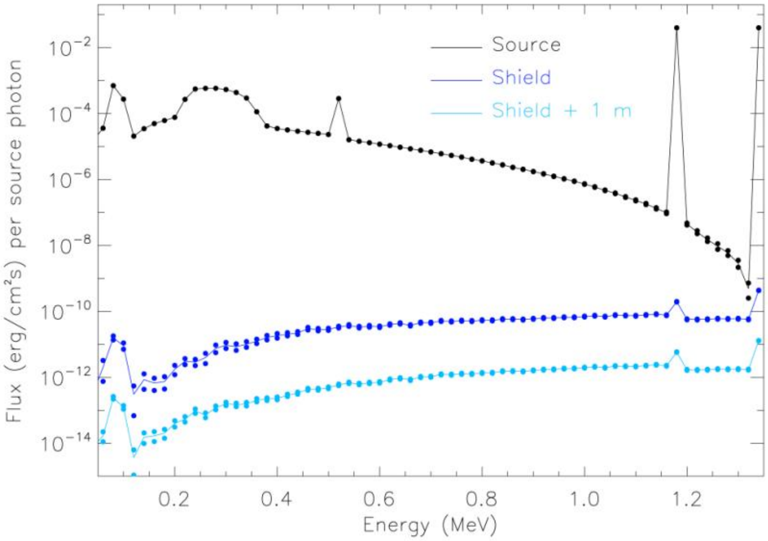

The black line represents the flux collected by a detector in the immediate vicinity of the source. It clearly shows two main peaks at the energies of the photons emitted by the Co-60 (1.1732 and 1.3325 MeV) and a continuum at lower energies caused by the scattering of these photons with the surrounding air. As expected, the energy distribution generated by the photons emitted by the Co-60 source is different when measured behind a thick lead shield (blue line) and at 1 meter afar from the lead shield (cyan line). It is interesting to observe that apart the overall decrease in intensity, air fluorescence and bremsstrahlung radiation from the shield, significantly influence the spectral features of the region at lower energy (<6 MeV).

4. Conclusions

In the examples illustrated here, the radiation field of a small Co-60 source inside its irradiator and packaged in a drum for transport can be fully characterized in terms of geometric and energy distribution by a Monte Carlo simulation. These results are general, and can be appropriately scaled to represent the radiation field of similar geometries with gamma sources of different activity. The same approach can be easily adopted for evaluating the radiation field of more complex geometries or assemblies of drums. The results presented here provide useful insights in the process of preparing a packaging for transport. These simple models suggest that this approach can be efficient for screening a number of packaging configurations and flagging those potentially not compliant with regulations, that will require a more thorough care in the packaging process. Furthermore the knowledge of the details of the radiation field can be useful for optimizing the geometry of the transport cargo, and becomes essential when a variety of packaging are transported or stored, in order to prevent hazardous situations during their handling, and hence preventing unnecessary doses to the workers and the populations. In fact, in spite of the small doses involved in the examples illustrated here, the driver of a truck transporting the assembly of drums illustrated in *figure 2* might receive a dose comparable to that received with a radiograph [12] during the transport.

The modeling approach illustrated here has been proved useful for investigating the spectral energy distribution of the gamma radiation emitted by a source in different geometric and physical conditions (*figure 3*). This level of information about the radiation field of a radioactive source has several applications, for example in those activities in the field of Nuclear Safety & Security and Nuclear Non-Proliferation that imply prompt detection of radioactive materials (e.g., prevention of stealing, smuggling, and diversion). The ability of instrumentation to detect radioactive materials is strongly dependent on the amount of material examined and the geometry of observation. As expected, and graphically illustrated in *figure 3*, the main spectral peaks of Co-60 at higher energy are dramatically reduced by a shield, and the photon flux is reduced by the distance from the source. This simple case might represent the challenge of detecting a Co-60 source carried by a truck and mixed with metal scraps when field instrumentation is used (e.g., a portal) and the radioactive material is moving (e.g., the truck). Modeling distinct radioactive sources along with observation and detector geometries might yield to a full characterization of the instrumental ability to detect a given radioactive source in the case of an actual measurement.

Additionally, lower energy portion of the spectrum are modified by scattered photons. Such modifications depend on the surrounding materials (e.g., shielding materials, air fluorescence) and the source radiation. Characterization of those spectral regions might be an alternative for improving the detection sensitivity for specific radioactive materials.

References

1. IAEA *“Gamma irradiators for radiation processing”* (2005) IAEA, Vienna, Austria.

2. JOSHI, C.P., DHANESAR, S., DARKO, J., KERR, A., VIDYASAGAR, P.B., AND SCHREINER, L.J. “*Practical and clinical considerations in Cobalt-60 tomotherapy”* J. Med. Phys. **30** (2009) pp. 137-140.

3. FLEETWOOD, D.M., WINOKUR, P.S., SCHWANK, J.R. *“Using laboratory X-ray and cobalt-60 irradiations to predict CMOS device response in strategic and space environments”* IEEE Transactions on Nuclear Science **35** (1988) pp. 1497-1505.

4. MACHI, S. *“Radiation technology for sustainable development”* Radiat. Phys. Chem. **46** (1995) pp. 399–410.

5. DROBNY, J.G. *”Radiation technology for polymers”* (2003) CRC Press, New York.

6. ACTON, J.M., ROGERS, M.B., ZIMMERMAN, P.D. *“Beyond the Dirty Bomb: Re-thinking Radiological Terror”* (2007) Survival: Global Politics and Strategy **49** pp. 151-168.

7. MARZO, G.A., GIORGIANTONI, G., SEPIELLI, M. “Radiation Field of Packages Carrying Spent Co-60 Radioactive Sources” (2012) *Waste Management Conference,* Phoenix, Arizona, USA, n. 12437.

8. X-5 MONTE CARLO TEAM *“MCNP – A General N-Particle Transport Code, Version 5 – Volume I: Overview and Theory”* LA-UR-03-1987 (2003) Los Alamos National Laboratory, USA.

9. BRIESMEISTER, J.F. *“Monte Carlo N-particle Transport Input”* LA-12625-M (1997) Los Alamos National Laboratory, USA.

10. ANS-6.1.1 WORKING GROUP *“American National Standard Neutron and Gamma-Ray Flux-to-Dose Rate Factors”* (1977) American Nuclear Society, LaGrange Park, USA.

11. ICRP COMMITTEE 3 TASK GROUP *“Data for protection against ionizing radiation from external sources: Supplement to ICRP Publication 15”* ICRP-21 (1971) Internal Commission on Radiological Protection, Pergamon Press.

12. WALL, B.F. AND HART, D. “Revised radiation doses for typical X-ray examinations” The British Journal of Radiology **70** (1997) pp. 437-439.

THE IDEAL TENSILE STRENGTH OF TUNGSTEN AND TUNGSTEN ALLOYS BY AB-INITIO CALCULATIONS

Simone Giusepponi and Massimo Celino

ENEA, C. R. Casaccia, via Anguillarese 301, 00123 Rome, Italy
simone.giusepponi@enea.it; massimo.celino@enea.it.

Abstract

We employ first-principles total energy method based on the density functional theory with the generalized gradient approximation to investigate the ideal tensile strengths of bcc tungsten and its alloys. The results can provide a useful reference for tungsten as plasma facing material in the Tokamak system for nuclear fusion.

Introduction

Tungsten (W) and W alloys are the most promising candidates for plasma facing materials (PFM) in Tokamak due to their good thermal properties such as high thermal conductivity, high melting temperature and low sputtering erosion. However, as a PFM, W will be exposed to hydrogen (H) and Helium (He) ions during the burn of deuterium-tritium (D–T) plasma in fusion reaction. It must not only withstand radiation damage, but also keep intrinsic mechanical properties and structural strength. Thus, the mechanical property is an extremely important factor to be considered in developing W alloys as a PFM. The ideal tensile strength of W can be a useful reference for the preparation and design of W as a PFM, because it sets an upper limit of the tensile strength. The ideal strength sets an upper bound on the attainable stress that makes a material become unstable with respect to fracture by the spontaneous separation of atomic planes. The upper limit of the tensile strength is of great interest for strong solids in atomic models, since the theoretical strength is an intrinsic material property that is determined by the behavior of valence electrons and ions. The ideal tensile strength of pure W in the [0 0 1] direction has been already investigated using first-principle pseudopotential method by Roundy et al. [1] and by Yue-Lin Liu et al. [2], and has been investigated by Šob et al. [3] using the full-potential linearized augmented plane wave (FLAPW) method. However, these works do not provide an exhaustive description of the deformation behavior in the [0 0 1] direction for W alloys. In order to provide a reference for the W and W alloys for PFM applications we systematically performed first-principles computational tensile tests to obtain the ideal tensile strength and detailed information about the behavior in [0 0 1] direction using first-principle method. This study is a first simulation step to investigate the structural and mechanical properties of W under H or He radiation. To address the study of W and its alloys the ab-initio CPMD (Car-Parrinello Molecular Dynamics) code has been used. This numerical code allows the accurate study of materials taking into account explicitly the contribution of the electronic structure. It will be possible to perform both total energy calculations on predefined atomic structures and to study the evolution of the material changing the external temperature. Firstly a reliable physical model for W will be prepared, then total energy calculations will be performed to check if the model can reproduce experimental structural properties. The same procedure will be performed for W alloys obtained substituting an W atom with a Re, Ta and V atom. Then ab-initio calculations on the lattice constant, bulk modulus, enthalpy of atomization, formation enthalpy of defects and ideal tensile strength of the W and its alloy (W-Re, W-Ta and W-V) will be computed.

Computational details

Our calculations have been performed using the CPMD code [4,5]. CPMD code is an ab-initio electronic structure and molecular dynamics program using a plane wave/pseudopotential implementation of density functional theory [6,7]. At the beginning we tested three different kind of pseudopotentials for W, both LDA and GGA, then we chose the suitable one and we tested pseudopotentials for substitutional defect atoms (Re, Ta and V). All the calculations are performed in the supercell approximation with periodic boundary conditions meant to mimic an infinitely extended system. We considered a cubic supercell composed by a 3 × 3 × 3 array of cubic conventional cells, and 54 W atoms. The role of substitutional defects in W bulk is investigated replacing a W atom with a Re, Ta and V atom (see *figure 1*).

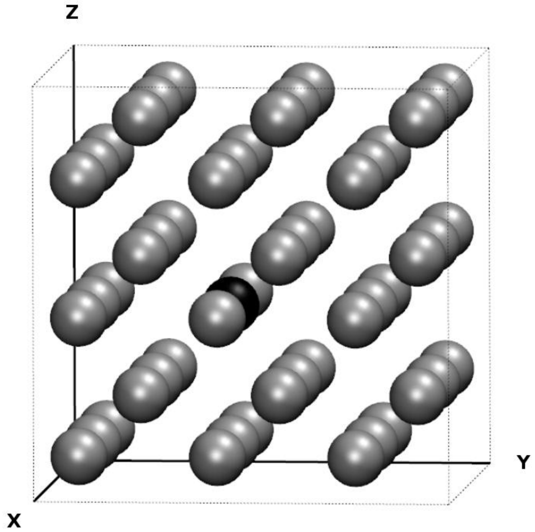

Figure 1*: Simulation cell for the first-principles total energy calculations. Substitutional atom is in black*

Thus we considered four cases: i) a supercell of 54 W atoms (pure W); ii) a supercell of 53 W atoms and a Re atom (W-Re alloy); iii) a supercell of 53W atoms and a Ta atom (W-Ta alloy); iv) a supercell of 53 W atoms and a V atom (W-V alloy). Two preliminary checks were made on the equilibrium cell size and on the bulk modulus. The lattice step a is defined as the length of the edge of the conventional cubic cell, for the bcc structure; the lattice step size a_0 is the a of equilibrium, where the energy of the system shows a minimum. DFT calculations of energy for different values of a around the estimated a_0 were performed and the value of a_0 was obtained fitting quadratically the results found; a_0 will be at the minimum of the quadratic function. The bulk modulus is defined by the relation: $B = -V\, dp/dV$. At $T = 0\ K$, $dU = -pdV$, then the bulk modulus B is

$$B = V_0 \left| \frac{d^2 E}{dV^2} \right|_{V=V_0}$$

Furthermore, by first-principles total energy calculations, we computed enthalpy of atomization and formation enthalpy of defects. Enthalpy of atomization H_a is defined by formula

$$H_a = \frac{E_{tot} - NE_W}{N}$$

where E_{tot} is total energy of bulk system with N atoms of W, E_W is total energy of a single W atom and $N = 54$. For W alloys enthalpy of atomization H_a is defined by the formula

$$H_a = \frac{E_{tot} - (N-1)E_W - E_X}{N}$$

where in this case E_{tot} is the total energy of bulk system with N-1 atoms of W and one substitutional atom (Re or Ta or V). Formation energy of the defect ΔE is defined by the formula

$$\Delta E = [E_{tot}^X + E_W] - [E_{tot} + E_X]$$

where E_{tot} is total energy of bulk system with N atoms of W, E_{tot}^X is total energy of bulk system with $N-1$ atoms of W and one substitutional atom (Re or Ta or V).

In the first-principles computational tensile test, an uniaxial tensile strain is applied to the chosen crystalline direction of bcc W and bcc W alloys. One starts with the calculation of the total energy of unloaded material. Then the crystal is elongated along the loading axis (in this report the [0 0 1] direction) by a fixed amount ε, which is equivalent to applying some tensile stress σ (unrelaxed condition). To ensure uniaxial loading, the dimensions of the crystal in directions perpendicular to the loading axis are relaxed by finding the minimum of the total energy as a function of these dimensions. Then, at each strain step, the structure was fully relaxed until all other five components vanished except that in the tensile direction (relaxed condition). We thus obtained the total energy E as a function of the strain ε (see Figure 2). For the uniaxial tensile strain, the tensile stress σ is calculated from the formula

$$\sigma = \frac{1}{\Omega(\varepsilon)} \frac{\partial E}{\partial \varepsilon}$$

where E is the total energy and $\Omega(\varepsilon)$ is the volume at a given tensile strain of ε. The tensile stress for each strain step can be calculated, and thus the stress-strain relation and the ideal tensile strength can be obtained. This approach was repeated for bcc W and for bcc W alloys, having obtained total energy-strain relations and stress-strain relations. The ideal tensile strength σ_m corresponds to the maximum of the stress-strain relation which is related to the inflexion point in the total energy-strain relation. We fitted total energy-strain relation with a cubic function and by vanishing of the second order derivative of this function, we calculated the inflexion point, that is the strain ε_m, and afterwards the value of σ_m.

Results and discussion

Firstly we have tested three different kind of pseudopotentials for W, both LDA and GGA. The Goedecker-Teter-Hutter pseudopotential with PADE approximant-LDA exchange-correlation potential (W-PADE), the Bachelet-Hamann-Schlüter LDA exchange-correlation pseudopotential (W-BHS) [8], and the Goedecker-Teter-Hutter pseudopotential with PBE approximant-GGA exchange-correlation potential (W-PBE) [9]. The electronic wave functions are expanded in a plane-wave basis set with a kinetic energy cut-off equal to *80 Ry*. The latter value was optimized by preliminary calculations on W-PADE W-BHS and W-PBE tungsten pseudopotentials. For each tungsten pseudopotentials, we calculated the equilibrium cell size a_0, the bulk modulus B, the enthalpy of atomization H_a, the ideal tensile strength σ_m and the related strain ε_m. *table 1* shows values for these physical quantities. Despite W-PBE tungsten pseudopotential has a value for a_0 bigger respect to the reference one (*3.16 Å* [10]), this pseudopotential has a very good value for B and H_a.

Table 1: *Calculated values of equilibrium cell size a_0, bulk modulus B, enthalpy of atomization H_a, tensile stress σ_m and related strain ε_m for W-PADE W-BHS and W-PBE tungsten pseudopotentials.*

	a_0 (Å)	B (GPa)	H_a (kJ/mol)	σ_m (GPa)	ε_m (%)
W-PADE	3.14	320	1128	36.94	11.92
W-BHS	3.15	399	1157	36.26	11.53
W-PBE	3.23	294	872	26.75	11.69

Moreover the value for σ_m and ε_m are in good agreement with those calculated by Roundy et al. ($\sigma_m = 29.5$, $\varepsilon_m = 13\%$) [1], by Yue-Lin Liu et al. ($\sigma_m = 29.1$, $\varepsilon_m = 14\%$) [2] and by Šob et al. ($\sigma_m = 28.9$, $\varepsilon_m = 12\%$) [3]. W-PADE and W-BHS tungsten pseudopotentials have very good values for equilibrium cell size, but they have big values for B, H_a and in particular for the ideal tensile strength σ_m. We chose for tungsten the pseudopotential W-PBE, so we employed for remaining calculations the CPMD code with Goedecker-Teter-Hutter pseudopotentials with PBE approximant-GGA exchange-correlation potential for tungsten, rhenium, tantalum and vanadium. The electronic wave functions are expanded in a plane-wave basis set with a kinetic energy cut-off equal to *80 Ry*. The latter value was checked by additional calculations on Re-PBE, Ta-PBE and V-PBE pseudopotentials. The calculated equilibrium lattice constant for bcc W, $a_0 = 3.23$ Å, is in good agreement with the corresponding experimental value of *3.16 Å*, with a difference within *2%*. Bulk modulus gives good result too: our calculation gives $B = 294$ *GPa*, that is in good agreement (within *5%*) with experimental value of *310 GPa*. Results for W-Re, W-Ta and W-V alloys are showed in *table 2*. In *table 2* we also report both enthalpy of atomization H_a and formation energy of defect ΔE.

Table 2: *Calculated values of equilibrium cell size a_0, bulk modulus B, enthalpy of atomization H_a and formation energy of defect ΔE for pure W and W alloys.*

	a_0 (Å)	B (GPa)	H_a (kJ/mol)	ΔE (eV)
W pure	3.23	294	872.4	-
W - Re	3.23	293	874.7	-1.284
W - Ta	3.24	288	866.9	3.046
W - V	3.23	291	871.9	0.253

The dependence of the total energy *E* vs. *ε* along the crystallographic axis [0 0 1] is shown in *figure 2* for the four cases: W pure, W-Re, W-Ta and W-V alloys. Gray symbols are related to energies for unrelaxed conditions, black symbols are related to energies for relaxed conditions and black solid lines are cubic fitting function.

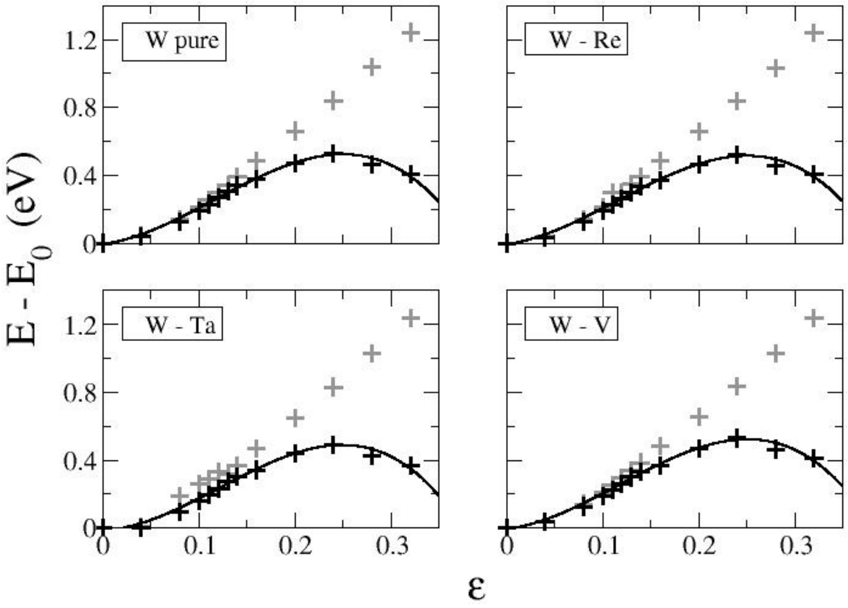

Figure 2*: Total energy E per atom as a function of strain ε for uniaxial deformation in [0 0 1] direction in bcc W and W alloys (W-Re, W-Ta, W-V); E_0 is the ground-state energy of bcc W and W alloys. Energies for unrelaxed conditions are shown in grey symbols, those for relaxed conditions are shown in black symbols. Solid black line are cubic fitting functions.*

The tensile deformation along the [0 0 1] direction corresponds to the Bain's path which transforms continuously the bcc into fcc structure, and the structures between them are tetragonal [11,12]. The deformed structures may be parameterized in terms of the *c/a* ratio and the relative change of the volume. If we ascribe the value $c/a = 1$ to the bcc structure, then the fcc structure is obtained for $c/a = \sqrt{2}$ on the tetragonal path. It was shown by Craievich et al. [11] that for the volume conserving Bain's path the total energy exhibits symmetry dictated extrema for structures of higher symmetry, namely for bcc and fcc in this case. The same is true for the Bain's path corresponding to uniaxial loading [12,13]. The total energy of tungsten has a minimum at the bcc structure and a maximum at the fcc structure ($\partial E/\partial\varepsilon = 0$), with an inflexion point in between ($\partial^2 E/\partial\varepsilon^2 = 0\,;\partial^3 E/\partial\varepsilon^3 \neq 0$). We fitted total energy-strain relations for relaxed condition of *figure 2* with cubic functions. By vanishing of the second order derivative of the cubic function, we calculated the inflexion point ε_m, and afterwards the value of the ideal tensile strength

$$\sigma_m = \frac{1}{\Omega(\varepsilon_m)}\left|\frac{\partial E}{\partial\varepsilon}\right|_{\varepsilon=\varepsilon_m}$$

where E is the total energy and $\Omega(\varepsilon_m)$ is the volume at the tensile strain ε_m. By vanishing of the first order derivative of the cubic function we calculated the strain ε_M related to the maximum of the total energy-strain relation. Calculated values of σ_m, ε_m and ε_M for tungsten and tungsten alloys are showed in *table 3*.

Table 3: *Values of the ideal tensile strength* σ_m *and the related strain* ε_m *for tungsten (W pure) and tungsten alloys (W-Re, W-Ta and W-V);* ε_M *is the value of the strain at the maximum of the total energy-strain relation.*

	σ_m (GPa)	ε_m (%)	ε_M (%)
W pure	26.75	11.69	25.04
W - Re	26.24	11.62	25.10
W - Ta	26.17	12.25	24.96
W - V	27.08	11.85	25.12

Conclusion

The ideal tensile strengths in the [0 0 1] direction of bcc tungsten pure crystal and its alloys (W-Re, W-Ta and W-V) has been investigated by using first-principles total energy method based on the density functional theory. The validity of the numerical model has been extensively checked by computing several structural properties of pure W and its alloys. We have calculated lattice constants, bulk modulus, enthalpies of atomization and formation enthalpy of defects in very good agreement with experimental results. Despite the low concentration of defects (less than 2%), results highlight that the presence of substitutional defects in W bulk is able to produce measurable variations respect to pure tungsten crystal. The bulk modulus decreases for all the W alloys. The ideal tensile strength in the [0 0 1] direction decreases in presence of Re or Ta, instead it increases in W-V alloy.

Acknowledgments

The computing resources and the related technical support used for this work have been provided by CRESCO-ENEAGRID High Performance Computing infrastructure and its staff; see www.cresco.enea.it for information. CRESCO-ENEAGRID High Performance Computing infrastructure is funded by ENEA, the "Italian National Agency for New Technologies, Energy and Sustainable Economic Development" and by national and European research programs.

References

[1] ROUNDY D., KRENN C. R., COHEN M. L., MORRIS J. W. *"The ideal strength of tungsten"* Phil. Mag. A **81** (2001) pp. 1725-1747.

[2] YUE-LIN LIU, HONG-BO ZHOU, YING ZHANG, SHUO JIN, GUANG-HONG LU. *"The ideal tensile strength and deformation behavior of a tungsten single crystal"* Nucl. Inst. Met. Phys. Res. B **267** (2009) pp. 3282-3285.

[3] ŠOB M., WANG L. G., VITEK V. *"Theoretical tensile stress in tungsten single crystals by full-potential frist-principles calculations"* Mat. Scien. Engin. A **234-236** (1997) pp. 1075-1078.

[4] CAR R., PARRINELLO M. *"Unified approach for Molecular Dynamics and Density-Functional Theory"* Phys. Rev. Lett. **55** (1985) pp. 2471-2474.

[5] CPMD V3.15.1 Copyright IBM Corp 1990-2011, Copyright MPI fuer Festkoerperforschung Stuttgart 1997-2001.

[6] HOHENBERG P., KOHN W. *"Inhomogeneous electron gas"* Phys. Rev. **136** (1964) pp. B864-B871.

[7] KOHN W., SHAM L. J. *"Self-consistent equations including exchange and correlation effects"* Phys. Rev. **140** (1965) pp. A1133-A1138.

[8] BACHELET G. B., HAMANN D. R., SHCLÜTER M. *"Pseudopotentials that work: From H to Pu"* Phys. Rev. B **26** (1982) pp.4199-4228.

[9] PERDEW J. P., BURKE K., ERNZERHOF M. *"Generalized gradient approximation made simple"* Phys. Rev. Lett. **77** (1996) pp. 3865-3868.

[10] PEARSON W. B. *"A handbook of Lattice Spacings and Structures of Metals and Alloy"* Pergamon Press, Oxford.

[11] CRAIEVICH P. J., WEINERT M., SANCHEZ J. M., WATSON R. E. *"Local stability of nonequilibrium phases"* Phys. Rev. Lett. **72** (1994) pp.3076-3079.

[12] ALIPPI P., MARCUS P. M., SHEFFLER M. *"Strained tetragonal states and Bain paths in metals"* Phys. Rev. Lett. **78** (1997) pp. 3892-3895.

[13] MILSTEIN F., FARBER B. *"Theoretical fcc→bcc Transition under [100] Tensile Loading"* Phys. Rev. Lett. **44** (1980) pp. 277-280.

Benchmark of the CPMD code on CRESCO HPC Facilities for Numerical Simulations of a Magnesium Nanoparticle

Simone Giusepponi[a], Massimo Celino[b], Salvatore Podda[a], Giovanni Bracco[a], Silvio Migliori[a]
a) ENEA-UTICT; b) ENEA-UTTMAT

Introduction

Solid-state metal hydrides are considered useful for storing hydrogen although materials suitable for practical use are still under development. Magnesium is an important candidate in this respect as it can reversibly store about 7.6 wt% hydrogen, is light weight and is a low-cost material. However, its thermodynamic parameters are not completely favorable and the reaction with hydrogen often shows sluggish kinetics. Different treatments in Mg based materials have been proposed to overcome these drawbacks. One of these is tailoring Mg nanoparticles in view of an enhancement on the reaction kinetics and thermodynamics of the Mg-MgH_2 phase transformation [1-3]. Because metallic nanoparticles often show size dependent behavior different from bulk matter, a better understanding of their physical-chemical properties is necessary. For this purpose, we want to set up a numerical model to perform first principle calculations based on the density functional theory (DFT), using CPMD code. To evaluate the suitable computational demand, we performed benchmarks of the CPMD code on the HPC ENEA CRESCO computing facilities.

Computational Details

Car-Parrinello Molecular Dynamics (CPMD) code [4,5] is an *ab-initio* electronic structure and molecular dynamics (MD) program which uses a plane wave/pseudopotential implementation of density functional theory [6,7]. It is mainly targeted at Car-Parrinello MD simulations but also supports geometry optimizations, Born-Oppenheimer MD, path integral MD, response functions, excited states and calculation of some electronic properties. In *ab-initio* molecular dynamics simulation, the forces acting on atoms are calculated from an electronic structure calculation repeated every time step (“on the fly”). Thanks to electronic structure calculation which uses density functional methods, simulations of large systems with hundreds of atoms are now standard. Originally developed by Roberto Car and Michele Parrinello for applications in solid state physics and material science, this method has also been used with great success for the study of molecular systems. Applications of *ab-initio* Car-Parrinello Molecular Dynamics simulations range from the thermodynamics of solids and liquids to the study of chemical reactions in solution and on metal and oxide surfaces.

For all the calculations we employed the CPMD code with Goedecker-Teter-Hutter pseudopotentials for magnesium, together with Pade approximant LDA exchange-correlation potentials [8-10]. The electronic wave functions are expanded in a plane-wave basis set with a kinetic energy cut-off equal to 80 Ry. The latter value is optimized by preliminary calculations both on simple molecules and on the crystalline structures of metallic HPC Mg (lattice constant: $a_{Mg} = b_{Mg} = 3.15$ Å, $c_{Mg} = 1.62*a_{Mg}$). Experimental observations have showed that Mg nanoparticles annealed at 300 °C show evaporation, void formation, and void growth in the Mg core both in vacuum and under a high pressure gas environment. This is mainly due to the outward diffusion and evaporation of Mg with the simultaneously inward diffusion of vacancies leading to void growth (Kirkendall effect [11]). To approach numerical studying of Mg nanoparticles, starting from the magnesium bulk, we have considered the cluster built from the

Mg atoms inside a 12 Å radius sphere centered on a Mg atom. To take in consideration the Kirkendall effect, we then have removed the inner Mg atoms inside a 5.6 Å radius sphere. The system is composed of a hollow nanoparticle of 266 magnesium atoms as shown in *figure 1*, where magnesium atoms are in blue, outer sphere is in gray, and inner red sphere is the void space due to the Kirkendall effect.

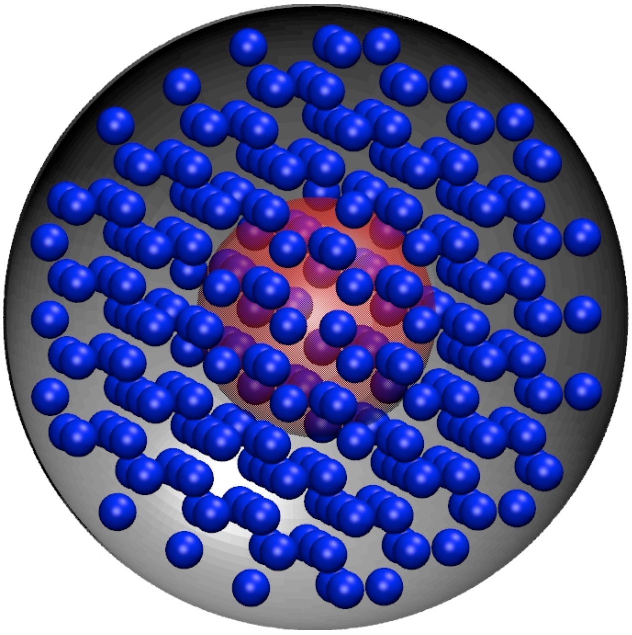

Figure 1: *Mg nanoparticle. Magnesium atoms are in blue, outer sphere is in gray and, inner red sphere is the void space due to the Kirkendall effect.*

ENEA CRESCO computing facilities

CPMD code runs on many different computer architectures and allows good scalability up to a large number of processors depending on the system size. We use the CPMD compiled with Intel Fortran Compiler, MKL (Math Kernel Library), ACML (AMD Core Math Library) and MPI (Message Passing Interface) parallelization on the high performance ENEA CRESCO computing facilities. The benchmark results demonstrate the high performance of the CPMD parallelization on CRESCO architectures and the good scalability up to hundreds of cores.

CRESCO (Computational Research Center for Complex Systems [12]) is an ENEA (Italian National Agency for New Technologies, Energy and Sustainable Economic Development [13]) Project, co-funded by the Italian Ministry of University and Research. The performance for the CRESCO HPC system ranked 125 in June 2008 top500 list with Rmax= 17,14 Tflops in the HPL benchmark. Please find below same of the hardware and software specifics.
The ENEA CRESCO computing facilities are based on the multi-core x86_64 architecture and is made up of various clusters: we tested the CRESCO cluster located in Portci, Casaccia and, Frascati ENEA centers. The CRESCO cluster in Portici consists of two main sections: section **POR_1** for high memory request and moderate parallel scalability; section **POR_2** for limited memory and high scalability. We are interested in the analysis of the **POR_2** section performance. This section has 340 compute nodes that are equipped with three types of Intel Xeon Quad-Core processors. The CRESCO clusters in Casaccia (**CAS**) and in Frascati (**FRA**) are equipped with AMD Opteron processors. Hardware details of the clusters are reported in *table 1*. The Operating System (OS) for the three clusters is the Red Hat Enterprise Linux version 2.6.18-194.26.1.el5. We compiled the CPMD version 3.15.1 using the same version of the mathematical library MKL. On CRESCO clusters **POR_2** and **CAS** we used ifort compiler version 11 and OpenMPI version 1.2.8; and on CRESCO cluster **FRA** we used ifort version 12 and OpenMPI version 1.4.2. Finally we performed a further test on the CRESCO cluster **FRA** choosing as mathematical library the ACML version 5.1.0. *table 1* summarizes some of the hardware and software characteristics. Further details are reported in Ref. [13].

Table 1: *Some of the hardware and software characteristics for the CRESCO clusters.*

	CRESCO Clusters					
	POR_2a	**POR_2b**	**POR_2c**	**CAS**	**FRA_mkl**	**FRA_acml**
Processor	Intel Xeon Quad-Core Clovertown E5345	Intel Xeon Quad-Core Nehalem E5530	Intel Xeon Quad-Core Westmere E5620	AMD Opteron 6 Core 2427	AMD Opteron Magny Cours 12 core 6174MS	
Clock (GHz)	2.33	2.4	2.4	2.2	2.2	
Cores for node	2 x 4	2 x 4	2 x 4	2 x 6	2 x 12	
Total cores	2048	448	224	180	456	
RAM	16 GB			32 GB	64 GB	
Compiler	Ifort 11.0.083				Ifort 12.0.2.137	
MPI Flavor	OpenMPI 1.2.8				OpenMPI 1.4.2	
Math. Lib.	MKL 10.0.1.014					ACML 5.1.0

Results and Discussions

The Kohn-Sham method of DFT simplifies calculations of the electronic density and energy of a system of N_e electrons in an external field without solving the Schroedinger equations with $3N_e$ degrees of freedom, but it takes into consideration the electronic density as the fundamental quantity (with only 3 degrees of freedom). The total ground-state energy of the system can be obtained as the minimum of the Kohn-Sham energy which is an explicit functional of the electronic density. This leads to a set of equations (Kohn-Sham equations) that has to be solved self-consistently in order to yield density and the total energy of the electronic ground-state. In the calculations, starting from an initial guess for the electronic density, the Kohn-Sham equations are solved iteratively until convergence is reached. To find the better computational demand, we calculated the average time for iteration in the resolution of the Kohn-Sham equations.

Table 2: *Average time (s) for iteration in function of the number of cores for the CRESCO clusters. In the second column we reported the peak memory requirement (PMR) for core (Mbytes). The best times are colored in green.*

N. cores	PMR for cores (MBytes)	CRESCO clusters					
		POR_2a	**POR_2b**	**POR_2c**	**CAS**	**FRA_mkl**	**FRA_acml**
24	2697.0	3197	3854	3606	580.8	**445.0**	-
32	2028.5	586.2	310.4	**308.7**	442.5	340.6	320.4
48	1359.6	403.5	233.0	**209.7**	303.6	233.8	223.3
64	1025.0	310.1	179.0	**166.3**	247.5	185.9	176.1
96	690.5	224.1	131.7	**124.8**	224.1	136.6	130.3
128	522.2	154.1	90.68	**88.32**	142.8	100.4	95.49
192	356.0	136.4	83.50	80.40	-	72.35	**69.19**

In *table 2* and *figure 2*, we reported the average time for iteration in function of the number of cores for the three CRESCO clusters. At the beginning, for 24 cores case, we observed that the times for the cluster **POR_2** are much longer than the times for cluster **CAS** and **FRA**. This is due to the peak memory requirement (PMR) for core that is 2697.0 Mbytes, whereas clusters **POR_2a**, **POR_2b** and, **POR_2c** have 2048 Mbytes for cores. For the others cases the cluster **POR_2c**, which is equipped with processors Intel Xeon Quad-Core Westmere E5620, has the fastest times, except for the 192 cores case, where as the cluster **FRA** has the best performance.

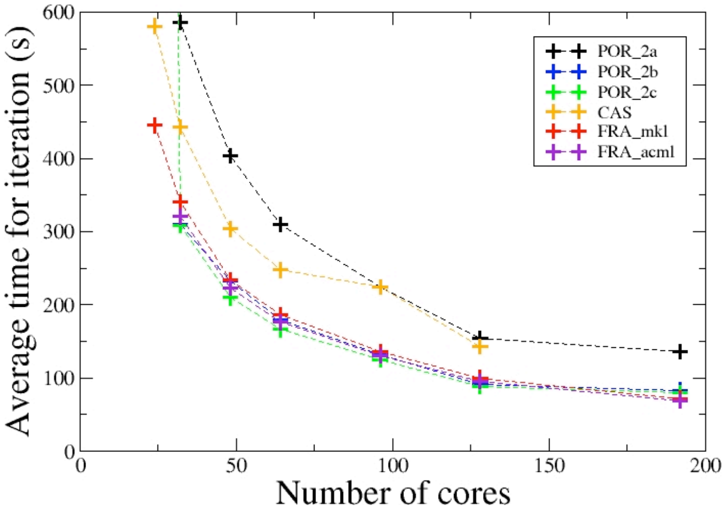

Figure 2: *Average time (s) for iteration in function of the number of cores for the different processors on the CRESCO clusters.*

However, the times for the clusters **POR_2b**, **POR_2c** and, **FRA** are very similar. This is also highlighted in the *figure 2*, where the blue, green and red lines are overlapped. Finally, using ACML library, we observed the performance improvement of the cluster **FRA** which has AMD Opteron Magny Cours 6174MS processors. The times in the last column (**FRA_acml**) in *table 2* are reduced in the range of 4.5-6.0 % compared to those in column **FRA_mkl** in which MKL library were used. It is worth pointing out that we have used the Intel compiler even on AMD processors. In *figure 3* is shown the speed up. For each cluster, the speed up was calculated with respect to the 32 cores time. We observed a good scalability of the code on all the clusters, with the best linear scaling for the CRESCO cluster **FRA** with both MKL and ACML libraries. From the speed up data we also calculated efficiency that is shown in Figure 4. This figure confirms the CRESCO cluster **FRA** as the most efficient. In fact, it has an efficiency higher than 75%.

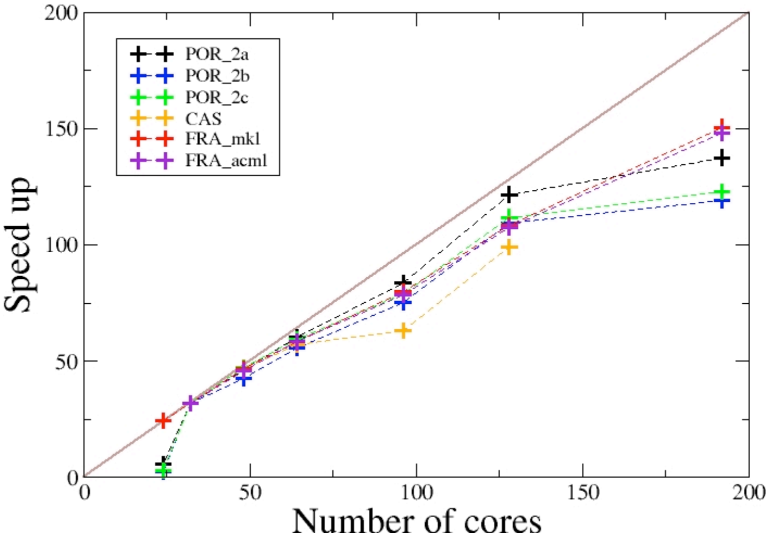

Figure 3: *Speed up for the different processors on the CRESCO clusters. The speed up was calculated with respect to the 32 cores time.*

Summary

Magnesium is seen as one of the most important candidates in the solid media hydrogen storage. However, to reach this aim same disadvantages have to be overcome. In this context Mg nanoparticles could solve some drawbacks of the bulk material. In view of an extensive characterization of Mg nanoparticles by numerical simulations, and to evaluate the suitable computational demand, we performed benchmarks of the CPMD code on the HPC ENEA CRESCO computing facilities. The benchmark results demonstrate the high performance of the CPMD parallelization on CRESCO clusters architectures and the good scalability up to hundreds of cores.

Acknowledgment

The computing resources and the related technical support used for this work have been provided by CRESCO-ENEAGRID High Performance Computing infrastructure and its staff; see Ref. [12] for information. CRESCO-ENEAGRID High Performance Computing infrastructure is funded by ENEA, the “Italian National Agency for New Technologies, Energy and Sustainable Economic Development” and by national and European research programs.

References

[1] PASQUINI L., CALLINI E., PISCOPIELLO E., MONTONE A., VITTORI ANTISARI M. *"Metal- hydride transformation kinetics in Mg nanoparticles"* Appl. Phys. Lett. **94** (2009) 041918.

[2] KRISHNAN G., KOOI B. J., PALASANTZAS G., PIVAK Y,. DAM B. *"Thermal stability of gas phase magnesium nanoparticles"* J. Appl. Phys. **107** (2010) 053504.

[3] PASQUINI L., CALLINI E., BRIGHI M., BOSCHERINI F., MONTONE A., JENSEN T. R., MAURIZIO C., VITTORI ANTISARI M., BONETTI E. *"Magnesium nanoparticle with transition metal decoration for hydrogen storage "* J. Nanopart. Res. **13** (2011) pp. 5727-5737.

[4] CAR R., PARRINELLO M. *"Unified approach for Molecular Dynamics and Density-Functional Theory"* Phys. Rev. Lett. **55** (1985) pp. 2471-2474.

[5] CPMD V3.15.1 Copyright IBM Corp 1990-2011, Copyright MPI fuer Festkoerperforschung Stuttgart 1997-2001.

[6] HOHENBERG P., KOHN W. *"Inhomogeneous electron gas"* Phys. Rev. **136** (1964) pp. B864-B871.

[7] KOHN W., SHAM L. J. *"Self-consistent equations including exchange and correlation effects"* Phys. Rev. **140** (1965) pp. A1133-A1138.

[8] GOEDECKER S., TETER M., HUTTER J. *"Separable dual-space Gaussian pseudopotentials"* Phys. Rev. B **54** (1996) pp. 1703-1710.

[9] HARTWIGSEN C., GOEDECKER S., HUTTER J. *"Relativistic separable dual-space Gaussian pseudopotentials from H to Rn"* Phys. Rev. B **58 (**1998) pp. 3641-3662.

[10] KRACK M. *"Pseudopotentials for H to Kr optimized for gradient-corrected exchange-correlation functionals"* Theor. Chem. Acc. **114** (2005) pp. 145-152.

[11] SMIGELSKAS A. D., KIRKENDALL E. O. *"Zinc Diffusion in Alpha Brass"* Trans. AIME **171** (1947) pp. 130-142.

[12] www.cresco.enea.it.

[13] http://www.afs.enea.it/project/eneagrid/Resources/CRESCO_documents/index.html.

A CFD INVESTIGATION OF SYNGAS SPARK IGNITION ENGINES

Emanuele Fanelli[1*], Annarita Viggiano[2], Giacobbe Braccio[1] and Vinicio Magi[2]

[1] *ENEA, Technical Unit for Trisaia Technologies (UTTRI), Trisaia*
[2] *University of Basilicata, Department of Environmental Engineering and Physics, Potenza*

[*] E-mail address: emanuele.fanelli@enea.it

1. Introduction

In the last two decades, specific interest has been addressed towards Internal Combustion Engines (ICEs) powered by bio-fuels. The growing interest for bio-fuels is related to constantly increasing stringent exhaust gases regulations and to a remarkable request of reduction of CO_2-emissions. In the same direction (CO_2-emissions reduction) and, additionally with the aim to minimize the dependence from crude oil, several alternative fuels have gained attention in the automotive industry. The fuels of bio-origin can provide a feasible solution to worldwide petroleum crisis by promising a sustainable development, energy conservation and environmental preservation. Gasoline and diesel-driven engines are the major sources of Green-House Gases (GHG) emissions [1-3]. Scientists around the world have been explored several alternative energy sources including biomass derived fuels, biogas, primary alcohol, vegetable oils, biodiesel, etc. These alternative energy sources are largely environmental-friendly but their use needs further investigations in relation to the specific applications. Some of them can be used directly while others need to be formulated to bring their relevant properties closer to those of conventional fuels.

This work deals with some features of spark ignition engines powered by syngas. The ENEA GRID Cresco resources have been used to perform accurate simulations using an advanced parallel CFD code.

2. Syngas combustion properties

Syngas is mainly a mixture of hydrogen (H_2) and carbon monoxide (CO). Others components such as carbon dioxide (CO_2), nitrogen (N_2), methane (CH_4), steam (H_2O) and small amounts of hydrocarbons may also be present depending on both the syngas process production and the gasified solid matter (coal, biomass, etc.). In order to promote the syngas utilization for power and propulsion applications, an analysis of its combustion properties, such as self-ignition delay, flame speed, extinction limits and heat release rate over a wide range of fuel composition, equivalence ratios and operating conditions, is required. Specifically, hydrogen has a lower auto-ignition temperature than natural gas and reacts rapidly with oxygen, thus obtaining a high burning velocity [4]. This means that moving from hydrocarbon fuels to syngas, detailed studies about its flammability range, flame propagation speeds and safety issues are required. While the flame propagation and stability characteristics of lean premixed system have been investigated for conventional hydrocarbon-air mixtures, not much is known about the characteristics of alternative gaseous fuels. Nevertheless, it must be highlighted that, in the last years, many research activities were addressed towards a comprehensive characterization of the syngas combustion. Detailed reaction mechanisms for $H_2/CO/O_2$ were developed and a wide range of flame structures can be predicted by such mechanisms [5-11]. Furthermore, several studies have been addressed to understand the impact of syngas composition on flashback, blowout, dynamic stability, auto-ignition behaviour [12-15], and on premixed flame speeds [16]. Other studies have numerically investigated the effect of syngas dilution with N_2 and H_2O on CO_2 and NO_x emissions, respectively, [17], or are devoted to get more accurate predictions of both the influence of CO in H_2/CO auto-ignition [18], and the evaluation of flame speed [16], especially at high pressure.

3. The model

Modeling of internal combustion engines is a complex process that involves several coupled physical and chemical phenomena. To simplify the entire computational procedure, the problem is usually decomposed into several sub-models (liquid-phase spray dynamics, gas-phase fluid dynamics, gas-phase chemical kinetics, etc.), each of which described by a specific mathematical formulation. Once the appropriate physical model is identified, the governing equations are solved by means of an accurate and efficient numerical method.

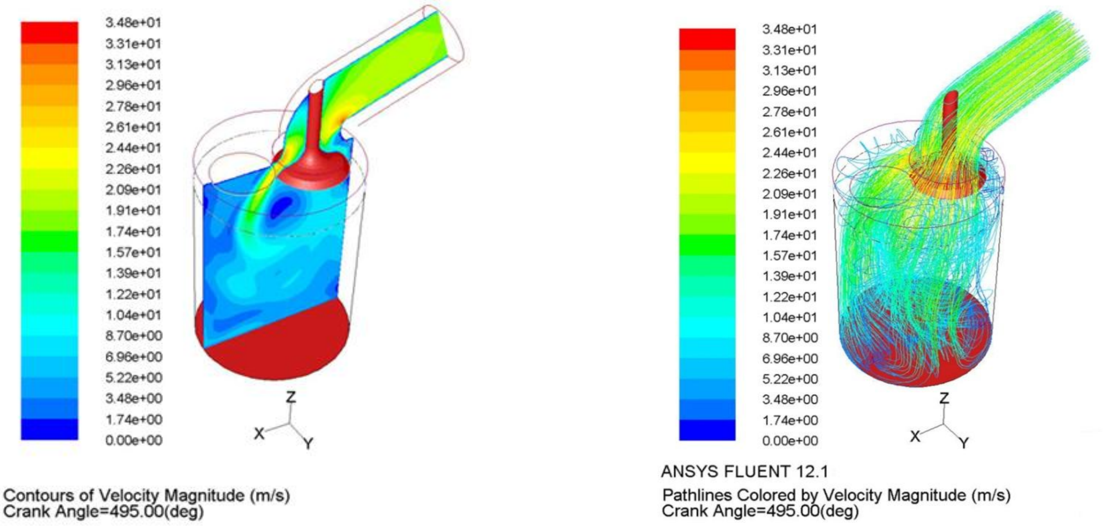

(a) **(b)**

Figure 1. *Velocity flow field details for 50:50 H_2/CO mixture, compression ratio 8:1, equivalence ratio 0.6:* ***(a)*** *contours of velocity magnitude during intake stroke. On the top is distinguishable the intake valve, on the bottom the piston head;* ***(b)*** *pathlines.*

In the combustion chamber of ICEs, high Reynolds numbers occur such that the flow field is highly turbulent. Hence the flow field requires modelling of turbulence by means of accurate and reliable models. The main characteristic of any turbulent flow is the presence of velocity fluctuations, that enhance the mixing of transported quantities such as energy, species concentration and momentum. The role of turbulence in the combustion process is important; in fact it increases the mixing between air and fuel. The description of a turbulent flow-field requires the solution of governing equations that must take into account the influence of the turbulent fluctuations by means of a direct solution (Direct Numerical Simulation – DNS - approach) of such fluctuations. However, this approach requires enormous computational effort. In fact, it is known that, in a multi-dimensional (3D) Direct Numerical Simulation, the number of grid points is proportional to $Re^{9/4}$, while the number of time steps is proportional to $Re^{3/4}$. It follows that the total computational cost is proportional to Re^{3}. In engines, very large Reynolds numbers occur; therefore, DNS of engines flows is impractical. For these reasons, several strategies have been developed to avoid the resolution of the smallest time and length scales. For instance, an alternative approach to DNS is based on an average evaluation of turbulent fluctuations by means of the solution of the Reynolds-averaged governing equations (Reynolds-Averaged Navier-Stokes - RANS - approach).

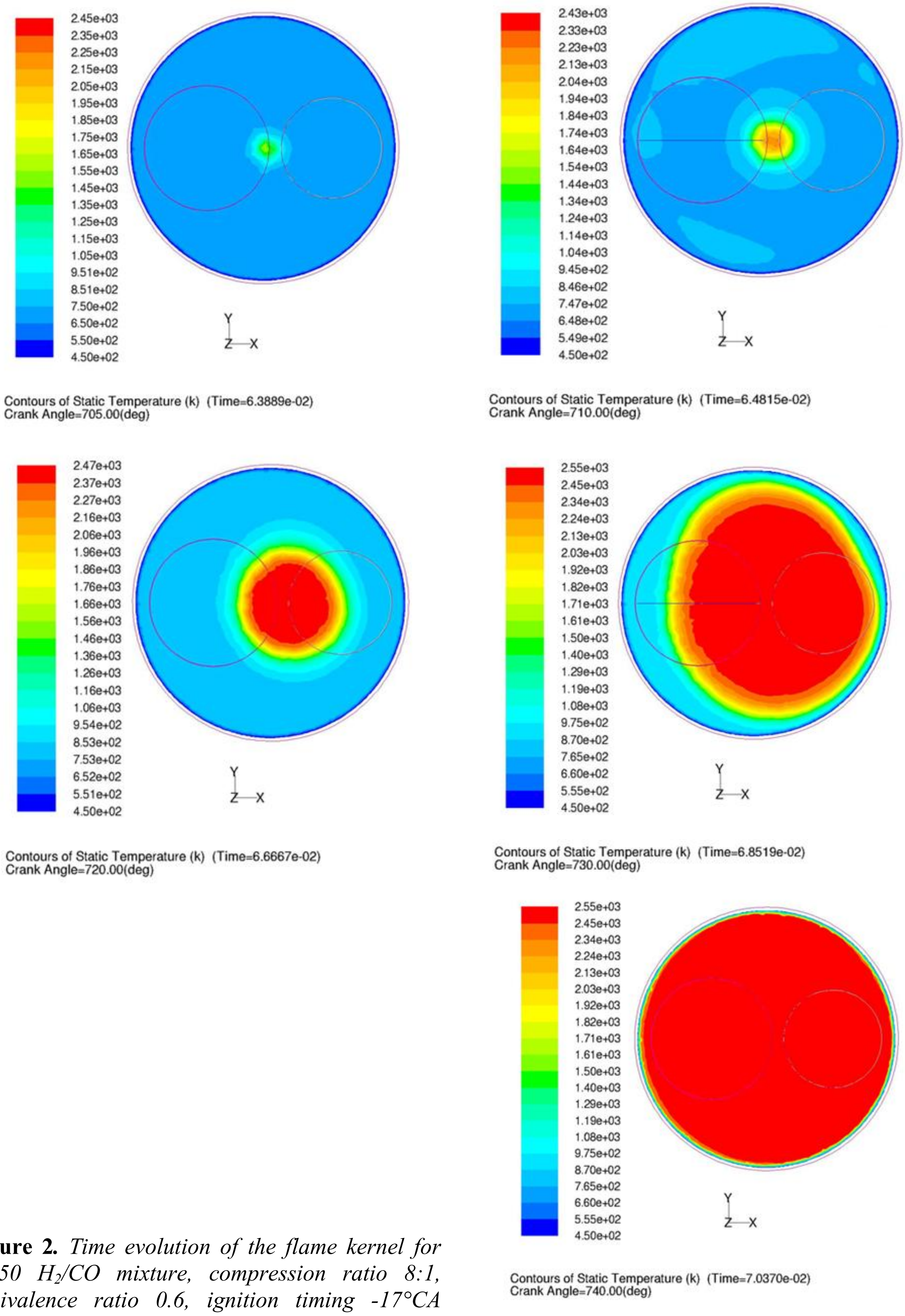

Figure 2. *Time evolution of the flame kernel for 50:50 H_2/CO mixture, compression ratio 8:1, equivalence ratio 0.6, ignition timing -17°CA BTDC (703°CA) – TDC at 720°CA. Time is in sec.*

Actually, RANS is still the most popular technique for ICEs simulation and optimization. This approach greatly reduces the required computational efforts but introduces additional terms that need to be modelled in order to achieve a closure for the problem. In the scientific literature, a very large number of turbulence models is available, but none of them provides a comprehensive description of all the processes involved in the turbulence flow field. This is because information are unfortunately lost in the averaging procedure. Generally, turbulent viscosity models are used to describe the effects of the fluctuating variables. Among the turbulent viscosity models, the most frequently employed is the two-equation $k-\varepsilon$ model [19]. Ansys Fluent® code has been used to perform the simulations: RANS equations are solved, $k-\varepsilon$ turbulence model has been set to close the turbulent problem, while premixed ECFM (Extended Coherent Flamelet Model) has been employed for the fuel combustion. This choice is acceptable based on the characterization of syngas flames on Borghi's diagram, where the ECFM field of applicability is limited on the top by the $Ka=1$ line (strongly wrinkled flames – where typically ICEs work). ECFM model assumes that the smallest turbulence length scales (Kolmogorov eddies) are larger than the laminar flame thickness, hence the effect of turbulence is to wrinkle the laminar flame sheet. More details about these models can be found in the literature [20]. Experimental results [21-23], have been used to model the flame structure, while experimental sets of pressure and heat release profiles [24], have been considered to validate the proposed model.

4. Results

Figure 1 shows the velocity flow field details for a 50:50 H_2/CO mixture with compression ratio 8:1 and equivalence ratio of 0.6. *Figure 2,* shows the time evolution of the flame kernel for the same engine. A good agreement with experimental results has been found. This guarantees and validates the model. Such model can be used to evaluate the performances of engines fuelled by syngas obtained from biomass gasification. Different syngas compositions (obtained from different biomass gasification processes) can be considered, and their effects on engine performances can be computed. Furthermore, the model can be successfully used as a design and optimization tool, by evaluating the effects induced on engine performance curves by mechanical modifications (piston head design, intake and exhaust ducts rearrangement, turbocharging, etc.) or by different operating conditions. Finally, benefits from strategies for pollutant emissions reduction and fuel consumption reduction (EGR, lean combustion, etc.) can be evaluated before their implementation.

References

[1] T. Johansson and S. McCarthy, "Global warming post-Kyoto: continuing impasse or prospects for progress?," *Energy Dev Rep Energy*, pp. 69-71, 1999.

[2] DG. Kesse, "Global warming-facts, assessment, countermeasures.," *J Pet Sci Eng*, no. 68, pp. 26-157, 2000.

[3] X. Cao, "Climate change and energy development: implications for developing countries.," *Resour Policy*, no. 7, pp. 29:61, 2003.

[4] X. Qin, H. Kobayashi, and T. Niioka, "Laminar burning velocity of hydrogen-air premixed flames at elevated pressure," *Exp Thermal Fluid Sci*, vol. 21, no. 58, 2000.

[5] R.A. Yetter, F.L. Dryer, and H. Rabitz, "A comprehensive reaction mechanism for carbon monoxide/hydrogen/oxygen kinetics," *Combust Sci Tech*, vol. 79, no. 97, 1991.

[6] R.A. Yetter, F.L. Dryer, and H. Rabitz, "Flow reactor studies of carbon monoxide/hydrogen/oxygen kinetics," *Combust Sci Tech*, vol. 79, no. 129, 1991.

[7] W. Wang and B. Rogg, "Reduced kinetic mechanisms and their numerical treatment. I. Wet CO flames," *Combust Flame*, vol. 94, no. 271, 1993.

[8] T.J. Kim, R.A. Yetter, and F.L. Dryer, "New results on moist CO oxidation: High pressure, high temperature experiments and comprehensive kinetic modeling," *Proc Combust Inst*, vol. 25, no. 759, 1994.

[9] M.L. Rightley and F.A. Williams, "Analytical approximations for structures of wet CO flames with one-step reduced chemistry," *Combust Flame*, vol. 101, no. 287, 1995.

[10] M.L. Rightley and F.A. Williams, "Burning velocities of CO flames," *Combust Flame*, vol. 110, no. 285, 1997.

[11] J. Li et al., "A comprehensive kinetic mechanism for CO, CH2O, and CH3OH combustion," *Int J Chem Kinet*, vol. 39, no. 109, 2007.

[12] Q. Zhang, D.R. Noble, A. Meyers, K. Xu, and T. Lieuwen, "Characterization of fuel composition effects in H2/CO/CH4 mixtures upon lean blowout," in *GT2005-68907 - ASME Turbo Expo*, Reno, Nevada, 2005.

[13] T. Lieuwen, V. McDonell, E. Petersen, and D. Santavicca, "Fuel flexibility influences on premixed combustor blowout, flashback, autoignition and stability," in *GT2006-90770 - ASME Turbo Expo*, Barcelona, Spain, 2006.

[14] D.R. Noble et al., "Syngas mixture composition effects upon flashback and blowout," in *GT2006-90470 - ASME Turbo Expo*, Barcelona, Spain, 2006.

[15] T. Lieuwen, V. McDonell, D. Santavicca, and T. Sattelmayer, "Burner development and operability issues associated with steady flowing syngas fired combustors," *Combust Sci Tech*, vol. 180, no. 1169, 2008.

[16] J. Natarajan, T. Nandula, T. Lieuwen, and J. Seitzman, "Laminar flame speeds of synthetic gas fuel mixtures," in *GT2005-68917 - ASME Turbo Expo*, Reno, Nevada, 2005.

[17] D.E. Giles, S. Som, and S.K. Aggarwal, "NOX emission characteristics of counterflow syngas diffusion flames with airstream dilution," *Fuel*, vol. 85, no. 1729, 2006.

[18] G. Mittal, C.J. Sung, and R.A. Yetter, "Autoignition of H2/CO at elevated pressures in a rapid compression machine," *Int J Chem Kinet*, vol. 38, no. 516, 2006.

[19] B. Launder and D. Spalding, *Mathematical models of turbulence.* Longdon: Academic Press, 1972.

[20] Ansys-Inc., *ANSYS FLUENT 12.1 User's Guide*., 2009.

[21] T. Lieuwen, V. Yang, and R. Yetter, *Synthesis gas combustion. Fundamentals and Applications*. Boca Raton: CRC Press - ISBN: 978-1-4200-8534-1, 2010.

[22] U. Gerke, K. Steurs, P. Rebecchi, and K. Boulouchos, "Derivation of burning velocities of premixed hydrogen/air flames at engine-relevant conditions using a single-cylinder compression machine with optical access," *International journal of hydrogen energy*, vol. 35, pp. 2566-2577, 2010.

[23] J. Gottgens, F. Mauss, and N. Peters, "Analytic approximations of burning velocities and flame thicknesses of lean hydrogen, methane, ethylene, ethane, acetylene, and propane flames," in *Twenty-fourth symposium of combustion*, 1992, pp. 129-135.

[24] Anil Singh Bika, Luke Franklin, and David B. Kittelson, "Engine knock and combustion characteristics of a spark ignition engine operating with varying hydrogen and carbon monoxide proportions," *International Journal of hydrogen energy*, vol. 36, pp. 5143-5152, 2011.

Molecular Dynamics simulations of $Cu_{64}Zr_{36}$ metallic glasses

[1]J. Zemp, [2]M. Celino, [1]B. Schönfeld and [1]J. F. Löffler

[1]*ETH Zurich, Metal Physics and Technology, HCI F 525, Wolfgang-Pauli-Str. 10, 8093 Zürich, Switzerland.* [2]*ENEA, C. R. Casaccia, Via Anguillarese 301, 00123, Rome, Italy*

*Corresponding Authors:Jérôme Zemp
E-mail: jerome.zemp@mat.ethz.ch. Tel.: +41 (0)44 633 61 71

Abstract

This report covers the first year of a project where the structure of $Cu_{64}Zr_{36}$ metallic glasses is simulated by Molecular Dynamics. An amorphous sample is produced by quenching from the melt. The pair correlation functions of the liquid and the glass are calculated and compared for different temperatures. The topological short-range order is analyzed by the Voronoi tessellation method. The most prominent atomic arrangements in the glass are Cu-centered icosahedra. Subsequently, the sample was uniaxially compressed to investigate the mechanical deformation in metallic glasses. A stress-strain curve was measured, which shows stress drops in the plastic regime that might stem from shear-transformation zones. However, larger systems have to be investigated to observe shear-band formation, which is known to be present in the real material.

Introduction

Metallic glasses (MGs) are amorphous alloys with unique mechanical, electric, and magnetic properties. They are produced by rapid quenching from the melt. The critical cooling rate to avoid crystallization is on the order of 10^6 K s^{-1} for conventional binary metallic glasses (MGs) and 10^2 K s^{-1} for bulk metallic glasses (BMGs) [1]. Therefore, the critical casting thickness of MGs is limited to a few micrometers, while BMGs have a casting thickness larger than 1 mm. Usually BMG-forming systems contain more than three different elements with large differences in the atomic sizes. However, also binary Cu–Zr can be cast into a metallic glass with a thickness of 2 mm [2], which is exceptional for a binary system. The advantage of a binary system is that the structural description becomes more feasible, when compared to multi-component systems, so that it is better suited for structural investigations. The structure of metallic glasses is characterized by the absence of any long-range translational order. Only short- and medium-range order exist and can be observed by means of x-ray diffraction (XRD) or extended x-ray absorption fine structure (EXAFS). The actual arrangement of the atoms, however, is difficult to determine by experimental techniques and thus computational methods such as Molecular Dynamics (MD) are employed. In fact, MD is not only capable of simulating the static structure of metallic glasses but can also be used to simulate dynamic properties, e.g. plastic deformation or relaxation. Plastic deformation in metallic glasses works fundamentally different than in crystals, where the strain is mostly carried by dislocations. The deformation in MGs is highly localized in so-called shear-bands, which have a thickness of several nanometers. In this study the structure of amorphous $Cu_{64}Zr_{36}$ is simulated by MD simulations. Initially a metallic glass is produced by quenching from the melt. The sample will then be mechanically deformed to investigate the structural origins of and changes during plastic deformation.

Methods

The MD simulations were carried out using the LAMMPS simulation package [3] and the embedded-atom potential provided by Mendelev et al. [4]. An amorphous $Cu_{64}Zr_{36}$ sample with a total number of 11'664 atoms was prepared in multiple steps. Starting from a cubic atomic arrangement, the sample was heated to 2000 K and equilibrated for 2 ns (10^6 time steps). Next, the sample was quenched to 50 K using a cooling rate of 0.1 and 0.01 K ps^{-1}, respectively. Slight changes in the pair correlation functions were observed so that we decided to continue with the slower cooling rate to obtain a more realistic simulation. The computation time when using 128 processors is about 0.005 s per time step, so that the entire simulation time (including the melting, equilibration and quenching) is of the order of days.

Pair correlation functions were calculated at 2000 K, 1200 K, 800 K, 680 K, and 50 K after equilibration for 0.2 ns and averaging the data from 50 successive configurations taken with a time interval of 1 ps. The total and partial coordination numbers were calculated by counting the nearest-neighbor atoms. The radial cut-off value was defined as the radius where the pair correlation function has its first minimum beyond the nearest-neighbor peak. To study the topological short-range order, the Voronoi tessellation method was applied for the liquid alloy (2000 K) and the glass (50 K). A Voronoi polyhedron (VP) is assigned to every atom, so that every point inside the VP is closer to the central atom than to any other atom in the structure. Every VP has its own Voronoi index (VI) $<n_3\ n_4\ n_5\ n_6>$, where n_i is the number of i-edged faces of the VP. For example, the VI of an icosahedral atomic arrangement is <0 0 12 0> as the corresponding VP is a dodecahedron. The frequency of different VI provides information on the most prominent structural patterns that are present.

After analyzing the static structure we studied plastic deformation of metallic glasses. The sample is uniaxially compressed in the z-direction with free movement in the x- and y-direction, a deformation rate of 2×10^7 s^{-1}, and periodic boundary conditions.

Results and discussion

The structure of $Cu_{64}Zr_{36}$ was studied at 2000 K, 1200 K, 800 K, 680 K, and 50 K to follow the evolution of the atomic arrangements during cooling. When plotting the volume per atom against the temperature (*figure 1*) a discontinuity is observed at approximately 720 K, which corresponds to the glass transition temperature T_g, where the undercooled liquid freezes and forms a metallic glass.

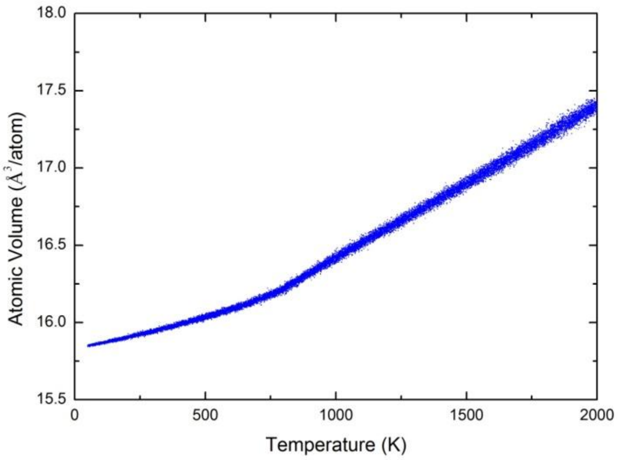

Figure 1: *Volume per atom depending on temperature during cooling. At 720 K a discontinuity indicates the glass transition.*

The value is close to the experimental T_g = 745 K. The respective pair correlation functions are shown in *figure 2*. During cooling the height of the first peak of the pair correlation function increases while the full width at half maximum decreases. This indicates that the atomic neighbor-shells are defined better at lower temperatures, especially when comparing the glassy and the liquid state. In addition, the second peak is becoming more structured at lower temperatures hinting at increased topological order in the next nearest-neighbor shell.

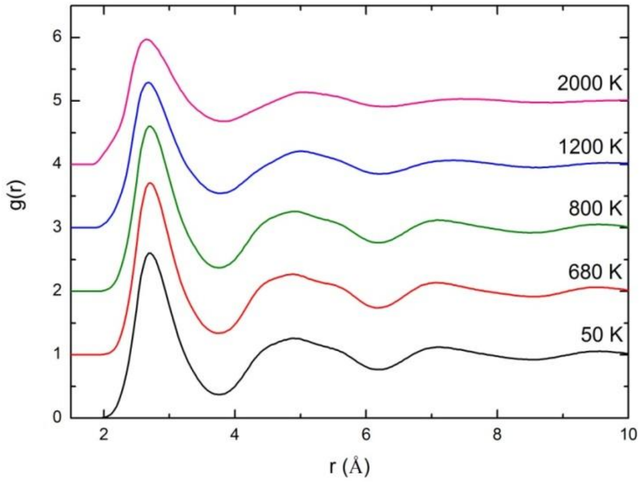

Figure 2: *Total pair correlation function g(r) at different temperatures during cooling. With decreasing temperature the first peak narrows and becomes larger indicating a better defined nearest-neighbor position. Additional features appear in the second peak meaning that also the next nearest-neighbors are arranged more systematically.*

A better understanding of the actual atomic arrangements is provided by the Voronoi tessellation method: At 2000 K 0.2% of all copper-centered clusters are full icosahedra (FI) (*figure 3a*) with a VI of <0 0 12 0> and 1.3% are distorted icosahedra (DI) (*figure 3b*) with a VI of <0 2 8 2>. After solidification the icosahedra are the most prominent clusters as their relative amount increases to 10.8 % FI and 7.1 % DI. This result agrees with earlier reports in the literature [5, 6].

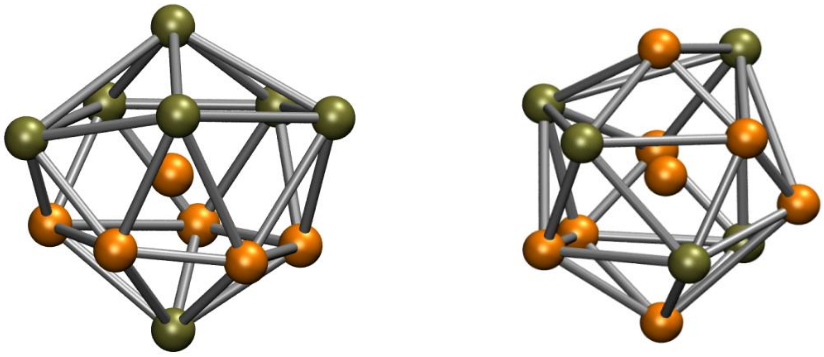

(a) (b)

Figure 3: *(a) Full Cu_6Zr_7 icosahedron with a VI of <0 0 12 0>; (b) Distorted Cu_8Zr_5 icosahedron with a VI of <0 2 8 2>. Copper atoms are colored orange and zirconium olive. The bonds are only drawn for better 3-dimensional visibility and do not represent physical bonds.*

In *table 1* the partial and total coordination numbers are shown and compared to results from the literature for *ab initio* calculations [7] and Reverse Monte Carlo (RMC) simulations [8].

	This work	*ab initio* [7]	RMC [8]
Cu-Cu	5.9	6.2	7.8
Cu-Zr	6.0	5.7	4.6
Zr-Cu	10.7	10.1	8.6
Zr-Zr	4.8	5.1	6.0
Total	13.3	13.1	13.2

Table 1: *Partial and total coordination numbers compared with the literature.*

While the results from *ab initio* simulations are close to the results in this work, the coordination numbers from RMC simulations are different. This is not further surprising as the RMC method simply produces an atomic configuration that reproduces XRD and EXAFS data, without considering a physical potential.
The mechanical properties of metallic glasses are characterized by a high yield strength and low plasticity due to the absence of dislocations. In metallic glasses, plasticity is highly localized in thin shear-bands with a thickness of some nanometers. The sample in this work, however, is smaller than the typical size of a shear-band which therefore cannot be observed. *Figure 4* shows the stress-strain curve recorded in compression with a deformation rate of 2×10^7 s^{-1}.

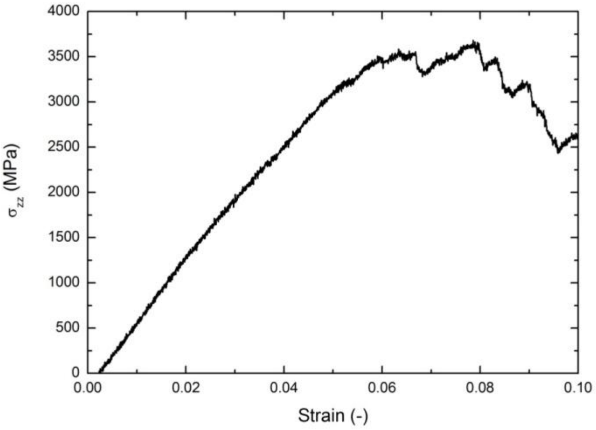

Figure 4*: Stress-strain curve in compression for a strain rate of 2×10^7 s^{-1}.*

The sample exhibits a yield strength of 3.5 GPa and an elastic strain of approximately 6%. The experimental values of $Cu_{64}Zr_{36}$ are ~2 GPa and ~2.2%, respectively [2]. When comparing these values one has to be aware of the much higher cooling rate in the simulation, which is 11 orders of magnitude faster than in the experiment. The stress drops in the plastic regime might be a result from local atomic rearrangements (shear transformation zones), which has to be checked.

Conclusions and Outlook

Amorphous $Cu_{64}Zr_{36}$ was simulated by using MD. The change of the topological short-range order is seen in the pair correlation functions, which were calculated at different temperatures during cooling. The Voronoi tessellation method unveiled an increase of icosahedra during glass formation. In the second part uniaxial compression was applied on the sample and a stress-strain curve was measured. However, to observe shear-band formation a larger sample (> 1 million atoms) is required, which will be built by several replicas of the sample from this work. The deformed sample will then be analyzed locally to identify the differences in- and outside the shear-band region.

References

[1] C. Suryanarayana, A. Inoue, *Bulk Metallic Glasses*. (CRC Press, ed. 1 edition, 2010), pp. 565.

[2] D. H. Xu, B. Lohwongwatana, G. Duan, W. L. Johnson, C. Garland, *Acta Mater.* **52**, 2621 (2004).

[3] S. Plimpton, *J. Comput. Phys.* **117**, 1 (1995).

[4] M. I. Mendelev, M. J. Kramer, R. T. Ott, D. J. Sordelet, D. Yagodin, P. Popel, *Philos. Mag.* **89**, 967 (2009).

[5] Y. Q. Cheng, H. W. Sheng, E. Ma, *Phys. Rev. B* **78**, 014207 (2008).

[6] Y. L. Sun, J. Shen, *J. Non-Cryst. Solids* **355**, 1557 (Sep 1, 2009).

[7] N. Jakse, A. Pasturel, *Phys. Rev. B* **78**, 214204 (2008).

[8] N. Mattern, P. Jóvári, I. Kaban, S. Gruner, A. Elsner, V. Kokotin, H. Franz, B. Beuneu, J. Eckert, *J. Alloy. Compd.* **485**, 163 (2009).

EMERGENT PHENOMENA IN BIOLOGICAL NETWORKS

Juan A. Almendral[1,2], Ricardo Bajo[1], Stefano Boccaletti[1], Javier M. Buldú[1,2], Ricardo Gutiérrez[1], Inmaculada Leyva[1,2], Adrián Navas[1], David Papo[1], Irene Sendiña-Nadal[1,2], Massimiliano Zanin[1,3,4]

[1] *Centre for Biomedical Technology, Technical University of Madrid, Spain*

[2] *Complex Systems Group, Universidad Rey Juan Carlos, Madrid, Spain*

[3] *Faculdade de Ciências e Tecnologia, Departamento de Engenharia Electrotécnica, Universidade Nova de Lisboa.*

[4] *Innaxis Foundation & Research Institute, José Ortega y Gasset 20, 28006, Madrid, Spain.*

Emerging Meso- and Macroscales from Synchronization of Adaptive Networks

Many systems of physical, biological and technological interest can be represented as ensembles of dynamical units interacting via complex architectures. The analysis of such systems has revealed that, despite their intrinsic differences, their structure is characterized by two unifying properties: (i) a power law (scale-free) scaling in the network connectivity, and (ii) the presence of modules (community structures) at a mesoscopic scale. Their interplay is believed to be the basis of the systems' functioning and performance.

In [5] a generic model of networked phase oscillators with directed and time-varying interactions coupled to the dynamics of the oscillators is studied. Numerical and analytical results on the synchronization properties (both at a local and a global scale) allow us to conclude that a competitive adaptive mechanism not only enhances synchronization, but also yields the simultaneous emergence of a mesoscale of communities and a scale-free distribution in the connection weights. The mechanism through which the dynamics reshapes the network structure is governed by the competition between the following two principles: (a) the connections between synchronized units are enhanced; (b) the available resources per unit to sustain interactions with the rest of the ensemble are limited (*figure 1*). Principle (a) is known to be relevant in neuronal plasticity, or spreading in sociology, under the terms of Hebbian learning and homophily, respectively. The limitation in the associative capacity given by principle (b) is known to play a relevant role in neuroscience (homeostasis), while in sociology it is related to the Dunbar's number. To our knowledge, this is the first model able to reproduce at once properties (i) and (ii).

Targeting the dynamics of complex networks

The theory of complex networks provides the necessary tools for the representation and subsequent study of the interaction among coupled dynamical entities. For a given coupling scheme between dynamical systems, and issue of great importance is how to make the network abandon it current time evolution (as defined by the equations of motion and the initial condition) and approach a given *goal dynamics*.

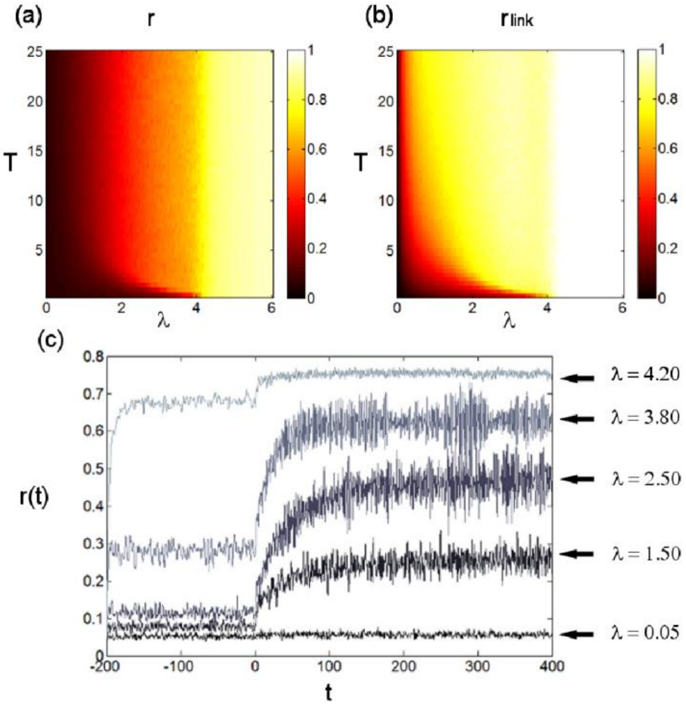

Figure 1. *Global (a) and c)) a local synchronization properties as a function of the coupling strength between oscillators (l) and the adaptation characteristic time (T).*

In the case of low-dimensional chaotic systems, traditionally this has been the aim of the targeting of dynamical system, a subject closely related to the field of chaos control, whose methods have laid the basis for a judicious manipulation of nonlinear dynamical systems. Whereas control methods have been proposed to stabilize one of the infinite set of unstable periodic orbits embedded in chaotic attractors, the idea behind the targeting procedure is to steer the dynamics of the system in the shortest possible time towards another orbit fully compatible with the equations of motion but starting from a different initial condition. For large ensembles of dynamical systems coupled via irregular architectures, the study of how to influence the natural dynamics via control or targeting strategies is still in its infancy.

In Ref [6] we propose a novel procedure to steer (target) a network's dynamics towards a given, desired evolution compatible with the equations of motion. A Master Stability Function approach based on a master-slave configuration is employed to assess the stability of the aimed dynamics through a pinning procedure based on a careful selection of nodes. We show that the node degree is a crucial element in the selection process, and provide hints that the targeting mechanism is most effective in scale-free architectures, which makes our approach applicable to a large majority of natural and man-made networked dynamical systems (*figure2*).

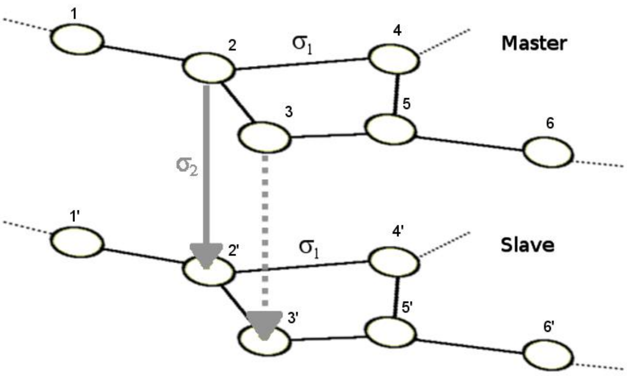

Figure 2. *Schematic representation of the targeting procedure based on a network initially evolving freely in time (slave system) and an identical copy of it evolving in time according to the goal dynamics (master system).*

Selection of relevant features in biological complex networks

In the last years, there has been an increasing interest in the analysis of genetic and metabolic data by means of complex networks [3]. Clearly, the study of how different genes interact can unveil new relevant knowledge that is not readily available by analyzing the behavior of individual and isolated genetic expressions. Following this principle, several works have analyzed co-expression networks, where nodesrepresent individual genes, and pairs of nodes are connected whenever there is a correlation in their expression [12]. Recently, a complementary strategy has been proposed, consisting in reconstructing connections between pairs of nodes when their expressions are outside the range observed in a reference condition; this methodology results in networks codifying abnormal behaviors of genes'expressions [11]. Thanks to this network based analysis, it is possible to extract information about two important issues: whether a given subject is suffering from the studied disease, and which elements (genes) of the graph are the main responsible for the pathological condition.

While this methodology has several advantages, it also requires the analysis of a large set of data, usually in the order of many thousands of genetic expressions, thus resulting in large networks that should be classified and analyzed. Clearly, this high computational cost is a limiting factor. In order to overcome this drawback, we have applied the well-known data mining technique of *feature selection* to the data set described in [11], in order to eliminate *ad priori* those genes and metabolites that appear to be not relevant for the final result.

Figure 3 shows how the result, in terms of the goodness of the analysis in predicting the severity of a disease, varies depending on the number of nodes included in the complex networks. Three are the advantages of this approach. Besides reducing the quantity of information to be processed (and thus the computational cost), the elimination of *noisy* genes results in an overall improvement of the accuracy of the method. Furthermore, reducing the number of genes also reduces the dimensionality of the problem, thus improving the statistical significance of the results.

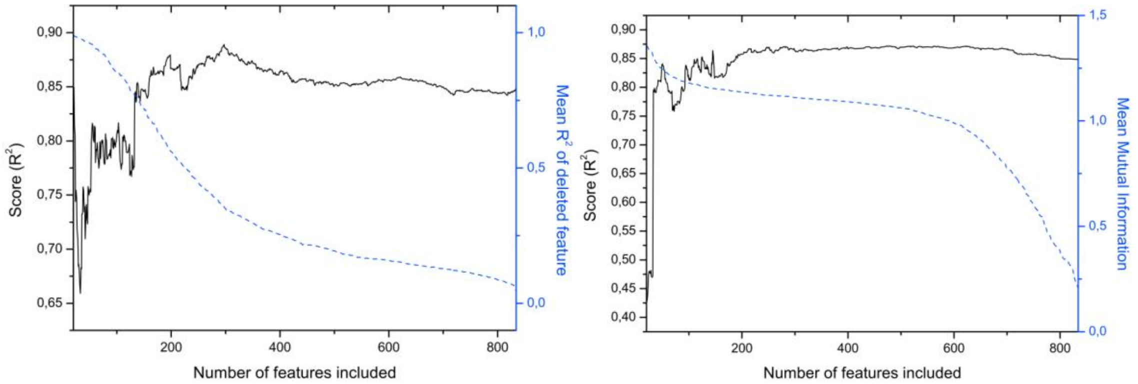

Figure 3. *Performance of two feature selection algorithms, namely goodness of linear fit (left) and mutual information (right). The black solid lines represent the score (i.e., the goodness in the assessment of the severity of the disease) as a function of the number of features included in the analysis; blue dashed lines indicates the value of the metric (R^2 and Mutual Information I) associated with the feature included in each step.*

Assortative and modular networks are shaped by adaptive synchronization processes

The majority of articles on complex networks have focused, until recently, on either the local scale structure of real complex systems or their macroscopic properties. However, neither of these descriptions can adequately describe the important features that complex systems exhibit due to their organization in modules. Since their seminal work [4] on uncovering the modular network structure in social and biological networks, it was evident that nature exhibits, in many cases, *communities* (groups of highly interconnected nodes that are sparsely connected to the rest of the network). Such a modular organization has only recently been recognized to be crucial in the way in which a complex system works [2].

Among the questions that must be addressed in order to provide a full understanding of modularity, one of the most important is that of growth and formation of such mesoscales in complex systems. Most existing models for network growth introduce modularity through topological arguments [7]. Yet, very little attention has been paid to mechanisms based on the dynamical behavior of the components, a common feature in many real systems. The modeling of growing mechanisms that enable the description of the real evolutionary processes involved in the formation of mesoscales is necessary.

On the other hand, another important open problem is the role of mesoscales in the production of a collective and coordinated dynamics. It is evident that the existence of communities in a task-performing network is closely related to the coexistence of two seemingly but not fundamentally opposite phenomena: the establishment of collective subtasks in the network (*segregation* of the network) and the coordination of those subtasks at a global scale (*integration*). The hierarchical nature of the function of complex systems is not yet fully elucidated; a thorough treatment of the relation between network structure and its dynamics at mesoscale level is also of interest.

A nice example of this open topic can be found in the neural system [8,9,10], for both the visual and audio areas, in which it is observed a functional segregation of anatomically and physiologically different areas and a global integration resulting in a unique perception. It is, then, needed to examine the relationship between the structural substrate of a complex system (its local scale) and its effective dynamics (its global scale) taking into account the connectivity patterns at the mesoscale.

In particular, a basic coordination task is *synchronization*: an ensemble of individuals adjusts their inner dynamics to that of the others. This is found in neural ensembles but other examples include fireflies flashing at the same rhythm, the muscle cells in the heart simultaneously beating, and an audience of a concert all applauding in unison to convince the artist to perform an encore [1].

In this paper, we study the integration/segregation problem from the viewpoint of complex networks, but considering that the network topology is not static but there is an adaptive mechanism acting on the links. Our goal is to identify under which conditions network synchronization occurs and what structural properties are present in the network topology when this happens. In particular, we experimentally compute the main descriptive structural properties of the network when it has been modified with the proposed mechanism, and it is elucidated the relationship between these results and the observed synchronization at both the local and global scale. Our main finding is that modularity and assortativity, both are global features, can naturally emerge in a network when evolving links are considered, that is, by means of dynamical properties at the local scale.

References

[1] ACEBRÓN J. A., BONILLA L. L., PÉREZ VICENTE C. J., RITORT F., SPIGLER R. *"The Kuramoto model: A simple paradigm for synchronization phenomena"* Reviews of Modern Physics **77** (2005) pp. 137-185.

[2] ALMENDRAL J. A., CRIADO R., LEYVA I., BULDÚ J. M., SENDIÑA-NADAL I. *"Introduction to Focus Issue: Mesoscales in Complex Networks"* Chaos **21** (2011) 016101.

[3] BARABÁSI A.-L., OLTVAI Z. N. *"Network biology: understanding the cell's functional organization"* Nature Reviews Genetics **5** (2004) pp. 101-113.

[4] GIRVAN M., NEWMAN M. E. J. *"Community structure in social and biological networks"* Proc. Natl. Acad. Sci. USA **99** (2002) pp. 7821-7826.

[5] GUTIÉRREZ R., AMANN A., ASSENZA S., GÓMEZ-GARDEÑES J., LATORA V., BOCCALETTI S. *"Emerging Meso- and Macroscales from Synchronization of Adaptive Networks"* Phys. Rev. Lett. **107** (2011) 234103.

[6] GUTIÉRREZ R., SENDIÑA-NADAL I., ZANIN M., PAPO D., BOCCALETTI S. *"Targeting the dynamics of complex networks"* Nature Sci. Rep. **2** (2012) 396.

[7] HUI-JUN J., HAO W., ZHONG-HUAI H. *"Explosive Synchronization and Emergence of Assortativity on Adaptive Networks"* Chinese Physics Letters **28** (2011) 056802.

[8] ISHIDA Y., HAYASHI T. *"Asymmetric Phenomena of Segregation and Integration in Biological Systems: A matching Automaton"* Lecture Notes in Computer Science **5712** (2009) pp. 789-796.

[9] SPORNS O., CHIALVO D., KAISER M., HILGETAG C. C. *"Organization, development and function of complex brain networks"* Trends in Cognitive Sciences **8** (2004) pp. 418-425.

[10] TONONI G., SPORNS O., EDELMAN G. M. *"A complexity measure for selective matching of signals by the brain"* Proc. Natl. Acad. Sci. USA **93** (1996) 3422-3427.

[11] ZANIN M., BOCCALETTI S. *"Complex networks analysis of obstructive nephropathy data"* Chaos **21** (2011) 033103.

[12] ZHANG B., HORVATH S. *"A General Framework for Weighted Gene Co-Expression Network Analysis"* Statistical Applications in Genetics and Molecular Biology **4** (2005).

Structural properties of CdS nanocluster by using ab-initio molecular dynamics simulation.

E Burresi[1,*] **M Celino**[2]
[1]*ENEA, Faenza Research Laboratories, via Ravegnana, 186, Faenza, 48018, Italy;*
[2]*ENEA C. R. Casaccia, via Anguillarese 301 00123 Rome, Italy*

*Corresponding Authors:Emiliano Burresi
E-mail: emiliano.burresi@enea.it

Abstract

In the report 2009-2010 preliminary structural calculations on Cd-Cd, S-S, Cd-S dimers and CdS cluster were performed and for this last system beginning calculation of formation energy was obtained.

In the last year our specific goal has been the study of a single wurtzite phase of cadmium sulfide cluster annealed up to 600K. Mean coordination number for internal and superficial atoms and other structural parameters were obtained in order to correlate the structural modifications of the cluster, for different temperatures, to his stability.

Introduction

Nanocrystalline semiconductors are characterized by novel and interesting structural and electronic properties, very different from bulk materials, subjects of intense research in recent years. One interesting possibility is the use of particle size as a control parameter in order to modulate band gap, which could allow novel development of materials for optical device applications.

In our case we focused the attention on the study of the cadmium sulfide nanocrystalline, a semiconductor with important application in devices for energy saving as light emission diode (LED). His structural characteristics, at experimental level, have a considerable and direct influence on his optical efficiency,depending, for example, from the phase crystalline (for CdS cubic or exagonal simmetry). Moreover it is well-know that the phase transformations of the nanocrystals are size-dependent and very different from bulk phase; it could occur that nanostructures have a melting point dissimilar from bulk by several orders of magnitude. The study of these transformations at atomistic level, could require too large efforts if an experimental approach is used; so the analysis of stability of the cluster at different temperatures, in function of his internal and superficial modifications, could be determined more easily by using some computational techniques like molecular dynamics simulation.In fact this approach allows to simulate the nanomaterials on the atomic scale, checking the motion of the atoms in function of the temperature, correlating the atomic layer displacements of the system to his stability. For these reasons, the main goal of our study has been to explore the structural modifications of CdS nanoparticles by using Car-Parrinello ab initio molecular dynamics.

Furthermore, in the last decade, some authors have also investigated several other properties of nanostructure materials by using computational approaches. Specific results for CdS clusters with different sizes were presented and their geometrical and electronic properties were computed by using ab-initio methods [1-2].

Recently, Wen and Melnik [3] performed an ab-initio molecular dynamics calculation on three different phases of CdS, wurtzite, graphite and rocksalt reporting their potential energy for each temperature between 300 K-450 K. Some results about structures and electronic properties of stoichiometric cadmium sulfide clusters are also reported by He-Ying and co-workers (2008) [2], where the behaviour of the energy gap between HOMO and LUMO orbitals as a function of cluster size is shown. Moreover, from theoretical point of view, Junkermeier [4] showed by means of Molecular Dynamics (MD) calculations that uncapped CdS nanoparticles with size around 2 nm are amorphous, in agreement with experimental results by Herron [5] and Vorokh [6].

Computational datails

Car-Parrinello Molecular Dynamics (CPMD) code has been employed to describe efficiently the electronic contribution to the ion dynamics [7]. We used a generalized gradient approximation BLYP for the exchange-correlation functional already implemented in CPMD package [8];.A CdS cluster with 48 atoms of cadmium and 48 atom of sulfur was built in the wurtzite phase; the temperature of annealing was set in the range from At each temperature, after thermal equilibration, at least 20000 time steps were used to compute averages. Moreover a CdS bulk structure was built to estimate the performance of DFT method by using the same conditions of the cluster calculations; lattice parameters and band gap energy were obtained for wurtzite supercell containing 5 unit cells and 500 atoms. Band structure was calculated for high symmetry point of the first Brillouin zone in hcp geometry. For all our calculations 32 processors were used.

Results and Discussion

In order to better determine the performance of the DFT scheme used in this work, we have taken in account a CdS supercells with wurtzite phase containing 5 unit cells (*figure 1*); cell parameters and band gap energy were calculated and subsequently compared with experimental results.

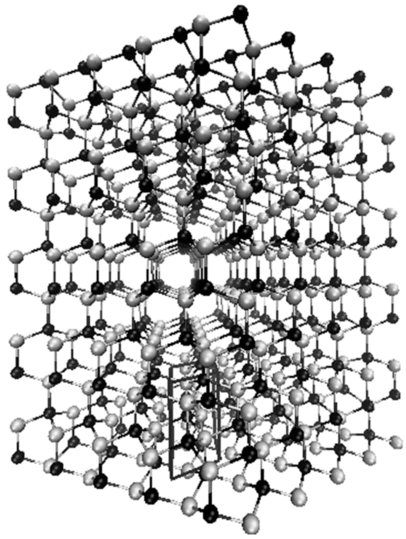

Figure1: *Graphic Rappresentation of CdS wurtzite structure as crystalline phase.*

For this type of calculation the best cell parameters and band gap energy was obtained by using this specific layout: for wurtzite supercell different cell parameters values a1 and a2 (in hexagonal symmetry they are equals) was employed in order to minimize the potential energy Then the best a1 and a2 values were set and a3 cell parameters was optimized so as to minimize the total potential energy .Using these cell parameters we have calculated the band structure of the CdS semiconductor (*figure 2*) whence it is possible to obtain the theoretical band gap.

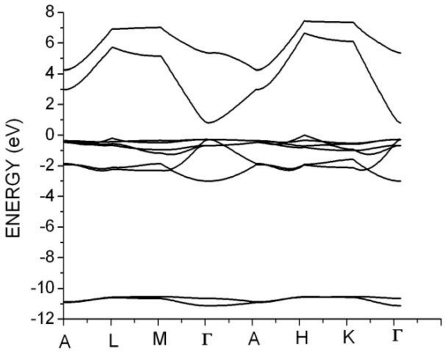

Figure 2*:* *Band structure of CdS wurtzite by using a Trouiller-Martins norm conserving pseudopotentials in DFT-BLYP approximation*

The best structure was found for a3/a1=1.59 to compare to 1.63, traditional values for ideal hcp structure. The values of band gap calculated on gamma point is set around 1 eV, rather different from experimental results. This underestimation of the band gap is well documented in several articles and review and it is typical for DFT-GGA approximation. Subsequently, on the initial structure of CdS cluster (*figure 3*), we performed CPMD molecular dynamics calculation at 10 K to equilibrate the geometry. Then, this equilibrated configuration has been used for an annealing of the cluster up to 400 K. The annealing has been performed slow enough to avoid unphysical melting of the cluster and abrupt changes on the surface. Subsequently the temperature has been raised further to characterize the behavior of the cluster at high temperatures.

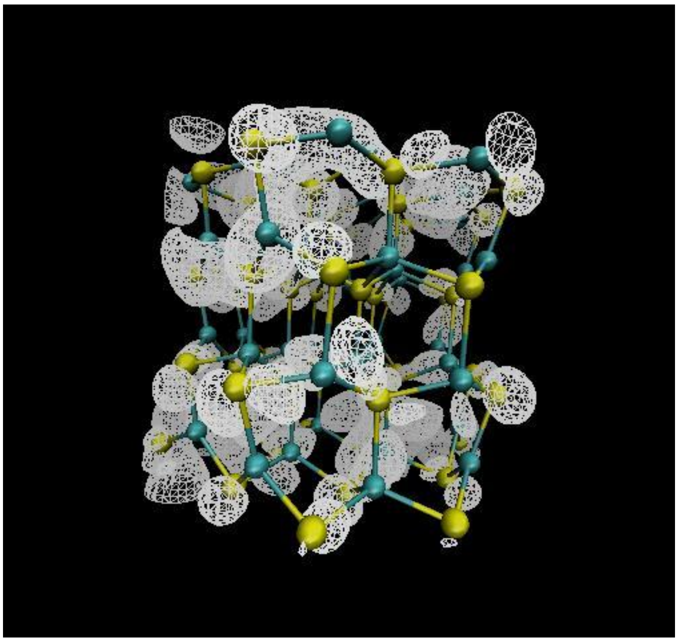

Figure 3: *Views of CdS wurtzite cluster. It is also reported the isosurface of a frontier orbital.*

Cd-S interatomic distance distribution and mean coordination number (MCN) of the clusters simulated were obtained for all temperatures. In order to calculate MCN, the first minimum of the radial distribution function was estimated and for each atom the nearest neighbor atoms were counted. Each atom with four nearest neighbor (C4) atoms has been classified as core while atoms with lower coordination have been classified as surface. For CdS at 10 K there are 34 atoms for core and 62 atoms for surface. To point out this behavior the fraction of the core and surface atoms were also reported for all the temperatures in *figure 4*. In general from 100 K to 330 K there are not changes in the coordination. We note that the coordination 4 increases after 340 K up to 400 K; on the contrary the superficial fraction undergoes an important reduction; at 400K the fractions for core and surface atoms stay constant respect previous four temperatures, around 0.39 and 0.61 respectively.

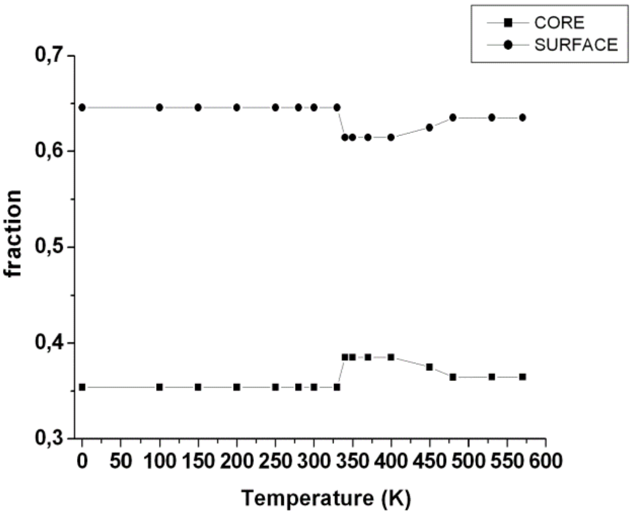

Figure 4*: Fraction of core atoms and surface atoms as a function of temperature.*

Above 400 K the opposite behavior is reached: the number of core atoms decreases from 37 to 35, consequently an augmented of superficial fraction has been observed for CdS450,CdS480,CdS530 and CdS570 (CdS cluster at 450,480,530 and 570 K); for CdS450 the number of C4 atoms decreases from 37 to 36, for CdS480 from 36 to 35,staying on this last value for the subsequent temperatures up to 600 K.

Moreover MCN (Mean Coordination Number) was determinated for core structure obtaining 4 as a value for all the temperatures. Then MCN have not changed during the annealing, confirming that the order inside the cluster has been preserved. For higher temperatures, more precisely over 400 K, the fraction of surface increases and also the coordination number. Around 480 K the raising of superficial fraction is quite clear: so regarding the energy aspect , this changing is probably due to the superficial effects which became important on the stability of the cluster, particularly for cluster with high superficial fraction like our system. In this framework, between 400 K and 480 K, it is conceivable that the surface attempt to reorganize, increasing the coordination numbers (*figure 5*).

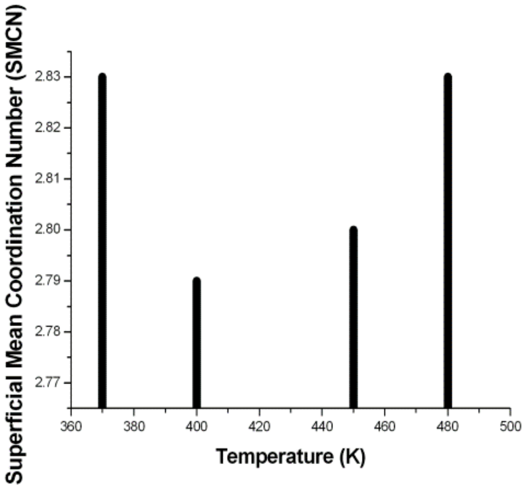

Figure 5: *Superficial Mean Coordination Number (SMCN) for CdS cluster. For SMCN a short range of temperatures has been reported in order to show in particular the superficial reorganization of the cluster.*

Moreover to compare the stability of the 340 K atomic structure with the perfect wurtzite it is necessary to cancel out the temperature contribution to the total energy. For this reason the structure at 340 K was quenched instantaneously at 10 K (CdS340Q10). The new quenched structure has a lower formation energy respect to the starting configuration CdS0 obtaining an energy gain of about 120 kcal/mol.

Mean coordination numbers for CdS340Q10 were calculated and reported in *figure 6*: we obtained the same values of the structure equilibrated at 340 K. This result confirms that the cluster preserves the same structure before and after quenching process. Then the quenching process correctly cancelled out the temperature contribution without changing of the structure.

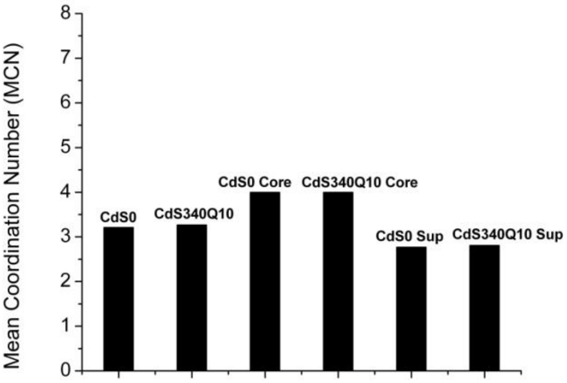

Figure 6: *MCN for whole cluster equilibrated at 10 K and 340K subsequently quenched at 10K. For the same structures the core and superficial contributions were also reported.*

It is important to stress how the increase of stability over 340 K is strongly connected with the arrangement of the atoms which appears to be more orderly.

In conclusion the superficial strain effects were found to be predominant in this system. The temperature allows the cluster to probe every compatible and realistic configuration; in this way all the possible configurations accessible are taken in account, allowing to the system to approach towards a minimum energy configuration. This behaviour has been carefully analyzed from a structural point of view by using coordination numbers and interatomic distances distributions.

References

[1] Datta S, Kabir M, Saha-Dasgupta T, and Sarma DD "*First-Principles Study of Structural Stability and Electronic Structure of CdS Nanocluster*" J Chem Phys **112** (2008) pp. 8206-8214

[2] He-Ying C, Zhao-Xin L, Guo-Li Q, De-Guo K, Si-Xin Wu, Yun-Cai Li, and Zu-Liang Du "*First-Principles study of structures and electronic properties of cadmium sulphide cluster"* 17 (2008) pp. 2478-2483

[3] Wen B and Melnik RVN "*First principles molecular dynamics study of CdS nanostructure temperature-dependent phase stability*" Appl Phys Let **92** (2008) pp. 261911

[4] Junkermeier CE and Lewis JP *Amorphous nature of small CdS nanoparticles: Molecular dynamics simulations.* Phys Rev B **79** (2009) pp. 125323

[5] Herron N, Wang Y, and Eckert H "*Synthesis and Characterization of Surface-Capped, Size-Quantized CdS Clusters, Chemical Control of Cluster Size*" J Am Chem Soc **112** (1990) pp. 1322-1326

[6] Vorokh AS, Kozhevnikova NS, and Rempel AA *"Transition of the CdS Disorder Structure to the Wurtzite Structure with an Increase in the Nanoparticle Size".* Bull Russ Academy of Sci : Physics **72** (2008) pp. 1395-1398

[7] Car R and Parrinello M "*Unified Approach for Molecular Dynamics and Density-Functional"* Theory Phys Rev Lett **55** (1985) pp. 2471-2474

[8] CPMD, http://www.cpmd.org/, Copyright IBM Corp 1990-2008. Copyright MPI für Festkörperforschung Stuttgart 1997-2001.

GCMC prediction of hydrogen storage in Li-doped carbon nanotube arrays

Simone Mirabella[1], Massimo Celino[2] and Giuseppe Zollo[1]

[1]*Dipartimento di Scienze di Base e Applicate per l'Ingegneria,*
Università di Roma "La Sapienza", via A. Scarpa 14-16, Rome, Italy
[2]*ENEA, C. R. Casaccia, via Anguillarese 301, 00123 Rome, Italy*
massimo.celino@enea.it; giuseppe.zollo@uniroma1.it

Abstract

The recent discovery of the enhanced hydrogen adsorption in Li doped single walled carbon nanotubes is revised. The adsorption isotherms have been calculated by means of grand canonical monte carlo simulations using accurate parameters obtained by fitting ab-initio data. In the pressure range explored and for the tube bundles geometry chosen it is shown that, contrarily to recent analogous studies, the adsorption is still below the target fixed by the United States Department of Energy.

Introduction

Single Walled Carbon Nano-Tubes (SWCNTs) and Multi-Walled Carbon Nano-Tubes (MWCNTs) have been considered as ideal candidates for hydrogen storage in the light of some experimental results, dating back to the end of the '90s [1], that supported this idea. In particular it was stated that carbon based adsorbing media could have easily fulfilled the target indicated by the Department of Energy (DOE) of the United States of 6.5 wt % by 2010 and 9 wt % by 2015 of hydrogen content as the minimum extractable loading for addressing the commercial storage needs.

Since then, many theoretical and experimental articles appeared with controversial results providing a large spread of experimental data on CNTs. In recent review papers [2-4] this controversy has been discussed evidencing a clear convergence to much more modest results, still far below the DOE requirements.

Theoretical predictions of the hydrogen storage in CNTs have been attemped with different approaches such as classical models [5-8], quantum mechanics [9-11] and hybrid models [12] supporting recent, more accurate, experiments and evidencing that the reason of the poor uptake performance of CNTs is tightly related to the physical limits affecting the molecular hydrogen interaction with bare carbon based adsorbing media. It has been reported by several authors on both theoretical and experimental basis that doping of CNT with metal species such as Li [13-16], Pt [17], Pd [18] or Ti [19] can greatly affect the adsorption.

In particular the Li doped CNTs case is considered particularly promising due to some experimental studies reporting significant uptake data [14] and also because it has been reported that transition metals, such as Ti, tend to form metallic aggregates that may limit the uptake.

In Ref. [16] Grand-Canonical Monte Carlo (GCMC) simulations have been performed, with Lennard-Jones (LJ) interaction potentials between the species involved, showing that Li doping can increase significantly the hydrogen storage if appropriate doping schemes and SWCNTs array geometry are adopted. However the LJ parameters used were not derived explicitly for the system under study and it is not clear how a better definition of such parameters can affect the conclusions drawn.

Moreover it should be considered that Li doping can induce also hydrogen chemisorption and therefore it is not clear how chemisorbed atomic hydrogen can affect the molecular hydrogen physisorption.

Therefore, in this article we report on GCMC calculations, using ab-initio derived LJ potential parameters, of the hydrogen adsorption isotherms in Li doped SWCNTs arrays.

Computational details

GCMC simulations have been performed at different pressure values taking into consideration the relationship between the hydrogen chemical potential and the gas pressure via the hydrogen fugacity considered explicitly for the whole pressure range explored. The energy of the system is quantified by computing the LJ potential. LJ is usually employed to approximate the interaction between pairs of neutral atoms or molecules.

$$E = 4\epsilon \quad \frac{\sigma}{r}^{12} - \frac{\sigma}{r}^{6}$$

ε is the depth of the potential well; σ is the finite distance at which the inter-particle potential is zero; r is the distance between the particles. The r^{-12} term, which is the repulsive term, describes Pauli repulsion at short ranges due to overlapping electron orbitals and the r^{-6} term, which is the attractive long-range term, describes attraction at long ranges (van der Waals force, or dispersion force).

The LJ potentials for the gas-gas and the carbon-gas interactions have been defined using LJ parameters derived recently on the basis of accurate adsorption measurements at cryogenic temperatures and making use of the Lorentz-Berthelot rules for the C-H_2 interactions [20]. The C-H_2 interaction has been treated explicitly for each carbon nanotube having at least one carbon atom within a certain "cutoff" distance (here considered 0.7 nm) from the hydrogen molecule; for each SWCNT entirely outside the cutoff distance from H_2, we have considered the interaction with the entire tube using the Stan & Cole formula [21] because at large distance the atomistic granularity of the tube has little effect. Similarly to C-H_2, also the interaction H-H_2, between the chemisorbed hydrogen atom and an hydrogen molecule, and the interaction Li-H_2, between the Li doping atom and the molecular hydrogen, have been treated using an LJ potential with new parameters that have been derived by fitting with a LJ potential the total energy of the system, obtained by ab-initio calculations, with the hydrogen molecule placed at various distances from the decorated site.

All the ab-initio calculations have been performed employing the CPMD (Car-Parrinello Molecular Dynamics) code [22] based on Density Functional Theory (DFT) and plane wave basis pseudopotential method [23,24]. The exchange-correlation functional has been approximated in the framework of Generalized Gradient Approximation (GGA) [25] using the Becke-Lee-Yang-Parr (BLYP) functional [26,27]. The electronic wave functions are expanded in a plane-wave basis set with a kinetic energy cut-off equal to 85 Ry. The latter value was optimized by preliminary calculations on simple molecules, on the diamond crystalline structure of carbon and on the nanotube nanostructure. A supercell of 25 Å has been found sufficient to minimize the interaction among the images in the periodic boundary conditions used by CPMD code. A semi-empirical correction of the total energy for the long range dispersion forces and energy [28] has been used in all the total energy ab-initio calculations concerning the physisorption configurations on an hydrogen molecule at the (10,10) SWCNT, either bare of functionalized with H or Li atoms.

The adsorption simulations have been performed taking into account two systems: one and three (10,10) armchair SWCNTs organised in triangular symmetry. The supercells have been constructed with large void regions around the SWCNT in order to make accessible the surface adsorption sites without artifacts. Indeed also the GCMC simulations have been performed in the frame of periodic boundary conditions by using the minimum distance image convention.

Results and discussion

One of the main problems affecting GCMC predictions of hydrogen storage in doped CNTs is the usage of reliable classical potentials for the impurity atoms. We have chosen to maintain the LJ functional form of the inter-atomic potential for any kind of interacting atoms involved in the system. Therefore we have re-calculated, in the frame of accurate GGA DFT total energy calculations, the LJ parameters for the H_c-H_2 (H_c is the chemisorbed atomic H) and the Li_c-H_2 (Li_c is the chemisorbed atomic Li) have been fitted to the total energy of the system.
For the H_c-H_2 case we have first optimized the configuration of a hydrogen atom covalently bonded to a carbon atom on the exterior surface of the tube; then we have placed a hydrogen molecule, with three possible orientations with respect to the tube axis, at different distances from the chemisorbed hydrogen atom along the direction orthogonal to the tube axis (see *figure1*). The same total energy curve has been produced also without the hydrogen atom chemisorbed on the tube wall and the total energy difference

$$\Delta E_{H_c-H_2} = E\ \ SWCNT{:}\,H_c - H_2\ \ - E(SWCNT - H_2)$$

has been fitted with a LJ functional form.
The same procedure has been used to obtain the LJ parameters for the Li_c-H_2 interaction:

$$\Delta E_{Li_c-H_2} = E\ \ SWCNT{:}\,Li_c - H_2\ \ - E(SWCNT - H_2)$$

The fitting procedure to get the LJ parameters ε and σ has been performed on the energy curve that is obtained by averaging those obtained with the three orientations of the hydrogen molecule.

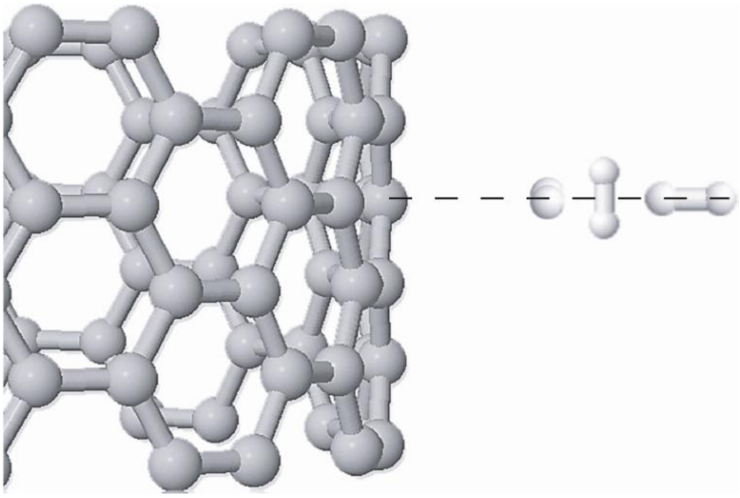

Figure 1: *Schematic drawing of the three orientation of the hydrogne molecule with respect to the SWCNT side-wall.*

The hydrogen gravimetric capacity of one and three SWCNTs decorated with Li impurities have been calculated for different values of pressures and different Li coverages. The Li atoms have been placed at the above described equilibrium "top" position above a carbon atom and distributed randomly throughout the exterior area of the tubes.

The Li coverage of the samples has been considered in the whole range between 0 and 100% of the "top" positions available and thus a significant fraction of un-active Li atoms may be located in the interstitial space in the case of the triangular arrangement of the CNTs bundle. An example of atomic configuration composed by three SWCNTs decorated with 20% of Li atoms is shown in *figure 2*.

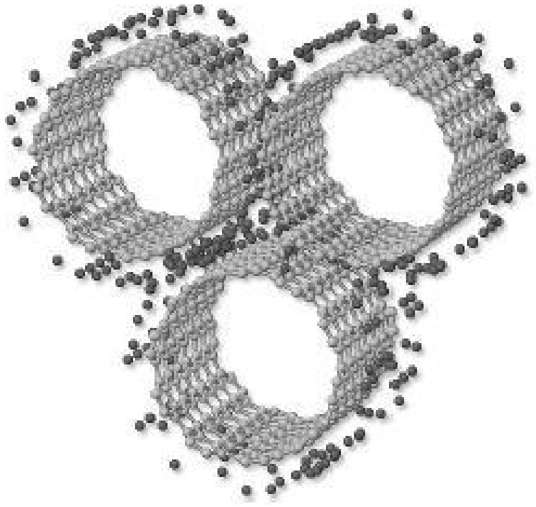

Figure 2: *Three SWCNTs decorated with Li atoms chemisorbed on the surfaces.*

Then hydrogen molecules are added randomly to the system to fill the simulation cell. Hydrogen molecules are placed taking into account the density of the gas phase. Then, GCMC simulations have been performed to compute the adsorption of the hydrogen molecules taking into account the interactions potentials previously determined by ab-initio calculations. For all the cases studied at various values of temperature and Li/C content, the hydrogen uptake is at least doubled in Li decorated CNTs with respect to hydrogenated ones at 100 K; at 300 K the uptake performance is greatly enhanced by at least six times making clear that the positive role of Li impurities can be appreciated more at larger temperature values.

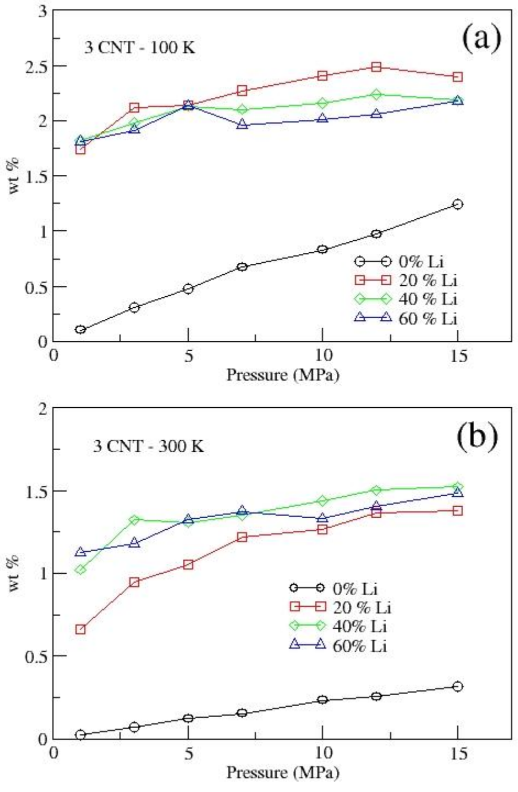

Figure 3: *Gravimetric percentage of physisorbed H_2 for the system composed by an array of three SWCNTs decorated with Li atoms versus external pressure. (a) T= 100 K, (b) T= 300 K.*

In *figure 3* is reported the gravimetric percentage of physisorbed H_2 on the system composed by an array of three SWCNTs decorated with Li atoms versus the external pressure. The isotherms at 100 K show various aspects that are worth to be remarked: decoration of CNTs with Li atoms enhances significantly the hydrogen storage with respect to the bare CNT bundle, especially in the lower range of pressure values (between 1 and 7 MPa); moreover, the curves do not show any marked difference between the hydrogen uptake for the three coverage values sampled when the pressure is below 5 MPa. Surprisingly, as the Li content increases above 20%, the hydrogen uptake performances at 100 K deteriorate markedly so that, for instance, in bundles with 60% of Li coverage, the H_2 adsorption excess is about 20% lower than the same quantity calculated in a bundle with only 20% of Li coverage in the pressure range 10-12 MPa. Of course this behavior reflects the heavier weight of the adsorbing media that lowers the gravimetric storage by increasing the denominator of this quantity. Thus the positive role played by Li impurities to improve the hydrogen uptake has a limit in making the adsorbing medium heavier. Moreover it is evident that in Li functionalized CNT bundles, the uptake increase with the pressure scales less steeply with respect to the case of pristine CNTs, with a decreasing slope as the Li coverage increases. As mentioned before, a part of Li atoms is un-active being located at the interstitial volume between the tubes; nevertheless the amount of Li impurities at "active" adsorption sites, i.e. groove or outer surface sites, scales as the ratio of the nominal Li content and therefore the behavior shown is not affected by the presence of un-active Li atoms. This behavior is clearly exposed in *figure 4* where the gravimetric percentage of physisorbed H_2 of both isolated and array of SWCNTs are compared. The isolated SWCNT is able to adsorb in percentage more hydrogen molecules than the other system.

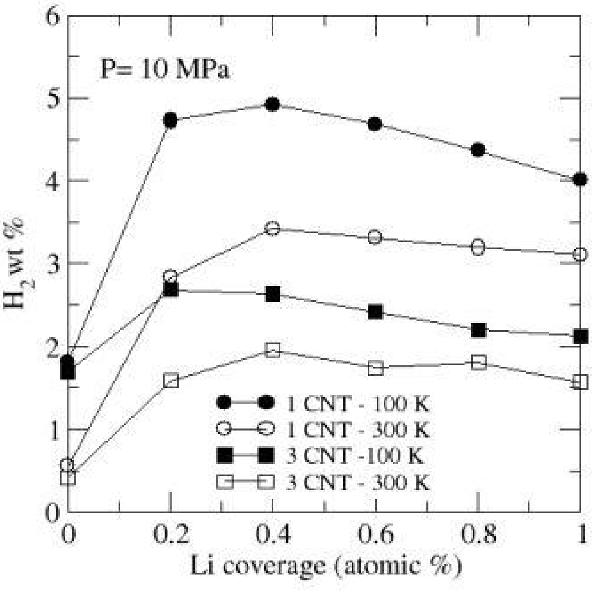

Figure 4: *Gravimetric percentage of physisorbed H_2 on isolated and array of three SWCNTs decorated with Li atoms at different coverage ratios and P=10 MPa.*

Thus in the Li decorated samples the uptake curve reaches a maximum value in the range between 20% and 40% of Li content while for larger values the gravimetric hydrogen excess decreases due to the heavier weight of the adsorbent medium. The coverage curves at P= 10 MPa evidence that the hydrogen storage value degrades with the Li content more markedly at 100 K rather than at room temperature showing that the maximum storage value of nearly 5 wt% is obtained in isolated SWCNTs at T= 100 K with Li coverage of 40%.

Conclusions

As concluding remarks we have calculated the hydrogen gravimetric storage excess in hydrogenated and Li decorated SWCNTs, both isolated and in arrays of three CNTs. The calculations have been performed joining accurate DFT simulations, aimed to obtain the hydrogen physisorption binding energies in the vicinity of Li or atomic hydrogen impurities, and GCMC simulations to calculate both the hydrogen storage and the isotherms at different values of temperature, pressure and impurities content. The calculations for the largest sample containing three tubes arranged in a triangular structure have been performed using a hybrid model including a collective interaction between the tubes and the hydrogen molecules in case they are enough far away. Calculations show that Li decoration greatly enhances the hydrogen uptake that remains, however, below the targets indicated for commercial use of hydrogen storage media.

Acknowledgments

Computational resources have been provided by ENEA under the ENEA-GRID CRESCO project. We warmly acknowledge ENEA and its HPC staff for contributing to the present article.

References

[1] A. C. Dillon, K. M. Jones, T. A. Bekkedahl, C. H. Kiang, D. S. Bethune and M. J. Heben, Nature **386**, 377 (1997).

[2] G. E. Ioannatos and X. E. Verykios, International Journal of Hydrogen Energy **35**, 622 (2010).

[3] K. L. Lim, H. Kazemian, Z. Yaakob, W. Daud and W. R., Chem. Eng. & Tech. **33**, 213226 (2010).

[4] C. Liu, Y. Chen, C. Z. Wu, S. T. Xu and H. Cheng, Carbon **48**, 452 (2010).

[5] F. Darkrim and D. Levesque, J. Chem. Phys. **109** (1998).

[6] Y. Ma, Y. Xia, M. Zhao, W. R. and L. Me, Phys. Rev. B **63**, 11542211542. (2001).

[7] G. Stan, M. J. Bojan, S. Curtarolo, S. M. Gatica and M. W. Cole, Phys. Rev. B **62**, 2173 (2000).

[8] Q. Wang and J. K. Johnson, J. of Chem. Phys. **110**, 577 (1999).

[9] J. S. Arellano, L. M. Molina, A. Rubio, M. Lopez and J. A. Alonso, IEEE Transactions on Nanotechnology **3**, 304-310 (2004).

[10] C. Bauschlicher and C. So, Nanoletters **2**, 337 (2002).

[11] S. Lee and Y. Lee, App. Phys. Lett. **76**, 2877 (2000).

[12] X. Zhang, D. Cao and J. Chen, J. of Phys. Chem. B **107**, 4942-4950 (2003).

[13] S. K. Bhatia and A. L. Myers, Langmuir **22**, 1688 (2006).

[14] P. Chen, X. Wu, J. Lin, and K. L. Tan, Science **285**, 91 (1999).

[15] L. Chen, Y. Zhang, N. Koratkar, P. Jena and S. K. Nayak, Phys. Rev. B **77**, 033405 (2008).

[16] J. Cheng, X. Yuan, X. Fang, and L. Zhang, Carbon **48**, 567 (2010).

[17] C. Yeung, V. L. Lei, J. of Phys. Chem. C **112**, 7401 (2008).

[18] H. Xiao, S. Li, and J. Cao, Chem. Phys. Lett. **483**, 111-114 (2009).

[19] T. Yildirim and S. Ciraci, Phys. Rev. Lett. **94**, 175501 (2005).

[20] T. X. Nguyen, J. S. Bae, Y. Wang, and S. K. Bhatia, Langmuir **25**, 4314 (2009).

[21] G. Stan and M. W. Cole, Surf. Sc. **395**, 280291 (1998).

[22] CPMD, http://www.cpmd.org/, Copyright IBM Corp 1990-2008, Copyright MPI fur Festkorperforschung Stuttgart 1997-2001.

[23] P. Hohenberg and W. Kohn, Physi. Rev. **136**, B864-B871 (1964).

[24] W. Kohn and L. J. Sham, Physical Review **140**, A1133-A1138 (1965).

[25] A. Becke, Phys. Rev. A **38**, 3098 (1988).

[26] C. Lee, W. Yang, and R. G. Parr, Phys. Rev. B **37**, 785 (1988).

[27] S. Goedecker, M. Teter, and J. Hutter, Phys. Rev. B **54**, 1703 (1996).

[28] S. Grimme, J. Comput. Chem. **27**, 1787 (2006).

High resolution wave energy resources assessment along the Italian coasts

G. Sannino[1], L. Liberti[2], A. Crillo[1]

(1) ENEA –UTMEA-CLIM, via Anguillarese 301, 00123 Rome, Italy
(2) ISPRA, via Vitaliano Brancati 48, 00144 Rome, Italy

1.Introduction

Wave energy appears to be one of the most promising among the renewable resources. It is estimated that it will undergo a significant growth in the next decades as soon as the Wave Energy Converters (WECs) technology becomes more mature [1]. Feasibility studies of wave energy plants require a detailed knowledge of energy occurrence, of its temporal and spatial variability and of its distribution among different sea states. At present, an extensive and accurate estimation of wave energy for the Italian seas is not yet available. Wave energy atlases rely on wave measurement obtained by buoys, satellite and output from model hindcasts. In recent years, several authors presented global wave energy atlases, see for example [2], [3], [4] and [5]. However, these atlases lack the spatial resolution required to identify suitable locations for wave energy production with reasonable spatial accuracy, especially in relatively small basins like the Mediterranean. Moreover these works were not explicitly devoted to wave energy potential evaluation and do not directly provide wave energy data. Currently a high-resolution study of wave energy distribution in the Mediterranean appears to be lacking. Filling this gap is the main purpose of the present work.

2.Model description and validation

Wave simulations were performed using a parallel version of the WAM wave model Cycle 4.5.3 [6]. The model domain covers the entire Mediterranean Sea at a uniform resolution of 1/16° (667x251 nodes in spherical coordinates), corresponding to a linear mesh size of 5-7 km. By extending the computational domain over the entire Mediterranean, we were able to describe the wave climate along the Italian coast at relatively high spatial resolution taking into account both local wave generation and propagation from distant areas, avoiding errors introduced by nesting procedures. Model bathymetry was calculated from the General Bathymetric Chart of the Oceans (GEBCO) 30 arc-second gridded data set [7]. The model was forced with six-hourly wind fields obtained from ECMWF operational analysis (www.ecmwf.int) at ¼° spatial resolution. *Figure 1* shows computational domain and model

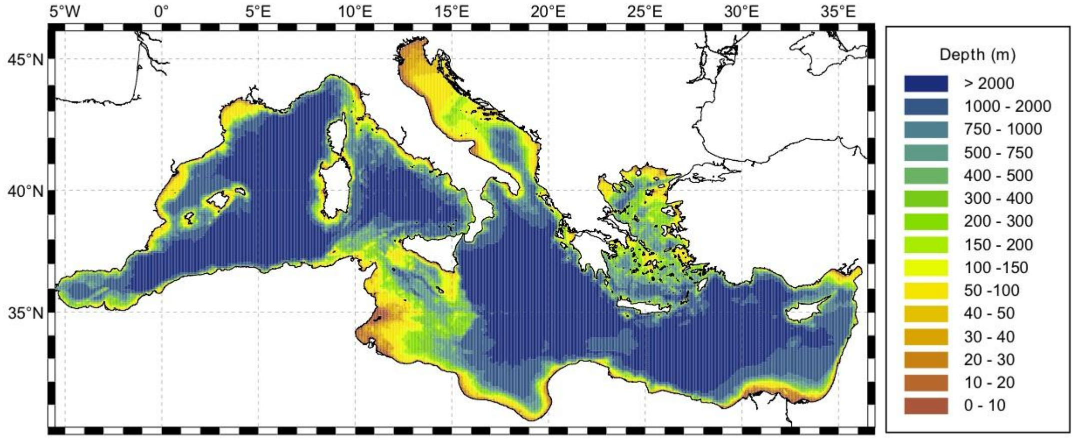

Figure 1: *Model computational domain and bathymetry.*

bathymetry. Wave climate simulations were performed for the period 2001-2010.
Model results were positively validated against satellite and buoy measurements. An extensive validation of the model has been recently carried out by [8].

3.Model Results and Discussion

Following [9], in deep water, the available energy flux per unit crest can be expressed as:

$$J = \frac{\rho g^2}{64\pi} T_e H_s^2 \tag{1}$$

where *J* is the energy flux in Watt per meter of wave crest, *g* is the gravity acceleration, *r* the sea water density assumed to be 1025 kg/m^3, *Hs* the significant wave height and *Te* the wave significant period. *Te* represents the period of a sinusoidal wave having the same energy content of the sea state [10].

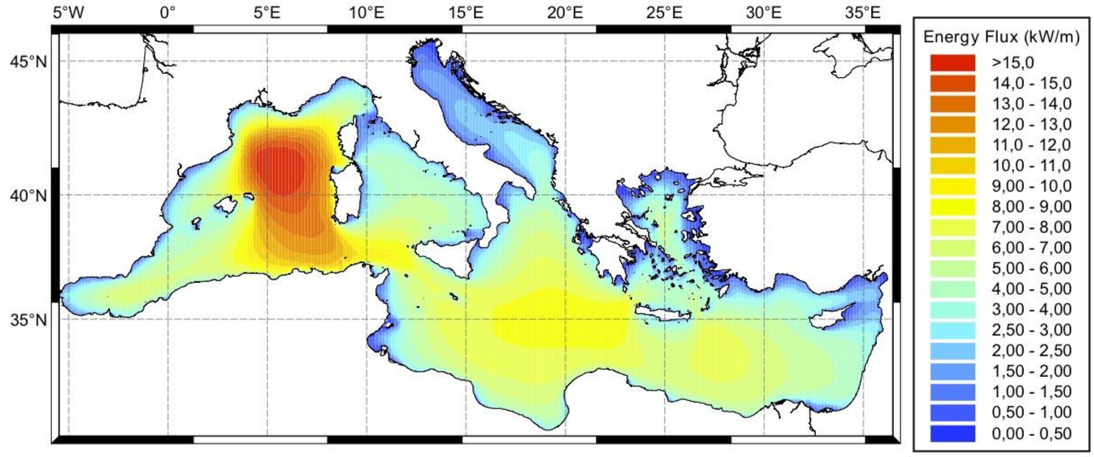

Figure 2: *Distribution of average power per unit crest in the Mediterranean between 2001 and 2010.*

Figure 2 shows a map of the available wave power flux per unit crest averaged over the entire 10 years simulation period in the Mediterranean. The most productive area, showing average values above 12 kW/m, is located in the western Mediterranean between the Balearic Islands and the western coast of Sardinia. Wave power in this area is most easily accessible from the coasts of Sardinia, Balearic Islands and north Africa. The neighboring region located in the Sicily channel, off the north-western and southern Sicilian coasts, is also very productive with an average wave energy flux per unit crest that reaches 9 kW/m. Slightly lower wave power appears to be available in central Mediterranean and southern Ionian Sea with average values not exceeding 8 kW/m near the coast. The Adriatic sea, where average wave power does not exceed 3 kW/m, is one of the least productive regions. Similar values are observed in the most sheltered parts of the Ionian and Tyrrhenian between the mainland and Corsica and near the Messina Strait.

A more detailed overview of the wave power distribution along the western Sardinia and western Sicily coasts is shown in *figures 3* and *4* where the average wave power per unit crest for the entire simulated period is calculated along a line placed approximately 12 km offshore. Along western Sardinia the average power ranges from 7.5 to almost 12 kW/m. The highest values are observed on the northern and southern sections of the coast, between Alghero and Asinara Island and near San Pietro Island; along the intermediate section of the coast lower values between 8.5 and 10 kW/m are found.

Around the northern and southern limit of the western Sardinia coastline average wave power drops sharply as soon as the exposure to the waves coming from W and NW declines.

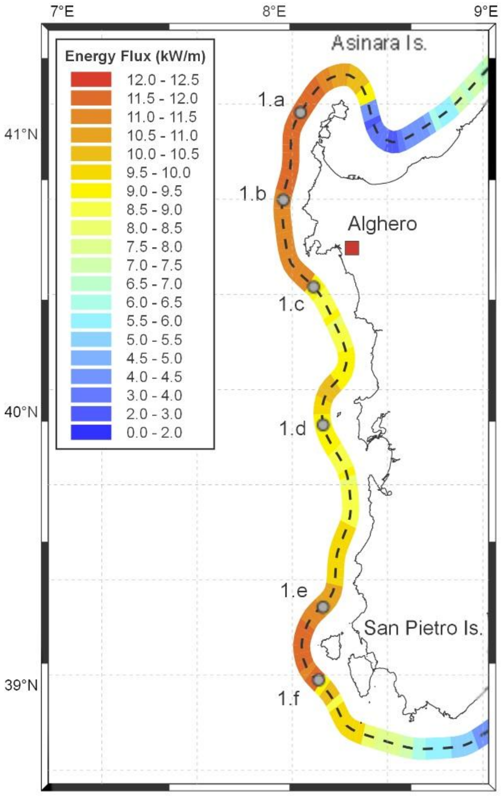

Figure 3: *Distribution of average wave power flux per unit crest on western Sardinia coastline. Values are calculated on a line located 12 km off the coast. Dotted grid lines are 50 km apart. Wave climate at marked locations is described in Figure 5.*

The north-western and southern coasts of Sicily have a lower potential with average wave power ranging between 2.5 and 6.5 kW/m. On the northern coast west of Palermo average wave power flux is between 4 and 5 kW/m gradually increasing to values between 5 and 6 kW/m between San Vito Lo Capo and Trapani. The most productive area is located along the coastal stretch that lies north of Mazara del Vallo where average power is above 6 kW/m reaching values around 7 kW/m near Favignana Island. The rest of the southern coast is the least productive with average power flux below 4.5 and as low as 2.5 kW/m. The only exception is the area between Punta Secca and Capo Passero where values are almost everywhere near 5 kW/m. Similarly to what was previously observed on the Sardinia coast there is a sharp decline in average power east of Palermo and north of Capo Passero. *Figures 3* and *4* show that average wave power exhibits a non-negligible spatial variability even at spatial scales of the order of 20 km. For instance, the average wave power just a few kilometres south of Alghero decreases almost 20%.

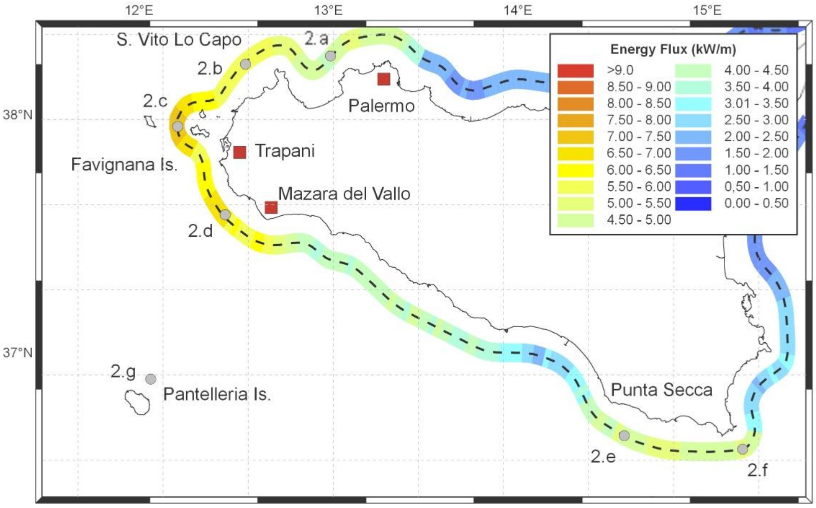

Figure 4: *Same as 3 but on western north-western and southern Sicily coastline.*

The average power is a useful parameter to identify promising areas for wave energy production; however, its values arise from the contribution of individual sea states distributed over a range of wave heights, periods and directions.

From an engineering point of view, since the WECs effectively operate on specific ranges of wave heights and periods, the feasibility study for wave energy production should be carried out considering the most representative sea states in terms of energy production.

In *figure 5* is provided an overview of the spatial variability of the distribution of wave power among heights, periods and directions at selected locations along western Sardinia.

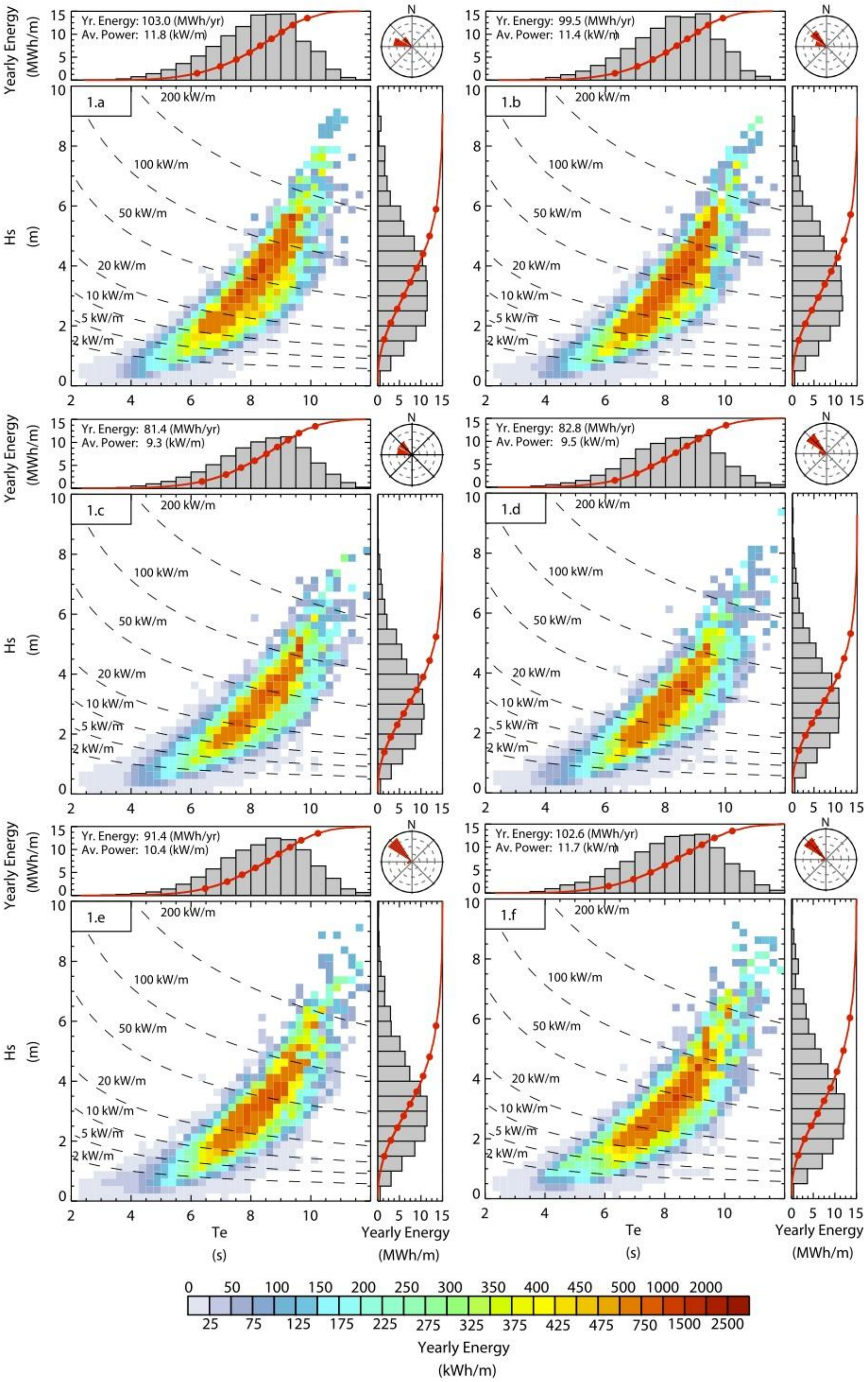

Figure 5: *Distribution of wave energy as a function of significant wave period and significant wave height at points located along the western coast of Sardinia (see figure 3 points 1.a to 1.f). The lower left panel of each figure shows the average yearly energy associated with sea states identified by Te and Hs couples. Dotted lines mark reference power levels. Upper panel shows the energy distribution as a function of Te only; right panel as a function of Hs only. Red lines in the upper and right panels are the cumulative energy as a percentage of the total. Red dots on the cumulative lines marck each 10th percentile. Rose plot in the upper right panel shows energy distribution over wave incoming direction. Each circle represents 20% fractions of the total energy.*

In the lower left panel of the figure, the scatter plot represents the distribution of yearly average energy in terms of *Te* and *Hs*, evaluated over the 10 years simulated period. Contribution to the total energy given by individual sea states are lumped together in 0.25 s intervals of *Te* and 0.25 m intervals of *Hs*.

Wave power contributions of individual 3-hour sea states obtained from the model output are calculated using equation 1. Lines of constant power are drawn on the scatter plots to highlight wave power variability. On the upper and right panels of each scatter plot two histograms represent the distribution of average yearly wave energy over *Te* and *Hs* respectively. The intervals used in the histograms are twice the size of the intervals used in the scatter plot for better graphic representation.

In each histogram a red line represents the cumulated percentage of total energy available in terms of *Te* and *Hs*. Red markers are placed every 10*th* percentile on the cumulated line. In the upper-right panel a rose diagram describes the directional distribution of average yearly energy over 30° wide direction bins. Each concentric circle represents 20% contribution to the total wave energy. The plots in *figure 5* refer to points located along western Sardinia coast (see *figure 3*).

Sea states with significant wave heights between 2 to 4 m and significant periods between 8 and 10 s appear to carry a considerable amount of the total energy, both around 40%. There are however some notable differences between the various locations. Points 1.a and 1.b, located in the northern section of the coastline, only 50 km away, have similar values of average power flux and its distributions among *Te* and *Hs* are also nearly the same, however the directional distribution appears to be quite different with dominant directions shifted almost 45 degrees apart. In this two locations the amount of power provided by the most extreme sea states, with *Hs* above 4 m, is around 40% of the total, while in the remaining locations this contribution reduces to about 30%. This is observed for points 1.c and 1.d, which are far less energetic than point 1.a and 1.b, but also for points 1.e and 1.f which share the same power levels of the first two points. Similarly, points 1.c and 1.d have the same energy content but different directional distributions.

As a final remark we observe that while the overall profitability of a given site could be evaluated in terms of the average energy production, taking into account its distribution over wave heights, periods and directions, the inter-annual fluctuations define the variability of the expected yearly revenues. In order to estimate the magnitude of the inter-annual fluctuation we take into account the Coefficient of Variation *COV* which was proposed by [4] as a measure of wave power temporal variability. *COV* is defined as:

$$COV = \frac{\sigma}{\mu}$$

where σ and μ are defined in our analysis as the average and the standard deviation of the yearly mean wave power flux respectively. *COV* measures the variability of the observations with respect to their average value.

Figure 6 shows the spatial distribution of the *COV*. Average inter-annual fluctuations of average power flux above 20% of the overall average, corresponding to *COV* > 0.2 are commonly observed around the Italian peninsula. It appears that the fluctuation range is higher in sheltered areas. The highest *COV* values are observed in the southern Tyrrhenian where it exceeds 0.4, in parts of the Ionian, and in the region between the mainland and Corsica where it reaches values above 0.3. Along the western coast of Sardinia and along the north-western and southern coast of Sicily the inter-annual fluctuations are milder with *COV* < 0.25.

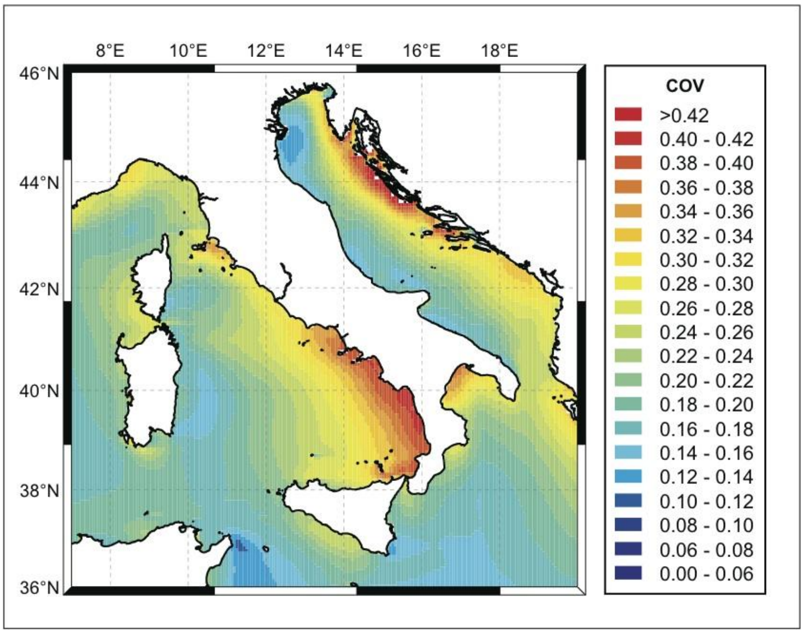

Figure 6: Distribution of the Coefficient of Variation (COV) of the yearly average power fluxes for years 2001-2010 around Italy.

To conclude, the results of the present analysis confirm that western Sardinia and southern and western Sicily are the most promising areas along the Italian coast for wave energy production also in terms of inter-annual variability.

References

[1] Association EOE. Oceans of energy European Ocean Energy Roadmap 2010-2050. Tech. Rep.; European Ocean Energy Association; 2010.

[2] M. CA. A global wave energy resource assessment. In: Proceedings of the Eighteenth Eighteenth International Offshore and Polar Engineering Conference, Vancouver, BC, Canada. 2008.

[3] Barstow S, Mørk G, Lønseth L, Mathisen JP. Worldwaves wave energy resource assessments from the deep ocean to the coast. In: Proceedings of the 8th European Wave and Tidal Energy Conference, Uppsala,Sweden. 2009.

[4] Mørk G, Barstow S, Kabuth A, Pontes MT. Assessing the global wave energy potential. In: Proceedings of the 29th International Conference on Ocean, Offshore Mechanics and Arctic Engineering. 2010.

[5] Arinaga RA, Cheung KF. Atlas of global wave energy from 10 years of reanalysis and hindcast data. Renewable Energy 2012;39(1):49–64. doi:10.1016/j.renene.2011.06.039.

[6] Gunther H, Behrens A. The wam model validation document version 4.5.3. Tech. Rep.; Institute of Coastal Research Helmholtz-Zentrum Geesthacht (HZG); 2011.

[7] GEBCO. http://www.gebco.net/data and products/gridded bathymetry data/, 2010.

[8] Liberti L., A. Carillo, G. Sannino. Wave energy resource assessment in the Mediterranean, the Italian perspective. Submitted Ren. Energy

[9] Waters R, Engstrom J, Isberg J, Leijon M. Wave climate off the Swedish west coast. Renewable Energy 2009; 34(6):1600 –6.

[10] Iglesias G, Carballo R. Wave energy resource in the Estaca de Bares area (Spain). Renewable Energy 2010;35(7):1574 –84. doi:10.1016/j.renene.2009.10.019. Special Section: IST National Conference 2009.

FLUKA SIMULATIONS FOR THE TOP-IMPLART BEAM MONITORING SYSTEM

E. Basile[1], A. Carloni[1], D. M. Castelluccio[2], E. Cisbani[1], S. Frullani[1]

[1]*Istituto Superiore di Sanità – Roma*
[2]*ENEA – Istituto di Radioprotezione - Bologna*
Corresponding author: emilia.basile@iss.infn.it

Abstract

This paper follows that produced for the 2009/2010 period of utilization of the ENEA GRID CRESCO system **[1]**, when the infrastructure was used to perform simulations in order to place the basis for the development of a fast Treatment Plan System (TPS) for proton therapy in the context of the TOP-IMPLART **[2]**, a joint project between ENEA, ISS and IFO.

In the 2010/2011 period the CRESCO system has been used for conducting simulations with the FLUKA code **[3]** **[4]** in order to develop the beam monitor system of the TOP-IMPLART accelerator and to optimize its characteristics. The work aimed at verifying that the presence of the chamber between the beam line and the patient would not alter noticeably the dose delivery. In the future these two research lines could be unified in an accelerator advanced control system.

Introduction

The ENEA GRID CRESCO resources have been used for research in the TOP-IMPLART project context **[2]**. The project aims to realize an innovative proton therapy facility, which features a LINAC as accelerating device. Out of all advantages in the use of a LINAC there are no emissions of synchrotron radiation, modularity of implementation and possibility to operate at any duty factor with high repetition rate and pulse current modulation. Moreover the system is designed to actively modulate the beam energy (up to 250 MeV), so the therapeutic beam can be employed in a fully active 3D+1 scanning mode, that is beam transverse position (X/Y), energy (depth Z), and pulse intensity (instantaneous released dose) are actively varied on a pulse-to-pulse basis. This active scanning produces a highly conformal dose distribution and then it requires, during each treatment, a very reliable and precise on-line beam monitoring system so as to determine point-wise the dose delivered to the patient, allowing eventually the system to shutdown promptly when divergences from the TPS calculated dose occur.

TOP-IMPLART beam monitoring system.

The beam monitor system has to accurately measure beam position, direction and intensity profile at each pulse. The system specifications are defined on the TOP-IMPLART beam characteristics basis: the monitor system should have rapid response (< 1 msec) and wide dynamic range (10^4 at least) with good sensitivity (about 100 fC), in order to detect the accelerator beam current, which is delivered with a 1-3,5 μs long pulse at a repetition frequency of 10-100 Hz, and which can be actively varied over three magnitude orders, from 0.1 μA to 10 μA (average intensity up to 3.5 nA), as requested by clinical applications. Moreover the monitor system should have good spatial resolution (about 1/10 mm) and it should be light and compact in order to perturb as little as possible the primary beam.

The developed monitoring detector **[5]** is based on Pad-Strip ionization chambers with an active area of about 7x7 cm^2 (in the final version an active area of at least 10x10cm^2 is foreseen) and a gas gap of few millimeters, where a mixture of inert gas (N or Ar and CO_2) is continuously flushed. The chamber has an inlet window of Mylar (15μm thick) and aluminum (5μm), which acts as cathode while the anode has been realized with a (50μm) kapton support holding a pattern of (15μm) square gold plated copper pads facing the inner volume, and a series of parallel 15μm thick strips placed on the opposite side of it. Inner pads are alternatively connected to the strips on the external side of the anode readout foil via microscopic connectors so as to ensure the collection of the charges in one direction while the other pads are connected altogether, ensuring the charge collection orthogonally to the previous ones (see *figure 1*).

Figure 1. *Microscopy picture of the anode layout;*
on the left:(pad side), on the right: back (strip side).

The anode readout foil has been produced at TS-DEM, CERN, obtaining a pad map with a pitch of 875 μm while the gap between each pad is 0.12 mm, ensuring therefore a quasi-homogeneity of the readout foil material. With the above mentioned features the plane spatial resolution has an accuracy better than 0.2 mm. Calculated chamber Water Equivalent Tissue (WET) is less than 0.18 mm. The total number of channels is 80 on each axis. These channels are read by dedicated autoranging electronics, which dynamically adapt the capacitance to the incoming charge in order to attain a wide dynamic range **[6]**. The electronics are conceived to control various channels cascading several backplanes. In this way modifications to the total number of channels can be achieved without substantial changes in the system architecture.

In order to develop and optimize the beam monitor prototype characteristics, several simulations have been carried out **[7]** **[8]**.

Simulations

The need of a highly conformal dose delivery in proton therapy requires an accurate monitoring of the beam parameters on a pulse by pulse basis. In this context, the FLUKA code **[3]** **[4]**, has been used with the aim of observing, for two different chamber settings, not only the energy loss of the beam within the detector (see *figure 2*) and the amount of secondary particles produced, but even the transversal and longitudinal beam spread variation due to the interposition of the detector in the beam line.

This variation is obtained by comparing the deposited energy in water phantoms with and without the interposition of the chamber between the beam source and the target (a simplified phantom patient, represented by a water cylinder) at several energies ranging from 18 to 230MeV with Gaussian-like shaped beams of FWHMs ranging between 0.2-1 cm.

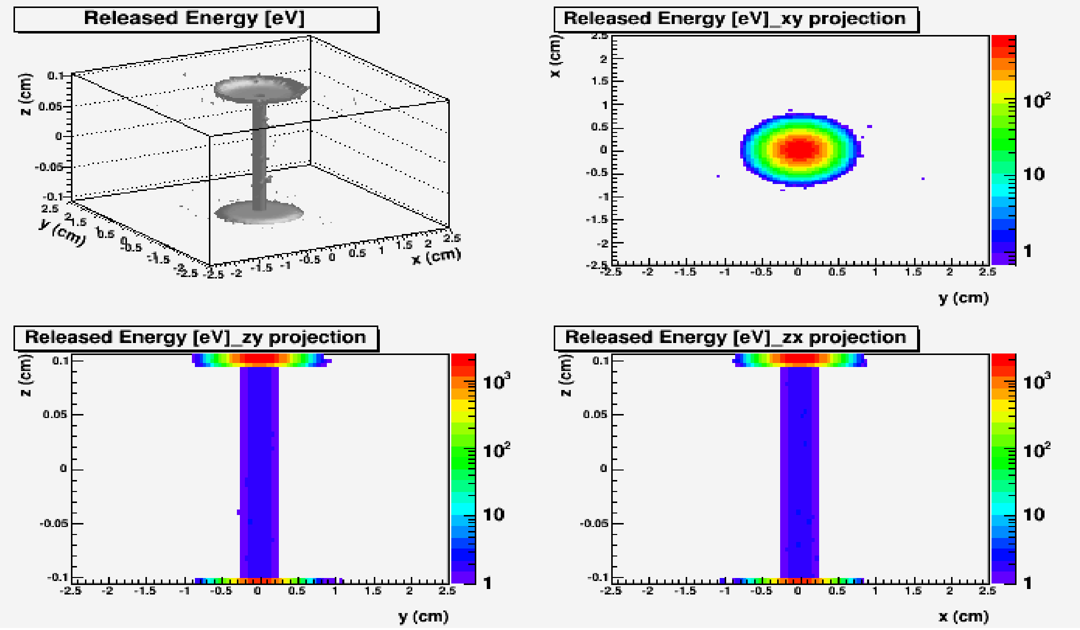

Figure 2. *Example of energy loss within the chamber and on its entrance window and exit readout foil.*

The results of the simulations have been therefore analyzed so as to characterize the induced effects and eventually improve the design of the chamber. The two above mentioned different configurations of the detector are: a so called "standard detector" and a "final detector", the latter one reflecting, under any aspect, the prototype under development while, the standard prototype representing a more conventional ionization chamber. The standard chamber features copper pads and strips which are 25µm thick while in the final chamber, the pads and strips are 15µm thick.

The FLUKA Monte Carlo code implementation of these detectors has been developed using the combinatorial geometry features in which the Boolean operations of union, intersection and subtraction are employed. Each solid in this context, is built by assembling different planes and solids: for example, a simple anodic pad is a complex intersection system of several planes, while each strip is a parallelepiped as shown in *figure 3*.

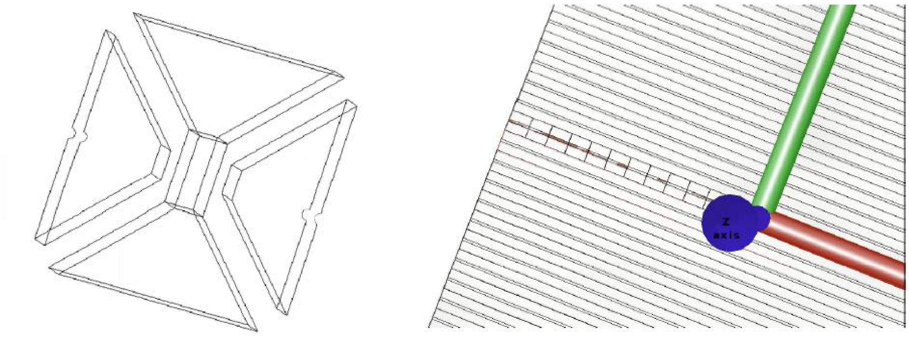

Figure 3. *On the left: pad structure. On the right: strip replicas.*

Moreover a special FLUKA card called "Lattice" provides for replicas of a single unit as many times as requested. Hence after having set up a single strip and a single pad on the anode, their replicas have been obtained by the use of the mentioned instruction. The water phantom has been instead conceived as a simple cylinder coaxial with the beam line as shown in *figure 4*.

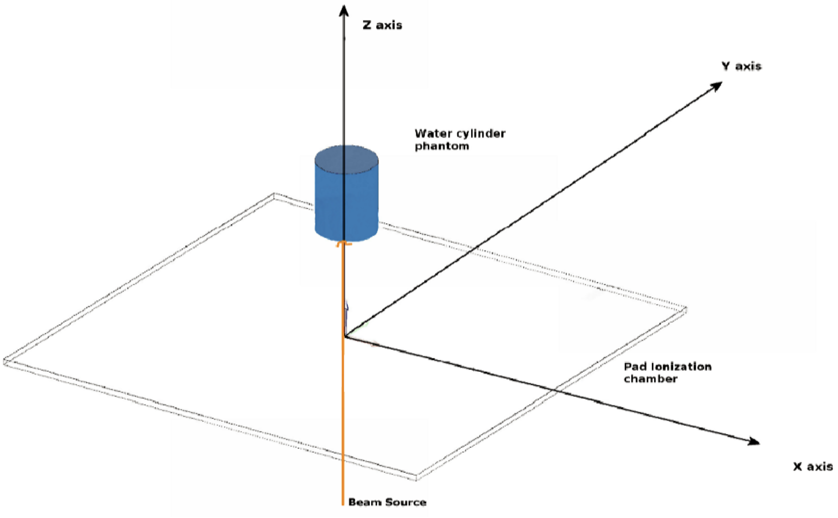

Figure 4. *The simulation geometry.*

In order to achieve data with good statistics, each simulation has been carried out with 20M events. The run on one Intel Xeon at 2.800 GHz takes about 80 hours, while on the ENEA GRID\CRESCO infrastructure it takes only about 1 hour, so the time needed for a job is 80 times less! Thus the major advantage in the use of the CRESCO resources is the significant time saving due both to faster processors and job parallelization. In fact, a single serial job of 20M events has been decomposed into 20 jobs of 1M events running at the same time on as many processors.

The jobs has been submitted mainly on the *cresco_serh144* and on the *large_24h* queues through the *cresco2-f1.portici.enea.it* hosts, spending a total CPU time of 0.877 years (7684.30 hours).

Simulations details are described in **[8]**.

Discussion and results

The results of several simulations ran with or without the two types of chamber interposed between the beam and the phantom and related to both the chambers are much similar, therefore only the ones evaluated for the final chamber are reported here.

Data have demonstrated that at clinical energies (>130MeV) either the beam longitudinal and the beam transverse spread (parallel and perpendicular to the direction of the primary proton beam respectively) do not vary significantly during treatments and the pad-strip chamber can be used as on-line monitor for proton therapy treatments.

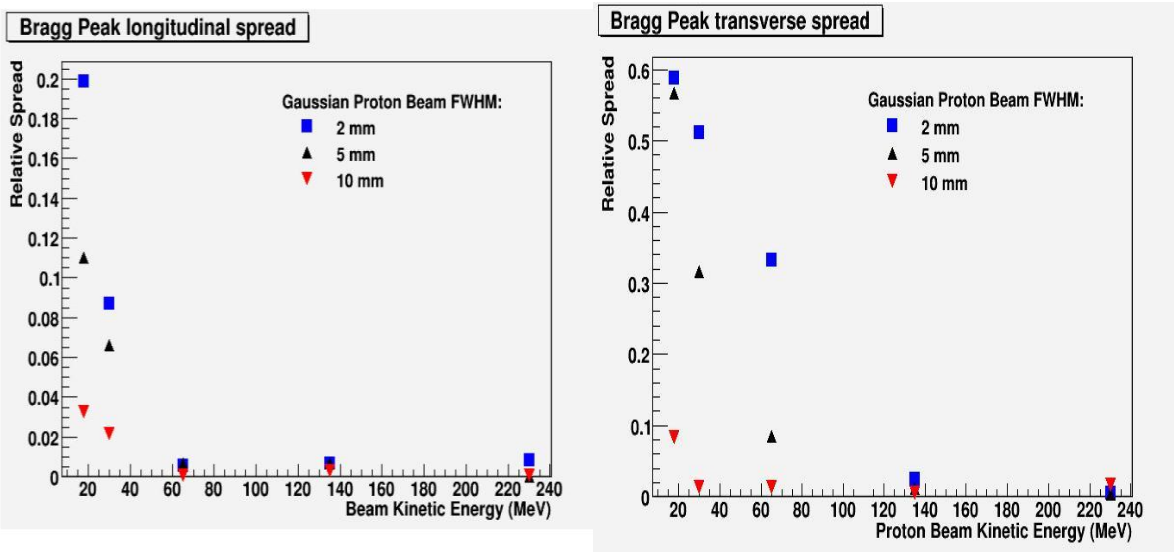

Figure 5. *Bragg peak transverse and longitudinal spread for different beam energies and cross sections.*

For example, as shown in *figure 5*, the relative variation of the Bragg peak longitudinal spread is lower than 1% above 65MeV while the transverse spread drops below 3% above 135MeV.

In order to evaluate unwanted dose due to secondary particles, the total number of neutron produced per primary proton in the chamber in the energy range between 18 MeV and 230 MeV has been estimated from FLUKA simulations. The first results, to be consolidated and validated, are shown in *figure 6*.

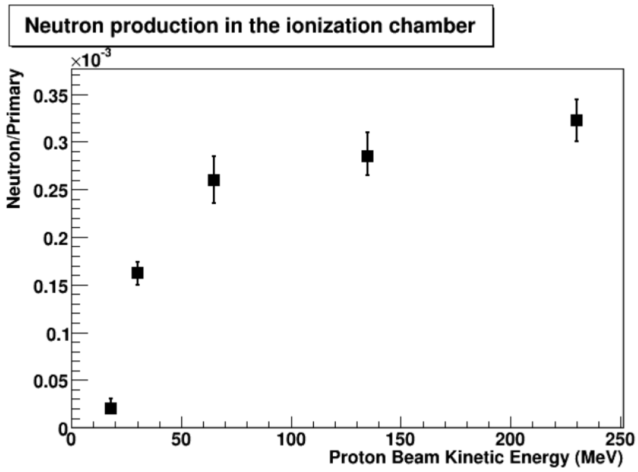

Figure 6. *Neutron production per incident proton, at different energies.*

Perspectives and conclusions

In protontherapy treatments the absorbed dose must be accurately determined and must be compared with the planned dose. The basic task of the beam monitor system is to give information about the beam parameters during the treatments, without perturbing the dose delivery; however an advanced online diagnostic system could be developed by harmonizing several radiotherapy equipments and components: TPS, Radiobiology, Dosimetry and Beam Diagnostics.

In fact a fast TPS (integrated with the beam monitor information) could get in input, in real time, the data about beam position, direction and intensity and could evaluate the assessed dose versus the planned one; then this fast TPS could recalculate, in real time, the dose still to be delivered in order to feed, as feedback, the new beam parameters to the accelerator control system.

In this context the support of computing resources is fundamental. Several efforts have been done in order to find an analytical description of the dose release, eventually to implement in a custom TPS **[1] [9]**. Moreover a beam monitor system prototype has been developed **[5] [6] [7] [8]**. In both cases the CRESCO system resources have been used and in the future they will be used for running the simulations needed to the research.

BIBLIOGRAPHY

[1] Basile E., Castelluccio D. M., Cisbani E., Frullani S., "*Integration of FLUKA simulations for TOP-IMPLART treatment planning system*", High Performance Computing on CRESCO infrastructure: research activities and results 2009-2010, (2011), ENEA, ISBN: 978-88-8286-242-8.

[2] Ronsivalle C., Carpanese M., Marino C., Messina G., Picardi L., Sandri S., Basile E., Caccia B., Castelluccio D.M., Cisbani E., Frullani S., Ghio F., Macellari V., Benassi M., D'Andrea M., Strigari L., "*The TOP-IMPLART Project*", Eur. Phys. J. Plus (2011) 126: 68, 1-15.

[3] Ferrari A., Sala P.R., Fassò A., Ranft J., "*FLUKA: a multi-particle transport code*", CERN 2005-10 (2005), INFN/TC_05/11, SLAC-R-773.

[4] Battistoni G., Muraro S., Sala P.R., Cerutti F., Ferrari A., Roesler S., Fassò A., Ranft J., "*The FLUKA code: Description and benchmarking*", Proceedings of the Hadronic Shower Simulation Workshop 2006, Fermilab 6-8 September 2006.

[5] Basile E., Carloni A., Castelluccio D.M., Cisbani E., Colilli S., De Angelis G., Fratoni R., Frullani S., Giuliani F., Gricia M., Lucentini M., Santavenere F., Vacca G., "*An online proton beam monitor for cancer therapy based on ionization chambers with micro pattern readout*", MPGD2011 proceedings, Kobe, Japan, 29/08/2011-1/09/2011, J. Inst **7** C03020 (2012), 1-11.

[6] Basile E., Carloni A., Castelluccio D.M., Cisbani E., Colilli S., De Angelis G., Fratoni R., Frullani S., Giuliani F., Gricia M., Lucentini M., Santavenere F., Vacca G., "*Autoranging Readout Electronics for the Monitoring System of the TOP-IMPLART Proton Therapy Beam",* 2011 IEEE NSS-MIC, Valencia, Spain, 22-29/10/2011, 2011 IEEE Nuclear Science Symposium Conference Record, NP2-S-47, pag. 717-720.

[7] Castelluccio D.M., "*A novel realtime beam monitoring system in proton therapy treatments, Thesis*", Scuola di Specializzazione in Fisica Sanitaria, La Sapienza University of Rome, (2010), http://www.iss.infn.it/webg3/pub/tesi/2010-spec-castelluccio.pdf

[8] Carloni A., "*Characterization of proton beams using Pad-Strip ionization chambers for online measurement of relative dose on "Phantoms" in cancer therapy with protons*", Master Thesis, La Sapienza University of Rome, (2011), http://www.iss.infn.it/webg3/pub/tesi/2011-master-carloni.pdf

[9] Basile E., "*Integration of Monte Carlo simulation in radiotherapeutic treatment planning with proton beam*", Thesis, Scuola di Specializzazione in Fisica Sanitaria, La Sapienza University of Rome, (2010), http://www.iss.infn.it/webg3/pub/tesi/2010-spec-basile.pdf

LARGE-SCALE PARALLEL SIMULATIONS OF BIO MEMBRANES BY HYBRID PARTICLE-FIELD MOLECULAR DYNAMICS TECHNIQUE

Antonio De Nicola, Giuseppe Milano

Dipartimento di Chimica e Biologia, Università degli Studi di Salerno

Introduction

Recently, Milano and Kawakatsu developed a hybrid particle-field simulation technique where self-consistent field theory (SCF) and molecular dynamics (MD) are combined. In collaboration with Prof. T. Kawakatsu (Tohoku University) and Prof. D. Roccatano (Jacobs University Bremen) we developed a specific coarse-grain model of phospholipids suitable for hybrid particle-field simulations. Phospholipids are an important class of biomolecules. Their amphiphilic nature allows them, when they are dissolved in water, to self-assembly into a lipid bilayer with lipid tails shielded from water and polar head groups exposed to the polar environment. In living organism, lipid bilayer form cellular membranes. Since the biological membranes are involved in several important processes, they have attracted the interest of the computational biophysics community. From the computational point of view these simulations are still very expensive to study process occurring on the mesoscopic scale by atomistic models. The coarse-grained (CG) method has been successfully applied to several problems involving biomolecules and more in general soft matter.

Result and Discussion

The computational efficiency of the MD-SCF approach allows studying large-scale system, larger than those available with standard CG approach. Another advantage of the MD-SCF is to employ models with chemical specificity. The specific CG models, particle-field, developed by us are able to reproduce structural properties of reference standard CG model (particle-particle). In particular we studied the self-assembly of phospholipid bilayer of most important biologic represents [1]. In *figure 1* is depicted a of phospholipid bilayer and electron density profiles of particle-field and particle-particle models.

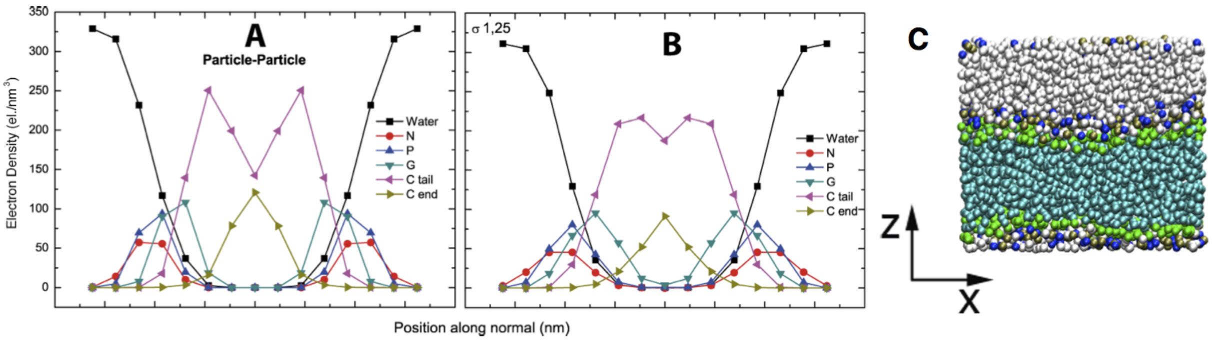

Figure 1: *Electron Density Profile of DPPC phospholipid: A) Particle-Particle reference model. B) Particle-Field model. C) Representation of resulting self-assembly DPPC membrane.*

In a following work we extended the study of the particle-field model for aqueous solutions of phospholipids. In particular, the transferability of the model in the correct reproduction of non-lamellar phases has been validated against reference particle-particle simulations. By varying the water content, the model is able to correctly describe the different morphologies that are experimentally observed such as micelles and reverse micelles [2]. In *figure 2* are reported the different phases reproduced by the particle-field model.

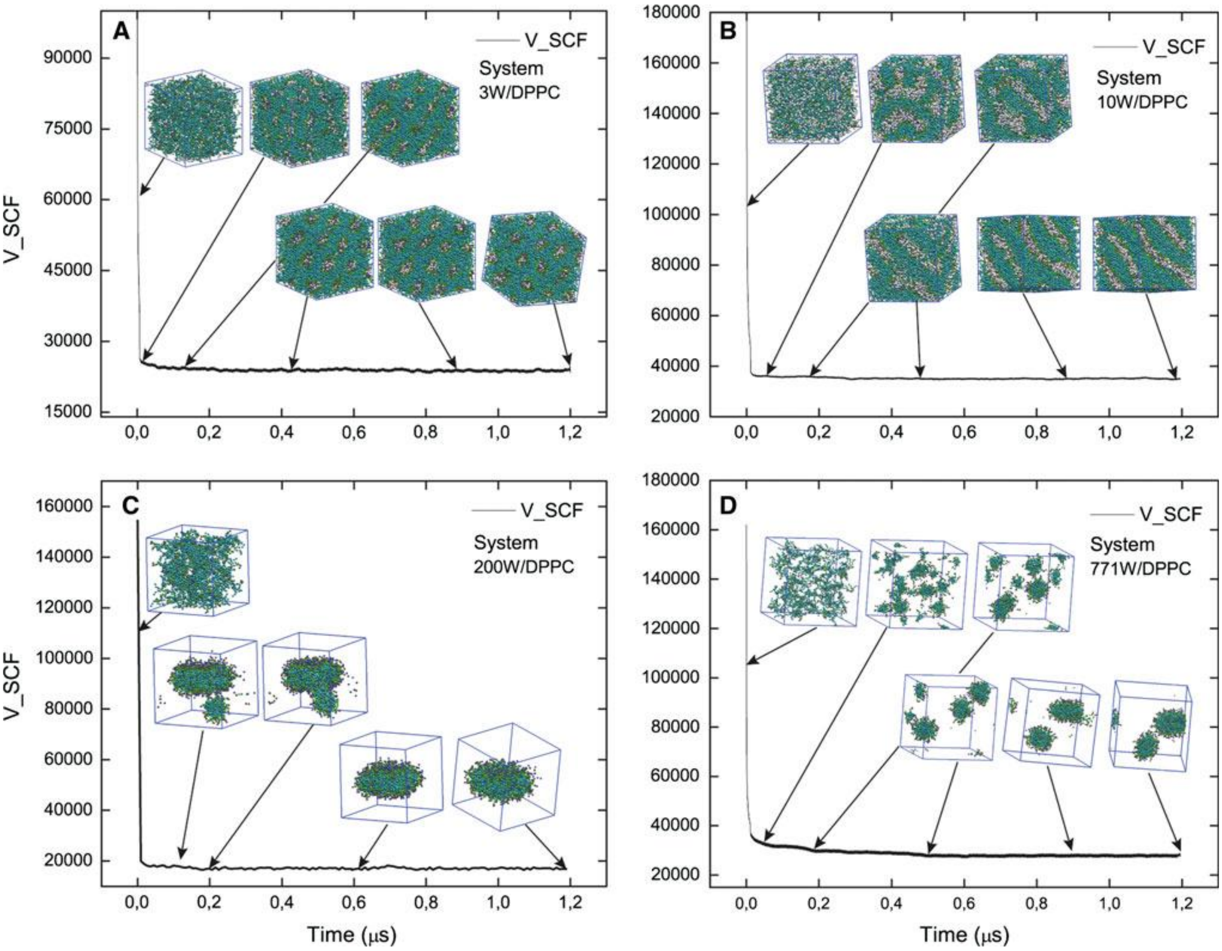

Figure 2: *Time behaviour of the MD-SCF potential for different systems composition. A) reverse micellar hexagonal phase, B) lipid bilayer phase, C) single bicelle formation, D) micellar phase.*

In order to study the self-assembly that occur on mesoscopic scale we need to perform simulation of large systems ($\approx 10^6$ particles). We presented in a paper the parallel implementation of MD-SCF scheme, in witch the self-consistent field theory and particle models are combined. The peculiar formulation of the hybrid method, considering single particles interacting with density fields, the most computationally expensive part of the hybrid particle-field MD simulation can be efficiently parallelized using a straightforward particle decomposition algorithm.

Benchmarks of simulations, including comparison of serial MD and MD-SCF program profiles, serial MD-SCF and parallel MD-SCF program profiles, and parallel benchmarks compared with efficient MD program Gromacs 4.5.4 are tested [3]. In *figure 3* we report the performance comparison between MD-SCF parallel implementation code and Gromacs 4.5.4.

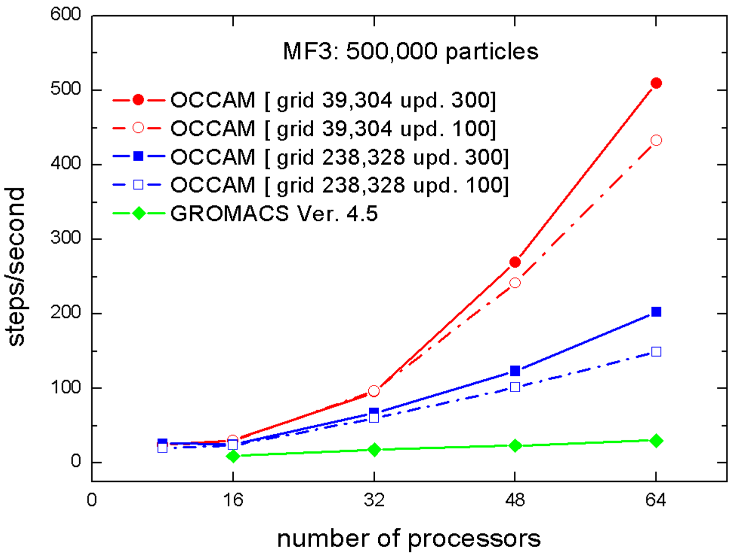

Figure 3: *steps/second comparison of OCCAM (MS-SCF implementation) and Gromacs 4.5.4. The system simulated is formed by Lennard-Jones fluid.*

The results of benchmarks indicate that the proposed parallelization scheme is very efficient and opens the way to molecular simulations of large-scale systems with reasonable computational costs.

References:

[1] De Nicola, A.; Zhao, Y.; Kawakatsu, T.; Roccatano, D.; Milano, G. Hybrid Particle-Field Coarse-Grained Models for Biological Phospholipids. *J. Chem. Theory Comput.* **2011**, *7*, 2947–2962.

[2] De Nicola, A.; Zhao, Y.; Kawakatsu, T. Validation of a hybrid MD-SCF coarse-grained model for DPPC in non-lamellar phases. *Theoretical Chemistry* ... **2012**.

[3] Zhao, Y.; De Nicola, A.; Kawakatsu, T.; Milano, G. Hybrid particle-field molecular dynamics simulations: Parallelization and benchmarks. *J. Comput. Chem.* **2012**, *33*, 868–880.

ı̣π-Face Donation from the aromatic N-substituent of N-Heterocyclic Carbene Ligands to Metal and Its Role in Catalysis

Raffaele Credendino, Laura Falivene and Luigi Cavallo

Dipartimento di Chimica e Biologia, Università degli Studi di Salerno

Introduction

NHC ligands[1-4] have been successfully tested in a number of rather different chemical transformations, such as Rh- and Ir-catalyzed hydrosilylation,[3,5] C-H activation[3,6,7] and hydrogenations,[8,9] Au-catalyzed cyclization of polyunsaturated substrates[10] and C-H activation of acetylenes,[11] Cu-catalyzed borylation reactions,[12,13] and finally in the Ni-catalyzed dehydrogenation of ammonia-borane to H_2.[14] However, the fields where the largest impact is foreseen are the Nobel reactions 2005 and 2010, which means Ru-catalyzed olefin metathesis[15,16] and Pd-catalyzed cross-coupling reactions.[3,17-19] The most updated model of the M-NHC bond consists of a dominating σ-donation from the HOMO of the NHC ligand, centered on the carbene C atom, to empty d orbitals of the metal. This σ-bond is reinforced by donation from π orbitals on the NHC ligand to empty d orbitals of electron deficient metals. However, NHC can also act as π-acid ligands, by accepting backdonation from filled d orbitals of electron rich metals. The main characteristic of this entire bonding scheme is that the M-NHC interaction occurs via σ and π bonds between the metal and the carbene atom. As common in science, this scenario is being perturbed by new experiments. For example, Plenio et al. demonstrated that the redox potential of several Ru, Pd, Ir and Rh NHC-based complexes depends on the nature of the substituents at the para position of the N-xylyl rings,[20-24] This was found puzzling since communication through the σ-bonds is unlikely, seven bonds separate these substituents from the redox-active metal center, and communication through the π-orbitals is equally unlikely, the aromatic ring of the N-substituent is orthogonal to the NHC ring.[23] Intrigued by these experimental results, we decided to analyze the M-NHC interaction in complexes presenting groups with different electronic properties in the para position of the aryl N-substituent to provide a theoretical support to the hypothesis that that communication between the NHC ligand and the metal center could occur through π-face donation.[20,22] To tune the computational protocol we first tested the chosen DFT tool to reproduce the experimental redox potential, $E_{1/2}$, of the Ir and Ru complexes shown in *Chart 1*. The good agreement we found between calculated and experimental $E_{1/2}$ allowed us to perform a detailed analysis of the influence of the various substituents on the M-NHC bond. This knowledge is used to investigate the electronic property of the metal center in newly developed Ru-catalysts.[28-30]

Results and Discussion

To shed light on the mechanism through which the Y group (*chart 1*) in the para position of the N-substituents is able to destabilize the neutral species and to stabilize higher oxidation states, we analyzed the electron density in selected systems. First, we compared the difference in the electron density, $\rho^{+}-\rho$, between the cationic and the neutral species of the reference system. This plot indicates which is the redistribution of the electron density after oxidation.

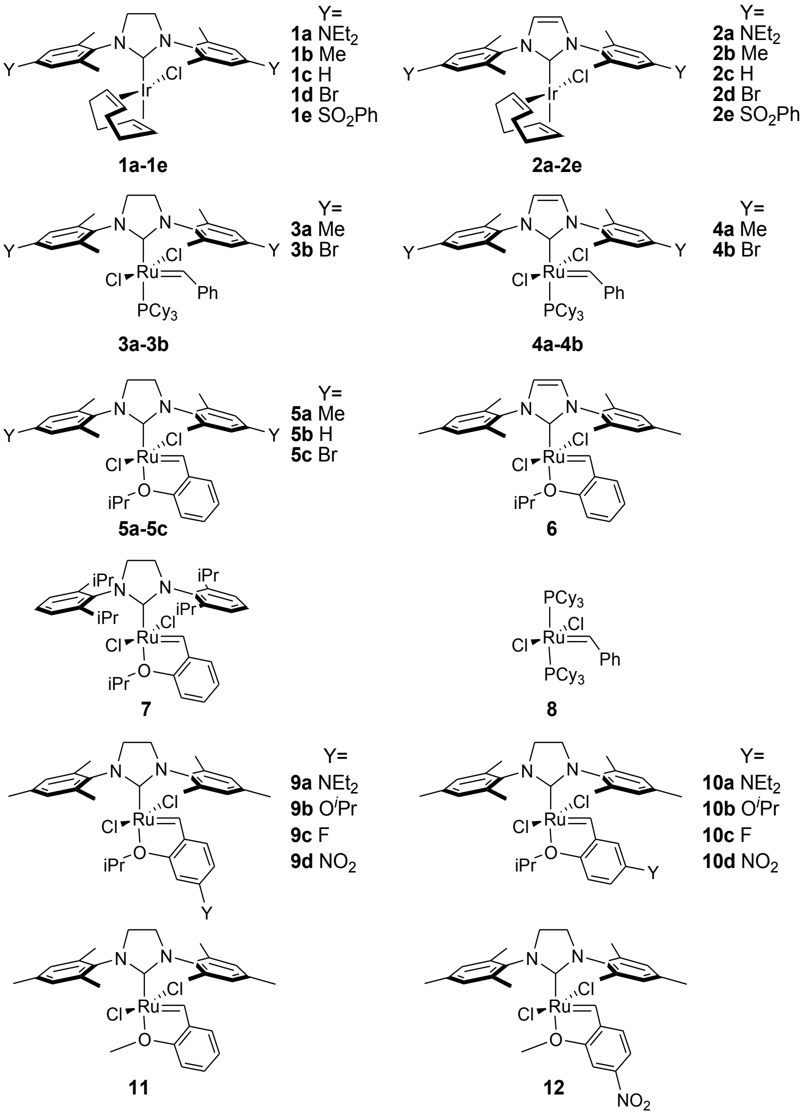

Chart 1. *Systems investigated in the present study.*

The electron density difference $\rho^{+}-\rho$ is plotted in the plane of the NHC ring as well as in the plane orthogonal to it *figure 1a* and *figure 1b*, respectively. Within this definition red and blue lines (corresponding to positive and negative isocontour lines) indicate zones where the electron density is higher or lower in the cationic species, respectively. Inspection of *figure 1a* clearly shows the unexpected result that electron density at the metal, in the plane of the NHC ring, is higher in the cationic form rather than in the neutral form (see the red full lines around the Ru center in *figure 1a*). Indeed, in agreement with the HOMO composition described above, the plot of *figure 1b* clearly indicates that upon oxidation electron density is mainly removed from the metal center as well as from the chloride ligands (see the blue dashed lines around the Cl atoms in *figure 1b*).

Within this scheme, the effect of the Y groups in the para position of the N-substituents becomes easily rationalized. Electron donating groups reinforce electron density at the C_{ipso} of the NHC ligand, thus enhancing their ability to donate to both the metal center and the alkylidene group, whereas electron withdrawing groups deplete electron density at the C_{ipso} of the NHC ligand, thus reducing their ability to donate electron density.

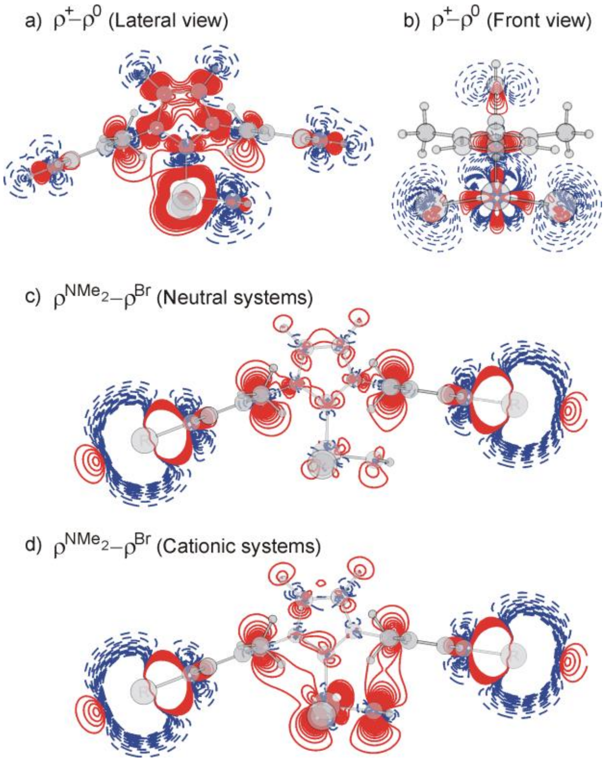

Figure 1. *Plots of the electron density difference between the cationic and the neutral species of the Ru-system* ***12b****, $\rho^{+}-\rho$, parts a-b, and between the neutral and cationic species of the Ru-systems* ***12a*** *and* ***12c****, $\rho^{NMe2}\rho^{Br}$, part c neutral systems, part d cationic systems. Red full and blue dashed lines indicate positive and negative isodensity lines, drawn between -0.01 and 0.01 a.u. with a spacing of 0.0005 a.u.*

In conclusion, all the analyses we performed illuminate that the mechanism transmitting the properties of the groups on the para position of the N-substituents to the metal center operates via the aromatic system on the N-substituent, with the C_{ipso} atom acting as key messenger between the Y group and the metal center. In case of the Ru systems, this mechanism involves also the alkylidene group. Further, our analysis clearly indicated that the Y groups have a double effect. They destabilize the HOMO in the reduced species and they reinforce the M-NHC interaction in the oxidized species.

References

(1) Arduengo, A. J.; Harlow, R. L.; Kline, M. *J. Am. Chem. Soc.* **1991**, *113*, 361.

(2) Glorius, F. Top. *Organomet. Chem.* **2007**, *21*, 1.

(3) Diez-Gonzalez, S.; Marion, N.; Nolan, S. P. *Chem. Rev.* **2009**, *109*, 3612.

(4) *Heterocyclic Carbenes in Transition Metal Catalysis and Organocatalysis*; Cazin, C. S. J., Ed.; Springer: Dordecht, 2011; Vol. 32.

(5) Wolfgang, A. H.; Lukas, J. G.; Christian, K.; Georg, R. J. A. *Angew. Chem. Int. Ed. Eng.* **1996**, *35*, 2805.

(6) Danopoulos, A. A.; Pugh, D.; Wright, J. A. *Angew. Chem. Int. Ed.* **2008**, *47*, 9765.

(7) Hanasaka, F.; Tanabe, Y.; Fujita, K.-i.; Yamaguchi, R. *Organometallics* **2006**, *25*, 826.

(8) Lee, H. M.; Jiang, T.; Stevens, E. D.; Nolan, S. P. *J. Am. Chem. Soc.* **2001**, *20*, 1255.

(9) Powell, M. T.; Hou, D.-R.; Perry, M. C.; Cui, X.; Burgess, K. *J. Am. Chem. Soc.* **2001**, *123*, 8878.

(10) Marion, N.; Lemiere, G.; Correa, A.; Costabile, C.; Ramon, R. S.; Moreau, X.; de Frémont, P.; Dahmane, R.; Hours, A.; Lesage, D.; Tabet, J. C.; Goddard, J. P.; Gandon, V.; Cavallo, L.; Fensterbank, L.; Malaria, M.; Nolan, S. P. *Chem. Eur. J.* **2009**, *15*, 3243.

(11) Fortman, G. C.; Poater, A.; Levell, J. W.; Gaillard, S.; Slawin, A. M. Z.; Samuel, I. D. W.; Cavallo, L.; Nolan, S. P. *Dalton Trans.* **2010**, *39*, 10382.

(12) Laitar, D. S.; Muller, P.; Sadighi, J. P. *J. Am. Chem. Soc.* **2005**, *127*, 17196.

(13) Kleeberg, C.; Dang, L.; Lin, Z.; Marder, T. B. *Angew. Chem. Int. Ed.* **2009**, *48*, 5350.

(14) Keaton, R. J.; Blacquiere, J. M.; Baker, R. T. *J. Am. Chem. Soc.* **2007**, *129*, 1844.

(15) Vougioukalakis, G. C.; Grubbs, R. H. *Chem. Rev.* **2009**, *110*, 1746.

(16) Samojłowicz, C.; Bieniek, M.; Grela, K. *Chem. Rev.* **2009**, *109*, 3708.

(17) Assen , E.; Kantchev, B.; O'Brien, C. J.; Organ, M. G. *Angew. Chem. Int. Ed.* **2007**, *46*, 2768.

(18) Marion, N.; Nolan, S. P. *Acc. Chem. Res.* **2008**, *41*, 1440.

(19) Würtz, S.; Glorius, F. *Acc. Chem. Res.* **2008**, *41*, 1523.

(20) Fürstner, A.; Ackermann, L.; Gabor, B.; Goddard, R.; Lehmann, C. W.; Mynott, R.; Stelzer, F.; Thiel, O. R. *Chem. Eur. J.* **2001**, *7*, 3236.

(21) Süßner, M.; Plenio, H. *Chem. Commun.* **2005**, 5417.

(22) Süßner, M.; Plenio, H. *Angew. Chem. Int. Ed.* **2005**, *44*, 6885.

(23) Leuthäußer, S.; Schwarz, D.; Plenio, H. *Chem. Eur. J.* **2007**, *14*, 7195.

(24) Leuthäußer, S.; Schmidts, V.; Thiele, C. M.; Plenio, H. *Chem. Eur. J.* **2008**, *14*, 5465.

(25) Wolf, S.; Plenio, H. *J. Organomet. Chem.* **2009**, *694*, 1487.

(26) Collins, M. S.; Rosen, E. L.; Lynch, V. M.; Bielawski, C. W. *Organometallics* **2010**, *29*, 3047.

(27) Thiel, V.; Hendann, M.; Wannowius, K.-J.; Plenio, H. *J. Am. Chem. Soc.* **2011**.

(28) Keitz, B. K.; Endo, K.; Patel, P. R.; Herbert, M. B.; Grubbs, R. H. *J. Am. Chem. Soc.* **2011**.

(29) Keitz, B. K.; Endo, K.; Herbert, M. B.; Grubbs, R. H. *J. Am. Chem. Soc.* **2011**, *133*, 9686.

(30) Endo, K.; Grubbs, R. H. *J. Am. Chem. Soc.* **2011**, *133*, 8525.

A WEB APPLICATION TO VISUALIZE CONTACTS AT THE INTERFACE OF BIOMOLECULAR COMPLEXES

Anna Vangone, Luigi Cavallo

Dipartimento di Chimica e Biologia, Università degli Studi di Salerno.
Email: avangone@unisa.it

Recently, we developed a novel tool for analyzing, visualizing and comparing the interface in protein-protein and protein-nucleic acids complexes, COCOMAPS [1].

Associations between biological molecules occur in a wide range of functional contexts. These associations include functional complexes between different protein partners, or between proteins and other molecules, such as nucleic acids. Availability of a 3D structure for a complex allows detailed analysis of the interaction at atomic level between the molecular partners, which is a fundamental step for possible biomedical and biotechnological applications. Moreover, the recent development of accurate docking softwares to predict the 3D structure of macromolecular complexes requires the accurate and tedious screening of all the possible solutions [2]. Although several web servers able to characterize in detail the interface of a biological complex have been developed, no one has been implemented to provide an immediate 2D graphical view of the interaction, a sort of fingerprint of the complex reporting the needed information in a ready-to-read form. To this aim, we believe that classical contact maps could be one of the tools of choise to identify uniquely and intuitively the surface of interaction between the interacting molecules. For this reason we decided to implement the COCOMAPS (bioCOmplexes COntact MAPS) web application as a user friendly tool for the analysis, visualization and comparison of surface of interaction in biological complexes.

All the programs under COCOMAPS have been written in python, taking advantage of python libraries such as SciPy and Matplotlib. A user-friendly interface allows to download input files direclty from wwPDB [3] or upload locally stored PDB formatted files. COCOMAPS outputs provide detailed information on a biocomplex interface, organized in contact maps and tables.

The first map, named "Black and White Contact Map", reports the inter-molecular contacts within a cut-off distance value chosen by user. The second one, named "Distance Range Map" reports in different colors contacts at increasing distances (7,10,13 and 16 Å) (see *figure 1, a*), while the third map, named "Properties Contact Map" presents each contact colored according to the physico-chemical nature of the two interacting residues: hydrophobic-hydrophobic, hydrophilic-hydrophilic and hydrophobic-hydrophilic.

The detailed information given are organized in table, about: i) interacting residues, defined on the basis of the cut-off distance, ii) residues at the interface, defined on the basis of the ASA values, and iii) intramolecular H-bonds (see *figure 1, b*).

A 3D visualization of the complex in Jmol and a ready-to-run PyMol [4] script are also provided.

a) Distance range contact map

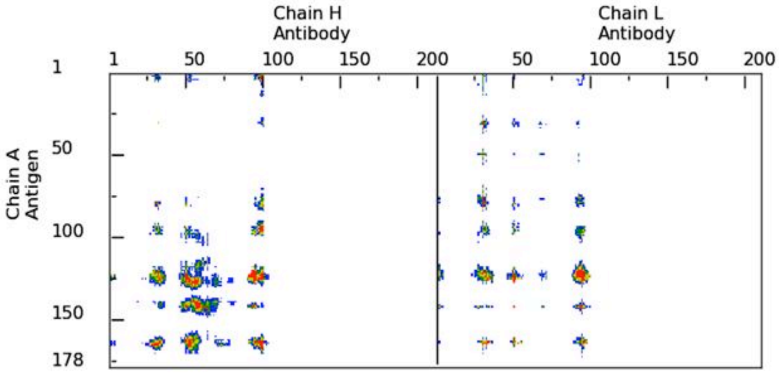

b) Interacting residue table

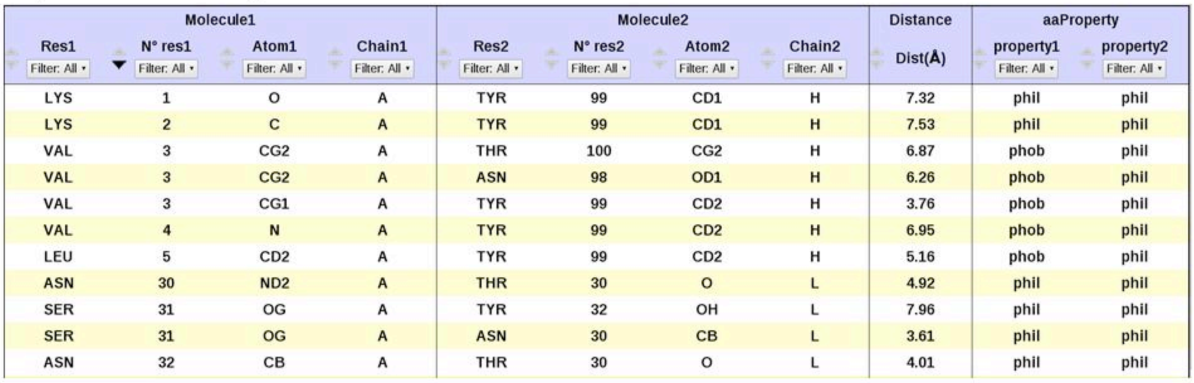

Molecule1				Molecule2				Distance	aaProperty	
Res1	N° res1	Atom1	Chain1	Res2	N° res2	Atom2	Chain2	Dist(Å)	property1	property2
LYS	1	O	A	TYR	99	CD1	H	7.32	phil	phil
LYS	2	C	A	TYR	99	CD1	H	7.53	phil	phil
VAL	3	CG2	A	THR	100	CG2	H	6.87	phob	phil
VAL	3	CG2	A	ASN	98	OD1	H	6.26	phob	phil
VAL	3	CG1	A	TYR	99	CD2	H	3.76	phob	phil
VAL	4	N	A	TYR	99	CD2	H	6.95	phob	phil
LEU	5	CD2	A	TYR	99	CD2	H	5.16	phob	phil
ASN	30	ND2	A	THR	30	O	L	4.92	phil	phil
SER	31	OG	A	TYR	32	OH	L	7.96	phil	phil
SER	31	OG	A	ASN	30	CB	L	3.61	phil	phil
ASN	32	CB	A	THR	30	O	L	4.01	phil	phil

Figure 1. *Sample COCOMAPS output for the complex of Ibalizumab antibody with the CD4 antigen (PDBcode: 3O2D). a) The top part of the COCOMAPS Interacting Residues Table. b) COCOMAPS "Distance Range Contact Map". Red, yellow, green and blue dots indicate contacts within 7, 10, 13 and 16 Å, respectively.*

In conclusion, COCOMAPS combines in a single tool the traditional analysis and 3D visualization of interfaces in biocomplexes with the effectiveness of the contact map view.

References:

1. Vangone, A.; Spinelli, R.; Scarano, V.; Cavallo, L.; Oliva, R., COCOMAPS: a web application to analyse and visualize contacts at the interface of biomolecular complexes. *Bioinformatics* **2011,** *27* (20), 2915-2916.

2. Janin, J., Protein-protein docking tested in blind predictions: the CAPRI experiment. *Mol Biosyst* **2010,** *6* (12), 2351-62.

3. Berman, H. M.; Westbrook, J.; Feng, Z.; Gilliland, G.; Bhat, T. N.; Weissig, H.; Shindyalov, I. N.; Bourne, P. E., The Protein Data Bank. *Nucleic Acids Res* **2000,** *28* (1), 235-42.

4. DeLano Scientific, L., http://www.pymol.org **2002**.

Investigating the transition mechanism of the DNA overstretching transition through molecular dynamics simulations

L. Bongini

Abstract

The overstretching transition of DNA is studied by means of atomistic molecular dynamics simulations. The difference in enthalpy and entropy between the compact and the extended state, the extension of the transition state, the entalpic contribution to the transition barrier and the stretch modulus of compact DNA all result in good to reasonable agreement with previous experimental estimates. Overstretched DNA adopts a highly dynamical and structurally disordered double stranded conformation which is characterized by a limited amount or residual base pairing but a rather efficient hydrophobic screening of apolar regions and a limited amount of non-native, intra-strand hydrogen bonding.

Introduction

Since the beginning of force spectroscopy, with the creation of the first magnetic and optical tweezers back in the end of the 80's, DNA has been the object of an extensive experimental effort which has greatly improved our understanding of the mechanical properties of this molecule [1]. One phenomenon that, nevertheless, still defies our efforts is DNA overstretching [2], the sudden elongation of more than 70% of its initial length experienced by double stranded DNA when pulled from its ends with forces higher than 60 pN (*figure 1*). Unfortunately a multiplicity of possible DNA structures appears to be consistent with the extension measured, from separated strands of single stranded DNA (ssDNA) [3] to variously coupled strands of elongated DNA, form the S-ladder [4] to the S-zipper [5]. In what follows we explore DNA overstretching by means of all-atoms molecular dynamics simulations and compare the results with recent experimental work.

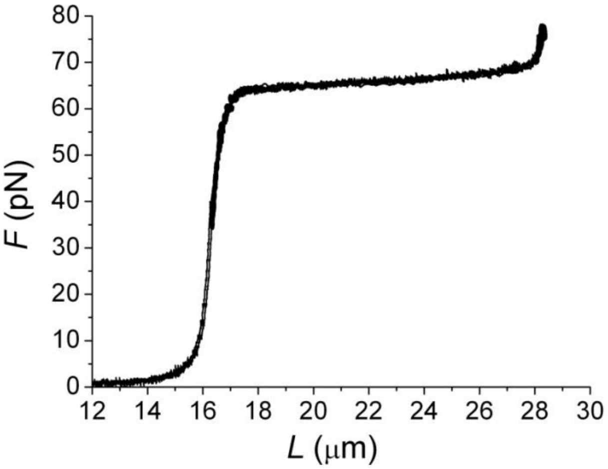

Figure 1. *Fully reversible force extension profile for overstretched λ-DNA, from* Bianco *et al.*

Instruments and methods

Since the discovery of DNA ovestretching several groups attempted to use steered molecular dynamics simulations to access the atomic detail of the overstretching transition [4,5,7,8]. However, since the timescales involved are of the order of the seconds while atomistic simulations are typically restricted to the ns range, this approach is bound to explore only transient conformations. Another possible approach to obtain information on the free energy profile of the transition is to attempt to sample the equilibrium by using temperature to accelerate the exploration of the configuration space and therefore, hopefully, convergence.

The overstretching free energy landscape of a random DNA 23-mer containing 9 AT and 14 CG pairs was sampled via atomistic molecular dynamics simulations coupled with umbrella sampling. The conformational space of the chosen oligomer was investigated by simulating the effect of a heat bath trough a Langevin dynamics on 24 different copies of the system. Each copy was subjected to a restraining harmonic potential on its end-to-end distance in order to fix the average rise between consecutive base pairs during a simulation. The explored interval of base pair rise ranges from 0.34 to 0.58 nm.

Simulations were performed with AMBER with an improved force field tailored for nucleic acids simulations [9]. An implicit solvent with the generalized Born solvation model and rescaled Born radius (igb=5) was chosen. Ionic strength was set to 100 mM. The different system copies were first heated at 400 K for 3 ns and then thermalized at 300 k for other 6 ns, until stabilization of the average enthalpy over a 1 ns window.

Results and discussion

In *figure 2* we report averaged equilibrium conformations corresponding to four different average rise between base pairs. AT base pairs have been colored in yellow. As already reported in [10] AT rich regions of the molecule show to be more compliant and undergo cooperative overstreching at a slightly earlier stage than CG rich ones.

Figure 2. *Averaged conformations corresponding to an average rise between consecutive base pairs of 0.45, 0.46, 0.47 and 0.56 nm respectively. AT base pairs are represented in yellow.*

In *figure 3* the structure corresponding to a 0.46 nm base pair rise displays an AT rich portion which is already elongated together with an almost perfectly B-structured CG rich one. Already at 0.47 nm rise, however also the GC rich region appears suddenly. In AT rich regions elongation almost immediately corresponds to breakage of base pairing. On the contrary, CG pairs tend to retain base pairing even at high extensions. As a consequence the overstretched state, upper structure in *figure 2*, corresponding to 0.56 nm rise, adopts a plastic configuration which is characterized by an almost complete breakage of the Watson-Crick pairing for AT pairs and an almost complete preservation of it for CG ones. The unpaired bases in strands of several consecutive A/T bases are highly dynamical but tend not to be solvated. Base staking in these unpaired regions is partially preserved, although often not with the original Watson-Crick neighbors. The other frequent alternative is the aromatic stacking of a base with the corresponding one on the opposite strand. In average A/T bases are stacked 58% of their time, with approximately two thirds of their stacking contacts being native and one third non native. Using a combination of native and non-native stackings, approximately 20% of A/T bases manages to stack both of its sides, while only 5% of them doesn't show any stacking interaction. Even in these cases, however, a certain amount of hydrophobic contact with neighboring bases might be present. Although in regions characterized by many consecutive C/G bases base pairing is almost always preserved, all the deviations from the standard stacking-pairing pattern already described for AT rich regions can also be observed. Yet, in this case the typical life time of such anomalous conformers is of the order of $\mathbf{10^2}$ fs and they concern no more than a CG pair at any given instant. As a consequence CG rich portions of the molecule adopt a much less compact conformation than AT rich regions since the opposite phosphate backbones are kept apart by the surviving native base pairings.

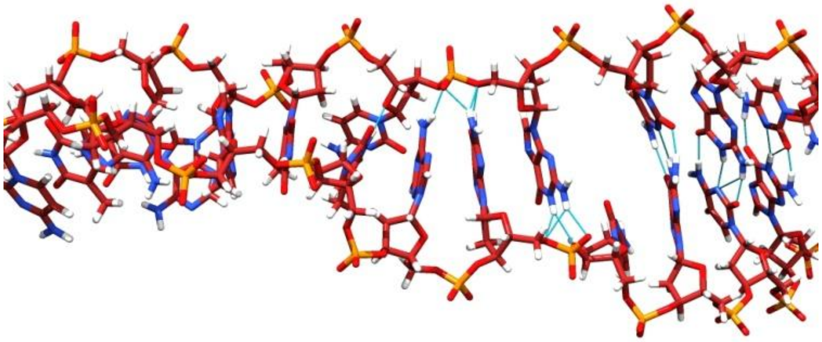

Figure 3. *Zoom of the 0.58 nm rise equilibrium configuration. Hydrogen bonds are in cyan. In the center of the image are shown bases binding the phosphate backbone of the opposite strand.*

The attachment between opposite strands is further reinforced by the occurrence of hydrogen bonds between unpaired A/T bases and one or more of the oxygens of the opposite phosphate backbone, as can be seen in *figure 3*, where a zoom of the overstretched structure presented in *figure 2* is proposed. Such inter-strand attachment might be further reinforced by a zipper structure were each base binding to the backbone of the opposite strand is also staked between two of the bases belonging to the opposite strand. This conformation is a very appealing candidate for a S-form since, maximizing at the same time hydrogen bonding, base stacking and hydrophobic screening, is characterized by a a very low enthalpy. The zipper conformation has indeed been observed in simulations at forces above 100 pN. It is, however unstable in the range of forces analyzed as testified by a control simulation that starting from this zipper, hydrogen bonded conformation quickly evolved to the CG-paired-AT-unpaired conformation previously described.

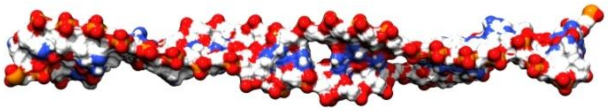

Figure 4. *Hydrophobicity surface of an overstretched conformation. Even in disordered regions the hydrophobic nucleobases clump together contrasting strand separation.*

Figure 4 shows the hydrophobicity surface of the extended conformation partial charges shows that the basic organization of B-DNA is retained, the highly charged backbones, which repel each other, are separated by a mostly hydrophobic region where the nucleobases by clamp together thus contributing to prevent strand separation. As a final structural remark we note that the helicity of the extended conformation resulting from the simulations is 32 bp per turn, 70% smaller than reported in [11, 12] but only 20% smaller than in [13].

As far as the energetics of the transition is concerned the umbrella sampling appoarch allows tio recover enthalpy and free energy profiles. While enthalpy is directly recovered from the output of the production runs, free energy was computed by analyzing the end-to-end fluctuations of each constrained trajectory with the weighted histogram method, in the implementation of the freely available WHAM program by Alan Grossfield. At the time scales investigated however the free energy profiles, whose average slope is $\boldsymbol{F_c}$ = 92 pN, high but reasonably near to the experimental value of the transition force, are still very noisy and it is difficult to assess whether at the transition force the free energy landscape is perfectly smooth or a slight free energy barrie exists. The total enthalpic difference between the compact and extended state is around 15 $\boldsymbol{k_B T}$ per base pair, somewhat higher than the expected 8.2 $\boldsymbol{k_B T}$ per base pair while the free energy difference is 3.5 $\boldsymbol{k_B T}$ per base pair (it should be 3.7 $\boldsymbol{k_B T}$ per base pair according to experiments [6]). By diagonalizing the mass weighted covariance matrix for each constrained trajectory trough the ptraj tool of AMBER also the vibrational entropy might be accessed. Vibrational entropy results strongly correlated to enthalpy (see *figure 5*). A careful analysis of the entropic profile, however, shows that it changes slightly before than enthalpy (see *figure 5*). This small difference is sufficient to create a bottleneck for the transition since the configurations characterized by high enthalpy and low entropy are less probable of both those characterized by low enthalpy and entropy and those characterized by high enthalpy and entropy.

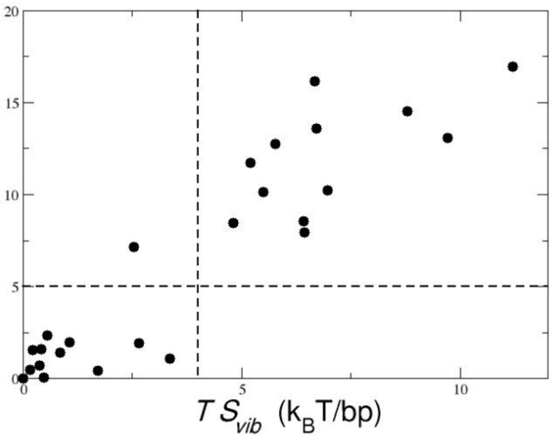

Figure 5. *Enthalpy and vibrational entropy for the overstretching of the 23-mer.Vibrational entropy is computed by diagonalization of the mass weighted correlation matrix. The isolated data point in the E>5 TSvib < 4*

The visual inspection of the configurations near the bottleneck allows to determine the structural basis of this phenomenon. As, already observed, overstretching takes place in a two step fashion, the AT rich regions overstretching first. The abrupt increase in enthalphy at 0.45 nm rise reflects the breakage of native hydrogen bonds resulting in the cooperative elongation of AT rich regions of the molecule. The subsequent overstretching of CG rich regions, taking place at 0.47 nm rise, does not result in an equally drastic enthalpic increase since, at first, CG regions tend to retain most of their native hydrogen bonds.

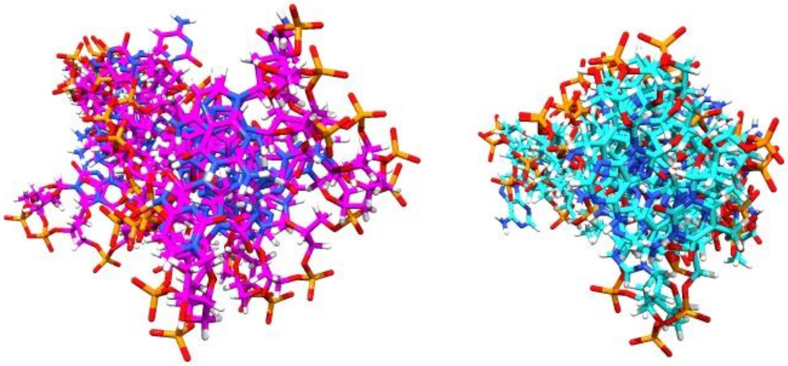

Figure 6. *Cross section of fully overstretched poly-CG (right) and poly-AT (left) DNA molecules. the cross section is 11.5* nm^2 *and 7.5* nm^2 *respectively.*

The two-step character of the transition also explains the advance in entropy increase with respect to enthalpy. As already stressed, regions with different CG content adopt different overstretched conformations, since AT rich regions tend to be more compact due to the presence of non-native interstrand hydrogen bonds or base stacking interactions which are prevented in CG rich regions by the presence of residual native base pairs. This difference in compactness (see *figure 6*) results in a difference in vibrational entropy, with the most compact conformation having a lower vibrational entropy.

Aknowledgements

Supported by IIT-SEED and Ente Cassa di Risparmio di Firenze (Italy).

References

1. BUSTAMANTE C., BRYANT Z., SMITH S. B. *"Ten Years of Tension: Single-Molecule DNA Mechanics"* Nature **421** (2003) pp. 423-427.

2. CLUZEL P., LEBRUN A., HELLER C., LAVERY R., VIOVY J. L., CHATENAY D., CARON F. *"DNA: An Extensible Molecule"* Science **271** (1996) pp.792-794.

3. WILLIAMS M. C., WENNER J. R., ROUZINA I., BLOOMFIELD V. A. *"Entropy and Heat Capacity of DNA Melting from Temperature Dependence of Single Molecule Stretching"* Biophys. J. **80** (2001) pp. 1932-1939.

4. KONRAD M. W., BOLONICK J. I. *"Molecular Dynamics Simulation of DNA Stretching Is Consistent with the Tension Observed for Extension and Strand Separation and Predicts a Novel Ladder Structure"* J. Am. Chem. Soc. **118**, (1996) pp. 10989-10994

5. BALAEFF A., CRAIG S. L., BERATA D. N. "*B-DNA to Zip-DNA: Simulating a DNA Transition to a Novel Structure with Enhanced Charge-Transport Characteristics"* J. Phys. Chem. A **115** (2011) pp. 9377–9391

6. BONGINI L., MELLI L., LOMBARDI V., BIANCO P. *"The energy landscape of DNA overstretching transition"* Submitted to Biophys J.

7. PIANA S. *"Structure and energy of a DNA dodecamer under tensile load"* N.A.R. **33**, (2005) pp. 7029-7038

8. LI H., GIESLER T. *"Overstretching of a 30 bp DNA duplex studied with steered molecular dynamics simulation: Effects of structural defects on structure and force-extension relation"* Eur. Phys. J. E **30**, (2009) pp. 325-32.

9. PEREZ A., MARCHAN I.; SVOZIL D.; SPONER J.; CHEATHAM, T.E.; LAUGHTON C.A.; OROZCO M. "*Refinement of the AMBER Force Field for Nucleic Acids: Improving the Description*

of alpha/gamma Conformers" Biophys. J., **92**, (2007) pp. 3817–3829.

10. PAIK D. H., PERKINS T. T. "*Overstretching DNA at 65 Pn Does Not Require Peeling from Free Ends or Nicks"* J. Am. Chem. Soc. 133 (2011) pp. 3219-3221

11. Léger, J. F., G. Romano, A. Sarkar, J. Robert, L. Bourdieu, D. Chatenay and J. F. Marko. *"Structural Transitions of a Twisted and Stretched DNA Molecule"* Phys. Rev. Lett. **83** (1999) pp. 1066.

12. SARKAR A., LEGER J. F., CHATENAY D., MARKO J. F. *"Structural Transitions in DNA Driven by External Force and Torque"* Phys. Rev. E Stat. Nonlin. Soft Matter Phys. **63** (2001) 051903.

13. BRYANT Z., STONE M. D., GORE J., SMITH S. B., COZZARELLI N. R. BUSTAMANTE C. *"Structural Transitions and Elasticity from Torque Measurements on DNA"* Nature **424**: (2003) pp. 338-341

Iron Corrosion-Resistance in Lead-Bismuth Eutectic Coolant by Molecular Dynamics Method

Artoto Arkundato[a,b], Zaki Suud[a], Mikrajuddin Abdullah[a],
SutrisnoWidayani[a], Massimo Celino[c]

[a]*Nuclear Physics and Biophysics Research Division, Physics Department*
Institut Teknologi Bandung, Jl. Ganesha 10, Bandung, Indonesia
[b]*Physics Department, Faculty of Mathematical and Natural Sciences*
Universitas Jember, Jl. Kalimantan III/25, Jember, Indonesia
[c]*ENEA, C.R. Casacia, Via Anguillarese 301, Rome, Italy*
email: a_arkundato@students.itb.ac.id

Abstract. In this present work, we report numerical study of iron corrosion in interaction with lead-bismuth eutectic. The goal of this work is to study how the oxygen can be used to reduce the corrosion rate of iron in lead-bismuth eutectic. The molecular dynamics method was applied to simulate corrosion process. By evaluating the diffusion coefficients, RDF functions, MSD curves of iron and also observed the crystal structure of iron before and after oxygen injection we concluded that a significant and efficient reduction can be achieved by injecting about 2% of oxygen into lead-bismuth eutectic.

Keywords: lead-bismuth eutectic coolant, corrosion, oxygen content, molecular dynamics method.

1. Introduction

Lead-bismuth eutectic (LBE) has been a potential candidate as a coolant material in advanced nuclear reactors design. It is also well known the steel cladding was severely corroded when they are exposed to LBE directly at high temperatures [1-2]. This crucial issue has presented a critical challenge in the use of LBE and then a full knowledge of corrosion characteristics and how to reduce corrosion are essential for safety of heat transfer systems in reactors. In our previous work we have used MD method to calculate the diffusion coefficient of iron in liquid lead/LBE [3]. In the present work we report the effect of oxygen injection into LBE to reduce the corrosion rate of iron in LBE by using MD method. We predicted the most effective oxygen injection for efficient iron corrosion reduction.

2. Fundamental theory

Molecular dynamics is a simulation technique in which the interacting atomic system is allowed to evolve for a specified period of time. In our work we used the Lennard-Jones (LJ):

$$U(r) = 4\varepsilon\left[\left(\frac{\sigma}{r}\right)^{12} - \left(\frac{\sigma}{r}\right)^{6}\right] \tag{1}$$

where σ and ε are the LJ potential parameters. To maintain the validation of LJ potential in our simulation, we used the potential parameters as reported by Shu and Davies for Fe-Fe and Pb-Pb interaction [4]; using the potential parameter of O-O interaction as reported by Lemmon and

Jacobsen [5]; and using the Bi-Bi interaction from the fitting of EAM pair potential [6]. Meanwhile for cross-interaction: Fe-Pb, Fe-Bi, Fe-O, Pb-Bi, Pb-O, and Bi-O we approached using the popular Lorentz-Berthelot formula:

$$\sigma_{AB} = \frac{(\sigma_{AA}+\sigma_{BB})}{2} \quad \text{and} \quad \varepsilon_{AB} = (\varepsilon_{AA}\cdot\varepsilon_{BB})^{1/2} \tag{2}$$

Table 1 summarizes the parameters of LJ potential that we used in our work. All simulations in our work was carried out by using the **MOLDY** molecular dynamics code [7].

Table 1. *The Lennard-Jones parameters that used in this research*

Pair Interaction	σ (Å)	ε (eV)	Pair Interaction	σ (Å)	ε (eV)
Fe-Fe	0.4007	2.3193	Fe-Pb	0.2766	2.7540
Pb-Pb	0.1910	3.1888	Fe-Bi	0.1538	2.6846
Bi-Bi	0.0590	3.0500	Fe-O	0.0639	2.7836
O-O	0.0102	3.4280	Bi-O	0.0245	3.1490
Pb-Bi	0.1061	3.1194	Pb-O	0.0441	3.2184

2.1 Diffusion Coefficient Calculation

Corrosion may be understood as a degradation of structural materials into its constituent atoms due to the chemical reactions with environment**.** The LBE coolant creates high temperature environment for reactor cladding that in turn causes corrosion. The degradation occurs due to high solubility of certain elements of the steel (Ni, Cr and Fe, mainly) into LBE [8]. Then liquid-metal corrosion for the most part simply depends on the solubility of the structural material/solid metal in the stagnant liquid metal.. In our work the corrosion phenomena was credible as a diffusion process where a fraction of Fe atoms leave their crystals bulk toward a high temperature coolant of liquid metal. We calculated the diffusion coefficients using three below successive equations:

$$MSD = \langle|\bar{r}(t) - \bar{r}(0)|^2\rangle \tag{3}$$

$$D = \lim_{t\to\infty}\frac{\langle|r(t) - r(0)|^2\rangle}{6t} \tag{4}$$

where *MSD* is mean-square displacement, *D* is diffusion coefficient, *r* is position of an atom and *t* is time. The temperature dependence of diffusion coefficient *D*(*T*), is evaluated by using the Arrhenius formula,

$$D(T) = D_0\exp(-A/RT) \tag{5}$$

where *T* is a temperature, *R* is the universal gas constant, and *A* is an activation energy of diffusion.

3. Simulation System

We modeled the corrosion by placing the iron (1729 atoms in bcc crystal structure, with lattice constant *a* = 2.8286 Å) in the center of LBE as in *figure1*. The gray color is Pb atoms, cyan color is Bi atoms and the indigo color is Fe atoms.

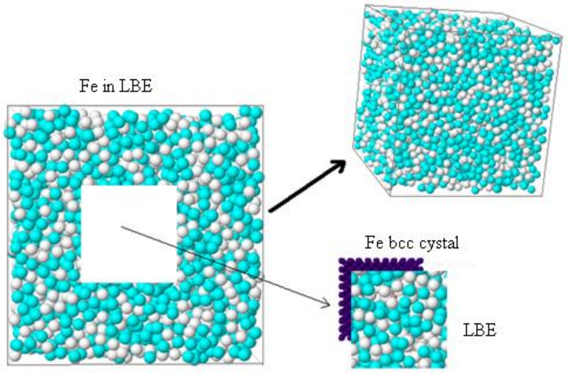

Figure 1. *Initial atomic configuration for FeLBE system (with Jmol at http://www.jmol.org).*

The liquid LBE was made from 2540 of Pb atoms (45.5%) and 3037 of Bi atoms (55.5%), with LBE density of 0.0274 atoms/Å^3. Dimension of whole system (FeLBE) is (63.2×63.2×63.2) Å^3.
To study the effect of oxygen injection then we spread the oxygen atoms evenly into LBE coolant with certain percentages (compared to the total number 5577 atomsof PbBi coolant): 28 (0.5%), 42(0.75%), 58(1.0%), 68(1.5%), 114(2.0%), 140(2.5%), 170(3.0%), and 192(3.5%) into coolant. The simulation was carried out at 750 ^{o}C. Then we calculate the diffusion coefficients to study the corrosion characteristic of iron.

4. Results and Discussion

4.1 Iron Diffusion in LBE without Oxygen Injection

Figure 2 is the plot of (1/*T*) vs. log *D*(*T*) from simulation data. The graph has linear equation:

$$logD(T) = -\frac{1020}{T} - 7.28 \qquad (6)$$

with correlation coefficient R^2 = 0.984. We can derive from this equation that the temperature dependent of iron diffusion coefficient in LBE is :

$$D(T)_{0\%} = 5.28 \times 10^{-8} \exp(-2340.18/T) \qquad [\mathrm{m^2/s}] \qquad (7)$$

Using this equation we can compute the diffusion coefficient at 750 ^{o}C, is:

$$D(T = 750^{\circ}\mathrm{C})_{0\%} = 2.33 \times 10^{-9} \qquad [\mathrm{m^2/s}] \qquad (8)$$

S.Banerjee has reported that the iron diffusion in LBE is $D_{\mathrm{Fe}\rightarrow\mathrm{LBE}}$ = 2.27 ± 0.11 x 10^{-9} m^{2}s^{-1} = (2.16 – 2. 38) x 10^{-9} m^2 s^{-1} at temperature 750 $^{\circ}$C [1]. Our calculation Eq.8 then is still in the range of Banerjee's result.

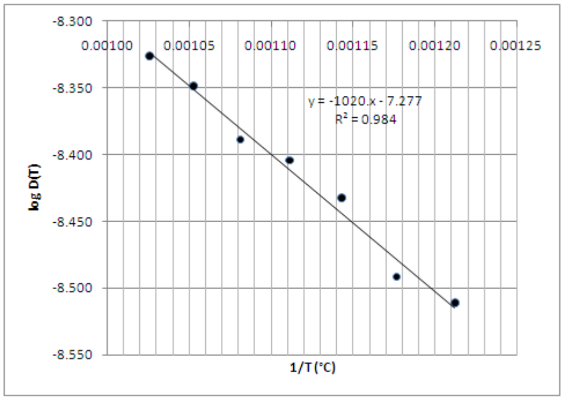

Figure 2. *Plot of 1/T vs. log D(T) for FeLBE system.*

4.2 Iron Diffusion in LBE with Oxygen Issue

Figure 3 shows MSDs from simulation at 750 °C with certain oxygen injection into the LBE coolant. Whereas the Fig.4 shows the diffusion coefficient for iron with certain oxygen injection.

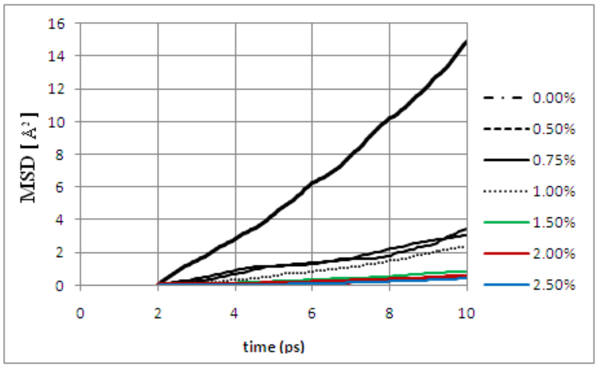

Figure 3. *MSD curves of iron diffusion at 750°C in LBE.*

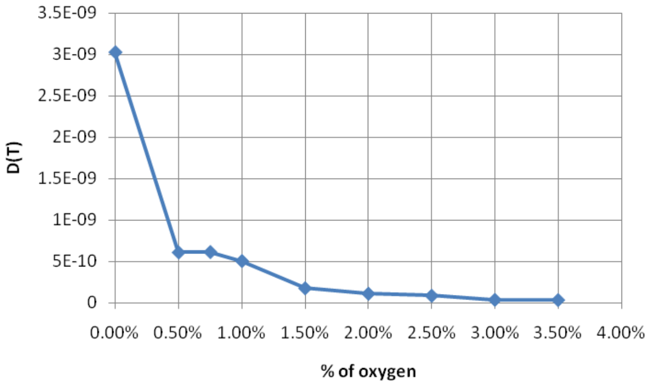

Figure 4. *The diffusion coefficient of iron in LBE for certain oxygen injection.*

From *figure 3* and *4* then we conclude that the effective and efficient oxygen injection to reduce the iron corrosion in LBE is about 2.0%. With 2.0% oxygen injection into LBE we can reduce the iron corrosion in approximately lowest level. An attractive picture of effect of oxygen injection is from the atomic structure of iron before and after the injection, as in *figure 5*.

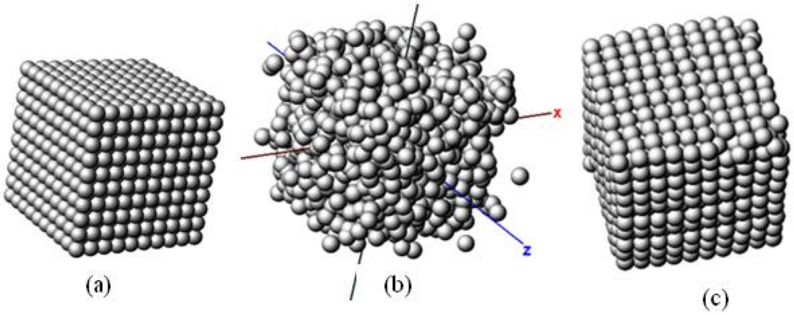

(a) (b) (c)

Figure 5. *The atomic structurel of iron: (a) before simulation, (b) after simulation without oxygen issue, (c) after issuing 2.0% of oxygen.*

Acknowledgments. The computing resources and the related technical support used for this work have been provided by CRESCO-ENEAGRID High Performance Computing infrastructure and its staff; see www.cresco.enea.it for information. CRESCO-ENEAGRID High Performance Computing infrastructure is funded by ENEA, the "Italian National Agency for New Technologies, Energy and Sustainable Economic Development" and by national and European research programs.

References

1. Jinsuo Zhang, Ning Li, '*Review of the studies on fundamental issues in LBE corrosion',* Journal of Nuclear Materials*,* 373, pp. 351-377, (2008).

2. G. K. Zelenskii, A. G. Ioltukhovskii, M. V. Leont'eva-Smirnova, I. A. Naumenko, and S. A. Tolkachenko, *Corrosion resistance of fuel element steel cladding in a lead coolant*, Metal Science and Heat Treatment, Vol. 49, Nos. 11 – 12, (2007).

3. Artoto Arkundato, Zaki Suud, Mikrajuddin, *Corrosion Study of Fe in a Stagnant Liquid Pb By Molecular Dynamics Methods*, AIP Conference Proceedings, Volume 1244, pp. 136-144, Issue Data June 22, 2010, (2010).

4. Shu Zhen and G.J. Davies, *L-J n-m Potential Energy Parameters*: *Calculation of the LJ n-m Pot Energy Parameters for Metals*, Phys. Stat. Sol. (a), 78, 595 (1983).

5. E.W. Lemmon, R.T. Jacobsen, *Int J. Thermophysics*, **25(1)** (2004) 21.

6. D.K. Belashchenko and O.I. Ostrovskii, *The Embedded Atom Model for Liquid Metals: Liquid Gallium and Bismuth Chemical Thermodynamics and Thermo-Chemistry,* Russian Journal of Physical Chemistry **80**, No.4 pp 509-522, Pleiades Publishing Inc, (2006).

7. K. Refson, *Moldy: A Portable Molecular Dynamics Simulation Program for Successive and Parallel Computers*, CPC **126**(3), 11 April 2000, pp. 309-328, Elsevier Science B.V., (2000).

8. Ahmed Moosa, *Oxidation and Corrosion Mechanism of Steel Alloys and Inconel 600 Alloy in Liquid–Lead-Bismuth Eutectic*, Eng. & Tech., Vol. 26, No. 11, (2008).

ORGANIC FUNCTIONALIZATION OF METAL OXIDE SURFACES: NUMERICAL SIMULATIONS OF PEPTIDES ADSORPTION ONTO TITANIA SURFACES USING QUANTUM-ESPRESSO AND GROMACS CODES ON CRESCO HPC

Caterina Arcangeli, Ivo Borriello, Massimo Celino

ENEA UTTMAT-DIAG C. R. Casaccia

Peptides that bind inorganic surfaces and template the formation of nanometer-sized inorganic particles are of great interest for the self- or directed assembly of nanomaterials for sensors and diagnostic applications. These surface-recognizing peptides can be identified from combinatorial phage-display peptide libraries, but little experimental information is available for understanding the relationship between the peptide sequence, structure at the titania surface, and function. First principles simulations based on Density Functional Theory (DFT) and classical Molecular Dynamics (MD) are carried out to investigate the structure and stability of single amino acids and of the full peptide adsorption on TiO_2 anatase (101). Our results shed light on the role played by some amino acids that are known to be essential in selective adsorption on TiO_2, as well as their structural conformation upon the surface.

Introduction

Investigations of the structure and properties of the interface between biological matter and titania surfaces has attracted a great deal of attention in recent years. Titania-biomolecule interfaces are of fundamental importance not only for developing biocompatible materials for surgical implants, but also for the bioinspired fabrication of nanostructured materials [1]. Many recent studies in this wide-ranging area have made use of the recognition properties between peptides and inorganic materials. Such recognition between peptides and titania has been explored by using combinatorial screening approaches including phage-display and cell-surface display [2]. Experimental characterization of the peptide-titania interface [3] has revealed that electrostatic interactions play a key role and that peptide flexibility may also be important [4]. In order to shed some light on this interaction, we set out to investigate computationally the binding of arginine, lysine, aspartic acid on the (101) surface of TiO_2 anatase, as they have been identified as potential peptide "docking points. In particular, DFT calculations will be employed to study the kind of binding mechanisms in terms of electronic charge transfer, adhesion energy and amino acids mobility upon the surface, with the aim to define an interaction model of the interaction selective-binding peptides and titania oxides. In addition MD simulations of the full peptide (13 amino acids) and titania surface in the presence of the solvent will be performed to investigate the role of the peptide flexibility and of the solvent on the interactions with the titania oxides.

Quantum-ESPRESSO and GROMACS codes

Quantum-ESPRESSO [5] is an integrated suite of computer codes for electronic-structure calculations and materials modeling. QUANTUM ESPRESSO implements a variety of methods and algorithms aimed at a chemically realistic modeling of materials from the nanoscale upwards, based on the solution of the density-functional theory (DFT) [6] problem, using a plane waves (PWs) basis set and pseudopotentials (PPs) [7] to represent electron–ion interactions. The codes are constructed around the use of periodic boundary conditions, which allows for a straightforward treatment of infinite crystalline systems, and an efficient convergence to the thermodynamic limit for aperiodic but extended systems, such as liquids or amorphous materials. Finite systems are also treated using supercells; if required, open-boundary conditions can be used through the use of the density-countercharge method [8].

Quantum-ESPRESSO can thus be used for any crystal structure or supercell, and for metals as well as for insulators. The basic computations/simulations that can be performed include: i) calculation of the Kohn–Sham (KS) orbitals and energies for isolated or extended/periodic systems, and of their ground-state energies; ii) complete structural optimizations of the microscopic (atomic coordinates) and macroscopic (unit cell) degrees of freedom, using Hellmann–Feynman forces and stresses; iii) ground state of magnetic or spin-polarized systems, including spin–orbit coupling and noncollinear magnetism; iv) ab initio molecular dynamics (MD), using either the Car–Parrinello Lagrangian or the Hellmann–Feynman forces calculated on the Born–Oppenheimer (BO) surface, in a variety of thermodynamical ensembles, including NPT variable-cell MD. Quantum-ESPRESSO code runs on many different computer architectures and allows good scalability till a large number of processors depending on the system size. We use a Quantum-ESPRESSO code compiled with Intel Fortran compiler, Math Kernel Library (MKL) and Message Passing Interface (MPI) parallelization on the high performance computer CRESCO [9], with a good scalability up to hundreds of cores.

GROMACS (GROningen MAchine for Chemical Simulations) [10] is a molecular dynamics (MD) package to simulate the Newtonian equations of motion for systems with hundreds to millions of particles. It is primarily designed for biomolecular systems like proteins and lipids, but due to its highly versatility and fast calculation of the non bonded interactions (that usually dominate simulations) it is currently applied also on non-biological systems. GROMACS implements a number of different force fields (i.e. functions and parameter sets to describe the potential energy of a system of particles, typically atoms) such as AMBER, CHARMM, OPLS and GROMOS. GROMACS uses scripts to convert molecular coordinates from a PDB file into formats it uses internally. Once a configuration file for the system (several molecules including solvent) has been created, the actual simulation run produces a trajectory file, describing the movements of the atoms over time. This trajectory file can then be analyzed and visualized with a number of supplied tools. GROMACS is open source software released under the GPL. The program is written for Unix-like operating systems and can be run in parallel on multiple CPU cores or a network of machines using the MPI library. We use the highly optimized parallel version 4.5.4 of GROMACS installed on the high performance computer CRESCO [9].

Computational details

Our study is based on DFT in the generalized gradient approximation (GGA) of Perdew, Burke, and Ernzerhof (PBE) [11], and the plane-wave pseudopotential scheme as implemented in the Quantum-ESPRESSO package. Vanderbilt-type ultrasoft pseudopotentials [12] have been used with a plane-wave energy cutoff of 30 and 300 Ry for the electronic wave functions and the total charge density, respectively. The optimized geometries are obtained using the Hellman-Feynman forces with the Broyden-Fletcher-Goldfarb-Shanno algorithm to minimize the total energy with respect to the atomic positions. By the above method, we firstly optimized pure anatase TiO_2 The Brillouin zone was sampled using a (4×4×4) Monkhorst-Pack k-point grid [13]. We utilized a (2×3) periodic slab to model the surface structure and properties, which contained four O-Ti-O trilayers and was separated by a vacuum gap of 20 Å thickness. The top two trilayers were relaxed, while the bottom two tri-layers were kept fixed to mimic the bulk region.

The MD simulations of the system composed by the peptide, the TiO_2 anatase (101) surface and the solvent are performed with GROMACS v4.5.4 following the simulation protocol of Kang *et al.* [14] by using the OPLSAA force field [15] modified by introducing the nonbonded parameters for TiO_2 surface [16, 17]. The water solvent molecules are modeled by the simple point charge SPC model [18]. The system composed by about 4400 atoms is energy minimized and after 200 ps of initial equilibration, data collection is started with trajectory saved every 0.2 ps. The simulation consists of a total run of 15 ns.

Results

The TiO_2 anatase (101) surface is very corrugated, with a characteristic sawtooth profile perpendicular to the 010 direction, as shown in *figure 1a*. On it, both fivefold- and sixfold-coordinated Ti atoms are present (Ti(5c) and Ti(6c) respectively), as well as twofold and threefold oxygens (O(2c) and O(3c) respectively). Each bridging oxygen O(2c) is bonded to one Ti (5c) atom and one Ti(6c) atom forming a Ti-O-Ti angle of nearly 102 degrees.

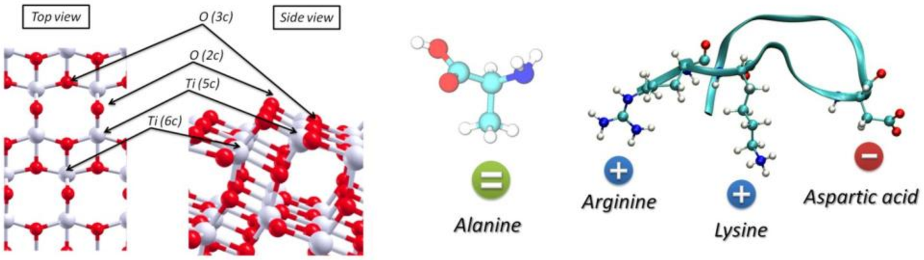

(a) (b) (c)

Figure 1: *Top and side view of TiO_2 (101) anatase surface reconstruction: low coordinated Ti(5c) and O(2c) atoms play a crucial role onto peptide adhesion mechanisms (a). Alanine is a neutral amino amioacid that does not bind to the TiO_2 surface: it is used as a term of comparison (b). TiO_2-binding peptide: the peptide backbone is shown as a ribbon while the relevant amino acids for adhesion mechanisms are represented through balls and sticks (c).*

The orbital rearrangements of the dangling bonds of the low coordinated Ti(5c) and O(2c) atoms determines a charge redistribution over the surface, giving rise to a negative charge localization around the O (2c) atoms, whereas a positive charge is distributed around the Ti(5c) atoms. This means that the positively charged amino acids arginine and lysine (*figure 1c*) are attracted by O (2c) atoms and negatively charged aspartic acid is attracted by Ti(5c) ones. In order to achieve information about the bonding energy of that amino acids as well as their mobility upon the surface, a great number of possible equilibrium configurations over the surface for each aminoacid has been explored. Starting from the arginine, we have found five equilibrium configurations. They are characterized by different orientation of the amino acid lateral chain with respect to the surface, as shown in *figure 2*. Arginine analogues are found through successive truncations of the lateral chain. The Relative Formation Energy (RFE), that is the energy difference between the entire system and the isolated molecule and surface, calculated at each configuration, clearly shows that both arginine and its analogues are characterized by the same bonding chemistry, so even the smallest analogue well represents the bonding properties of the entire amino acid.

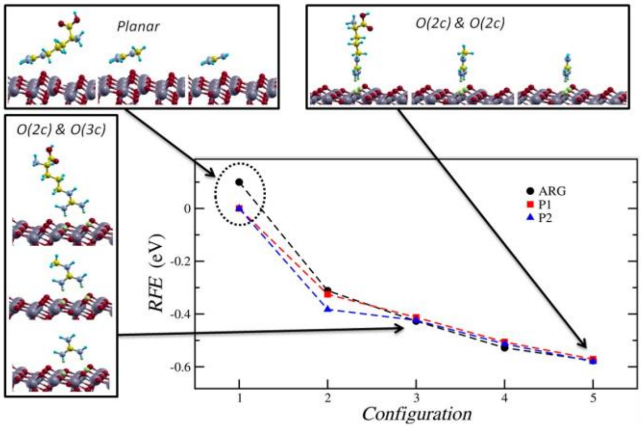

Figure 2: *Analysis of the possible adhesion configurations of arginine onto TiO_2 surface, to be compared with arginine analogues obtained by successive truncation of its lateral chain. The Relative Formation Energy (RFE) at each binding configuration concerning with arginine is very close to those related to the analogues.*

The lowest-energy (that is the most stable) equilibrium configuration is characterized by a vertical orientation of arginine with the terminal charged part oriented on O(2c) atom, as expected. Moreover, the bonding energy (that is the energy necessary to put arginine far from the surface) has been computed by comparing the total energy of entire system with the arginine bonded to the surface, and with the arginine at a distance of 10 Å from the surface. The result is shown in *figure 3*: no significant energy variation has been found by increasing the molecule-surface relative distance.

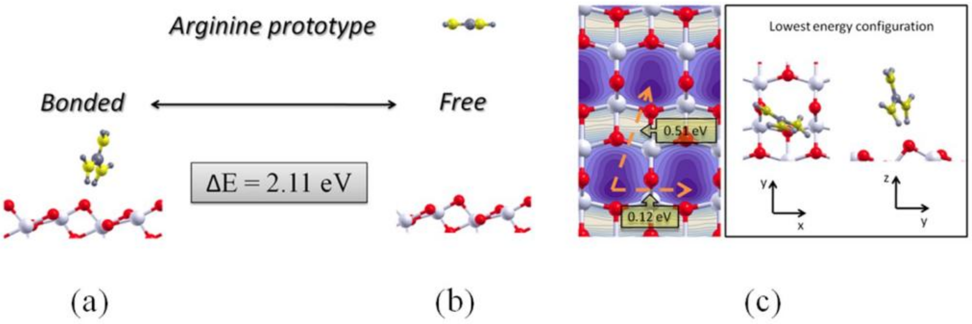

Figure 3: *The binding energy of arginine analogue to the TiO_2 anatase (101) surface has been evaluated as the total energy difference between the bonded (a) and the unbonded (a) configuration of the entire TiO_2-arginine system. Topological map of the TiO_2-arginine bonding energy (c).*

To answer the next question how arginine diffuses on this surface, we calculated the adiabatic Potential Energy Surface (PES). This PES is defined by relaxing the height of arginine analogue from surface (for a set of fixed lateral coordinates of central C atom, these coordinates form an equidistant grid with a spacing between the grid points of about 0.5 Å in [101] and [010] directions), as well as all coordinates of the top substrate atoms. As shown in *figure 3(a)*, we found the global minimum located at the O(2c) site (dark blue in *figure 3c*) and the global maximum is located at along the Ti(6c)-O(3c) bridge. According to the principle of minimum energy change, we proposed two diffusion pathways (evidenced by the arrows in *figure 3c)* between global minima. On these pathways, the energy barrier is even calculated and reported in *figure 3c.*

Our study will be extended to lysine, aspartic acid and the neutral alanine for comparison. These energy scales will allow us to determine the best amino-acid choice in adhesion and to shed light on the great number of experimental results relative to the individuation of TiO_2-selective binding peptides.

In addition to the accurate *ab-initio* characterization of the adhesion mechanism of single amino acids onto the TiO_2 surface we performed preliminary MD simulations of the adsorption of the full peptide onto the metal surface. The amino acid sequence of the peptide, AMRKLPDAPGMHC, is used to construct a totally unfolded structure which is in turn employed as starting configuration for MD simulation. The folding of the peptide in water is achieved within 20 ns of MD simulation as shown in *figure 4*.

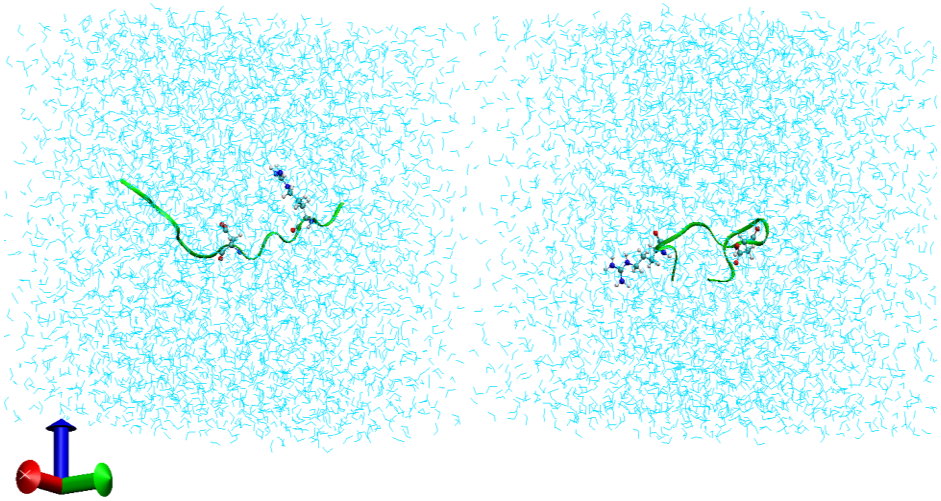

Figure 4: *Left: the starting totally unfolded peptide structure. Right: the peptide after 20ns-long MD simulation. The two residues crucial for the adhesion to the metal surface are depicted in ball and sticks.*

The obtained folded peptide is then placed close to the TiO_2 surface. The orientation is guided by the results obtained by the previous DFT approach. In particular the peptide is oriented with the lateral chains of the R and D amino acids perpendicular to the metal surface. In *figure 5* the configuration of the full system - composed of the folded peptide, the metal surface and the surrounding water molecules – at the the start and the end of MD simulation is shown.

This preliminary simulation shows that few nanoseconds of simulation are sufficient to form an interfacial water layer on the metal surface. The interfacial water molecules are quite stable and orientationally structured on TiO_2 surface forming an hydrogen bonding network induced by the surface. On the contrary the simulation time is not enough long to achieve the adsorption of the side chains of the peptide residues onto the surface. Therefore we will extend in the future the simulation time to investigate at atomic level the peptide adsorption behavior on the TiO_2 surface.

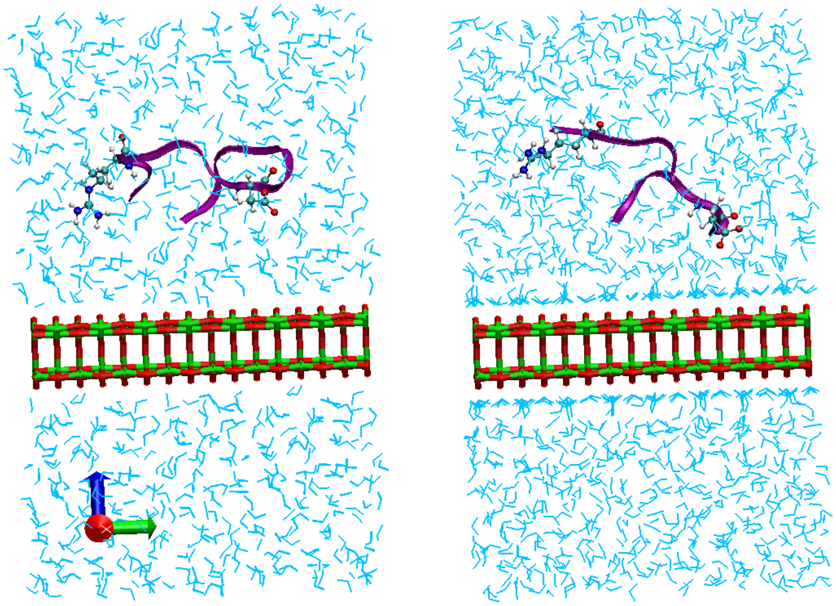

Figure 5: *Left: the system (TiO_2 surface relaxed + folded peptide + water molecules) at the start of the MD simulation. Right: the system at the end of the MD simulation. The two residues crucial for the adhesion to the metal surface are depicted in ball and sticks.*

Acknowledgment

We acknowledge the CRESCO Project High-performance Computing Facility, at the ENEA Portici Research Center, where most of the time-consuming simulations have been performed. We thank Dr. Giuseppe Aprea, Dr. Giulio Gianese and Dr. Simone Giusepponi for help with preliminary technical aspects and helpful discussion and suggestions.

REFERENCES

[1] Dickerson M. B., Sandhage K. H., Naik R. R., *"Protein- and Peptide-Directed Syntheses of Inorganic Materials"* Chem. Rev. **108** (2008) pp. 4935-4978.

[2] Gronewold T. M. A., Baumgartner A., Weckmann A., Knekties J., Egler C., *"Selection process generating peptide aptamers and analysis of their binding to the TiO2 surface of a surface acoustic wave sensor"* Acta Biomater. **5** (2009) pp. 794-800.

[3] Sano K.I., Shiba K. *"A hexapeptide motif that electrostatically binds to the surface of titanium"* J. Am. Chem. Soc. **125** (2003) pp. 14234-14235.

[4] Chen H. B., Su X. D., Neoh K. G., Choe W. S., *"Context-Dependent Adsorption Behavior of Cyclic and Linear Peptides on Metal Oxide Surfaces"* Langmuir **25** (2009) pp. 1588-1593.

[5] Quantum-ESPRESSO, http://www.quantum-espresso.org

[6] Parr R. G. and Yang W. *"Density Functional Theory of Atoms and Molecules"* Oxford University Press (1989).

[7] Pickett W. E., *"Pseudopotential methods in condensed matter applications"* Comput. Phys. Rep. **9** (1989) pp. 115-197.

[8] Dabo I., Kozinsky B., Singh-Miller N. E. and Marzari N., *"Electrostatics in periodic boundary conditions and real-space corrections"* Phys. Rev. B **77** (2008) pp. 115139-115151.

[9] Please visit the website http://www.cresco.enea.it for more information.

[10] GROMACS, http://www.gromacs.org/

[11] Perdew J.P., Burke K., and Ernzerholf M., *"Generalized Gradient Approximation Made Simple"* Phys. Rev. Lett. **77** (1996) pp. 3865-3868.

[12] Vanderbilt D., *"Soft self-consistent pseudopotentials in a generalized eigenvalue formalism"* Phys. Rev. B **41** (1990) pp. 7892-7895.

[13] Monkhorst H. J. and Pack J. D., *"Special points for Brillouin-zone integrations"* Phys. Rev. B 13 (1976) pp. 5188-5192.

[14] Kang Y., Li X., Tu Y., Wang Q., *"On the mechanism of protein adsoption onto hydroxylated and nonhydroxylated* TiO_2 *surfaces"*, J Phys Chem C **114** (2010) pp. 14496-14502.

[15] Jorgensen W., Maxwell D., and TiradoRives J., *"Development and testing of the OPLS all-atom force field on conformational energetics and properties of organic liquids"* J Am Chem Soc **118** (1996) pp. 11225-11236.

[16] Bandura A.V., Kubicki J.D., *"Derivation of Force Field Parameters for TiO 2 -H 2 O Systems from ab Initio Calculations"*. J Phys Chem B **107** (2003) pp. 11072-11081.

[17] Predota M., Bandura A.V., Cummings P. T., Kubicki J.D., Wesolowski D.J., Chialvo A.A., Machesky M. L., *"Electric Double Layer at the Rutile (110) Surface. 1. Structure of Surfaces and Interfacial Water from Molecular Dynamics by Use of ab-initio Potentials"* J Phys Chem B **108** (2004) pp. 12049-12060.

[18] Berendsen H.J.C., Postma J.P.M., van Gunsteren, W.F., Di Nola, A., and Haak, J.R, *“MD with coupling to an external bath*” J Chem Phys, **81** (1984) pp. 3684-3690.

Structure and molecular dynamics of a spherical cluster $Zr_{43}O_{86}$

Roberto Grena

Roberto.grena@enea.it
UTRINN-PCI - ENEA Casaccia Via Anguillarese, 301 00123 Roma

Structural properties and atomic scale dynamics of a small spherical cluster of zirconia (ZrO_2), with 43 atoms of Zirconium, are investigated using density functional theory and ab-initio molecular dynamics[1-3]. Zirconia nanoclusters with radius around 2 nm are experimentally investigated at the European Center of Ceramics (SCPTS) of Limoges (France), which supplied the experimental pair distribution function (PDF) of the nanoclusters and their approximative size. The aim of the work is to investigate if it is possible to reproduce the experimental PDF, and obtain insights of the atomic-scale structure and behaviour of such small clusters.
The work is made with the collaboration of Massimo Celino (ENEA) and of Olivier Masson, Philippe Thomas and Abid Berghout (SCPTS).

Computational methods

All the computations are made with CPMD code (plane wave - pseudopotentials) [4]. The starting configuration chosen at the beginning is a roughly spherical cluster cut from the cubic structure of zirconia (see *figure 1*), with 43 atoms of Zirconium. This is the smallest of three possible candidates compatible with the experimental size. Two different XC functionals are considered (BLYP and PBE, both of GGA type) [5-7]. As a general rule, BLYP is usually recommended for molecular systems, and PBE for extended systems; in this case we are in an intermediate situation.
Pseudopotential used are of Goedecker type [8] (hard pseudopotentials with relativistic corrections), and of Martins-Troullier type [9], with 12 valence electrons for Zr and 6 valence electrons for O. Three alternatives of computation are tried: BLYP-Go, PBE-Go, PBE-MT.

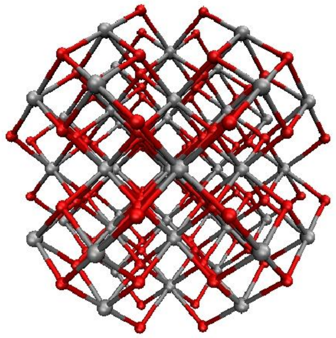

Figure 1: *Initial configuration of the cluster.*

Crystal structures

As a first test, before starting computations on clusters, the lattice size and stability of ZrO_2 was investigated with the three alternatives, for three zirconia crystal structures: monoclinic, tetragonal, and cubic. This is made in order to check the reliability of the functionals and pseudopotentials. *Figure 2* shows the results in the three cases (BLYP-Go, PBE-Go, PBE-MT). The qualitative results are correct (monoclinic is more stable than tetragonal, that is more stable than cubic; the volume is larger for monoclinic, and smaller for cubic). Equilibrium volume is overestimated (typical of GGA functionals) of a few %. The estimation of the pressure that induces phase transitions and a comparison with other works from literature support these results.
Table 1 shows the equilibrium volume and the minimum energy found, for the three cases.

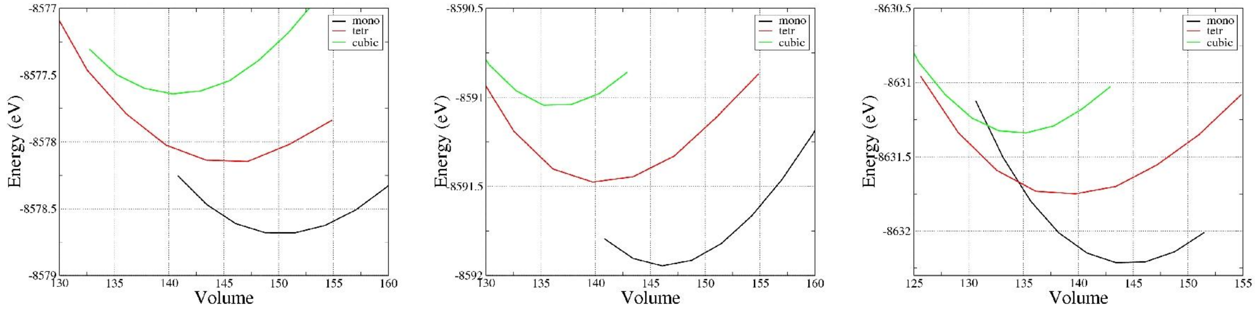

Figure 2*: Energy dependence on volume for the three different crystal structure (monoclinic, tetragonal, cubic), obtained with BLYP-Go (left), PBE-Go (centre) and PBE-MT (right).*

Table 1: *Equilibrium volumes and energies for the three lattice structure, with the three computation methods.*

	Monoclinic	Tetragonal	Cubic
BLYP-Go	V = 150.80 Å E = - 8578.68 eV	V = 145.59 Å E = - 8578.19 eV	V = 141.02 Å E = - 8577.64 eV
PBE-Go	V = 146.24 Å E = - 8591.93 eV	V = 141.99 Å E = - 8591.50 eV	V = 136.83 Å E = - 8591.07 eV
PBE-MT	V = 144.79 Å E = - 8632.24 eV	V = 140.39 Å E = - 8631.76 eV	V = 135.02 Å E = - 8631.35 eV

Geometric optimizations

The initial symmetric configuration of the cluster (*figure 1*) is slightly deformed introducing a random deviation of the initial coordinates with gaussian distribution ($\sigma \approx 0.02$ Å), to break the initial symmetry and let the relaxation start. Then the cluster is optimized. In two cases (BLYP-Go and PBE-Go), in order to obtain convergence, the relaxation is started at a very low cutoff (20 Ry) and then the cutoff is increased at the end of the relaxation, up to 150 Ry. PBE-MT was instead directly optimized with a cutoff of 80 Ry, since there were no convergence problems; the cutoff was not increased further, since the result was already clear. The loss of energy in the relaxation, with respect to the initial configuration, is 63.70 eV for BLYP-Go, 64.67 eV for PBE-Go, and 58.92 eV for PBE-MT (not comparable with the other two for the different cutoff). The resulting optimized clusters was shown in *figure 3*. The clusters have all loose oxigens and are strongly different from the initial structure. The PDFs obtained are shown in *figure 4*. None of the clusters reproduce the experimental PDF.

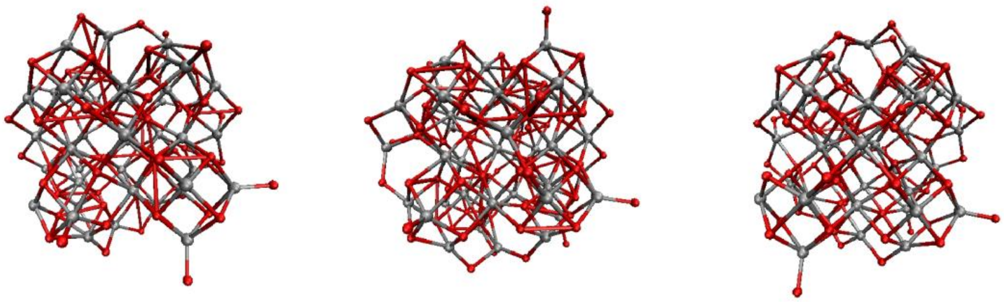

Figure 3: *Configurations obtained from geometrical optimization, for BLYP-Go (left), PBE-Go (centre) and PBE-MT (right).*

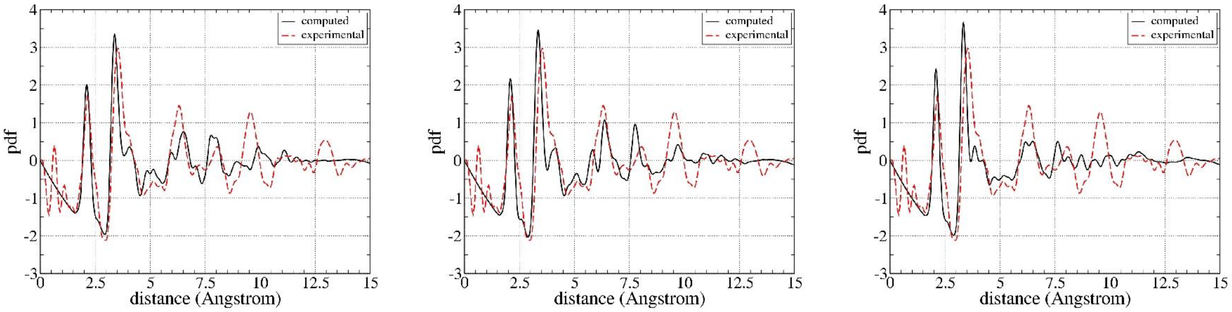

Figure 4: *PDFs obtained from geometrical optimization, for BLYP-Go (left), PBE-Go (centre) and PBE-MT (right).*

A test was made starting also from the monoclinic structure, with the same number of atoms, to see if the same features emerges using other structures; the test was made with PBE-MT. The result of the geometrical optimization starting from monoclinic structure is shown in *figure 5*, with the resulting PDF. The structure seems more compact than the resulting cluster from cubic starting structure, and no loose oxigens appear; however, it is very irregular and its PDF does not reproduce the experimental one. Its energy is higher of 0.73 eV than the energy of the optimized cluster from cubic structure.

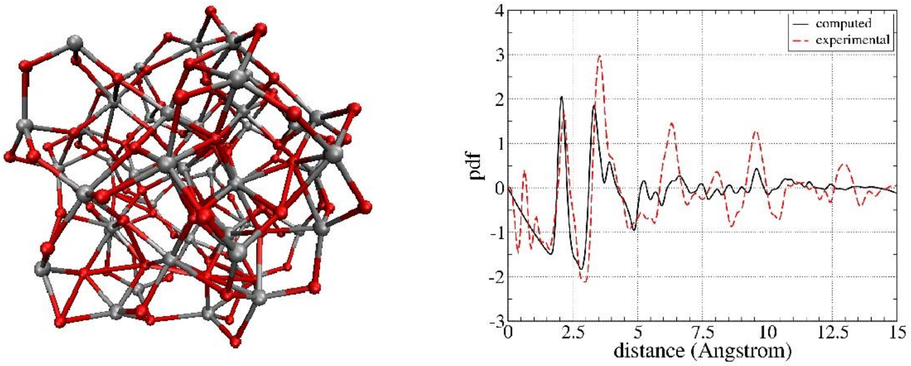

Figure 5: *Configuration obtained from geometrical optimization, starting from the monoclinic structure, for PBE-MT (left), and the resulting PDF (right).*

Car-Parrinello molecular dynamics computations

Car-Parrinello (CP) molecular dynamics simulations are made on the cluster, with two aims:

1) obtaining other possible energy minima, since the minima found with the geometrical optimization are not compatible with the experiment;
2) obtaining directly the PDF from molecular simulations, without introducing an artificial spreading of the atomic positions.

Minima from simulated annealing

Starting from the cubic configuration with small random displacements, a CP simulation with thermostat at 20 K is performed to lower the energy and find a possible minimum. Then the system is heated above 1000 K to modify its structure and re-cooled at 20 K to find another possible minimum, and so on.

The temperature evolution of the system and its Kohn-Sham (KS) energy are shown in *figure 6*, for BLYP-Go and PBE-Go (PBE-MT computation is in process). The calculation for BLYP-Go and PBE-Go is stopped after only 2 minima, since the cluster appears to be almost destroyed after the first re-heating and cooling.

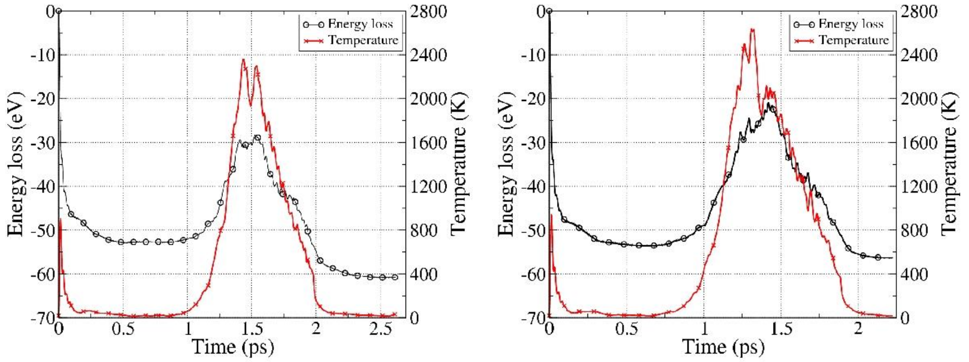

Figure 6: *Kohn-Sham energy and temperature evolution for a cluster in the annealing simulation, for BLYP-Go (left) and PBE-Go (right).*

Configurations found at the first minimum are shown in *figure 7*: the first row shows the configurations found from CP (with a final geometrical optimization), the second row shows the PDFs obtained. The configurations appear different from the cubic structure, but the clusters have good sphericity and they have no loose oxigens on the surface.

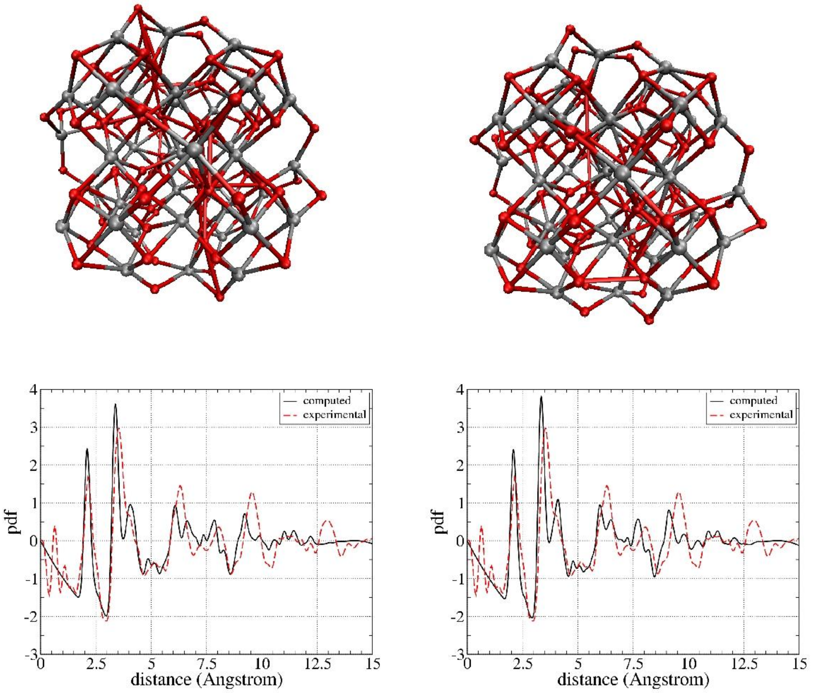

Figure 7: *Configurations obtained for the first minimum in the annealing. Left: BLYP-Go, right: PBE-MT. Below: PDFs obtained.*

However, their energy is above the energy of the clusters obtained from direct geometrical optimization. PDFs do not seem to reproduce the experimental results.

Configurations found at the second minimum are shown in *figure 8*, with the corresponding PDFs. After the heating and re-cooling, the cluster appears completely distorted, non-spherical, and with loose atoms. The PDFs shows that, apart from the first peaks of the nearest neighbours, no significant order is found at higher distances (the PDF is almost flat above 7 Å). Since the structure is almost lost, no further minima are computed. However, it must be noted that the energy found for this configuration in the BLYP-Go case is the lowest (it is lower of other CP results and also of direct geometrical optimization).

Table 2 summarizes the energies found for the different computations and minima. The zero of the energies is the energy of the initial cubic configuration.

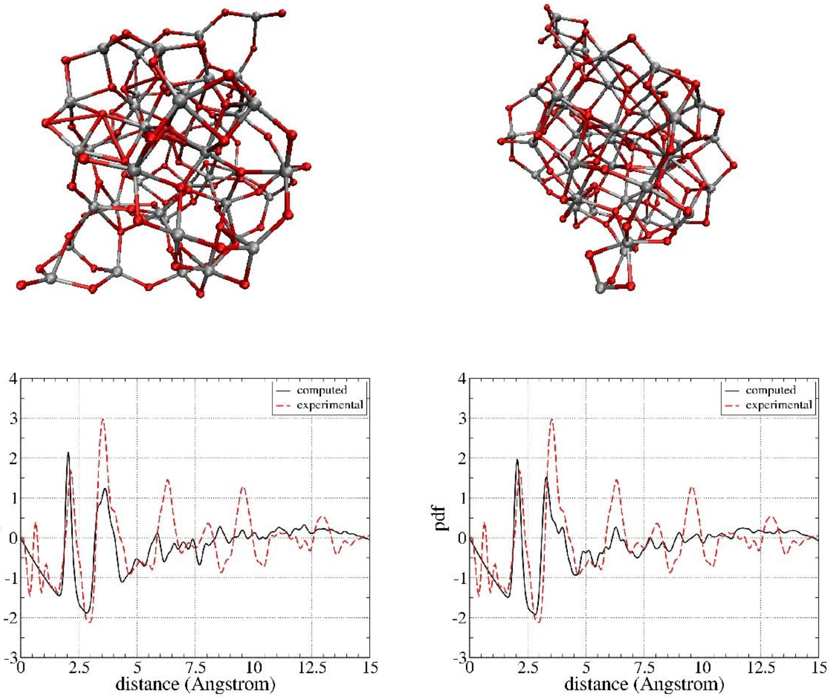

Figure 8: *Configurations obtained for the second minimum in the annealing. Left: BLYP-Go, right: PBE-Go. Below: PDFs obtained.*

Table 2*: Energies found (with respect to the cubic configuration) for the minima of the annealing. Also the energies found in the geometrical optimization are summarized.*

	BLYP - Go	PBE - Go	PBE - MT
CP min. 1 (g.o.)	- 56.83 eV	- 57.36 eV	
CP min. 2 (g.o.)	- 64.86 eV	- 60.21 eV	
g.o. from cubic	- 60.24 eV	- 61.72 eV	- 58.92 eV
g.o. from monoclinic			- 58.19 eV

PDF directly computed from CP

All the PDFs shown above are calculated from the equilibrium configuration, assigning a gaussian spread of 0.2 A to each atom. A more rigorous approach is the direct computation of PDFs from a thermally stabilized CP simulation; in this way, different thermal agitation of the various atoms can be accounted for. However, building a PDF require a quite large computational time. The PDF will depend on the starting configuration, since simulation times are too short to obtain transitions to other minima.

In *figure 9*, results are shown. The first two PDFs are obtained starting from the first minimum of the annealing, for BLYP-Go (left) and PBE-Go (center). A PDF obtained starting with the initial cubic configuration, thermalized at 293.15 K without initial quenching, is shown at the right (using PBE-Go).
Computations are in progress using PBE-MT.

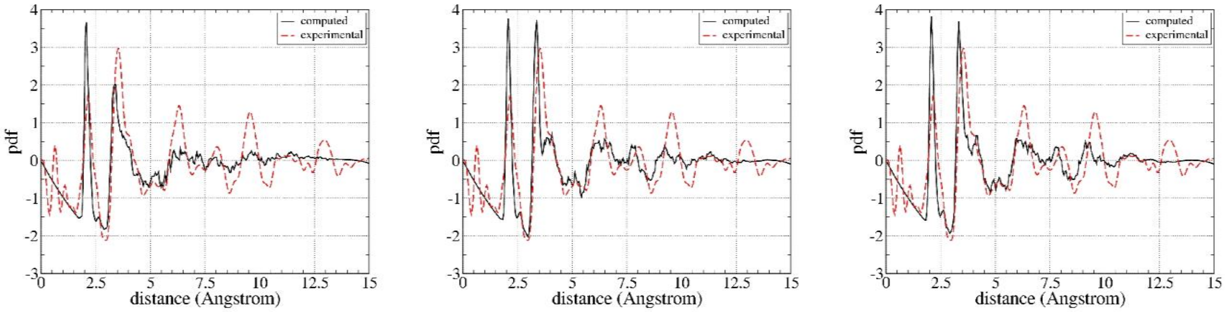

Figure 9: *PDFs obtained directly from CP simulations, for BLYP-Go starting from the first minimum found in the annealing (left), for PBE-Go from the first minimum (centre), and for PBE-Go starting from the cubic structure (right).*

One can see that the PDFs shows a sharper and higher first peak at Zr-O, while the peak Zr-Zr is significantly lowered and the structure at larger distance is almost lost (completely for BLYP-Go, while some shallow peaks remains for PBE-Go). There are no significant differences between a simulation made starting from the optimized cluster found in the first minima, and a simulation made starting directly from the cubic configuration.

Hydrated cluster

Since there is the possibility that experimental clusters have surface impurity (especially hydrogen or water), computations were made on a hydrated cluster, starting from the cubic configuration (shown in *figure 10*, left: the smallest atoms on the surface are hydrogens). A simple geometrical optimization does not converge. With a CP quenching at 20 K, the final result obtained is shown in the same figure, with PBE-MT. The result confirm the fact that hydrated clusters preserves better the cubic structure, a fact already seen in other simulations of different clusters. The PDF obtained (computed without considering Hydrogen atoms) is shown in the right part of Figure 10: it shows sharp peaks typical of regular structures. The structure is far too regular with respect to the experimental data.

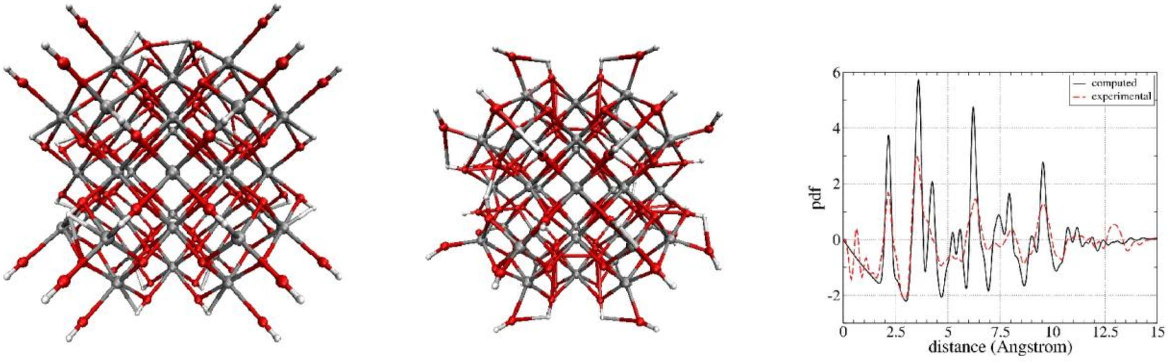

Figure 10: *Hydrated cluster: starting configuration (left), after a CP quenching to optimize geometry (center), PDF obtained (right).*

Conclusions and further works

Clusters with such a small size show energy minima with irregular configurations, except in the case of a hydrated cluster. The experimental PDF shows a more regular structure. This can be due to the fact that the chosen cluster is too small and it is not present in the experimental sample in significant amount; or to the fact that experimental clusters are partially hydrated.

Currently, calculations are in progress with PBE-MT for CP annealing. Geometrical optimization of a larger cluster ($Zr_{55}O_{110}$) is in progress. Computations with partially hydrated clusters are planned.

References

[1] P. Hohenberg, W. Kohn, Inhomogeneous electron gas, Physical Review 136 (1964), B864-B871.

[2] W. Kohn, L.J. Sham, Self-consistent equations including exchange and correlation effects. Physical Review 140 (1965), A1133-A1138.

[3] R. Car, M. Parrinello, Unified Approach for Molecular Dynamics and Density Functional Theory, Physical Review Letters 55 (1985), 2471-2474.

[4] W. Andreoni, A. Curioni, New advances in chemistry and material science with CPMD and parallel computing. Parallel Computing 26 (2000), 819-842.

[5] A.D. Becke, Density-functional exchange-energy approximation with correct asymptotic behavior, Physical Review A 38 (1988), 3098-3100.

[6] Lee, C.; Yang, W.; Parr, Development of the Colle-Salvetti correlation-energy formula into a functional of the electron density, Physical Review B 37 (1988), 785-789.

[7] J.P. Perdew, K. Burke, M. Ernzerhof, Generalized Gradient Approximation Made Simple, Physical Review Letters 77 (1996), 3865-3868.

[8] S. Goedecker, M. Teter, J. Hutter, Separable dual-space Gaussian pseudopotentials, Physical Review B 54 (1996), 1703-10.

[9] N. Troullier, J.L. Martins, Efficient pseudopotentials for plane-wave calculations, Physical Review B 43 (1996), 1993-2006.

An Immersed Volume Method for Large Eddy Simulation of compressible flows

D. Cecere*, E. Giacomazzi, N. Arcidiacono, F.R. Picchia, F. Donato

* donato.cecere@enea.it *UTTEI-COMSO ENEA C.R. Casaccia*

1. Introduction

The development of Large Eddy Simulation (LES) as a methodology for different kinds of turbulent flows, ranging from problems of scientific interest to those with engineering applications, has been possible due to the rapid increase in computational power. The primary goals of a successful LES in engineering computational fluid dynamic problems, are accuracy, robustness and handling of complex three-dimensional geometries. In fact many flow physical problem involve geometrical complexities with irregular boundaries that usually are not alligned with the grid. Two major classes of methods are suitable for treating arbitrarily complex geometries with cartesian grids and distinguished on the basis of their approach to impose boundary conditions in the cells cut by the solid interface. The first is the classical Immersed Bounday (IB) methods where special interpolations are adopted to set the value of dependent variables in the cut cells [1]. These methods are attractive because of their simplicity, but their major drowbacks are the occurrence of non-divergence free velocities in incompressible flows and spurius non physical pressure oscillations in compressible or density variable flows since it does't strictly conserve quantities as mass, momentum and kinetic energy near the irregular boundaries. A second class of IB methods is the cut-cell method (also called Cartesian grid method) introduced first by Clarke [2]. The cut-cell method is based on a finite-volume discretization of the flow equations in the cells cut by the immersed interface and the discrete conservation is verified. With a staggered grid, the density volume cell and the cells associated with each of the three velocity components are at different locations and will generally have a different shape when they are cut by an embedded boundary. A cut cell scheme for a staggered grid must deal with this extra complexity in a consistent manner. The purpose of this work is to present a new efficient, conservative, hybrid high-order accurate Cartesian cut-cell method, called Immersed Volume Method (IVM) for the compressible flows solved by a finite difference code on three dimensional not uniform cartesian staggered grids. The geometrical accuracy of the intersecting surface is determined only by the stereolithography representation (STL) and not by the IVM method. In fact, for each cut cell, unlike classical cut cell methods, the intersecting surface is not approximated by a plane but the STL triangulation is retained (see zoomed in view in *figure 1* where intersecting surfaces with different normals can be identified). This method is also suitable for the extension to solid/fluid heat conduction and to moving boundaries. The full geometrical characteristics of the cut cells are identified in a preprocessor procedure. Flow variables fluxes are computed in the cut cells and in a second adjacent layer to couple IVM with the finite difference method of the general code. The IVM method solves exactly the flow variables in the cut cells and links the velocities and energy fluxes to the thermodynamic variable changes, overcoming in this way the drowbacks of classical IB methods. The flow variables are stored at the cut-cell centroid and, to ensure numerical stability for small cells, the basic idea is to combine several neighbouring cells together by adopting a slave-master cell merging technique [3] so that the interfaces between merged cells are ignored and waves can travel in a newly combined larger cell without reducing the global time step.

2. Immersed Volume Method

In the Immersed Volume Method a finite volume approach is applied to the two cell's layers (unlike general cut cell methods) adjacent to the solid surface. The first layer consists of cells that are directly cut from the solid surface, while the latter is formed by fluid cells that are in contact with cut cells. The presence of this second layer is needed to connect the finite volume method with the finite difference scheme of the general code. Because of the staggering arrangement, momenta are located half a cell width from thermodynamic variables and consequently four control volumes are defined associated to the three momenta and scalars (density, total energy, chemical species). Rather than storing the flow variables at a Cartesian cell center, the variables are collocated at the true cut-cell volume centroid and the fluxes of these variables are estimated at the centroids of the faces bounding the cut-cell. In order to do this, for each of the four general variable (scalars and velocities), the geometric characteristics of the cut control volume have to be known. The geometric features of a 3D cartesian cut cell as the mass volume centroid, the volume of fluid, the polyhedron faces's areas and centroids are then used to evaluate interpolation of variables and to calculate the fluxes in the solution of the Navier-Stokes equations. A triangulated surface mesh is used to represent the boundary surface (see zoom in *figure 1*). After calculating all geometric properties of the cut cells, the problem associated to small cut cells is solved by means of a merging technique [3]. The complete set of filtered transport equations expressing the conservation of mass, momentum, species, energy and the thermodynamic equation of state describing the gas behaviour are solved. While the flux evaluation is straightforward in structured grid areas, it becomes more difficult on partial surfaces at fine-coarse cell interfaces and near boundaries. In the proposed formulation, a third order least-squares method is utilized to obtain a discretization scheme which is flexible in terms of the local mesh topology and the presence and shape of embedded boundaries. Because of the staggered approach and in order to avoid spurious oscillations, the least square method is replaced by a Moving Least Square method (MLSM) in the calculation of the velocities on the slave's face cell and in the general evaluation of temperature, enthalpy and species gradients in case of reactive flows. The inviscid surface fluxes are formulated using a modified version of the advection upstream splitting method (AUSM). The general convective or diffusive term Qi in the transport equation for a second layer cell is:

$$Q_i = \left[f_{i,p}^{IVM} c_{i,p} + f_{i,n}^{IVM} c_{i,n} + f_{i,p}^{fd} \left(1 - c_{i,p}\right) + f_{i,n}^{fd} \left(1 - c_{i,n}\right) \right] / Vol_{2l}$$

where Vol_{21} is the volume of the second layer cell, $f_{i,p}^{IVM}$ is the flux, on the positive face p (n, stands for the negative one) with normal i, calculated by the finite volume solver of the IVM method, f_i^{fd}, p that calculated by the general finite difference code and the coefficient $c_{i,p}$ is 1 if the positive (negative) face is in contact with a cut cell, 0 otherwise. The dynamic Smagorinsky model is adopted for the evaluation of turbulent viscosity and fractal model is used to couple turbulence and combustion [4].

3. Numerical results and conclusions

The accuracy and robustness of the Immersed Volume Method is validated by computing two three-dimensional test cases. The first is the LES of the Bakic experiment [5] of the flow past a sphere ith a sting at Re = 51500, the second is the LES of a stoichiometric preheated (650K) premixed Methane/Air flow past a cube at Re = 3200 in a square duct. The first simulation is the LES of the Bakic experiment [5] of the flow past a sphere with a sting.

The Reynolds number based on the free-stream velocity is defined as

$Re_D = \frac{\rho_\infty U_\infty D}{\mu_\infty} = 51500$, with D being the sphere diameter (0.0614m).

A cartesian computational domain -: [-1.7D, 5D]x[-4.88D, 4.88D]x[-4.88D, 4.88D] is used with 280x140x140 points in the z (stream-wise), x and y directions respectively. The grid is locally refined near the surface of the sphere, along the stick (that has a diameter d of 0.13D) and near the separation regions. *Figure 1* shows axial velocity snapshot and isosurfaces of pressure. It's clearly identified the strong recirculation region downstream the sphere with a dimension of approximately one diameter, the compression region in front of the sphere and the expansion on the sphere surface at the separation region.

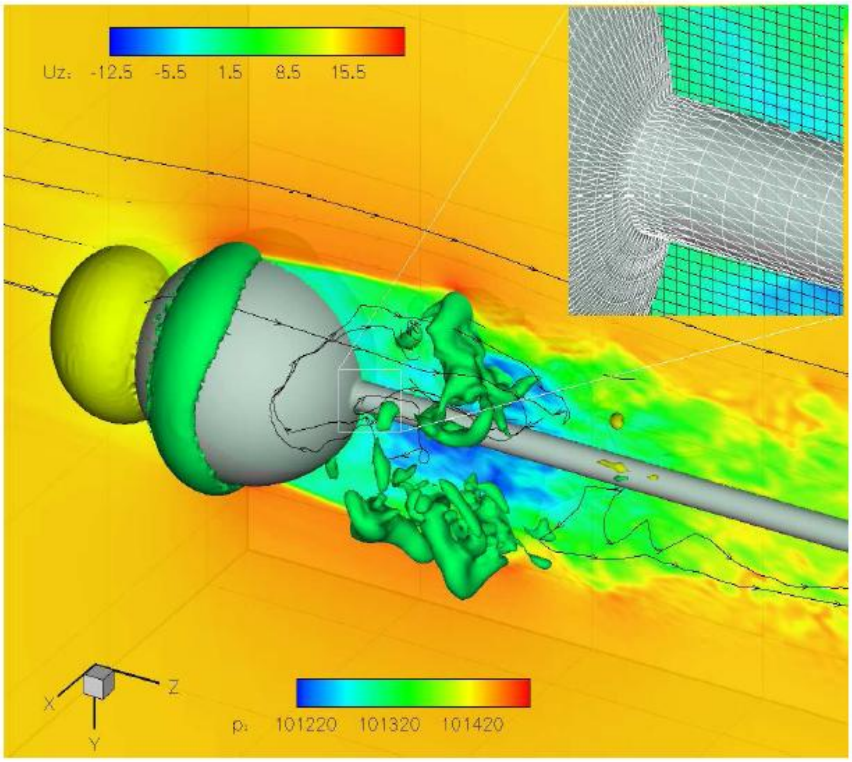

Figure 1: *Instantaneous axial velocity; pressure isosurfaces at 101317 Pa and 101409 Pa. Zoomed in view: STL of the solid surface (white lines) and simulation grid (black lines).*

The flow past a cube with combustion is chosen as an appropriate validation test case, because of its sharp edge boundaries, cut cells with internal volume and faces' centroids and sharp density and velocities gradients. The Reynolds number based on bulk quantities at the duct section (assuming its half width as reference length) crossing the cube leading edge $Re_{LED} = 3200$ and the maximum Mach number is ~ 0.05. For the three-dimensional simulation of a uniform flow past a cube, a computational domain -:[−2L, 3.5L]x[−2L, 2L]x[−2L, 2L] is used, L being the cube size. The cartesian not uniform domain has 120x80x80 grid points in the axial and span-wise directions. It is clearly visible the separation region that occurs near the lower edge of the cube and the consequent formation of a lateral first recirculation region at the side walls immediately after the separations. The flame is attached in the second recirculation region downstream of the cube bluff-body and because the first lateral vortex is able to go up stream up to the leading edge of the cube (see *figure 2*).

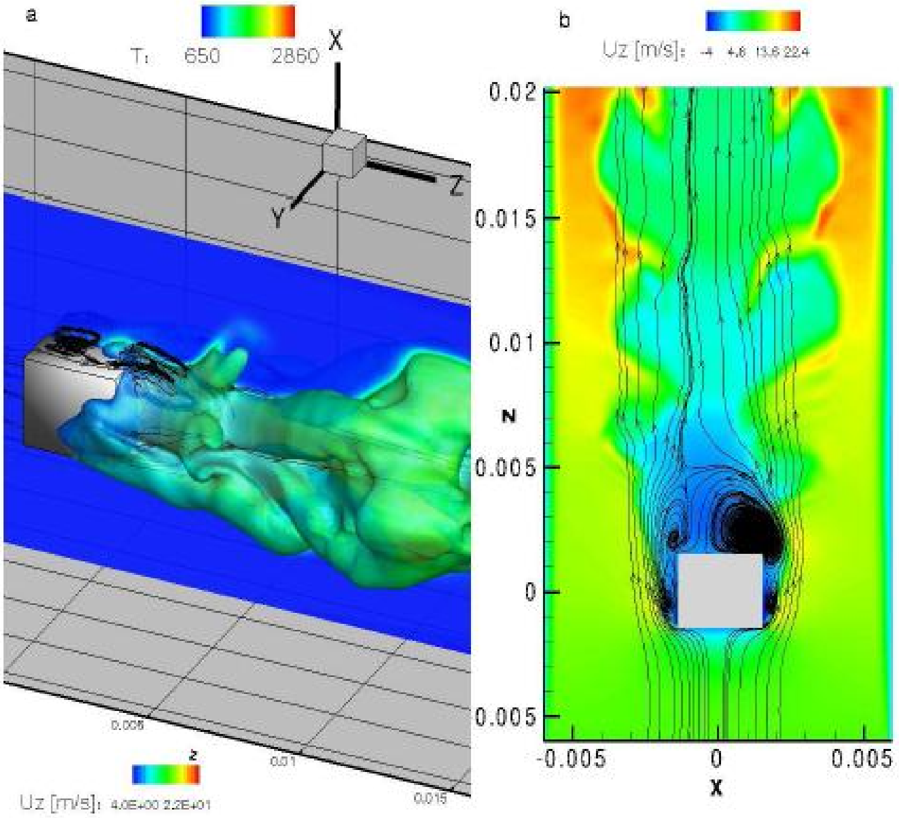

Figure 2: *Premixed flame past a cube: a) Temperature isosurface (1500K) coloured by axial velocity Uz and Temperature slice; b) x-z plane of instantaneous Uz with streamlines.*

A cut-cell based Cartesian grid method for three-dimensional compressible flows and not-uniform staggered grid is presented for the first time. The robustness of IVM method is tested with high Reynolds numbers LES without adopting multi-grid techniques. A LES of premixed bluff body flame is also presented to demonstrate the capability of the method to strictly conserve quantities as mass overcoming the drawbaks of classical IB methods.

7. References

[1] E.A. Fadlun, R. Verzicco, P. Orlandi, J.Mohd-Yusof, Combined immersed-boundary finite difference methods for three-dimensional complex flow simulations, J. Comput. Phys. 161(2000) 35-60.

[2]. D. Clarke, M. Salas, H. Hassan, Euler calculations for multi-elements airfoils using Cartesian grids, AIAA J. 24 (3) (1986) 353-358.

[3]. M.H. Chung, Cartesian cut cell approach for simulating incompressible flows with rigid bodies of arbitrary shape, Comput. Fluid 35 (2006) 607-623.

[4]. E. Giacomazzi, V. Battaglia and C. Bruno, The Coupling of Turbulence and Chemistry in a Premixed Bluff-Body Flame as Studied by LES, Combustion and Flame, 138 (2004) 320-335.

[5]. V. Bakic, M. Schmid, B. Stankovic, Experimental Investigaion of Turbulent Structures of Flow Around a Sphere, Thermal Scinces, 10 (2006), 97-112.

Normal and lognormal SABR and multiscale SABR models: option pricing and calibration

Lorella Fatone
Dipartimento di Matematica e Informatica, Università di Camerino, e-mail: lorella.fatone@unicam.it

Francesca Mariani
Dipartimento di Scienze Economiche, Università di Verona, e-mailfrancesca.mariani@univr.it

Maria Cristina Recchioni
Dipartimento di Management, Università Politecnica delle Marche, e-mail: m.c.recchioni@univpm.it

Francesco Zirilli
Dipartimento di Matematica "G. Castelnuovo", Università di Roma "La Sapienza", e-mail: f.zirilli@caspur.it

We propose a multiscale SABR model to describe the dynamics of forward prices/rates. This model consists of a system of three stochastic differential equations whose independent variable is time and whose dependent variables are the forward prices/rates and two stochastic volatilities varying on two different time scales. Let R and R^+ be respectively the sets of real and of positive real numbers, let t be a real variable that denotes time and x_t, $v_{1,t}$, $v_{2,t}$, t□0, be the stochastic processes that describe respectively the forward prices/rates and the two stochastic volatilities associated to the forward prices/rates. The dynamics of the stochastic processes x_t, $v_{1,t}$, $v_{2,t}$, $t>0$, is defined by the following system of stochastic differential equations:

$$dx_t = |x_t|^{\beta}(v_{1,t}dW_t^{0,1}+v_{2,t}dW^{0,2}_t),\ t > 0, \qquad (1)$$

$$dv_{1,t} = \varepsilon_1 v_{1,t}\, dW^1_t, \qquad t > 0, \qquad (2)$$

$$dv_{2,t} = \varepsilon_2 v_{2,t}\, dW^2_t, \qquad t > 0, \qquad (3)$$

where the quantities ε_i, i = 1,2, and β are real positive constants such that $\varepsilon_1 \leq \varepsilon_2$ and $\beta \in [0,1]$. The fact that $v_{1,t}$, $v_{2,t}$, $t > 0$, vary on different time scales is expressed by the condition $0 < \varepsilon_1 << \varepsilon_2$. The processes $W^{0,1}_t$, $W^{0,2}_t$, W^1_t, W^2_t, $t > 0$, are standard Wiener processes such that $W_0^{0,1} = W_0^{0,2} = W_0^1 = W^2_0 = 0$, and $dW^{0,1}_t$, $dW^{0,2}_t$, dW^1_t, dW^2_t, $t > 0$, are their stochastic differentials. The correlation structure of the model is defined by the following assumptions:

$$< dW^1_t\, dW^2_t > \ = \ 0\ ,\ t > 0, \qquad (4)$$

$$< dW^{0,1}_t\, dW^1_t > \ = \ \rho_{0,1}\, dt,\ t > 0, \qquad (5)$$

$$< dW^{0,1}_t\, dW^2_t > \ = \ 0\ ,\ t > 0, \qquad (6)$$

$$< dW^{0,2}_t\, dW^1_t > \ = \ 0\ ,\ t > 0, \qquad (7)$$

$$< dW^{0,2}_t\, dW^2_t > \ = \ \rho_{0,2}\, dt,\ t > 0, \qquad (8)$$

$$< dW^{0,1}_t\, dW^{0,2}_t > \ = \ 0,\ t > 0, \qquad (9)$$

where $< \cdot >$ denotes the expected value of $\cdot$ and the quantities $\rho_{0,1}$, $\rho_{0,2} \in (-1,1)$ are constants known as correlation coefficients. The autocorrelation coefficients of the previous stochastic differentials are equal to one. When the model is multi-scale (i.e. when $0 < \varepsilon_1 << \varepsilon_2$) the meaning of the assumptions (4), (5), (6), (7), (8), (9) is that the stochastic differentials on the right hand side of (1), (2), (3) associated to the two (long and short) time scales are independent. When the condition $0 < \varepsilon_1 << \varepsilon_2$ holds it is likely to observe abrupt changes in the forward rates/prices variable.
The equations (1), (2), (3) are equipped with the initial conditions:

$$x_0 = \tilde{x}_0, \qquad (10)$$

$$v_{1,0} = \tilde{v}_{1,0}, \qquad (11)$$

$$v_{2,0} = \tilde{v}_{2,0}, \qquad (12)$$

where $\tilde{x}_0$, $\tilde{v}_{i,0}$, $i = 1,2$, are random variables that we assume to be concentrated in a point with probability one. For simplicity we identify the random variables $\tilde{x}_0$, $\tilde{v}_{i,0}$, $i = 1,2$, with the points where they are concentrated. We assume $\tilde{v}_{i,0} > 0$, $i = 1,2$.

The stochastic differential equations (1), (2), (3), the initial conditions (10), (11), (12), the assumptions on the correlation coefficients (4), (5), (6), (7), (8), (9) and the conditions on the coefficients β, $\varepsilon_i > 0$, $i = 1,2$, define the multiscale SABR model. Note that equations (2), (3) are a two factor volatility model. This model generalizes the SABR model introduced in 2002 by Hagan et al. [1] that is defined by the following system of stochastic differential equations:

$$dx_t = |x_t|^{\beta} v_t dW_t, \; t > 0, \qquad (13)$$

$$dv_t = \varepsilon \, v_t \, dQ_t, \qquad t > 0, \qquad (14)$$

where $\beta \in [0,1]$ and $\varepsilon > 0$. The coefficients β and ε of (13), (14) are known respectively as β-volatility and as volatility of volatility. Moreover W_t, Q_t, $t > 0$, are standard Wiener processes such that $W_0 = Q_0 = 0$, dW_t, dQ_t, $t > 0$, are their stochastic differentials and we have:

$$< dW_t \, dQ_t > \; = \; \rho \, dt, \; t > 0, \qquad (15)$$

where $\rho \in (-1,1)$ is a constant called correlation coefficient. The equations (13), (14) are equipped with the initial conditions:

$$x_0 = \tilde{x}_0, \qquad (16)$$

$$v_0 = \tilde{v}_0, \qquad (17)$$

where $\tilde{x}_0$, $\tilde{v}_0$ are random variables that we assume to be concentrated in a point with probability one and that, for simplicity, we identify with the points where they are concentrated. Moreover we assume that $\tilde{v}_0 > 0$. Note that equation (14) is a one factor volatility model.
Several empirical studies have shown that two factors volatility models describe the behaviour of financial prices more accurately than one factor volatility models (see for example [2], [3] and the references therein). These studies motivate the introduction of multiscale SABR models. We study the normal and lognormal SABR and multiscale SABR models. The normal and lognormal SABR models correspond respectively to the choices $\beta = 0$ and $\beta = 1$ in equation (1) (multiscale SABR) and in equation (13) (SABR). Under the hypotheses (4), (5), (6), (7), (8), (9) on the correlation coefficients in [4] closed form and "easy to use" formulae for the

transition probability density functions of the normal and lognormal multiscale SABR models and for the prices of the corresponding European put and call options are deduced. The formulae for the transition probability density functions are three dimensional integrals of explicit integrands. However due to the special form of the integrands these three dimensional integrals can be evaluated using a standard quadrature rule at the computational cost of a two dimensional integral.

The computational cost can be further decreased using ad hoc quadrature rules. In fact the integrals are Fourier integrals of integrands containing the product of two copies of a function evaluated in two different points. This function is a one dimensional integral of an explicitly known integrand. Once chosen a grid in the conjugate variable of the Fourier transform the integrals that define the two copies of the function mentioned above can be evaluated in parallel. That is combining the FFT algorithm with the special features of the integrands ad hoc quadrature rules to evaluate the transition probability density function and the corresponding option prices for the normal and lognormal multiscale models have been developed. These quadrature rules allow a fully parallelizable and scalable evaluation of the models.

The method used to study the multiscale SABR models is applied to the study of the normal and lognormal SABR models [4]. For these models some new closed form formulae for the transition probability density functions of their state variables and for the prices of the European call and put options are deduced. The transition probability density functions of the normal and lognormal SABR models are expressed as one dimensional integrals of explicit integrands.

In the normal SABR model case the formula for the transition probability density function deduced in [4] is an elementary formula that can be used instead of formula (120) of [5]. This last formula is the one commonly used in mathematical finance and is based on the Mc Kean formula [1], [5] for the heat kernel of the Poincaré plane. In the lognormal SABR model case the formula for the transition probability density function deduced in [4] is a special case of a new formula that gives the transition probability density function of the Hull and White stochastic volatility model [6] in presence of (possibly nonzero) correlation between the stochastic differentials appearing on the right hand side of the prices/rates and volatility stochastic differential equations. The formulae for the transition probability density functions deduced in [4] are based on some recent results of Yakubovic [7] on the heat kernel of the Lebedev Kontorovich Transform. A calibration problem for the normal and lognormal SABR and multiscale SABR models is studied. The calibration problem considered uses as data a set of option prices observed at a given time and is formulated as a constrained nonlinear least squares problem [4].

Let us show some numerical results obtained solving this calibration problem using real data. We restrict our attention to the lognormal SABR and multiscale SABR models.

We consider the daily observed values of the U.S.A. five-Year Interest Rate Swap expressed in percent and the corresponding futures prices having maturity September 30th, 2011 and the prices of the corresponding European call and put options with expiry date September 19th, 2011 and strike prices $K_i = 106+0.5*(i-1)$, $i = 1,2,...,18$. The rates, the futures prices and the option prices are observed in the period going from September 14th, 2010, to July 20th, 2011. The futures and option prices are daily prices and are the closing price of the day. The strike prices K_i, $i = 1,2,...,18$, of the options are expressed in hundreds of base points.

Using these option prices as data we calibrate the lognormal models every day for approximately two months, that is we calibrate the lognormal models in the period going from September 14th, 2010 to November 15th, 2010. In this period there are significant oscillations in the value of the futures prices. In fact, for example, on October 12th, 2010 the futures price is 112.093 and on November 15th, 2010 the futures price goes down to 107.875. In the first part of the period (September 14th, 2010- October 14th, 2010) the oscillations of the futures price are small and in the second part (October 14th, 2010- November 15th, 2010) in particular around the end of October 2010 there is a fall of the futures price.

The parameter values obtained in the calibration of the lognormal models are shown in *figure 1*. We can see from *figure 1* that the values of the parameters remain substantially unchanged in the two months period except for the values of the parameters ε and ε_2 that show a significant change at the end of October 2010 and during the first fifteen days of November 2010. Moreover we use the parameter values obtained with the calibration of the lognormal SABR and lognormal multiscale SABR models to forecast the option prices one day in the future during the two months period mentioned above [4].

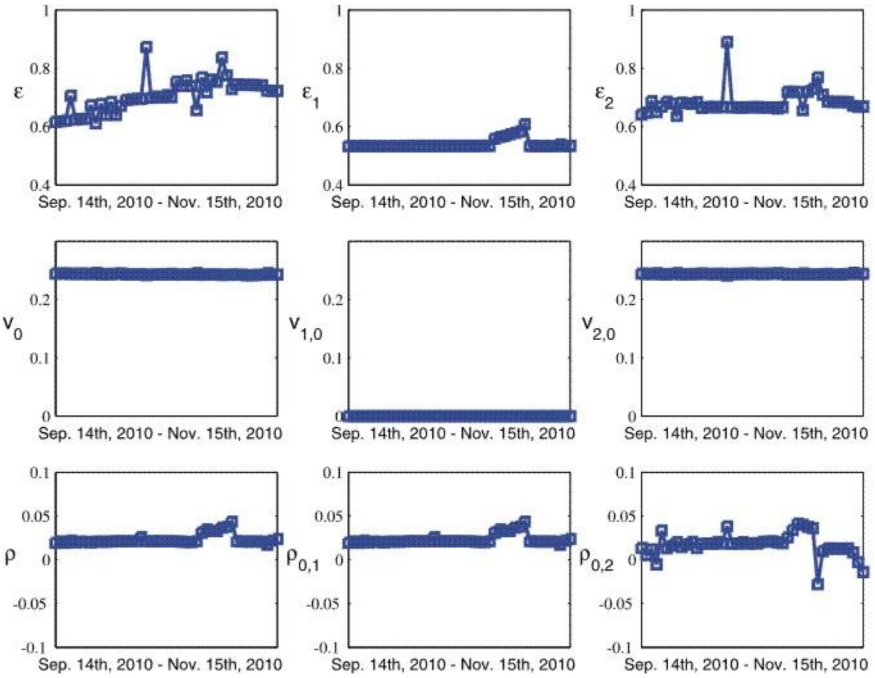

Figure 1: *Parameter values versus time to maturity obtained calibrating the lognormal SABR and multiscale SABR models every day for two months in the period going from September 14th, 2010 to November 15th, 2010 (interest rate swap experiment).*

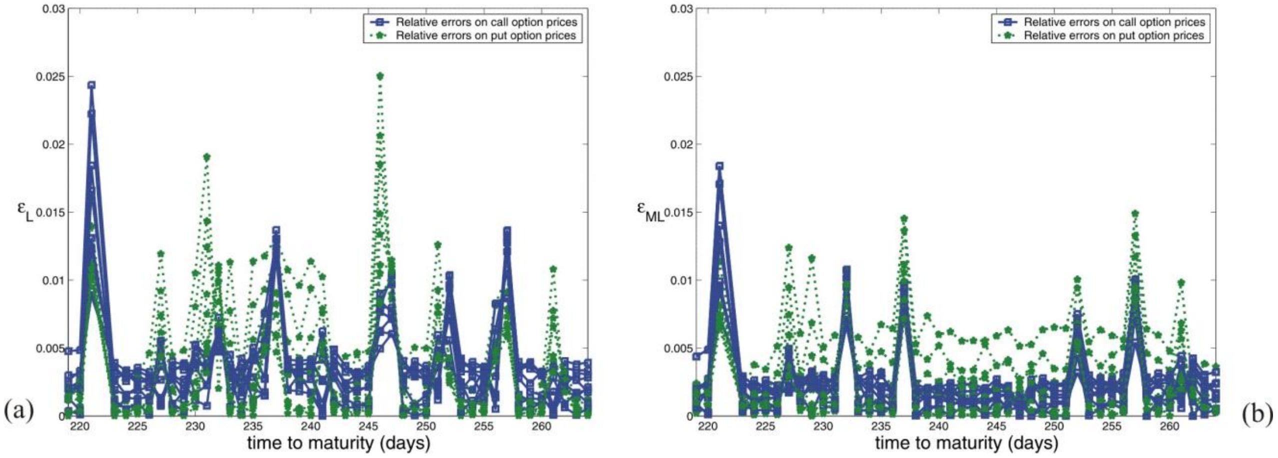

Figure 2: *Relative errors on the forecast prices one day in the future of call and put options obtained using lognormal SABR model (a) and lognormal multiscale SABR model (b) versus time to maturity expressed in days. The period considered goes from September 14th, 2010, to November 15th, 2010 (interest rate swap experiment).*

The forecast option prices are obtained using as value of the underlying asset the value observed the day of the forecast. Finally *figure 2* shows the relative errors on the forecast option prices one day ahead of the current day obtained using the parameter values shown in *figure 1*.
We can see that the lognormal multiscale SABR model gives more accurate approximations than the lognormal SABR model in particular the average and the worst case of the relative errors are respectively 0.0037, 0.028 for the lognormal SABR model and 0.0025, 0.025 for the multiscale SABR model. That is the lognormal multiscale SABR model improves substantially the lognormal SABR model. This is particularly evident in the forecasting of at the money option prices.

The work of the authors and of their coauthors in mathematical finance is illustrated in the website: http://www.econ.univpm.it/recchioni/finance .

References

[1] HAGAN, P. S., KUMAR, D., LESNIEWSKI, A. S., WOODWARD, D. E. "*Managing smile risk*" Wilmott Magazine, September (2002) pp. 84-108. http://www.wilmott.com/pdfs/021118_smile.pdf .

[2] FATONE, L., MARIANI, F., RECCHIONI, M.C., ZIRILLI, F. *"An explicitly solvable multi-scale stochastic volatility model: option pricing and calibration problems"* Journal of Futures Markets **29**(9) (2009) pp. 862-893 (http://www.econ.univpm.it/recchioni/finance/w7).

[3] FATONE, L., MARIANI, F., RECCHIONI, M.C., ZIRILLI, F. *"The analysis of real data using a multiscale stochastic volatility model"* European Financial Management (2011) doi: 10.1111/j.1468-036X.2010.00584.x (http://www.econ.univpm.it/recchioni/finance/w9).

[4] FATONE, L., MARIANI, F., RECCHIONI, M.C., ZIRILLI, F. *"Some explicitly solvable SABR and multiscale SABR models: option pricing and calibration"* submitted to Finance & Stochastics (2012) (http://www.econ.univpm.it/recchioni/finance/w14).

[5] HAGAN, LESNIEWSKI, A. S., WOODWARD, D. E. *"Probability Distribution in the SABR Model of Stochastic Volatility"*, (2005) downloadable from http://lesniewski.us/papers/working/ProbDistrForSABR.pdf .

[6] HULL, J., WHITE, A. *"The pricing of options on assets with stochastic volatilities*" The Journal of Finance **42** (1987) pp. 281-300.

[7] YAKUBOVICH, S.B. *"The heat kernel and Heisenberg inequalities related to the Kontorovich-Lebedev transform*" Communications on Pure and Applied Analysis **10**(2) (2011) pp. 745-760.

NUMERICAL MODELLING OF WALL EFFECTS IN SLAGGING COAL GASIFIERS.

Fiorenzo Ambrosino, *ENEA - UTICT-HPC, C.R. Portici*
Francesco Saverio Marra, *Istituto di Ricerche sulla Combustione – CNR, Napoli*
Andrea Aprovitola, *Istituto di Ricerche sulla Combustione – CNR, Napoli*

Introduction

The development of low emission coal combustion technologies is a key issue to ensure energy availability in the near future, before that new energy technologies based only on fully renewable sources will became able to supply all the energy demand. Indeed coal combustion is considered to be among the main primary energy supply that will be used for very long time. The Integrated Gasification Combined Cycles (IGCC) technology is among the most promising ones to enable low emissions production of energy from coal. Therefore, the modelling of coal gasification processes is an important step for the proper design of new primary energy transformation plants.

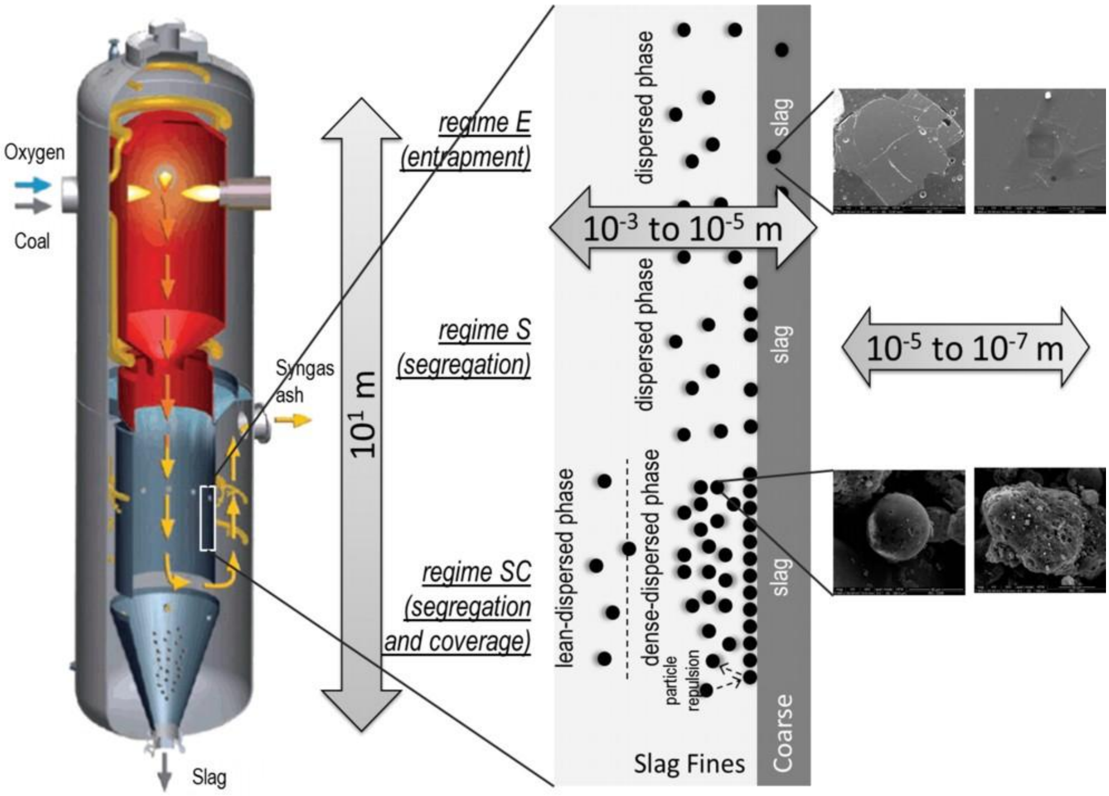

Figure 1. *Major scales involved in the char/slag interaction. In the center, the definition of the possible regimes that can establish close to the slag covered walls of the gasifier. Rightmost figures: SEM results from samples collected in the slag coarse layer (top) and in the slag fines layer [1].*

Entrained-flow gasifiers adopted in these plants are characterized by operating conditions that promote ash migration/deposition onto the reactor walls, whence the ash is drained as a molten phase. The optimal design of gasifiers, to control the flow pattern and therefore the residence times of fed coal particles, is essential to rise the performance and lower the environmental impact of such systems. Because of the wide range of spatial and temporal scales involved in these phenomena, numerical simulation of the fate of the flying fine char particles is a difficult and very computationally expensive task. The CRESCO [2] computing facilities have offered the opportunity to develop numerical models able to predict important aspects of the fate of coal and ash particles that strongly influence the performance of coal gasifiers.

Despite the fact that several entrained-flow gasifiers have been in operation for decades, modeling coal gasification under entrained-flow conditions is still a challenging goal with broad areas of uncertainty. The recent literature on entrained-flow gasification is addressing the fate of char particles as they impinge on the wall slag layer [3-5]. Montagnaro and Salatino [6] highlighted the relative importance of the parallel pathways of coal conversion consisting of entrained-flow of carbon particles in a lean-dispersed gas phase vs. segregated flow of a dense curtain of char particles in the proximity of the gasifier walls.

Comprehensive models, supported by CFD-based detailed descriptions of flow, temperature and concentration fields, consider the relevance of complex hydrodynamics and multiphase flow to the gasifier performance [7-12]. Almost all of these models rely on the Reynolds Average Navier-Stokes (RANS) [11] approach to take into account the effect of the turbulence on the flow field, actually solving for field variables averaged in time. The time averaging procedure strongly limits the predictive capabilities of the simulations. Hence RANS closure do not allow an overall description of the unsteady phenomena like turbulent dispersion of particles, coal particle combustion, homogeneous gas phase reactions, turbulence-wall and particle-wall interactions. Despite such limitations, the adoption of this approach is unavoidable to limit the computational power required. Entrained-flow gasifiers are indeed characterized by a wide range of turbulence scales. Typical integral scale dimensions are on the order of 10 m, while the Kolmogorov scale can be estimated on the order of 0.1 mm, being the bulk Reynolds number, computed adopting the plug-flow velocity and the gasifier diameter, on the order of 10^6. Even adopting this level of approximation, the computational resource required is huge and several simplifications need to be introduced. Specifically, within this approach the particle-boundary interaction is modelled by means of empirical models that already postulate the leading interaction mechanism.

To really predict this mechanism more detailed models, coupling the Lagrangian particle tracking with a Large Eddy Simulation (LES) or a Direct Numerical Simulation (DNS) approach, are required for the Eulerian gas phase. Their application to full-scale configurations is computationally prohibitive but they allow exploring the physical behaviour of near-wall particle segregation and the role of relevant parameters if performed in simplified flow configurations.

The aim of this study is to demonstrate the possibility to gather information from models developed at different scales and levels of approximation to numerically investigate phenomena occurring at the smallest scales in a gasifier, when computational resources as those available at the CRESCO facilities [2], are used. A particular emphasis is devoted to the char particles-slag interaction.

Adopting the OpenFOAM [13] toolkit, a multi-level procedure is built to obtain a multilevel RANS and LES approach. The adoption of OpenFOAM offered the advantage, in investigating very computationally expensive CFD problems, to be not limited from licencing cost in the adoption of a high number of computational cores. In the proposed multilevel procedure, RANS-based simulations of the full-scale geometry with coal particles injection and tracking aim to obtain the general behaviour of the flow field and particle trajectories. Then, a very detailed model, based on the Discrete Particle Method (DPM) for the solid phase [14] and the LES approach for the gas phase [15], has been adopted.

The procedure, that is still under construction, is illustrated with reference to a simple configuration, proposed by Sommerfeld and Qiu [16]. This configuration provides a kind of benchmark, and extensive data have been published on this configuration, both from experimental measurements [16] and numerical investigations with both RANS [16] and LES [17] approaches. This paper reports the contribute given by the use of the CRESCO [2] computing facilities.

Activity Description

The Euler-Lagrangian (E-L) approach for the gas and particle phases respectively is a good compromise to model predictively the particle dispersion in gas and focus on the mechanisms of wall-particle interaction.
In OpenFOAM, the spatial discretization of the gas phase equations is performed with a FV method on arbitrary 3D domains, partitioned through unstructured meshes of polyhedral cells. In this work, aiming to a prompt generalization of the model toward conditions of non-uniform temperature, the equations for a weakly-compressible fluid flow are solved adopting a semi-implicit, pressure-velocity, iterative solution method (PISO).
A one-way coupling approach is considered. It means that the particle phase motion is affected by fluid phase flow conditions but the contrary does not hold. This is considered a valid assumption if the particle volumetric concentration is not too high (dispersed regime) as it happens to be the case for usual coal load in gasifiers.

Being the ratio of particles density over fluid density very large (order 10^3), it is possible to neglect the added mass, Basset (history effect), Magnus (rotation of the particle), Saffman (slip-shear lift force), pressure and buoyancy components of the force acting on the particle. Tracked particles are considered point-wise. They are assumed to be rigid hard spheres. So the Basset-Boussinesq-Oseen (BBO) equation can be reduced to the equation of motion for a point-particle [18], that only considers the drag and gravitational force. The equations of particles motion were solved via a Lagrangian particle tracking (LPT) algorithm. Relevant forces acting on particles are Stokes drag and buoyancy. The drag coefficient is assumed to be function of Reynolds particle number. Gravity is not considered in the detailsed LES level.

The algorithm implemented in OpenFOAM for the LPT is described in [19] in which is shown the TrackToFace method. This method practically consists of moving the particle between faces it crosses in the time step duration. At each time step it is easy to find the cell in witch the particle is having a very efficient algorithm. It is also able to run in parallel.
To optimize the performances of RANS computations the parcel object is used instead of the particle. A parcel is a group of identical particles considered to be coincident so they have all the same trajectory.

In the first step of the multilevel approach, an Unsteady-RANS (U-RANS) method has been applied to describe the motion of Eulerian gas phase in the gasification chamber investigated by Sommerfeld and Qiu [15]. Terms in the model equations describing the contribution of turbulent transport are closed adopting the compressible version of the $k - w$ SST model [20].

Further details on the model are available in [21].
A sketch of the prototype gasifier geometry is reported in *figure 2* (*left*), where all lengths are non-dimensionalised using the radius R = 0.032 m of the outer wall of the external annular jet as the reference length. Two gas streams are coaxially injected into the main cylindrical chamber. The outer stream feeds gas, while the inner stream feeds gas loaded with particles. The main chamber extends for 1.5 m, corresponding to 7.8-times the diameter of the main chamber (0.192 m). The mass flow rates of the feeding are 9.9×10^{-3} kg s^{-1} and 38.3×10^{-3} kg s^{-1} related to the central gas jet and the annular swirled gas jet, respectively. The swirl number, computed as the ratio of the axial flux of angular momentum to the axial flux of linear momentum, is assumed equal to 0.47 for all the following computations.

The char particles migration on the slag layer is favoured by the turbulent motion induced by the swirl applied at the inlet of the flow domain. The turbulent structures, whose dimensions are on the order of the swirler diameter, possess an anisotropic behaviour and their computation is strongly influenced by the domain boundaries conditions. For this reason, a time-dependent description of their dynamics is preferred to a time-averaged approach to investigate the deposition mechanisms. The U-RANS method is therefore adopted [15].

The computational mesh adopted is multi-block and structured, and it is composed of about 150000 cells. An additional volume is added at the outlet section of the gasifier, to allow a better reproduction of the recirculation region in a manner similar to the simulations reported in Apte et al. [17]. For the continuous phase, all parameters defining boundary conditions and thermodynamic fluid properties are chosen so as to reproduce the reference case [16]. Simulations were performed involving a number of particles from 10^5 to 10^6, a level of detail that allowed to obtain a clear picture of the multiphase flow behaviour responsible for char deposition phenomena.
These simulations enabled to estimate the effect of swirl and tangential flow on the bulk-to-wall char particle deposition rate and to identify the input parameters for the detailed LES based models.

In *figure 2* (*right*), the particles pathlines, obtained by post-processing the computed particle positions for several time steps from 6 to 9 s and coloured according to the velocity magnitude of the tracing particles, are shown together with the contour of the gas axial velocity component in the midplane section. The different behaviour of the two classes of particles is clearly recognizable: lighter particles are drawn by the flow field after few rebounds when they firstly hit the walls, while heavier particles are substantially unaffected by drag, continuing to rebound along all the gasifier length. Different zones of the gasifier with respect to the behaviour of particle migration to the wall can be (at least qualitatively) identified, depending upon the particle diameter. The first zone, close to the inlet section, is in shadow with respect to the particle trajectories. The second successive zone is characterized by an intense particle deposition rate, mainly due to the centrifugal motion induced by the swirl flow. In the third region particles remain confined within a thin zone close to the walls: smaller particles remain substantially deposited on the walls, moving very slowly well inside the boundary layer; coarser particles maintain a substantial level of inertia and continue to rebound at the walls, following spiral-like trajectories close to the walls. Eventually, a fourth zone is identified at the end of the gasifier, where disturbances induced by the approaching outlet section lift the particles from the wall. From this picture, it is possible to conceive two idealized configurations for the detailed simulation of the particle behaviour in the second and third zone, as it will be illustrated in the next section.

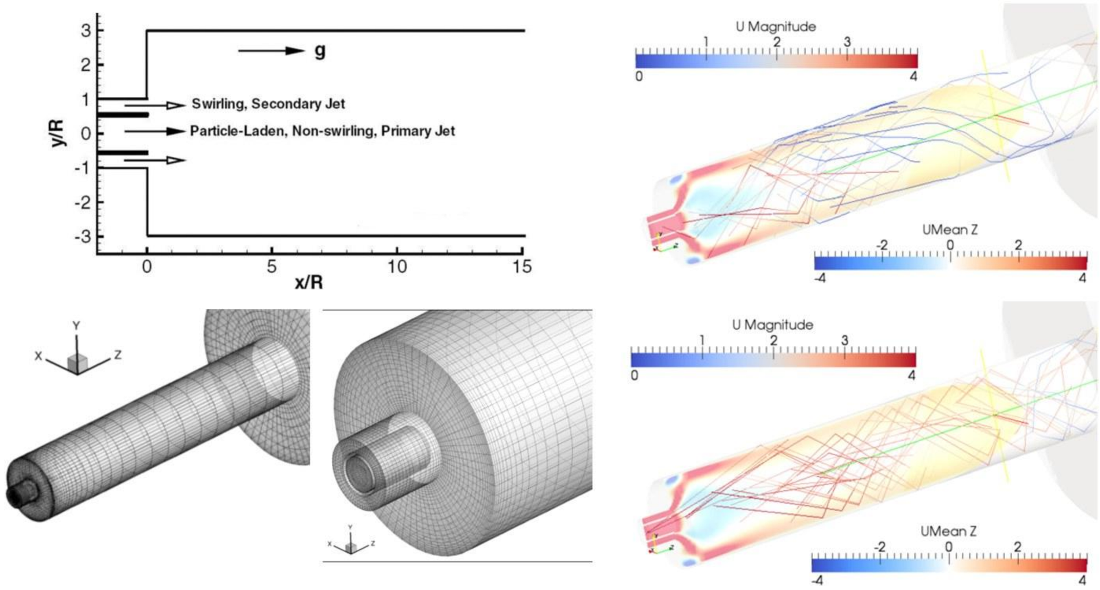

Figure 2: *Left: schematic diagram of the entrained-flow gasifier and computational domain and grid for the 3D RANS computations adopted at level 2 of the procedure.*
Rigth: particles pathlines in the gasifier for $d_p = 45\ \mu m$ *(top) and* $d_p = 102\ \mu m$ *(bottom). U magnitude scale* $(m\ s^{-1})$ *refers to particle velocity,* U_{mean} *Z scale* $(m\ s^{-1})$ *refers to mean flow axial velocity.*

In the second step of the multilevel procedure the LES method to solve the model equations of the Eulerian continuous phase is adopted. This class of problem usually needs a very big computational power due to both the high number of computational cells required to properly select the cut-off threshold of the LES filter and the high number of particles to track. Turbophoresis effects of the fluid phase on particle motion are very sensitive to the dimension of the resolved turbulence scales. Therefore, to model correctly the particle-wall interaction phenomena, there is the need of a good resolution of the mesh size near the wall and an appropriate turbulence model. The one equation dynamic model for Sub Grid Scale (SGS) terms is used. Gravity force is not considered in the momentum source term. The gas model used is the perfect gas.

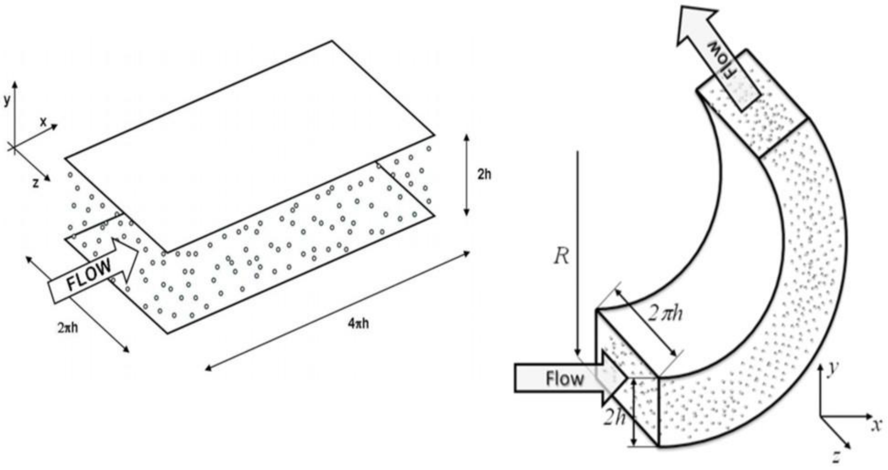

Figure 3: *Periodic planar channel (left) and periodic curved channel (right) configurations adopted at level 3 of the computational procedure; h = 0.02 m.*

The two configurations considered, as emerging from results of the RANS model, are a periodic planar channel and a periodic curved channel (*figure 3*). The first configuration aims at characterizing an essentially parallel wall-bounded turbulent flow; the second one aims at characterizing a non-parallel tangential wall-bounded turbulent flow. These two configurations are solved by considering bounding walls with variable properties, in order to simulate the presence of a slag with different levels of coverage. In this work, only a very simple representation of the wall properties, and consequently of the particle-wall interaction, is considered: only the normal restitution coefficient is varied to reproduce different levels of normal momentum exchange during the collision of particles with the wall as due to a fully-molten slag or a partially-molten slag, therefore having different values of elasticity, or a fully-covered slag over which a thin layer of deposited solid particles may induce elastic behaviour. The gravitational term has been neglected, so the particle motion is only driven by the drag force. Two different clouds of 100000 particles have been considered, both with parcels made of one particle each. In the first cloud, particles have $d_p = 45$ μm (St = 5) while, in the second cloud, particles have $d_p = 102$ μm (St = 25). These clouds are the same adopted in the reference simulation [22].

After the establishment of the fully-developed turbulent flow, particles are simultaneously injected at random positions in the channel, all with zero velocity. Then each particle is tracked independently. Together with the fact that near walls, the mesh size required to correctly reproduce by the LES approach the viscous sub-layer becomes very small, of the same order of magnitude of the particle diameter, these are the main reasons demanding for the computational power available at CRESCO.

Four different values of the coefficient of restitution were tested: $\varepsilon = 0.2$, $\varepsilon = 0.5$, $\varepsilon = 0.8$ and $\varepsilon = 1$. Results for these configurations are illustrated in [1] and [23]. They clearly show the ability of the model to catch the different dynamics of particles accumulation and segregation occurring near the slag layer changing the main parameters. It is recalled here that LES results do confirm the occurrence of a region near the wall slag layer in which particles impacting on the slag accumulate to an extent that depends on the system fluid-dynamics, on particles Stokes number and on the coefficient of restitution relevant to particle-boundary interaction.

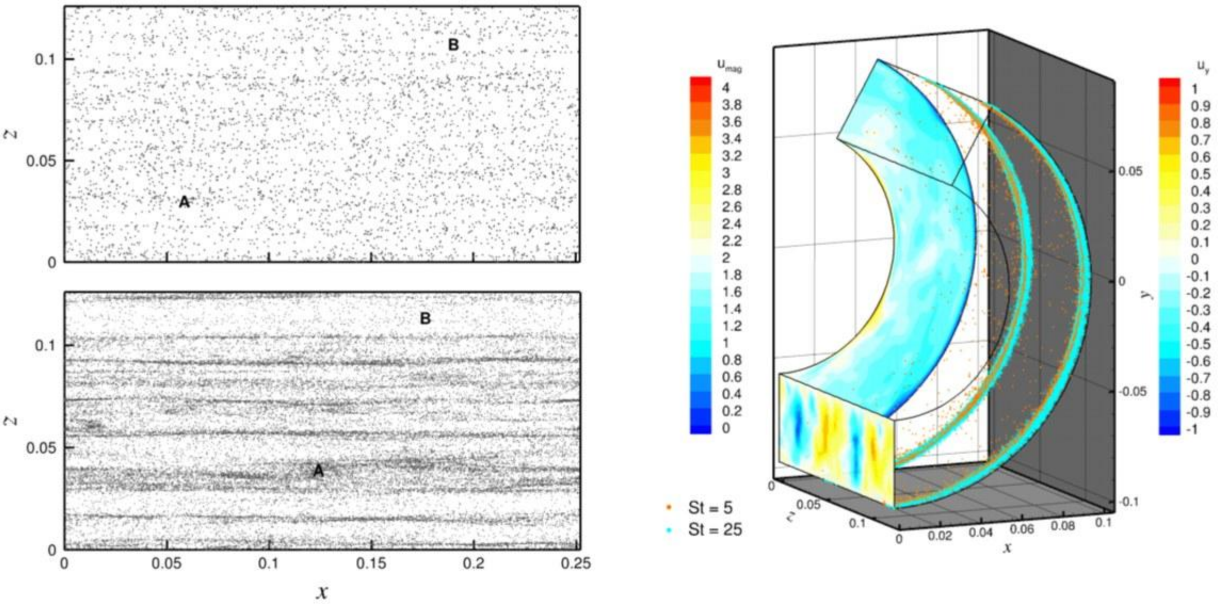

Figure 4: *Left: snapshots of the particles distribution near the wall (maximum distance less than 1 mm) after 1200 s from injection in the planar channel flow case with coefficient of restitution* $\varepsilon = 0.2$, *St = 5 (top) and St = 25 (bottom). Right: computed distribution of particles after 80 s from injection, for either St = 5 or St = 25 and* $\varepsilon = 1$, *together with sections of the instantaneous velocity field (values in* $\mathrm{m\ s^{-1}}$*).*

All simulations have been run on the CRESCO HPC facilities provided by the ENEA (Italy). The second section of the facility has been used so the computations were made on

Xeon Quad-Core Clovertown E5345 processors (2.33GHz, 1333MHz, 8MB L2), 16 GB RAM or dual Intel Xeon Quad-Core Turbo Boost Nehalem E5530 processors (2.40GHz, 8MB L3), 16GB RAM or dual Intel Xeon Quad-Core Turbo Boost Westmare E5620 processors (2.40GHz, 8MB L3), 16GB RAM. The high performamce computing demand is notable. The optimum number of cores established for these runs has been found to be 64 for the RANS level and 96 for both LES level configurations.

For the gasifier configuration a typical RANS simulation of the particle laden flow (one-way coupling model between fluid and particle phases, 2 particle clouds for a total of by about 300000 parcels tracked by the LPT algorithm) has required about 90 hours of wall time of parallel computing (64 cores) to compute 5 seconds of motion.

For the planar channel configuration, a typical LES simulation of the particle laden flow (one-way coupling model between fluid and particle phases, 8 particle clouds each of them made by 100000 particles all tracked by the LPT algorithm) has required about 650 hours of wall time (that is about a month) of parallel computing (96 cores) to compute the 1200 seconds of the motion required to reach statistically steady state conditions.

Numerical simulation results do confirm the establishment of a region near the wall slag layer, the dense-dispersed annular phase referred to in the Introduction, leading to the formation of the slag fines. Interestingly, the segregation of char particles near the wall is more evident for the curved channel flow geometry, a more realistic case, and is enhanced for coarser particles. Particle accumulation appears to take place within a relatively short time since particle injection. The establishment of this dense-dispersed phase is considered to be beneficial to carbon gasification, due to the increased mean residence time in the gasifier of char particles belonging to this phase.

Acknowledgements

This work is a collaboration between ENEA, in particular with the technical unit UTICT-HPC, and the Istituto di Ricerche sulla Combustione (IRC) of the CNR. It is also part of the PhD research work of the first author [23] at the Department of Chemical Engineering (DIC) of the University of Naples Federico II. Authors are very grateful to Prof. Piero Salatino and Prof. Fabio Montagnaro of the University of Naples Federico II.

References

[1] AMBROSINO, F., APROVITOLA, A., BRACHI, P., MARRA, F.S., MONTAGNARO, F. AND SALATINO, P. *"Char-Slag Interaction During Entrained-Flow Gasification: From Experimental Evidence To Numerical Simulations"*. 12th International Conference on Multiphase Flow In Industrial Plant, Ischia, 21-23 September 2011

[2] BRACCO, G., PODDA, S., MIGLIORI, S., D'ANGELO, P., QUINTILIANI, A., GIAMMATTEI, D., DE ROSA, M., PIERATTINI, S., FURINI, G., GUADAGNI, R., SIMONI, F., PEROZZIELLO, A., GAETANO, A. DE, PECORARO, S., SANTORO, A., SCIO, C., ROCCHI, A., FUNEL, A., RAIA, S., APREA, G., FERRARA, U., NOVI, D., , GUARNIERI, G. *"CRESCO HPC System Integrated into ENEA-GRID Environment"*. In: FINAL WORKSHOP OF GRID PROJECTS, PON RICERCA 2000-2006, (2009).AVVISO 1575.

[3] SHANNON, G.N., ROZELLE, P.L., PISUPATI, S.V. AND SRIDHAR, S., (2008). "*Conditions for entrainment into a FeO_x containing slag for a carbon-containing particle in an entrained coal gasifier."* Fuel Processing Technology, **89**, 1379–1385.

[4] LI, S. AND WHITTY, K.J., "*Ash Deposition Behavior during Char-Slag Transition under Simulated Gasi_cation Conditions." Energy & Fuels*, (2009) **23**, 1998–2005.

[5] LI, S., WU, Y. AND WHITTY, K.J., *"Ash Deposition Behavior during Char-Slag Transition under Simulated Gasification Conditions"* Energy & Fuels, (2010) **24**, 1868–1876.

[6] MONTAGNARO, FABIO, & SALATINO, PIERO. "Analysis of char-slag interaction and near-wall particle segregation in entrained-ow gasi_cation of coal". Combustion and Flame **157** (2010), pp. 874-883.

[7] SEGGIANI, M., Modelling and simulation of time varying slag flow in a Prenflo entrained-flow gasifier (1998). Fuel, **77**, 1611–1621.

[8] FLETCHER, D.F., Haynes, B.S., Christo, F.C. and Joseph, S.D., "*A CFD based combustion model of an entrained flow biomass gasifier"*; Applied Mathematical Modelling, (2000) 24, 165–182.

[9] CHEN, C., HORIO, M. AND KOJIMA, T., "Use of numerical modeling in the design and scale-up of entrained ow coal gasifiers" Fuel, (2001) **80**, 1513–1523.

[10] VICENTE, W., OCHOA, S., AGUILLÓN, J. AND BARRIOS, E., *"An Eulerian model for the simulation of an entrained flow coal gasifier"* Applied Thermal Engineering, (2003) **23**, 1993–2008.

[11] WATANABE, H. AND OTAKA, M., "*Numerical simulation of coal gasification in entrained flow coal gasifier"* Fuel, (2006) **85**, 1935–1943.

[12] WU, Y., SMITH, P.J., ZHANG, J., THORNOCK, J.N. AND YUE, G., *"Effects of turbulent mixing and controlling mechanisms in an entrained flow coal gasifier"* Energy & Fuels, (2010) **24**, 1170–1175.

[13] OpenFOAM The Open Source Computational Fluid Dynamics (CFD) Toolbox website, http://www.opencfd.co.uk/openfoam/

[14] LOTH, E., TRYGGVASON, G., TSUJI, Y., ELGHOBASHI, S.E., CROWE, C.T., BERLEMONT, A., REEKS, M., SIMONIN, O., FRANK, T., ONISHI, Y. AND VAN WACHEM, B., Multiphase Flow Handbook. CRC Press, (2006).

[15] SAGAUT, P., Large Eddy Simulation for Incompressible Flows. Springer, (2001).

[16] SOMMERFELD, M. AND QIU, H.H., "*Characterization of particle-laden, confined swirling flows by phase-doppler anemometry and numerical calculation*"; International Journal of Multiphase Flow, (1993) **19**, 1093–1127.

[17] APTE, S.V., MAHESH, K., MOIN, P. AND OEFELEIN, J.C., *"Large-eddy simulation of swirling particle-laden flows in a coaxial-jet combustor International Journal of Multiphase Flow"*, (2003) **29**, 1311–1331.

[18] CROWE, C.T. AND MICHAELIDES, E.E., *Multiphase Flow Handbook*. CRC Press (2006).

[19] MACPHERSON, GRAHAM B., NORDIN, NIKLAS, & WELLER, HENRY G. *"Particle tracking in unstructured, arbitrary polyhedral meshes for use in CFD and molecular dynamics"*. Communications in Numerical Methods in Engineering, **25** (2009), pp. 263-273.

[20] MENTER, F. AND ESCH, T., *"Elements of Industrial Heat Transfer Prediction" 16th Brazilian Congress of Mechanical Engineering (COBEM)* (2001).

[21] F. AMBROSINO, A. APROVITOLA, P. BRACHI, F. S. MARRA, F. MONTAGNARO AND P. SALATINO. "*Open Source Codes for the Development of Multilevel Modelling of Entrained-flow Coal Gasifiers"*, 5th Open Source CFD International Conference, 3-4 November, Paris-Chantilly, France, 2011.

[22] MARCHIOLI, C., SOLDATI, A., KUERTEN, J.G.M., ARCEN, B., TANIRE, A., GOLDENSOPH, G., SQUIRES, K.D., CARGNELUTTI, M.F., & PORTELA, L.M. *"Statistics of particle dispersion in direct numerical simulations of wall-bounded turbulence: Results of an international collaborative benchmark test"* International Journal of Multiphase Flow **34** (2008) pp. 879-893.

[23] AMBROSINO, F. *"Wall effects in partcile-laden flows"* PhD thesis (2011), University of Naples Federico II.